Dissertation

Search for Neutral Higgs Bosons of the Minimal Supersymmetric Standard Model in the $\tau_e\tau_\mu$ Decay Mode at $\sqrt{s} = 7\,\mathrm{TeV}$ with the ATLAS Detector

Holger von Radziewski

Fakultät für Mathematik und Physik
Albert-Ludwigs-Universität Freiburg

Search for Neutral Higgs Bosons of the Minimal Supersymmetric Standard Model in the $\tau_e\tau_\mu$ Decay Mode at $\sqrt{s} = 7\,\mathrm{TeV}$ with the ATLAS Detector

Dissertation

zur Erlangung des Doktorgrades der
Fakultät für Mathematik und Physik der

Albert-Ludwigs-Universität
Freiburg im Breisgau

vorgelegt von
Holger von Radziewski

März 2014

Dekan:	Prof. Dr. Michael Růžička
Betreuer der Arbeit:	Prof. Dr. Markus Schumacher
Referent:	Prof. Dr. Markus Schumacher
Koreferent:	Prof. Dr. Gregor Herten
Prüfer:	Prof. Dr. Stefan Dittmaier
	apl. Prof. Dr. Horst Fischer
	Prof. Dr. Markus Schumacher

Datum der mündlichen Prüfung:
19. Mai 2014

Contents

1 Introduction

Over the last century, the evolution of particle accelerators has helped to broaden our understanding of the universe. Observations and measurements at numerous high-energy experiments have led to the evolution of a consistent Standard Model (SM) of particle physics [1,2], which describes the dominant interactions of elementary particles in a gauge theory. The observation of massive gauge bosons requires the inclusion of a mechanism of electroweak symmetry breaking (EWSB), which is accomplished by the Englert–Brout–Higgs–Guralnik–Hagen–Kibble [3] mechanism. This mechanism involves an omnipresent scalar field with non-vanishing vacuum expectation value (VEV) and implies the existence of a Higgs boson (H^{SM}) as an excitation of this field.

Conclusive proof for the existence (or non-existence) of such a particle remained elusive for more than 40 years despite the intense search efforts at the Large Electron–Positron Collider (LEP) and the Tevatron. The design properties of the Large Hadron Collider (LHC) and its experiments were strongly influenced by the requirement of covering the gap between the lower bound of 114.4 GeV from the LEP experiments and theoretical upper bounds on the Higgs boson mass, which is the only free parameter of the SM.

While EWSB can be included in the SM by virtue of the Englert–Brout–Higgs–Guralnik–Hagen–Kibble mechanism, a variety of open questions persist. There is no mechanism in the SM that protects the Higgs boson mass from large quantum corrections. SM parameters must therefore be fine-tuned to high precision to ensure that the Higgs boson mass falls into the desired range, which ensures vacuum stability and unitarity. Supersymmetry (SUSY) [4, 5] accomplishes this by introducing a superpartner particle for each particle of the SM—with a difference of $\pm\frac{1}{2}$ in spin to the respective SM particle. SUSY acts as a custodial symmetry to the Higgs boson mass: If SUSY were a perfect symmetry—implying equal masses of SM particles and their respective superpartners—the corresponding quantum corrections would cancel exactly. Superpartners of equal mass would have already been found in previous experiments if they existed. If it is realized at all in nature, SUSY must therefore be broken, and a mass scale of the order $\mathcal{O}(1\,\mathrm{TeV})$ of the superpartners is expected.

For this and other reasons, the Higgs sectors of the simplest supersymmetric extensions is of great interest—also after the discovery [6, 7] of a SM-like Higgs boson by A Toroidal LHC Apparatus (ATLAS) [8] and the Compact Muon Solenoid (CMS) [9] at a mass of about 126 GeV in 2012. The Minimal Supersymmetric Standard Model (MSSM) predicts the existence of three neutral and two charged Higgs bosons. Large portions of allowed parameter space for the Higgs sectors of supersymmetric models still exist, to which the LHC experiments are sensitive.

In large parts of the parameter space, the couplings of the neutral Higgs bosons to τ leptons and b-quarks are enhanced with respect to the SM, greatly improving the sensitivity of searches focusing on b-associated production and on decays into τ lepton pairs. The decay mode covered by this thesis ($h^0/A^0/H^0 \to \tau_e\tau_\mu$)[1] involves two leptonically decaying τ leptons[2]

[1] Unless the context requires it, the distinction between particles and anti-particles is dropped, e.g., e is used instead of $e^{\pm}$ for an electron or positron.

[2] τ leptons are distinguished by their decay mode: Hadronically decaying τ leptons are denoted by the symbol τ_{had}, while the leptonic decay modes are named for the flavor of the decay products: $\tau_{\mathrm{lep}} = \tau_e/\tau_\mu$.

and contributes to the combined sensitivity of the ATLAS experiment to supersymmetric Higgs sectors. These are evaluated in the $m_{h^0}^{\max}$ scenario and a scenario that assumes only one generic neutral Higgs boson.

Using data taken by ATLAS in 2011, the goal is to probe the region of the m_{A^0}–$\tan\beta$ parameter space which are excluded neither from the LEP experiments nor from the Tevatron. The studies presented within this thesis have been statistically combined with analyses concerned with other decay channels and jointly published by the ATLAS Collaboration in Ref. [10, 11].

The results supercede an analysis of inclusive $\tau_e\tau_\mu$ final states in $1.06\,\text{fb}^{-1}$ of ATLAS data [12], which was published in combination with other $\tau\tau$ decay channels in Ref. [13]. The extension to the full dataset of $4.7\,\text{fb}^{-1}$ taken in 2011 provides sufficient event yields to separately target events from b-associated Higgs boson production in a sample with exactly one b-tagged jet. A complementary sample without b-jets also receives a significant contribution from the gluon fusion signal process.

In order to avoid sources of systematic uncertainty attached to simulation, data-driven background estimation methods have been adopted and developed. The dominant $Z/\gamma^* \to \tau\tau$ background is estimated by the established embedding technique [14], which has been extended in the context of this thesis to better reproduce the impact of the trigger on the transverse momentum spectra of the final-state leptons. For the estimation of the multi-jet background, the low levels of correlation between the reconstructed charge of lepton signatures, isolation variables, and the final discriminant in multi-jet events are exploited by the $ABCD$ method [15]. In the context of this thesis, a method was developed to estimate residual correlations and consider them in the final result. Due to the enhanced role of the t-quark pair production contribution in the b-tagged sample, a data-driven estimation method has been developed for this thesis to enhance the overall sensitivity.

The SM is reviewed briefly in Chapter 2. An emphasis is placed on the electroweak sector and EWSB. The same Chapter motivates the extension of the model by supersymmetry (SUSY) and thus the search for neutral Higgs bosons in the MSSM, whose phenomenology is discussed in more detail.

Chapter 3 then summarizes the key features of the experimental apparatus, focusing on those most relevant to the search presented within this thesis. Chapter 4 gives an overview of the simulation of hadron collisions and introduces the relevant background processes.

Chapter 5 introduces the analysis strategy and the discriminants used to search for Higgs boson decays to τ lepton pairs which subsequently decay to different-flavor light lepton[3] pairs. A special emphasis is placed on the reconstruction of the mass of the Higgs boson candidate. Chapter 6 details the selection criteria applied to the reconstructed objects and to the overall events in the two signal samples. Chapter 7 elaborates on the various background estimation techniques employed in order to optimize the sensitivity of the analysis. Chapter 8 discusses the various sources of systematic uncertainty. Chapter 9 provides a statistical interpretation of the results, and Chapter 10, a conclusion.

[3]Charged leptons are denoted by the symbol $l = e/\mu/\tau$, while only light leptons are referred to by $\ell = e/\mu$.

2 Theory Basics

The Standard Model (SM) of particle physics [1, 2] describes the particles and interactions governing the phenomena of high-energy physics.

This Chapter gives an overview of the SM in Section 2.1, introducing the elementary particles and fields. The electroweak interaction is discussed in more detail, motivating the need for a mechanism of electroweak symmetry breaking (EWSB). Subsection 2.1.5 reviews the model and concludes the need for its extension.

Section 2.2 consequently introduces the class of supersymmetric models, which solve some of the limitations of the SM. The Minimal Supersymmetric Standard Model (MSSM) is taken into special account.

The Englert–Brout–Higgs–Guralnik–Hagen–Kibble mechanism[1] [3] is briefly introduced as a mechanism of EWSB in the context of the SM and the MSSM. A more thorough introduction can be found in Ref. [16] for the SM Higgs sector and in Ref. [17] for that of the MSSM.

Past and present findings from theory and various experiments are reviewed in Section 2.3, outlining constraints on the electroweak sectors of the SM and the MSSM. They define the context for the analysis presented within this thesis.

2.1. The Standard Model of Particle Physics

The SM is the result of the endeavor to develop a single theory to describe the interactions of elementary particles. In 1960, Glashow showed that electromagnetism and weak interactions of leptons can be described within a single theoretical framework [1]. The subsequent extensions to include the Higgs mechanism [3] for EWSB, electroweak interactions of quarks [2], and finally quantum chromodynamics (QCD) [18] yielded a gauge theory that proved to be capable of describing a wide range of high-energy phenomena at high precision.

The discovery of the W and Z bosons [19] and of third-generation fermions verified the existence of all its key ingredients by the year 2000 [20]—except for the Higgs boson. This made the search for the Higgs boson a crucial test for our understanding of electroweak interactions within the SM.

The SM contains elementary particles with spins of half-numbered multiples of $\hbar$ (*fermions*)[2] as constituents of matter. Forces between them are mediated by particles with a spin value of $\hbar$ (*bosons*[3]), which are associated to gauge fields and couple to the respective eigenstates of the interactions:

1. The *strong interaction* applies to particles carrying *color* charge. Among the elementary fermions, this defines the group of *quarks*. The force is mediated by massless *gluons*, which carry color charge themselves.

[1] In 2013, P.W. Higgs and F. Englert have been awarded the Nobel Prize in Physics for this work.

[2] In order to improve the readability and compatibility with the Figure style by the ATLAS Collaboration, $\hbar = c = 1$ is used throughout this thesis.

[3] In general, bosons may carry a spin equal to any integral multiple of $\hbar$.

Table 2.1.: Mass values of the three generations of fermions [21]. Electric charges are given in multiples of the elementary charge, quark masses refer to the $\overline{\text{MS}}$ scheme [22]. All fermions also have anti-particles of identical mass and opposite charge. The uncertainties on the masses of charged leptons are below the permille level.

	Generation			Electric Charge
	1	2	3	
Up-type quarks	$\boldsymbol{u}$ up quark	$\boldsymbol{c}$ charm quark	$\boldsymbol{t}$ top quark	$+2/3$
Mass [MeV]	$2.3^{+0.7}_{-0.5}$	1275 ± 25	$(173.5 \pm 0.6 \pm 0.8) \times 10^3$	
Down-type quarks	$\boldsymbol{d}$ down quark	$\boldsymbol{s}$ strange quark	$\boldsymbol{b}$ bottom quark	$-1/3$
Mass [MeV]	$4.8^{+0.7}_{-0.3}$	95 ± 5	$(4.18 \pm 0.03) \times 10^3$	
Neutrinos	$\boldsymbol{\nu_e}$ electron neutrino	$\boldsymbol{\nu_\mu}$ muon neutrino	$\boldsymbol{\nu_\tau}$ tau neutrino	0
Mass[eV]	< 2(95 % CL)	$< 0.19 \times 10^6$(90 % CL)	$< 18.2 \times 10^6$(95 % CL)	
Charged leptons	$\boldsymbol{e}$ electron	$\boldsymbol{\mu}$ muon	$\boldsymbol{\tau}$ tau lepton	-1
Mass [MeV]	0.511	106	1.78×10^3	

Table 2.2.: Bosonic mass eigenstates of the SM. Mass values are taken from [21]. Electric charges are given in multiples of the elementary charge.

Interaction	Mediator	Mass[GeV]	Electric Charge
Strong	Gluon (g)	0	0
Weak	W boson ($W^\pm$)	80.4	± 1
	Z boson (Z)	91.2	0
Electromagnetic	Photon (γ)	0	0

2. The *electroweak interaction* is the unified description of the *electromagnetic interaction* and the *weak interaction*. Its mediators are the massless *photon* (γ) and the massive gauge bosons (W^+, W^-, Z^0). They are superpositions of the gauge fields $\vec{W}_\mu$ and B_μ, which couple according to *weak isospin* (T^3_W) for $W^1_\mu, W^2_\mu, W^3_\mu$ and *hypercharge* (Y_W) for B_μ.

Of the interactions of the SM, only the weak force is mediated by massive gauge bosons. Massive gauge mediators require a mechanism of EWSB, as discussed in Subsection 2.1.2. The significant mediator masses are responsible for the small range $\mathcal{O}(10^{-16}\,\text{m})$ and hence for suppressing cross-sections of weak interactions at low energies. While electromagnetic interactions are effective over infinite ranges, the weak interaction has a limited range because the force carriers (W^+, W^-) are massive. The limited range of the strong interaction is a consequence of the color charge carried by the gluons.

Table 2.1 lists the three generations of fermions along with their masses and electric charges, Table 2.2 shows the same quantities for the gauge bosons.

2.1.1. Interactions of the Standard Model

The group representation of the SM is the direct product of groups with conserved quantities called *color* (C), *weak isospin* (T_W), and *weak hypercharge* (Y_W), respectively:

$$SU(3)_C \times SU(2)_L \times U(1)_Y. \tag{2.1}$$

Table 2.3.: Electroweak quantum numbers of fermionic electroweak eigenstates of the SM.

	Fermion Generations	Quantum Numbers			
	$i = 1, 2, 3$	$SU(2)_L$		$U(1)_Y$	$U(1)_{\text{em}}$
		T_W	T_W^3	Y_W	q
Quarks	$Q_L'^i = \begin{pmatrix} u_L^i \\ d_L'^i \end{pmatrix}$	$\frac{1}{2}$	$+\frac{1}{2}$ $-\frac{1}{2}$	$+\frac{1}{3}$	$+\frac{2}{3}$ $-\frac{1}{3}$
	u_R^i	0	0	$+\frac{4}{3}$	$+\frac{2}{3}$
	$d_R'^i$	0	0	$-\frac{2}{3}$	$-\frac{1}{3}$
Leptons	$L_L'^i = \begin{pmatrix} \nu_L'^i \\ l_L^i \end{pmatrix}$	$\frac{1}{2}$	$+\frac{1}{2}$ $-\frac{1}{2}$	-1	0 -1
	ν_R^i	0	0	0	0
	l_R^i	0	0	-2	-1

The first group describes QCD, i.e., the strong interaction of colored fermions (*quarks*) and its mediators (*gluons*). Its three quantum numbers specify the color components, called *red*, *green*, and *blue*. The properties of this group are discussed in more detail, e.g., in Ref. [23]. The relevant parts of its phenomenology are discussed in Section 4.1. Elementary fermions without color are called *leptons*.

The other two groups together describe the electroweak interaction. Due to its chiral nature [2], electroweak eigenstates are either right-handed singlets (denoted by a subscript R; $T_W = 0$) or left-handed doublets (denoted by a subscript L; $T_W = \frac{1}{2}$). The Gell-Mann–Nishijima relation

$$q = \frac{Y_W}{2} + T_W^3 \tag{2.2}$$

connects the electric charge q, which determines the electromagnetic interaction strength, to the electroweak quantum numbers.

The fermionic eigenstates each exist in three generations, which have identical electroweak quantum numbers and form the mass eigenstates shown in Table 2.1.

The quantum numbers of the electroweak eigenstates are summarized in Table 2.3. Like the mass eigenstates (see Table 2.1), they each exist in three generations. The mass eigenstates for up-type quarks (u_L^i)[4] and charged leptons (l_L^i) are identical to the flavor eigenstates, while the associated down-type quark mass eigenstates and neutrino mass eigenstates mix according to unitary matrices V_{ij}, U_{ij}:

$$\begin{pmatrix} d_L' \\ s_L' \\ b_L' \end{pmatrix} = \underbrace{\begin{pmatrix} V_{ud} & V_{us} & V_{ub} \\ V_{cd} & V_{cs} & V_{cb} \\ V_{td} & V_{ts} & V_{tb} \end{pmatrix}}_{\text{CKM matrix } V_{ij} \text{ [24]}} \begin{pmatrix} d_L \\ s_L \\ b_L \end{pmatrix} \tag{2.3}$$

$$\begin{pmatrix} \nu_{e,L}' \\ \nu_{\mu,L}' \\ \nu_{\tau,L}' \end{pmatrix} = \underbrace{\begin{pmatrix} U_{e1} & U_{e2} & U_{e3} \\ U_{\mu 1} & U_{\mu 2} & U_{\mu 3} \\ U_{\tau 1} & U_{\tau 2} & U_{\tau 3} \end{pmatrix}}_{\text{PMNS matrix } U_{ij} \text{ [25]}} \begin{pmatrix} \nu_{e,L} \\ \nu_{\mu,L} \\ \nu_{\tau,L} \end{pmatrix}. \tag{2.4}$$

[4]The imaginary number is $\imath$, while i denotes a counting index.

As a consequence of flavor mixing of left-handed neutrinos ν_L^i, they oscillate between generations and must therefore have masses. This can be explained, e.g., with the so-called type-one seesaw mechanism [26], which requires the existence of very heavy, sterile, right-handed neutrinos ν_R^i. Neutrino masses are neglected in the following.

The electroweak Lagrangian can be constructed from all states Ξ_j of the doublets $Q_L'^i, L_L'^i$ and singlets $u_R'^i, d_R'^i, \nu_R'^i, l_R'^i$ of the three generations and the covariant derivative D_μ:

$$\mathcal{L} = \sum_j \imath \bar{\Xi}_j \gamma^\mu D_\mu \Xi_j - \frac{1}{4} F_{\mu\nu} F^{\mu\nu} \qquad D_\mu = \partial_\mu + \imath g \frac{\vec{\sigma}}{2} \cdot \vec{W}_\mu + \imath g' \frac{Y_W}{2} B_\mu. \tag{2.5}$$

The field strength tensor $(F_{\mu\nu})$ consists of an Abelian component with a coupling g' to hypercharge

$$B_{\mu\nu} = \partial_\mu B_\nu - \partial_\nu B_\mu \tag{2.6}$$

and three non-Abelian components with coupling strength g to the weak isospin:

$$\vec{W}_{\mu\nu} = \partial_\mu \vec{W}_\nu - \partial_\nu \vec{W}_\mu - \imath g \vec{W}_\mu \times \vec{W}_\mu. \tag{2.7}$$

The observable gauge boson states are linear combinations of $\vec{W}_\mu$ and B_μ:

$$\begin{pmatrix} W_\mu^+ \\ W_\mu^- \\ Z_\mu \\ \gamma_\mu \end{pmatrix} = \begin{pmatrix} \frac{1}{\sqrt{2}} & \frac{-\imath}{\sqrt{2}} & 0 & 0 \\ \frac{1}{\sqrt{2}} & \frac{\imath}{\sqrt{2}} & 0 & 0 \\ 0 & 0 & \cos\theta_W & \sin\theta_W \\ 0 & 0 & -\sin\theta_W & \cos\theta_W \end{pmatrix} \begin{pmatrix} W_\mu^1 \\ W_\mu^2 \\ W_\mu^3 \\ B_\mu \end{pmatrix}. \tag{2.8}$$

The gauge fields W_μ^3, B_μ both have $T_W = q = 0$. They mix with an *electroweak mixing angle* (θ_W) and form the photon and the Z boson. The $W^\pm$ bosons carry electroweak isospin $T_W = \pm 1$ and couple exclusively to particles with non-vanishing electroweak isospin.

The Lagrangian is invariant under local gauge transformations, because the left- and right-handed fermions $(L(x), R(x))$ and the fields $(\vec{W}_\mu(x), B_\mu(x))$ transform as:

$$L(x) \mapsto L'(x) = e^{\imath(\vec{\alpha}(x)\cdot\vec{T} + \beta(x) Y_W)} L(x) \tag{2.9}$$

$$R(x) \mapsto R'(x) = e^{\imath\beta(x) Y_W} R(x) \tag{2.10}$$

$$\vec{W}_\mu(x) \mapsto \vec{W}_\mu'(x) = \vec{W}_\mu(x) - \frac{1}{g}\partial_\mu \vec{\alpha}(x) - \vec{\alpha}(x) \times \vec{W}_\mu(x) \tag{2.11}$$

$$B_\mu(x) \mapsto B_\mu'(x) = B_\mu(x) - \frac{1}{g'}\partial_\mu \beta(x). \tag{2.12}$$

The local gauge invariance carries the advantage of renormalizability if certain conditions are satisfied [27]. This avoids divergences and thus enables predictions at arbitrary precision from the evaluation of a perturbative series.

The Pauli matrices $(\vec{\sigma})$ are used as basis of $SU(2)_L$. Explicitly inserting the electroweak quantum numbers, Eq. (2.5) becomes:

$$\begin{aligned} \mathcal{L} = & \sum_j \imath \bar{\Xi}_j \gamma^\mu \partial_\mu \Xi_j \\ & - \bar{L}_L'^i \left(g \frac{\vec{\sigma}}{2} \cdot \vec{W}_\mu + g' \frac{Y_W}{2} B_\mu \right) L_L'^i - \bar{Q}_L'^i \left(g \frac{\vec{\sigma}}{2} \cdot \vec{W}_\mu + g' \frac{Y_W}{2} B_\mu \right) Q_L'^i \\ & - \bar{l}_R'^i \left(0 + g' \frac{Y_W}{2} B_\mu \right) l_R'^i - \bar{u}_R'^i \left(0 + g' \frac{Y_W}{2} B_\mu \right) u_R'^i - \bar{d}_R'^i \left(0 + g' \frac{Y_W}{2} B_\mu \right) d_R'^i \\ & - \bar{\nu}_R'^i \left(0 + 0 \right) \nu_R'^i - \frac{1}{4} \vec{W}_{\mu\nu} \vec{W}^{\mu\nu} - \frac{1}{4} B_{\mu\nu} B^{\mu\nu}. \end{aligned} \tag{2.13}$$

The observation of non-zero masses for the W and Z bosons poses a problem to this construction of the electroweak sector. This is because the addition of mass terms for gauge bosons or fermions in the Lagrangian would violate local gauge invariance and thus destroy renormalizability. Fermion masses are also forbidden by the difference in $SU(2)_L$ representations between left- and right-chiral fermions.

Ref. [28] describes another problem of this model: The s-wave component of the scattering amplitude of oppositely charged W boson pairs is proportional to the Mandelstam variable s. Unitarity imposes an upper bound on the real component of each partial wave amplitude. Therefore, an additional interaction is needed to conserve unitarity above $s = \frac{4\sqrt{2}\pi}{G_F} \approx (1.2\,\mathrm{TeV})^2$, where G_F is the Fermi constant.

EWSB by virtue of the Englert–Brout–Higgs–Guralnik–Hagen–Kibble mechanism provides an additional scalar field that serves this purpose.

2.1.2. Electroweak Symmetry Breaking and the Higgs Mechanism

In order to give masses to the electroweak gauge bosons and fermions while maintaining gauge invariance, a potential

$$V = -\mu^2\phi^\dagger\phi + \lambda(\phi^\dagger\phi)^2,\ \lambda > 0 \tag{2.14}$$

is considered, acting on a complex isospin doublet (ϕ) with $Y_W = 1,\ T_W = \frac{1}{2}$:

$$\phi = \begin{pmatrix}\phi_3 + \imath\phi_4\\ \phi_1 + \imath\phi_2\end{pmatrix},\ \phi_i \text{ real.} \tag{2.15}$$

Considering the transition from $\mu^2 \leq 0$ to $\mu^2 > 0$, the state of lowest energy ϕ_{vacuum} becomes degenerate (shown for two dimensions in Figure 2.1):

$$|\phi_{\text{vacuum}}| = \sqrt{\frac{\mu^2}{2\lambda}} = \frac{v}{\sqrt{2}}. \tag{2.16}$$

This defines the *vacuum expectation value (VEV)*:

$$v = \left(\sqrt{2}G_F\right)^{-1/2} \approx 246\,\mathrm{GeV}. \tag{2.17}$$

As the degenerate vacuum state emerges, the system spontaneously "chooses" a direction in ϕ, say $\phi_{\text{vacuum}} = \phi_1 = \sqrt{\frac{\mu^2}{2\lambda}}$. In the vicinity of this ground state, V is no longer symmetric in ϕ_i, but a function of ϕ_1 (and does not vary with $\phi_{2,3,4}$).

This loss of symmetry with respect to ϕ_1 in the ground state is called spontaneous symmetry breaking (SSB). The electroweak symmetry $SU(2)_L \times U(1)_Y$ is broken, and only the electromagnetic symmetry ($U(1)_{\text{em}}$) remains. Oscillations around ϕ_{vacuum} can be interpreted as quantum excitations resulting in physical particles. Massless and massive particles both have two degrees of freedom corresponding to transverse oscillations, and massive particles have an additional degree of freedom to accommodate longitudinal oscillations. Because V only varies with ϕ_1 in the ground state after SSB, oscillations in ϕ_2, ϕ_3, and ϕ_4 do not correspond to physical particles. Instead, the corresponding terms can be eliminated by applying a gauge transformation, leading to the so-called *unitary gauge*:

$$\phi = \begin{pmatrix}0\\ \phi_1\end{pmatrix} = \frac{1}{\sqrt{2}}\begin{pmatrix}0\\ v + H(x)\end{pmatrix}. \tag{2.18}$$

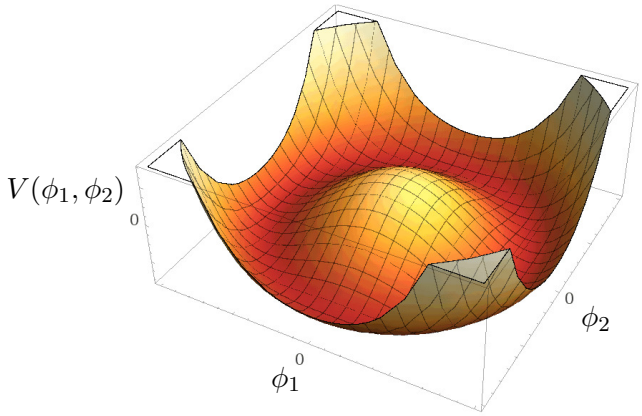

Figure 2.1.: Higgs potential $V(\phi_1, \phi_2)$ in two dimensions for the case of spontaneous symmetry breaking $\mu > 0$, drawn with WolframAlpha®.

The eliminated particles are called *Goldstone bosons*. In the unitary gauge, the corresponding degrees of freedom are absorbed by the longitudinal degrees of freedom of the (massive) W and Z bosons. By SSB, the electroweak Lagrangian (2.13) gains the following contributions in the gauge sector:

$$\begin{aligned}\mathcal{L}_{\text{SSB}} = \quad & \frac{\lambda v^4}{4} + \frac{1}{2}\partial_\mu H(x)\partial^\mu H(x) - \lambda v^2 H^2(x) - \lambda v H^3(x) - \frac{1}{4}\lambda H^4(x) \\ & + \frac{1}{8}\left(v + H(x)\right)\begin{pmatrix} W^{\mu 1} & W^{\mu 2} & W^{\mu 3} & B^\mu \end{pmatrix}\begin{pmatrix} g^2 & 0 & 0 & 0 \\ 0 & g^2 & 0 & 0 \\ 0 & 0 & g^2 & gg' \\ 0 & 0 & gg' & g^2 \end{pmatrix}\begin{pmatrix} W_\mu^1 \\ W_\mu^2 \\ W_\mu^3 \\ B_\mu \end{pmatrix}.\end{aligned} \tag{2.19}$$

The scalar field $H(x)$ (*Higgs field*) can be excited to produce a particle (*Higgs boson*) of mass $m_{H^{\text{SM}}} = v\sqrt{2\lambda}$ and with cubic and quartic self-couplings. The last term contains the couplings to the electroweak eigenstates of the gauge bosons. The couplings are proportional to the masses of the gauge bosons squared:

$$m_W = v\frac{g}{2} \qquad g_{H^{\text{SM}}W^+W^-} = \frac{2m_W^2}{v} \tag{2.20}$$

$$m_Z = v\frac{\sqrt{g^2 + g'^2}}{2} = \frac{m_W}{\cos\theta_W} \qquad g_{H^{\text{SM}}Z^0Z^0} = \frac{2m_Z^2}{v} \tag{2.21}$$

$$m_\gamma = 0 \qquad g_{H^{\text{SM}}\gamma\gamma} = 0. \tag{2.22}$$

The gauge boson masses are proportional to the VEV, and the masses of the W boson and the Z boson differ by a factor of $\cos\theta_W$, resulting from the mixing of W_μ^3 and B_μ.

The Higgs mechanism further allows the addition of so-called *Yukawa coupling* terms to generate fermion masses:

$$\mathcal{L}_{\text{Yukawa}} = \lambda_u \bar{Q}_L'^i u_R^i \phi + \lambda_d \bar{Q}_L'^i d_R'^i \tilde{\phi} + \lambda_l \bar{L}_L'^i l_R'^i \phi + \lambda_\nu \bar{L}_L'^i \nu_R'^i \tilde{\phi} + \text{h.c.} \tag{2.23}$$

While the up-type quarks and charged leptons receive mass by interaction with the Higgs field given in Eq. (2.18), down-type quarks interact with the charge conjugated Higgs field $\tilde{\phi} = \imath\sigma_2\phi^*$. The masses and couplings to the Higgs boson are:

$$m_f = v\frac{\lambda_f}{\sqrt{2}} \qquad g_{H^{\text{SM}}f\bar{f}} = \frac{m_f}{v}. \tag{2.24}$$

Using these coupling strengths, the production cross-sections and branching ratios of processes involving Higgs bosons can be computed, $m_{H^{\mathrm{SM}}}$ being the only free parameter.

2.1.3. Parameters of the Standard Model

Neglecting neutrino masses, the SM contains 19 free parameters:

- six quark masses and three masses of charged leptons,
- three mixing angles of the CKM matrix,
- one CP violating phase (U_{ij}),
- the Z boson mass,
- the Fermi constant ($G_F = \frac{\sqrt{2}g^2}{8m_W^2}$),
- the strong coupling strength (α_s,) and the fine-structure constant ($\alpha_{\mathrm{em}} = \frac{e^2}{4\pi}$) or the elementary charge ($e = g\sin\theta_W = g'\cos\theta_W$),
- the mass of the Higgs boson ($m_{H^{\mathrm{SM}}}$), and
- the CP-violating parameter (θ) of the strong interaction.

Massive Dirac neutrinos require seven additional parameters, which are not considered in this thesis:

- three neutrino masses,
- three mixing angles, and
- a CP-violating phase.

2.1.4. Production and Decay of Higgs Bosons

Two main factors determine the feasibility of the observation of Higgs bosons in a given process:

- The expected number of selected signal events should be as large as possible to limit the statistical uncertainty on the event yield, and
- the event topology should be sufficiently discriminable from more abundant background events.

The fulfillment of these conditions creates sensitivity to the signal process, i.e., a significant difference in likelihood of the background–only and the signal–plus–background hypotheses in expected outcomes predicted for either hypothesis.

Figure 2.2 shows the expected production cross-sections and decay branching ratios for SM Higgs bosons at the Large Hadron Collider (LHC) as a function of the mass of the Higgs boson. The dominant production processes for proton-proton collisions at a center–of–mass energy of $\sqrt{s} = 7\,\mathrm{TeV}$ are:

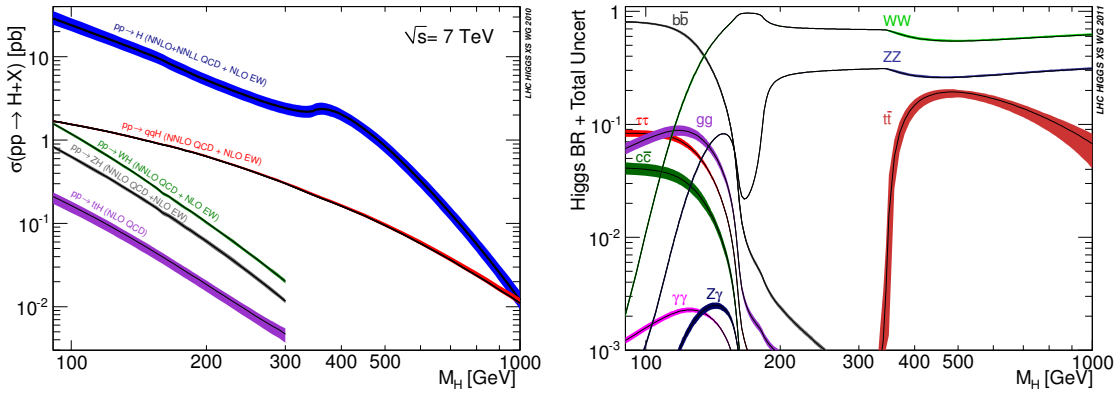

(a) Production mechanisms (b) Decay modes

Figure 2.2.: Comparison of the production cross-sections of the dominant production processes for pp collisions at a center–of–mass energy of 7 TeV (left) and decay branching ratios (right) of the SM Higgs boson as a function of the Higgs boson mass. [29].

Gluon Fusion ($pp \to H^{\mathrm{SM}}$) Gluons form a heavy virtual quark pair, which couples to the Higgs boson (see Figure 2.3(a)). A significant increase in cross-section is predicted at $m_{H^{\mathrm{SM}}} = 2m_t$, when a loop of t-quarks is on-shell. The production cross-section for gluon fusion eclipses all other SM Higgs boson production modes by about an order of magnitude below $m_{H^{\mathrm{SM}}} \approx 500\,\mathrm{GeV}$ at the LHC because of the abundance of energetic gluons and because the matrix element (ME) is proportional to $\lambda_t \alpha_s^2$. The cross-section for Higgs boson production in gluon fusion has been calculated in Ref. [29], using the QCD corrections at next–to–next–to–leading order (NNLO)+next–to–next–to–leading logarithm (NNLL) and the electroweak corrections at next–to–leading order (NLO) accuracy from Refs. [30, 31].

Vector Boson Fusion (VBF; $pp \to qqH^{\mathrm{SM}}$) Quarks or anti-quarks emit a virtual pair of vector bosons (W^+W^-/Z^0Z^0), which then produce a Higgs boson (see Figure 2.3(b)). The quarks subsequently hadronize, forming two highly energetic jets with large separation in pseudo-rapidity. This process is suppressed with respect to gluon fusion for two reasons: Firstly, the parton density of gluons with sufficient momentum is larger than the respective quark parton densities at LHC energies. Secondly, the leading gluon fusion diagram contains two strong vertices, while they are replaced by electroweak vertices in VBF. The ME is thus proportional to $\alpha_{\mathrm{ew}}^2 \frac{m_{W/Z}^2}{v}$. The cross-section for Higgs boson production in VBF has been calculated in Ref. [29] with QCD (electroweak) corrections at NNLO (NLO) accuracy, using HAWK [32], VBFNLO [33], and VBF@NNLO [34].

Higgs-Strahlung ($pp \to VH^{\mathrm{SM}}$, $V = W, Z$) The Higgs boson is produced in association with a vector boson, which decays into a pair of quarks or leptons (see Figure 2.3(c)). The ME is proportional to $\alpha_{\mathrm{ew}} \frac{m_{W/Z}^2}{v}$, so the production cross-section for the WH^{SM} process is comparable to VBF at $m_{H^{\mathrm{SM}}} \approx 90\,\mathrm{GeV}$ despite the involvement of one anti-quark. Because two distinct W bosons exist in contrast to only one Z boson, the cross-section of the ZH^{SM} process is smaller by a factor of approximately 2. The smaller available phase space volume leads to a faster decline of the $pp \to VH^{\mathrm{SM}}$

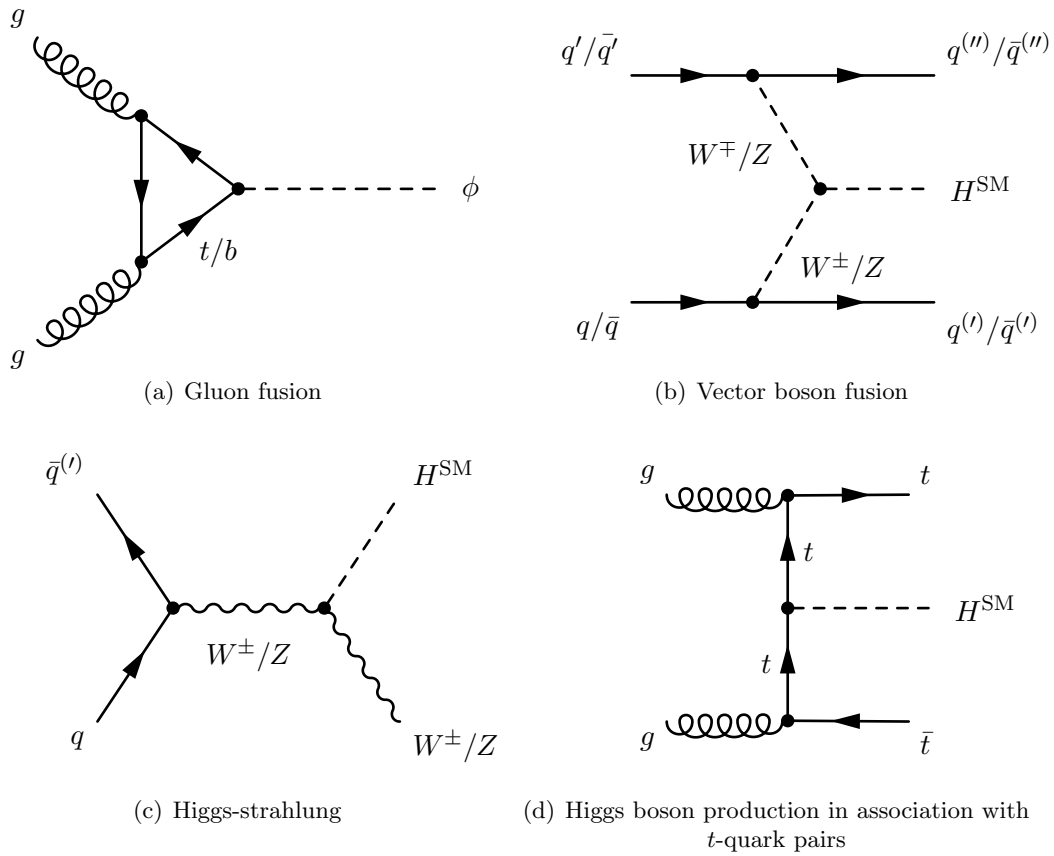

(a) Gluon fusion

(b) Vector boson fusion

(c) Higgs-strahlung

(d) Higgs boson production in association with t-quark pairs

Figure 2.3.: Leading order Feynman diagrams for the dominant production modes of neutral Higgs bosons (H^{SM}) in the SM: The gluon fusion (left) and VBF (right) processes are shown in the top row, while the Higgs-strahlung process (left) and Higgs boson production in association with t-quark pairs (right) are shown in the bottom row.

cross-section with growing Higgs boson mass values than gluon fusion or VBF. The cross-section for Higgs boson production in association with a vector boson has been calculated in Ref. [29] with QCD (electroweak) corrections at NNLO (NLO) accuracy, using VH@NNLO [35] and the procedures described in Refs. [35, 36].

Higgs Boson Production in Association with t-Quark Pairs A t-quark pair is produced, which couples to the Higgs boson (see Figure 2.3(d)). The production cross-section is greatly reduced by the large invariant mass of one Higgs boson and two t-quarks (despite the large factor of $\lambda_t \alpha_s^2$ in the ME). Consequently, the production cross-section is about one order of magnitude smaller than that of Higgs boson production in Higgs-strahlung. The calculation in Ref. [29] uses QCD corrections at NLO accuracy from Refs. [37].

The branching ratios for neutral SM Higgs bosons are governed by the dependence of Higgs boson couplings on the masses of the decay products as well as mass threshold effects. They have been calculated in Ref. [29] with HDECAY [38] and Prophecy4f [39].

$H^{\mathrm{SM}} \to b\bar{b}$ At low Higgs boson masses, before decays to heavy gauge bosons set in, b-quarks constitute the most massive elementary particles the Higgs boson can decay to. The coupling strength is proportional to the Yukawa coupling (λ_b). $H^{\mathrm{SM}} \to b\bar{b}$

is therefore the dominant decay mode in the mass range until about 135 GeV. The uncertainty of the result from Ref. [29] is about $1-2\,\%$ for $m_{H^{\mathrm{SM}}} < 135\,\mathrm{GeV}$ because the electroweak corrections have been calculated at NLO accuracy in the small Higgs boson mass approximation.

$\boldsymbol{H^{\mathrm{SM}} \to \tau\tau}$ τ leptons offer the largest branching ratio of all leptonic decay modes (with a coupling strength proportional to λ_τ) and therefore a better discrimination from background processes involving multi-jet production than hadronic decay modes. They carry the same $1-2\,\%$ uncertainty as $H^{\mathrm{SM}} \to b\bar{b}$ decays from the small Higgs boson mass approximation.

$\boldsymbol{H^{\mathrm{SM}} \to \gamma\gamma/gg}$ The decaying Higgs boson couples to a virtual quark pair, which then emits a pair of photons or gluons, producing jets in the final state in the latter case. The ME is thus proportional to $\lambda_t \alpha^2$ for the dominant t-quark loop with $\alpha = \alpha_{\mathrm{ew}}$ for $H^{\mathrm{SM}} \to \gamma\gamma$ and $\alpha = \alpha_s$ for $H^{\mathrm{SM}} \to gg$. While the branching ratio of decays into photon pairs is known to an accuracy of about $1\,\%$, the scale dependence of the QCD corrections at NNLO leads to an uncertainty of about $10\,\%$. The $H^{\mathrm{SM}} \to \gamma\gamma$ decay mode plays an important role in the LHC SM Higgs boson searches because the resolution of the invariant di-photon mass is very good in both experiments.

$\boldsymbol{H^{\mathrm{SM}} \to WW/ZZ}$ The decaying Higgs boson produces a pair of massive gauge bosons, whose decay products are then detected. Because of the large values of m_W and m_Z, decays to massive gauge bosons are suppressed for low Higgs boson masses. For Higgs boson masses above approximately 150 GeV, they eclipse all other decay modes because the respective MEs are proportional to $\alpha_{\mathrm{ew}} \frac{m_{W/Z}^2}{v}$. Comparing Eqs. (2.20) and (2.21) to Eq. (2.24), the growing dominance for larger Higgs boson masses can be understood: The denominator of Eq. (2.24) is proportional to $m_{H^{\mathrm{SM}}} = v\sqrt{2\lambda}$, while v cancels in Eqs. (2.20) and (2.21) when inserting the gauge boson masses. Outside the threshold region $m_{H^{\mathrm{SM}}} \approx 2m_{W/Z}$, the distinctness of W^+ and W^- bosons implies that $\frac{\mathcal{BR}(H^{\mathrm{SM}} \to W^+W^-)}{\mathcal{BR}(H^{\mathrm{SM}} \to Z^0Z^0)} \approx 2$. For Higgs boson mass values below 500 GeV, the uncertainty of the respective branching ratio is about $0.5\,\%$ [29].

$\boldsymbol{H^{\mathrm{SM}} \to t\bar{t}}$ Because of the large Yukawa coupling of t-quarks (λ_t), Higgs boson decays to t-quark pairs are the subdominant decay mode above the mass threshold of $m_{H^{\mathrm{SM}}} = 2m_t$. The corresponding branching ratio uncertainty first decreases from $5\,\%$ to $2\,\%$ at 500 GeV and then increases again for larger Higgs boson mass values because the uncertainty of the electroweak corrections grows with $m_{H^{\mathrm{SM}}}$ [29].

2.1.5. Limitations of the Standard Model

The SM with the Englert–Brout–Higgs–Guralnik–Hagen–Kibble mechanism offers a description of the phenomenology of high-energy physics, incorporating the electroweak and strong interactions in one consistent gauge theory.

However, the multitude of free parameters is commonly considered a weakness of the model: No mechanisms exist that constrain their values. Also, the evolution of the coupling strengths with growing center–of–mass energy does not feature a scale where all values coincide (see Figure 2.4), i.e., a scale of grand unification. Both statements are compatible with the hypothesis that the SM is merely a low-energy effective theory of a more fundamental theory with a particle content beyond the experimental reach of present high-energy physics experiments.

Other important arguments for the incompleteness of the SM are the exclusion of all SM particles as possible dark matter candidates (as argued in Ref. [40]) and the fact that the SM does not include gravity.

Within the Higgs sector, the Higgs boson mass is subject to large positive (negative) corrections from boson (fermion) loops, causing quadratic divergences, whose leading contributions are of the form:

$$(\Delta m_{H^{\mathrm{SM}}})^2 \approx \pm\lambda\Lambda_{\mathrm{UV}}^2, \tag{2.25}$$

with the ultraviolet momentum cutoff scale Λ_{UV} and a constant (λ). In order to keep the Higgs boson mass within the preferred range despite large positive and negative corrections, the parameters have to be fine-tuned at each order of perturbative calculations.

The same issue is often called the *hierarchy problem* [41–45]: The only energy scales relevant to the model are the Planck scale $\mathcal{O}(10^{19}\,\mathrm{GeV})$ and the scale of the vacuum expectation value ($v \approx 246\,\mathrm{GeV}$). The SM proposes no mechanism that accounts for the 17 orders of magnitude that separate the two scales.

Ideas to solve these problems include the theoretical frameworks of compositeness [44] or technicolor [42, 46]. However, it is hard to construct phenomenologically acceptable models with either class of models [47, 48].

The following Section introduces the class of supersymmetric models, which meet these challenges with greater ease.

2.2. Supersymmetry and the Minimal Supersymmetric Standard Model

This Section gives a conceptual overview of supersymmetry (SUSY), focusing on its simplest variety, the Minimal Supersymmetric Standard Model (MSSM). The consequences for the phenomenology of EWSB are summarized. More details can be found, e.g., in Refs. [17, 49].

2.2.1. Supersymmetry

As shown in Subsection 2.1.5, the SM offers an incomplete description of the phenomenology of particle physics, but excels at precision and consistency of its predictions. As a consequence, extending the SM by new symmetries and fields is preferable over attempting to construct a fundamentally different framework.

Supersymmetry [4, 5] extends the SM by adding partner particles[5] (called *sparticles*) for all SM particles in such a way that the spin difference between any SM particle and its supersymmetric partner (called *superpartners* in the following) is $\pm\frac{1}{2}$ and all other quantum numbers (and the mass[6]) are identical. They are connected via an operator Q and form chiral and gauge *supermultiplets*:

$$\begin{aligned} Q\,|\mathrm{fermion}\rangle &= |\mathrm{boson}\rangle \\ Q\,|\mathrm{boson}\rangle &= |\mathrm{fermion}\rangle\,. \end{aligned}$$

According to the Coleman-Mandula theorem [50], only a trivial combination of an additional space-time symmetry and the internal symmetries of the SM is possible. The Haag-Lopuszanski-Sohnius extension [51] examines all possible generators of such theories, concluding that Q presents the highest grade of symmetry.

[5] denoted by a tilde symbol

[6] This requirement is lifted for *broken* SUSY—see below.

Because loops involving the superpartners of SM fermions (bosons) lead to positive (negative) contributions to the mass of the Higgs boson (m_ϕ), SUSY acts as a custodial symmetry protecting it from loop corrections in Eq. (2.25), avoiding the need for fine-tuning while maintaining naturalness:

$$(\Delta m_\phi)^2 \approx \mp\lambda' \Lambda_{\mathrm{UV}}^2. \tag{2.26}$$

As shown in Refs. [52], the resulting corrections to the Higgs boson mass from fermions Eq. (2.25) and from their supersymmetric partners Eq. (2.26) cancel exactly if there are two supersymmetric partners of the same mass as the SM fermion, leading a coupling strength relation $2\lambda' = \lambda$. The same cancellation occurs for loop corrections involving SM bosons and loops involving their supersymmetric partners.

The Lagrangian of the MSSM is discussed in Subsection 2.2.2.

R-Parity

An important difference between the SM and supersymmetric models is the existence of renormalizible terms that violate the baryon number (B) or the lepton number (L).

$$B \equiv \begin{cases} +\frac{1}{3} & \text{for quarks and their superpartners (\textit{squarks})} \\ -\frac{1}{3} & \text{for antiquarks and antisquarks} \\ 0 & \text{for all others} \end{cases} \tag{2.27}$$

$$L \equiv \begin{cases} +1 & \text{for leptons and their superpartners (\textit{sleptons})} \\ -1 & \text{for antileptons and antisleptons} \\ 0 & \text{for all others} \end{cases} \tag{2.28}$$

Such terms are well-constrained from the non-observation of proton decays [49] and therefore motivate the introduction of a symmetry protecting B and L, called *R-parity* [5]. Its quantum number is multiplicatively conserved and includes spin (s):

$$P_R = (-1)^{3(B-L)+2s}. \tag{2.29}$$

This definition of P_R assigns $+1$ to all SM particles and -1 to their superpartners.

As a consequence, the lightest supersymmetric particle, which in most supersymmetric models with R-parity is the lightest neutralino [53–55], is stable. As it is electrically neutral and interacts only weakly, it constitutes a good candidate for cold dark matter [53, 54]. Also, superpartners of SM particles can only be produced in pairs.

2.2.2. The Minimal Supersymmetric Standard Model

The MSSM extends the SM by SUSY, introducing as few particles as possible (see Table 2.4).

For each SM fermion and boson, one superpartner is introduced.[7] EWSB requires a second doublet of Higgs fields to cancel gauge anomalies, which arise from the higgsinos. The second doublet also gives mass to quarks and squarks with positive weak isospin, which, in contrast to the SM, cannot be achieved with the conjugated field of the original Higgs boson doublet. Because of equal electroweak quantum numbers, the left- and right-handed superpartners of the SM fermions mix to form the squark and slepton mass eigenstates. The superpartners of the electroweak gauge bosons and those of the Higgs bosons also mix: The winos and charged higgsinos form four charginos, and the zino, photino, and neutral higgsinos mix to form four neutralinos.

[7] This gives rise to the denomination as $N = 1$ *SUSY*.

Table 2.4.: Additional gauge and mass eigenstates in the MSSM with respect to the SM along with their spin and R-parity quantum numbers [49]. Mixing in the first two generations is neglected.

	Spin	P_R	Gauge Eigenstates	Mass Eigenstates
Higgs bosons	0	$+1$	$H_u^0, H_d^0, H_u^+, H_d^-$	$h^0, H^0, A^0, H^\pm$
Squarks	0	-1	$\tilde{u}_L, \tilde{u}_R, \tilde{d}_L, \tilde{d}_R$ $\tilde{s}_L, \tilde{s}_R, \tilde{c}_L, \tilde{c}_R$ $\tilde{t}_L, \tilde{t}_R, \tilde{b}_L, \tilde{b}_R$	(same) (same) $\tilde{t}_1, \tilde{t}_2, \tilde{b}_1, \tilde{b}_2$
Sleptons	0	-1	$\tilde{e}_L, \tilde{e}_R, \tilde{\nu}_{e,L}, \tilde{\nu}_{e,R}$ $\tilde{\mu}_L, \tilde{\mu}_R, \tilde{\nu}_{\mu,L}, \tilde{\nu}_{\mu,R}$ $\tilde{\tau}_L, \tilde{\tau}_R, \tilde{\nu}_{\tau,L}, \tilde{\nu}_{\tau,R}$	(same) (same) $\tilde{\tau}_1, \tilde{\tau}_2, \tilde{\nu}_{\tau,1}, \tilde{\nu}_{\tau,2}$
Neutralinos	1/2	-1	$\tilde{B}^0, \tilde{W}^0, \tilde{H}_u^0, \tilde{H}_d^0$	$\tilde{N}_1, \tilde{N}_2, \tilde{N}_3, \tilde{N}_4$
Charginos	1/2	-1	$\tilde{W}^\pm, \tilde{H}_u^+, \tilde{H}_d^-$	$\tilde{C}_1^\pm, \tilde{C}_2^\pm$
Gluino	1/2	-1	$\tilde{g}$	(same)
Goldstino	1/2	-1	$\tilde{G}$	(same)

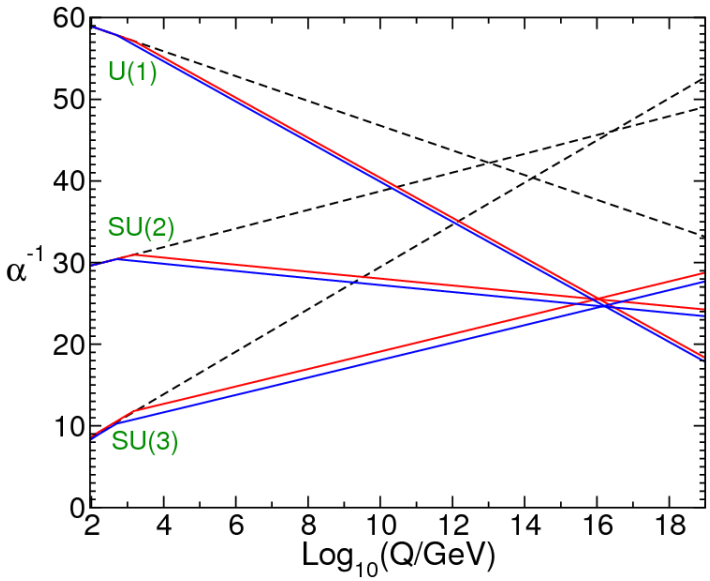

Figure 2.4.: Energy evolution of the inverse gauge couplings in the SM (dashed) and two MSSM scenarios [49]. The sparticle masses are taken to be 500 GeV (blue lines) or 1.5 TeV (red lines), and $\alpha_3(m_Z)$ is adjusted between 0.117 and 0.121 to achieve exact unification.

Table 2.5.: Chiral supermultiplets of the MSSM [49]. The fermions and sfermions each exist in three generations $i = 1, 2, 3$.

Supermultiplet	Spin 0	Spin 1/2
Q	$(\tilde{u}_L^i, \tilde{d}_L^i)$	(u_L^i, d_L^i)
$\bar{u}$	$\tilde{u}_R^{i*}$	$u_R^{i\dagger}$
$\bar{d}$	$\tilde{d}_R^{i*}$	$d_R^{i\dagger}$
L	$(\tilde{\nu}^i, \tilde{e}_L^i)$	(ν^i, e_L^i)
$\bar{e}$	$\tilde{e}_R^{i*}$	$e_R^{i\dagger}$
H_u	(H_u^+, H_u^0)	$(\tilde{H}_u^+, \tilde{H}_u^0)$
H_d	(H_d^0, H_d^-)	$(\tilde{H}_d^0, \tilde{H}_d^-)$

Another favorable feature of the MSSM is the possibility to achieve apparent gauge coupling unification [49]: As shown in Figure 2.4, the gauge couplings of the SM intersect at different energy scales. The introduction of superpartners at the TeV scale modifies the evolution of the couplings in such a way that the three couplings nearly coincide in value. Exact equality can be achieved by modifying α_s at the Z boson mass by approximately 3 % or by assuming different masses for the various superpartners [56].

The interactions between the chiral and the gauge superfields are constrained by SUSY and the gauge symmetries. The mass terms from interaction with the Higgs fields are similar to the SM, and the Yukawa couplings are constrained by their SM equivalents.

The model is thus constrained[8], except for the choice of the so-called *superpotential* W, which is a holomorphic function of the chiral superfields. In the absence of parameters with dimensions of [mass]^2 and without processes violating baryon or lepton number, it can be written as [49]:

$$W_{\text{MSSM}} = \bar{u}\mathbf{y_u}QH_u - \bar{d}\mathbf{y_d}QH_d - \bar{e}\mathbf{y_e}LH_d + \mu H_u H_d, \tag{2.30}$$

where $Q, \bar{u}, \bar{d}, L, \bar{e}, H_u, H_d$ are the chiral supermultiplets from Table 2.5, and $\mathbf{y_u}, \mathbf{y_d}, \mathbf{y_e}$ are 3×3 matrices containing the Yukawa couplings, which are known from SM measurements. Because the third-generation fermions are much heavier than those of the first and second generations, the components corresponding to t-quarks, b-quarks, and τ leptons dominate:

$$W_{\text{MSSM}} \approx y_t(\bar{t}tH_u^0 - \bar{t}bH_u^+) - y_b(\bar{b}tH_d^- - \bar{b}bH_d^0) - y_\tau(\bar{\tau}\nu_\tau H_d^- - \bar{\tau}\tau H_d^0) + \mu(H_u^+ H_d^- - H_u^0 H_d^0).$$

Supersymmetry Breaking

If SUSY was an exact symmetry, the supersymmetric partners of SM particles would carry the same masses as their SM counterparts and therefore be very easy to discover. If realized at all in nature, SUSY must therefore be broken, featuring sparticle masses beyond the present reach of accelerator-based experiments.

The requirement that quadratic divergences should cancel motivates the concept of *soft SUSY breaking*, implying that we can write the effective SUSY Lagrangian as:

$$\mathcal{L} = \mathcal{L}_{\text{SUSY}} + \mathcal{L}_{\text{soft}}. \tag{2.31}$$

[8] As shown later in this Subsection, the MSSM Higgs boson masses are no free parameters (as in the SM), but determined by the parameters m_{A^0} and $\tan\beta$.

$\mathcal{L}_{\text{SUSY}}$ preserves SUSY and describes the gauge and Yukawa interactions as well as the scalar potential. The soft SUSY-breaking term $\mathcal{L}_{\text{soft}}$ contains only mass terms and coupling parameters with positive mass dimension, avoiding quadratic divergences.

SSB of SUSY at the mass scale of the SM particles cannot exist because the mass spectrum of the superpartners would be too light [57]. SSB may therefore only occur in an inaccessible (or *hidden*) sector of a fundamental theory, mediated to the mass scale of the SM particles by a messenger field.

While various viable theories exist for the nature of the messenger field (notably Refs. [58–62], which are outlined, e.g., in Ref. [49]), the MSSM Lagrangian contains explicit soft SUSY breaking terms [49]:

$$\begin{aligned}\mathcal{L}_{\text{soft}}^{\text{MSSM}} = &-\frac{1}{2}\left(M_3\tilde{g}\tilde{g} + M_2\tilde{W}\tilde{W} + M_1\tilde{B}\tilde{B} + \text{h.c.}\right) \\ &- \tilde{Q}^\dagger \mathbf{m_Q^2}\tilde{Q} - \tilde{L}^\dagger \mathbf{m_L^2}\tilde{L} - \tilde{\bar{u}}^\dagger \mathbf{m_{\bar{u}}^2}\tilde{\bar{u}} - \tilde{\bar{d}}^\dagger \mathbf{m_{\bar{d}}^2}\tilde{\bar{d}} - \tilde{\bar{e}}^\dagger \mathbf{m_{\bar{e}}^2}\tilde{\bar{e}} \\ &- \left(\tilde{\bar{u}}\mathbf{a_u}\tilde{Q}H_u - \tilde{\bar{d}}\mathbf{a_d}\tilde{Q}H_d - \tilde{\bar{e}}\mathbf{a_e}\tilde{L}H_d + \text{h.c.}\right) \\ &- m_{H_u}^2 H_u^* H_u - m_{H_d}^2 H_d^* H_d - (bH_u H_d + \text{h.c.}).\end{aligned} \tag{2.32}$$

The first line contains mass terms for the gauginos, the second, for the sfermions. The third line describes trilinear couplings between scalar particles, and the last line describes additional terms within the Higgs potential.

Altogether, the MSSM introduces 105 additional parameters with respect to the SM, including the masses and mixing parameters of the superpartners [63]:

- 21 sfermion masses,
- 36 real mixing angles,
- 40 CP-violating phases,
- three real mass parameters and two phases in the gaugino sector, and
- two mass parameters and one phase in the Higgs sector.

However, there are numerous experimental constraints on the parameters of SUSY breaking, see Refs. [64, 65] for constraints relevant to the MSSM.

In order to reduce the number of free parameters, the following assumptions [63] can be made without a relevant phenomenological impact on the Higgs sector:

- At a (large) energy scale of grand unification (Λ_{GUT}), all gauginos have the same mass ($M_1 = M_2 = M_3 = m_{1/2}$), which is equivalent to the unification of the gauge couplings in a grand unified theory (GUT). Their values at lower scales can be derived from the renormalization group equations [63].
- The sfermion masses are equal to a value m_0 for all three generations at the GUT scale, and the Higgs mass parameters are also equal to m_0.
- The trilinear couplings ($\mathbf{a} = A_0\mathbf{1}$) are equal for all three generations at the GUT scale and diagonal.

The resulting model is called minimal supergravity (mSUGRA) or also constrained Minimal Supersymmetric Standard Model (cMSSM)[9] [63]. By eliminating all free parameters except

[9] Note that the name cMSSM can also refer to other sets of constraints, such as constraints from precision measurements (see below).

for $m_{1/2}$, m_0, A_0, $\tan\beta$, and the sign of μ, it provides a good framework for probing the Higgs sector. Furthermore, Subsection 2.2.3 describes a benchmark scenario which fixes all parameters but the tree-level parameters m_{A^0} and $\tan\beta$ to probe the properties of the MSSM Higgs sector.

Higgs Sector

As mentioned before, the charge-conjugated Higgs boson fields create gauge anomalies and can therefore not be used to create masses for the u-, c-, and t-quarks in the MSSM, in contrast to the SM. Also, the charge-conjugated Higgs boson fields cannot be used in the superpotential in Eq. (2.30) because terms such as $\bar{u}\mathbf{y_u}QH_d^*$ are not holomorphic in the chiral superfields. Renormalizability can be restored by introducing another doublet of complex scalar fields with opposite hypercharge ($Y_W = -1$) and a VEV of its own (v_u):

$$H_u = \begin{pmatrix} H_u^+ \\ H_u^0 \end{pmatrix} \qquad \text{VEV: } v_u \qquad Y_W = -1 \tag{2.33}$$

$$H_d = \begin{pmatrix} H_d^0 \\ H_d^- \end{pmatrix} \qquad \text{VEV: } v_d \qquad Y_W = +1. \tag{2.34}$$

The three longitudinal degrees of freedom are absorbed into the masses of the W and Z bosons, leaving five physical Higgs particles that are mixtures of the fields H_u and H_d, with two mixing angles, α and β. At the Born level, the Higgs sector depends on only two parameters. The mixing angle α connects the neutral CP-even Higgs bosons, and β the CP-odd and charged Higgs bosons with the respective Goldstone bosons. The mixing angle β can be related to the VEVs, which add up quadratically to the SM value:

$$\tan\beta \equiv \frac{v_d}{v_u} \qquad \sqrt{v_u^2 + v_d^2} \approx 246\,\text{GeV}. \tag{2.35}$$

The CP-even Higgs bosons (h_0 and H_0) can be written as:

$$\begin{pmatrix} h^0 \\ H^0 \end{pmatrix} = \sqrt{2} \begin{pmatrix} \cos\alpha & -\sin\alpha \\ \sin\alpha & \cos\alpha \end{pmatrix} \begin{pmatrix} \text{Re}\left(H_u^0\right) - v_u \\ \text{Re}\left(H_d^0\right) - v_d \end{pmatrix}, \tag{2.36}$$

the CP-odd Higgs boson (A_0) and the associated neutral Goldstone boson (G^0):

$$\begin{pmatrix} G^0 \\ A^0 \end{pmatrix} = \sqrt{2} \begin{pmatrix} \cos\beta & -\sin\beta \\ \sin\beta & \cos\beta \end{pmatrix} \begin{pmatrix} \text{Im}\left(H_d^0\right) \\ \text{Im}\left(H_u^0\right) \end{pmatrix}, \tag{2.37}$$

and the two charged Higgs bosons ($H^\pm$) with the charged Goldstone bosons ($G^\pm$):

$$\begin{pmatrix} G^- \\ H^- \end{pmatrix} = \begin{pmatrix} \cos\beta & -\sin\beta \\ \sin\beta & \cos\beta \end{pmatrix} \begin{pmatrix} H_d^- \\ H_u^{+*} \end{pmatrix} \tag{2.38}$$

$$\begin{pmatrix} G^+ \\ H^+ \end{pmatrix} = \begin{pmatrix} G^{-\dagger} \\ H^{-\dagger} \end{pmatrix}. \tag{2.39}$$

The masses of the MSSM Higgs bosons are connected at the tree level [66]:

$$m_{H^\pm}^2 = m_{A^0}^2 + m_{W^\pm}^2 \tag{2.40}$$

$$m_{H^0/h^0}^2 = \frac{1}{2}\left(m_{A^0}^2 + m_{Z^0}^2 \pm \sqrt{\left(m_{A^0}^2 + m_{Z^0}^2\right)^2 - 4m_{A^0}^2 m_{Z^0}^2 \cos^2 2\beta}\right). \tag{2.41}$$

Eq. (2.41) suggests that the lighter CP-even Higgs boson (h_0) should be lighter than the Z boson [67], which would have made it possible to discover it at the Large Electron–Positron Collider (LEP). However, the upper bound of the mass of the h^0 boson is subject to significant loop corrections, leading to an upper bound [68–70]:

$$m_{h^0} < 135\,\text{GeV} \tag{2.42}$$

if the supersymmetric particles that affect loop corrections are lighter than 1 TeV and the value of $\tan\beta$ does not exceed 50. Consequently, the non-observation of neutral MSSM Higgs bosons lighter than the Z boson by the LEP experiments [71] only excludes parts of the MSSM parameter space (see Subsubsection 2.3.2.3).

The two-dimensional sub-space which affects tree-level processes involving Higgs bosons is parameterized in $\tan\beta$ and the mass of the A^0 boson (m_{A^0}). This parametrization is commonly used for the interpretation of searches for neutral MSSM Higgs bosons.

Only seven of the other MSSM parameters have a strong impact on the Higgs sector. In order to probe the Higgs sector, they are set to benchmark values, such as the $m_{h^0}^{max}$ *scenario* [72]: The masses of the gauginos of the $SU(2)_L$ group are set to $M_2 = 200\,\text{GeV}$. They are connected to the $U(1)_Y$ gaugino masses by the relation: $M_1 = {}^5\!/_3 \tan^2\theta_W M_2$. The third-generation squarks dominate the sfermion loop contributions, and their masses are set to $m_{\tilde{b}_L} = m_{\tilde{t}_L} = m_{\tilde{b}_R} = m_{\tilde{t}_R} = 1000\,\text{GeV}$. The mixing parameter in the $\tilde{t}$ sector is set to $X_t = 2000\,\text{GeV}$. The mass parameter μ is set to a value of $+200\,\text{GeV}$, and the trilinear Higgs–$\tilde{t}$ coupling is: $A_t = X_t + \mu\cot\beta$. The gluino mass is set to 800 GeV, and no CP-violating phase is assumed in the gluino sector.

This scenario represents a parameter choice that maximizes the mass of the lightest CP-even neutral Higgs boson, leading to the smallest contour of the exclusion limit from LEP (see Subsubsection 2.3.2.3). It is therefore the default choice in the most recent Tevatron-based and LHC-based searches (see Subsubsection 2.3.2.3), whose results complement those from the LEP (see below).

The relation between the mass of the CP-odd Higgs boson (A^0) and the masses of the CP-even and the charged Higgs bosons is shown in Figure 2.6, using FeynHiggs 2.7.4 [69,73,74], taking into account the one-loop and the most important two-loop corrections. For large values of $\tan\beta$ and for m_{A^0} values significantly different from the *critical mass* (m_C) of approximately 130 GeV, either the lighter (for $m_{A^0} < m_C$) or the heavier (for $m_{A^0} > m_C$) neutral CP-even Higgs boson is nearly mass-degenerate with the A^0 boson.

The region where all three neutral Higgs bosons are approximately mass-degenerate is called the intense-coupling region. This scenario requires a very accurate mass reconstruction of Higgs boson candidates to distinguish it from the case of a single boson (as in the SM). A more thorough discussion of the intense-coupling region is given in Ref. [17].

The couplings of the neutral Higgs bosons of the MSSM are modified by functions of the mixing angles α and β with respect to the SM values as shown in Table 2.6. The A^0 boson has no tree-level coupling to gauge bosons. The couplings of the CP-even neutral MSSM Higgs bosons are connected by the sum rules:

$$g_{h^0 d\bar{d}} + g_{H^0 d\bar{d}} = \frac{1}{\cos^2\beta} \qquad g_{h^0 u\bar{u}} + g_{H^0 u\bar{u}} = \frac{1}{\sin^2\beta} \qquad g_{h^0 VV} + g_{H^0 VV} = 1. \tag{2.43}$$

As demonstrated in Ref. [75], α and β are connected. Their relation can be used to eliminate α from the equations that describe the masses and couplings of the Higgs bosons in favor of the cMSSM parameters.

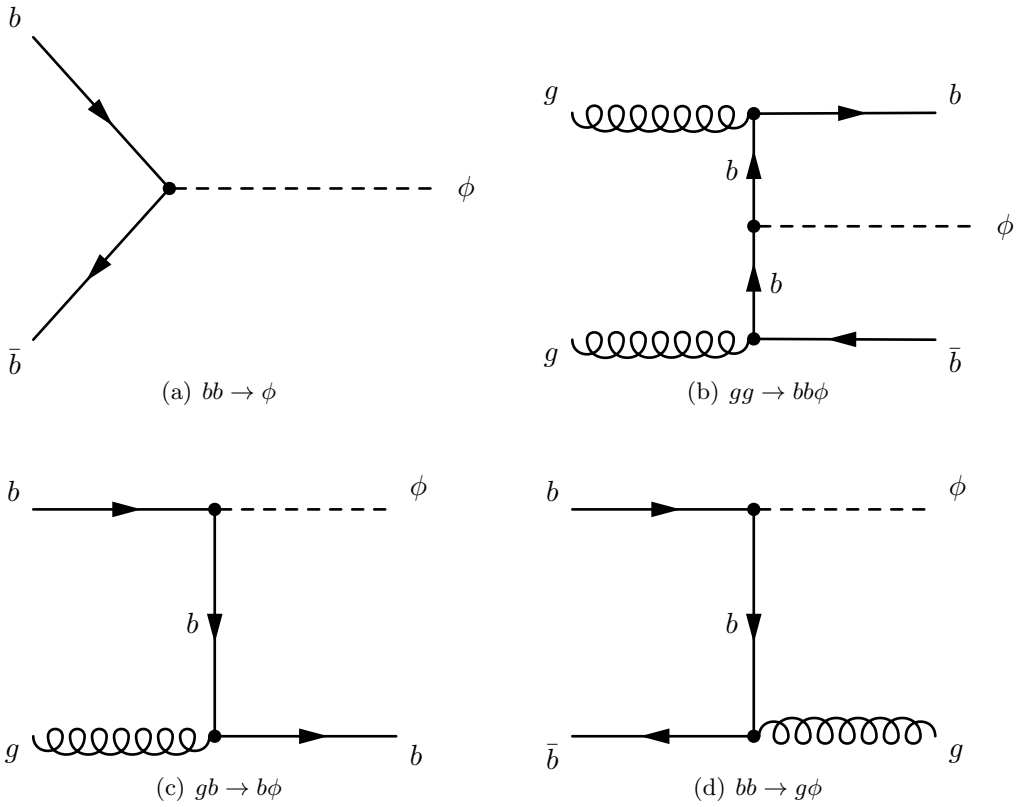

Figure 2.5.: Leading order Feynman diagrams for the b-associated production processes of neutral Higgs bosons (ϕ). Note that $gb \to b\phi$ and $bb \to g\phi$ are connected by crossing and do also have s-channel contributions. The $bb \to \phi$ and $bb \to g\phi$ processes can be considered b-associated in the 4FS, where a b-quark pair is produced by a splitting gluon.

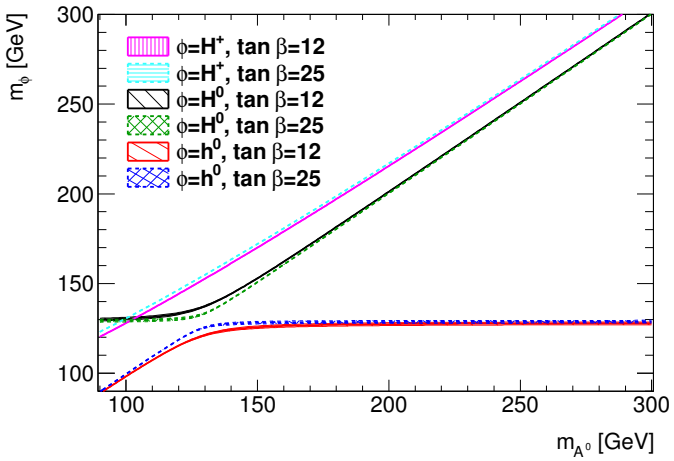

Figure 2.6.: Masses of the CP-even and charged Higgs bosons in dependence of the mass of the CP-odd Higgs boson (m_{A^0}) and the ratio of the VEVs ($\tan\beta$) in the $m_{h^0}^{\max}$ scenario. The mass values and uncertainties have been computed with FeynHiggs 2.7.4 [69, 73, 74].

Table 2.6.: Yukawa couplings and gauge boson couplings of the neutral MSSM Higgs bosons divided by the respective values for a SM Higgs boson [75]. The limit for $\tan\beta \gg 1$ is given for the cases of a heavy ($m_{A^0} \geq m_C$, upper value) and a light ($m_{A^0} < m_C$, lower value) CP-odd neutral Higgs boson in red.

	$\frac{g_{\phi u\bar{u}}}{g_{H^{\mathrm{SM}}u\bar{u}}}$	$\frac{g_{\phi d\bar{d}}}{g_{H^{\mathrm{SM}}d\bar{d}}}$	$\frac{g_{\phi VV}}{g_{H^{\mathrm{SM}}VV}}$
$\phi = h^0$	$\frac{\cos\alpha}{\sin\beta} \to 1$ $\to -f_1 + f_2/\tan\beta$	$-\frac{\sin\alpha}{\cos\beta} \to -f_1\tan\beta + f_2$ $\to \tan\beta$	$\sin(\beta-\alpha) \to 1$ $\to -f_1 + (1+f_2)/\tan\beta$
$\phi = H^0$	$\frac{\sin\alpha}{\sin\beta} \to f_1 - f_2/\tan\beta$ $\to -1$	$\frac{\cos\alpha}{\cos\beta} \to \tan\beta$ $\to -f_1\tan\beta + f_2$	$\cos(\beta-\alpha) \to f_1 + (1-f_2)/\tan\beta$ $\to -1$
$\phi = A^0$	$\frac{1}{\tan\beta}$	$\tan\beta$	0

The mixing angle α is eliminated from the couplings by introducing two functions [75]:

$$f_1 = \frac{\varepsilon'}{2(m_{H^0}^2 - m_{h^0}^2)} \qquad f_2 = \frac{m_{A^0}^2 + m_{Z^0}^2}{m_{H^0}^2 - m_{h^0}^2}, \tag{2.44}$$

where ε' is a function of the MSSM parameters that are fixed in the $m_{h^0}^{\max}$ scenario. For large values of $\tan\beta$, the couplings can then be approximated by the red terms given in Table 2.6, which apply to the cases $m_{A^0} < m_C$ and $m_{A^0} \geq m_C$. For large values of m_{A^0}, f_1 and f_2 converge to 0 and 1, respectively. In this *decoupling limit*, the Higgs sector of the MSSM thus becomes identical to that of the SM because the A^0 and H^0 bosons become kinematically inaccessible, while the couplings of the h^0 boson are equal to those predicted by the SM. Details are given in Refs. [17, 76].

2.2.3. Production and Decay of Neutral Higgs Bosons in the MSSM

At the LEP, Higgs-strahlung off Z bosons and the pair production process ($Z \to A^0h^0$) constitute the dominant production modes. At the Tevatron and the LHC, b-associated production (see Figure 2.5) and gluon fusion dominate.

This is due to the enhancement of the coupling to down-type fermions ($g_{\phi d\bar{d}}$) with growing values of $\tan\beta$ for the CP-odd and one of the CP-even Higgs bosons. As a consequence, the production and decay processes that involve b-quarks or τ leptons play a dominant role in searches at the LHC. Therefore, the gluon fusion process (driven by b-quark loops) and the production in association with b-quarks are the most promising production modes for large values of $\tan\beta$. Figure 2.7 shows the production cross-sections for both signal processes in the m_{A^0}–$\tan\beta$ plane of the $m_{h^0}^{\max}$ scenario. While the production cross-sections for the CP-odd Higgs boson simply decline with growing m_{A^0} and falling $\tan\beta$, the couplings of the CP-even Higgs bosons differ for the two cases $m_{A^0} < m_C$ and $m_{A^0} \geq m_C$, leading to a more complex dependency of the production cross-sections on m_{A^0} and $\tan\beta$.

Decays to b-quark pairs dominate with a branching ratio of about $80 - 90\,\%$, followed by decays to pairs of τ leptons with a branching ratio of $8 - 16\,\%$ for the $\tan\beta$ and m_{A^0} values considered (see Figure 2.8).

Because decays to τ leptons are probed, all three neutral Higgs bosons contribute to the signal. Figure 2.9 shows the combined signal cross-sections for gluon fusion and b-associated production with a subsequent decay to a τ lepton pair. From Figure 2.7, it is clear that the h^0 (H^0) boson contributes significantly less to the total signal for $m_{A^0} \geq m_C$ ($m_{A^0} < m_C$) than the other CP-even Higgs boson. Because of the limited resolution of the reconstructed di-τ invariant mass, it is very challenging to separately observe the three types of neutral

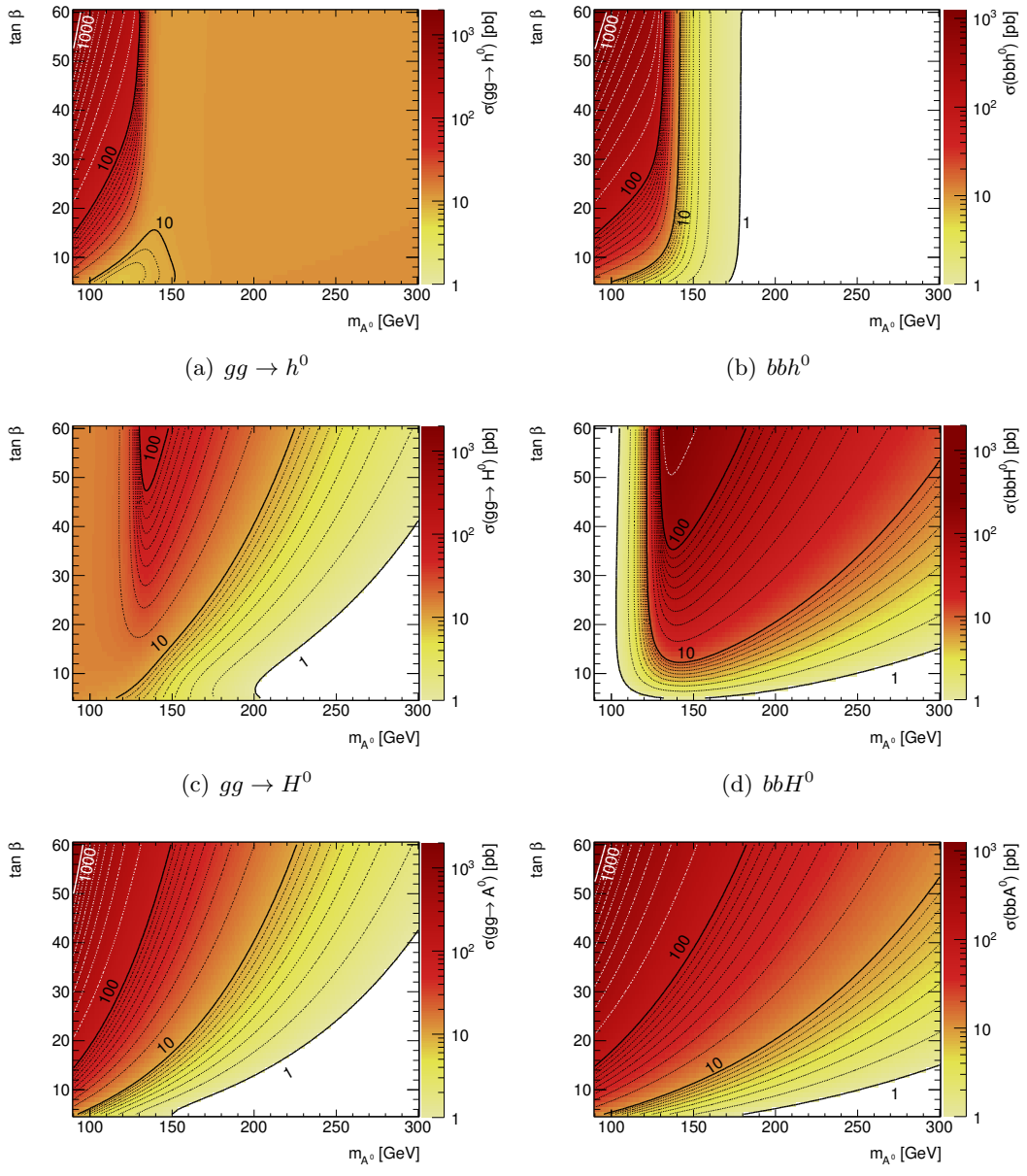

(a) $gg \to h^0$ (b) bbh^0

(c) $gg \to H^0$ (d) bbH^0

(e) $gg \to A^0$ (f) bbA^0

Figure 2.7.: Production cross-sections of the neutral MSSM Higgs bosons (line-wise) through gluon fusion (left) and b-associated production (right) in the $m_{h^0}^{\max}$ scenario, calculated with the recipe from Ref. [29], which uses Ref. [69, 73, 74, 77–80].

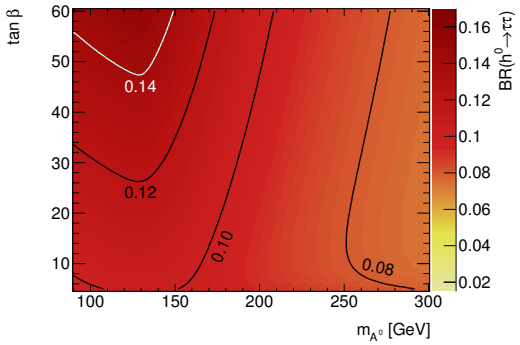

(a) BR $\left(h^0 \to \tau\tau\right)$

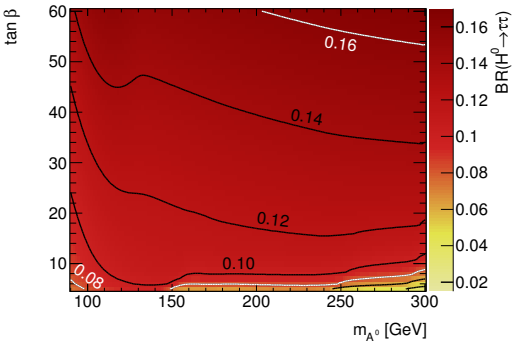

(b) BR $\left(H^0 \to \tau\tau\right)$

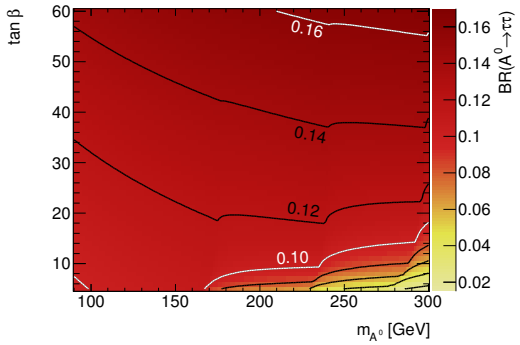

(c) BR $\left(A^0 \to \tau\tau\right)$

Figure 2.8.: Decay branching ratios of the neutral MSSM Higgs bosons in the $m_{h^0}^{\text{max}}$ scenario, calculated with FeynHiggs 2.7.4 [69, 73, 74], following the recipe from Ref. [29].

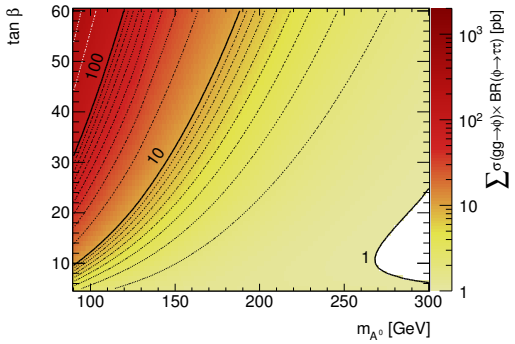

(a) $gg \to \phi$

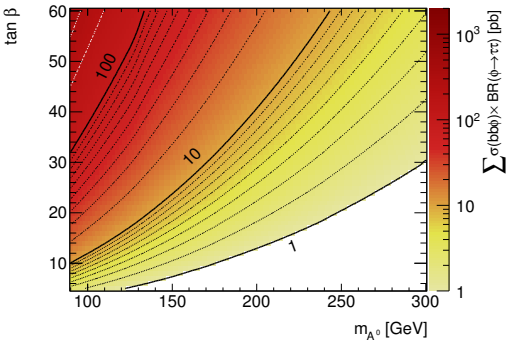

(b) $bb\phi$

Figure 2.9.: Total signal contributions of the gluon fusion (left) and b-associated production (right) processes in the $m_{h^0}^{\text{max}}$ scenario. The products of the production cross-section and the branching ratio, calculated with the recipe from Ref. [29], which uses Ref. [69, 73, 74, 77–80], have been summed for all three types of neutral Higgs bosons.

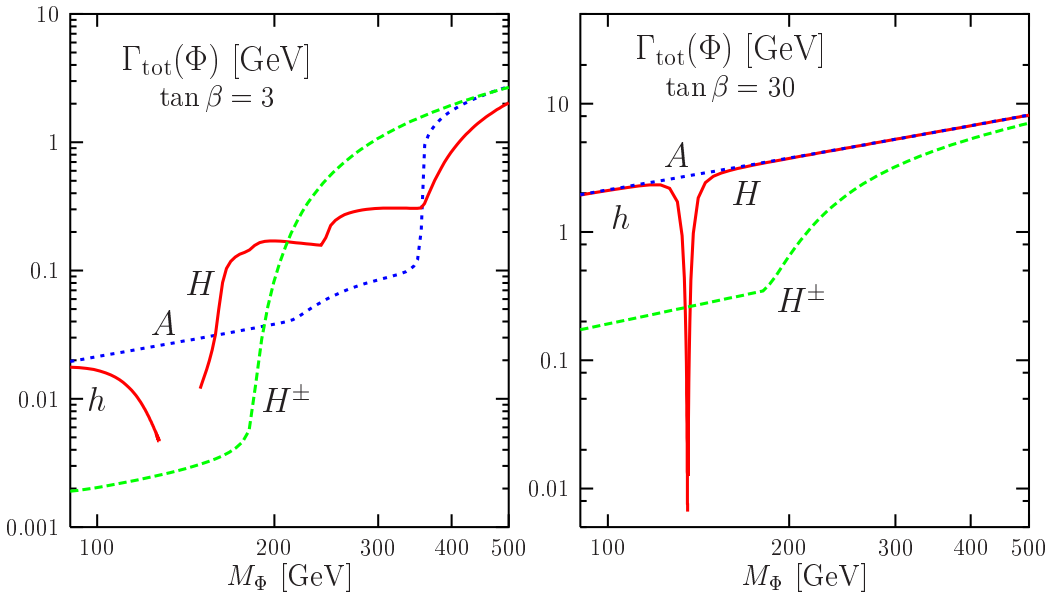

Figure 2.10.: Total decay widths of the MSSM Higgs bosons for $\tan\beta$ values of 3 (left) and 30 (right) [17].

Higgs bosons, and Figure 2.9 is a good indication of the signal cross-section falling into a given mass window.

The total decay width of the MSSM Higgs bosons is shown in Figure 2.10. Because of the large coupling to down-type fermions for large values of $\tan\beta$, features in the mass dependence of the partial widths of other decay modes only impact the total decay width for $\tan\beta = 3$. Due to the experimental di-τ mass resolution, which is larger or equal to 25 GeV for the analysis presented within this thesis, the decay width plays no role in this analysis.

2.3. Present Understanding of Electroweak Symmetry Breaking

This Section reviews the theoretical bounds, constraints from precision measurements, and results from direct searches for neutral Higgs bosons in the contexts of the SM and the MSSM.

2.3.1. Standard Model Interpretation

2.3.1.1. Theoretical Constraints

Even though the Higgs boson mass in the SM is a free parameter, three main theoretical considerations limit the possible mass range:

- As mentioned before, the Higgs mechanism in the SM can serve to restore unitarity in the scattering of oppositely charged W boson pairs [28]. This is only possible if the Higgs boson mass is less than about 850 GeV.
- The requirement that perturbation theory holds until a given scale (Λ)—implying the absence of a Landau pole—leads to an upper bound on the Higgs boson mass.
- Vacuum stability implies a positive value of λ in Eq. (2.14), which is impacted by radiative corrections. This implies a lower bound on the mass of the Higgs boson.

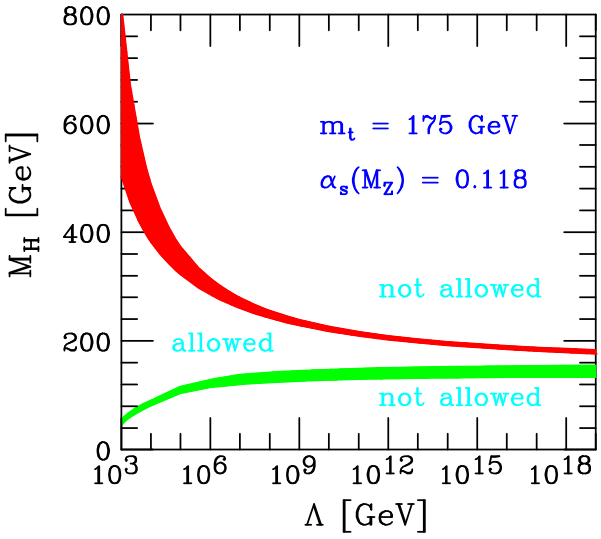

Figure 2.11.: Allowed Higgs boson mass range as a function of the scale (Λ) at which new physics processes become relevant [16, 81].

These bounds depend on the scale up to which the SM is valid as shown in Figure 2.11. The theoretical uncertainty of the bounds has been obtained by comparing the results with and without one-loop contributions as well as variations of the respective cutoff value of the quartic coupling (λ) and the evaluated impact of the α_s and t-quark mass uncertainties. The experimental sources of uncertainty are dominated by the t-quark mass $m_t = (175 \pm 6)\,\text{GeV}$ and $\alpha_s(m_{Z^0}) = 0.118 \pm 0.002$. The possible mass range shrinks significantly when requiring the SM to remain valid until a grand unification scale (Λ_{GUT}) of about $10^{16}\,\text{GeV}$.

2.3.1.2. Constraints on the SM Higgs Boson Mass from Precision Measurements

Because the interactions of Higgs bosons with SM particles have $m_{H^{\text{SM}}}$ as the only free parameter, indirect constraints can be derived from precision measurements of SM processes. Measurements of the hadronic vacuum polarization ($\Delta\alpha^{(5)}_{\text{had}}$), 14 results from measurements at the Z-pole, and measurements of the t-quark mass, W boson mass, and the W boson decay width have been combined by the LEP Electroweak Working Group [82, 83] (see Figure 2.12(a)). The Figure shows the goodness of the fit to results from high-energy experiments and to a set of results that also includes low-energy observables. The result of a theory-driven determination of the vacuum polarization is given for reference. From high-Q^2 results from the LEP, the Stanford Linear Collider (SLC), and the Tevatron as well as measurements of the hadronic vacuum polarisation, a Higgs boson mass of $m_{H^{\text{SM}}} = 89^{+35}_{-26}\,\text{GeV}$ is predicted [82].

The values of the t-quark mass, the W boson mass, and the hadronic vacuum polarization strongly impact the result: The relation of m_W and m_t depends on the Higgs boson mass, and the data from run 2 of the LEP and from the Tevatron are only compatible with light Higgs boson masses [82, 83].

2.3.1.3. Direct Searches for Higgs Bosons in the SM

Proof that the mechanism of EWSB indeed involves the presence of a Higgs field relies on the direct observation of Higgs boson decays. Such searches have been performed at the LEP, the Tevatron collider, and the LHC. They are summarized below. More detail about these searches is given in Ref. [89].

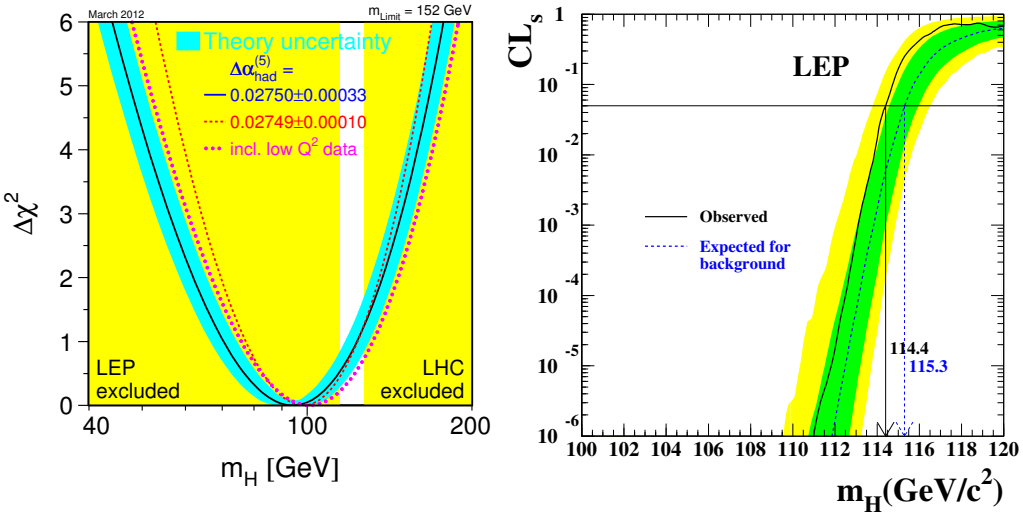

(a) Global $\chi^2 - \chi^2_{\min}$

(b) Exclusion limit from direct searches

Figure 2.12.: Global $\chi^2 - \chi^2_{\min}$ value of SM fit to precision data as a function of $m_{H^{\mathrm{SM}}}$ (left) [82, 83]: The plot shows the dependence on $m_{H^{\mathrm{SM}}}$ of the goodness of the fit to results from only high-energy experiments (solid line) and to a fit that also includes low-energy observables (magenta dots). The red dashed line is based on a calculation of total contribution of the five light quark flavors to the hadronic vacuum polarisation ($\Delta\alpha^{(5)}_{\mathrm{had}}$) from perturbation theory, reducing the level of systematic uncertainty. Taking theory uncertainties into account this leads to a limit of $m_{H^{\mathrm{SM}}} < 152\,\mathrm{GeV}$. The results from the direct searches at the LEP ($m_{H^{\mathrm{SM}}} > 114.4\,\mathrm{GeV}$ at 95 % CL [84]) and from CMS (excluding $127\,\mathrm{GeV} < m_{H^{\mathrm{SM}}} < 600\,\mathrm{GeV}$ at 95 % CL [85], labeled "LHC excluded") are also shown. The range excluded by CMS at the time was almost identical to the range excluded by ATLAS at 95 % CL [86] and covers the range excluded by the Tevatron experiments [87].
Upper end of excluded $m_{H^{\mathrm{SM}}}$ range for the statistical combination of the LEP2 direct Higgs boson searches (right), implying $m_{H^{\mathrm{SM}}} \leq 114.4\,\mathrm{GeV}$ at 95 % CL [84], using the CL_s technique [88] (see Chapter 9).

Higgs boson Searches at the LEP

The LEP experiments probed Higgs boson masses from 0 to 114.4 GeV: During the first period of LEP runs (LEP1), the accelerator was operated at center–of–mass energies $\sqrt{s}$ close to the mass of the Z boson. This enabled the exclusion of the mass range from approximately zero, where the lifetime of the Higgs bosons becomes relevant, up to Higgs boson mass values of 63.9 GeV (ALEPH [90]), 55.7 GeV (DELPHI [91]), 60.2 GeV (L3 [92]), and 59.6 GeV (OPAL [93]). The dominant production mode is Higgs-strahlung, where the Z boson decay mode to neutrino pairs offers the best sensitivity, followed by $Z \to e^+e^-/\mu^+\mu^-$ decays [89].

In the following years, the center–of–mass energy of the LEP was gradually increased to 209 GeV. Analysis strategies were refined, the luminosity was increased, and the findings of all four LEP experiments were combined. This expanded the mass reach to exclude $m_{H^{\mathrm{SM}}} \leq 114.4\,\mathrm{GeV}$ at 95 % CL [84], see Figure 2.12(b). Hadronic decay modes of the Z boson dominate the overall sensitivity [89].

Higgs boson searches at the Tevatron collider

At the $p\bar{p}$ collider Tevatron, gluon fusion is the dominant production mode for Higgs bosons. Higgs boson production in association with gauge bosons has the second-largest cross-section of all production modes [16]. By reconstruction of leptonic gauge boson decays, better signal–to–background ratios can be achieved in this mode, though. Therefore, the gauge-boson-associated production with $H^{\mathrm{SM}} \to b\bar{b}$ dominates the total sensitivity of the experiments for $m_{H^{\mathrm{SM}}} \lesssim 130\,\mathrm{GeV}$, while Higgs boson production from gluon fusion with $H^{\mathrm{SM}} \to W^+W^- \to \ell^+\ell^- + 2\nu$ dominates for larger values of $m_{H^{\mathrm{SM}}}$.

A statistical combination of both Tevatron experiments results in a 95 % CL exclusion of the ranges $90\,\mathrm{GeV} < m_{H^{\mathrm{SM}}} < 109\,\mathrm{GeV}$, which was already excluded by the LEP experiments [84], and $149\,\mathrm{GeV} < m_{H^{\mathrm{SM}}} < 182\,\mathrm{GeV}$. The $H \to b\bar{b}$ channel shows an excess of about two standard deviations, and the combined significance is about 2.6 standard deviations [94]. This is in good agreement with the discovery of a Higgs boson by the LHC experiments.

Discovery of a Higgs Boson at the LHC

The ATLAS and CMS experiments at the LHC (described in Chapter 3) have greatly extended the experimental reach by their searches for SM Higgs bosons at center–of–mass energies of 7 and 8 TeV, leading to the discovery of a Higgs boson with a mass of about $m_{H^{\mathrm{SM}}} = 126\,\mathrm{GeV}$ [6,7]. The sensitivity of the combination of the various search channels is dominated by Higgs boson decays to boson pairs:

Higgs boson decays into photon pairs can be searched for in all production modes because of the excellent photon energy resolution of both experiments. ATLAS [6] and CMS [7] distinguish several signal regions, based on the kinematic properties of the reconstructed photons and the presence of highly energetic jets. Due to the large available production cross-section and the great mass resolution, the di-photon channel had the largest observed significance of the Higgs boson-like particle in the ATLAS result [6]—and the second-largest significance for the CMS result [7]—despite the abundance of backgrounds and the low decay branching to photon pairs.

SM Higgs boson candidates decaying into two pairs of light leptons via on- or off-shell Z bosons ($H \to ZZ^* \to 4\ell$) offer a great mass resolution. Both ATLAS [6] and CMS [7] sort the $2e2\mu$, $4e$, and 4μ final states into separate channels to improve sensitivity. Both experiments obtain the largest contribution to the overall sensitivity from these channels near 126 GeV [6,7].

Decays into W boson pairs with $W^+W^- \to \ell^+\ell^- + 2\nu$ dominate the sensitivity for large values of $m_{H^{\mathrm{SM}}}$, while they constitute the third-largest contribution near the $m_{H^{\mathrm{SM}}}$ value that results in the largest observed significance. They are categorized by both ATLAS [6] and CMS [7] by the number of additional jets and the flavor of the final state leptons.

As shown in Figure 2.13, a statistical combination of all search channels leads to local p-values[10] of about 10^{-23} for $25\,\mathrm{fb}^{-1}$ of ATLAS data [96] and about 10^{-12} for $17\,\mathrm{fb}^{-1}$ of CMS data [95] as well as to an exclusion for heavier SM-like Higgs bosons almost up to the unitarity bound.

ATLAS and CMS found good agreement between the SM expectation and data: The ratios of observed to expected signal strengths in all decay channels are consistent with unity within (at most) two standard deviations (see Figure 2.14), implying consistency with the SM predictions for the couplings of Higgs bosons to τ leptons, heavy quarks, and vector

[10] The local p-value is the probability (assuming the background–only hypothesis) for the observed outcome or a more signal-like outcome.

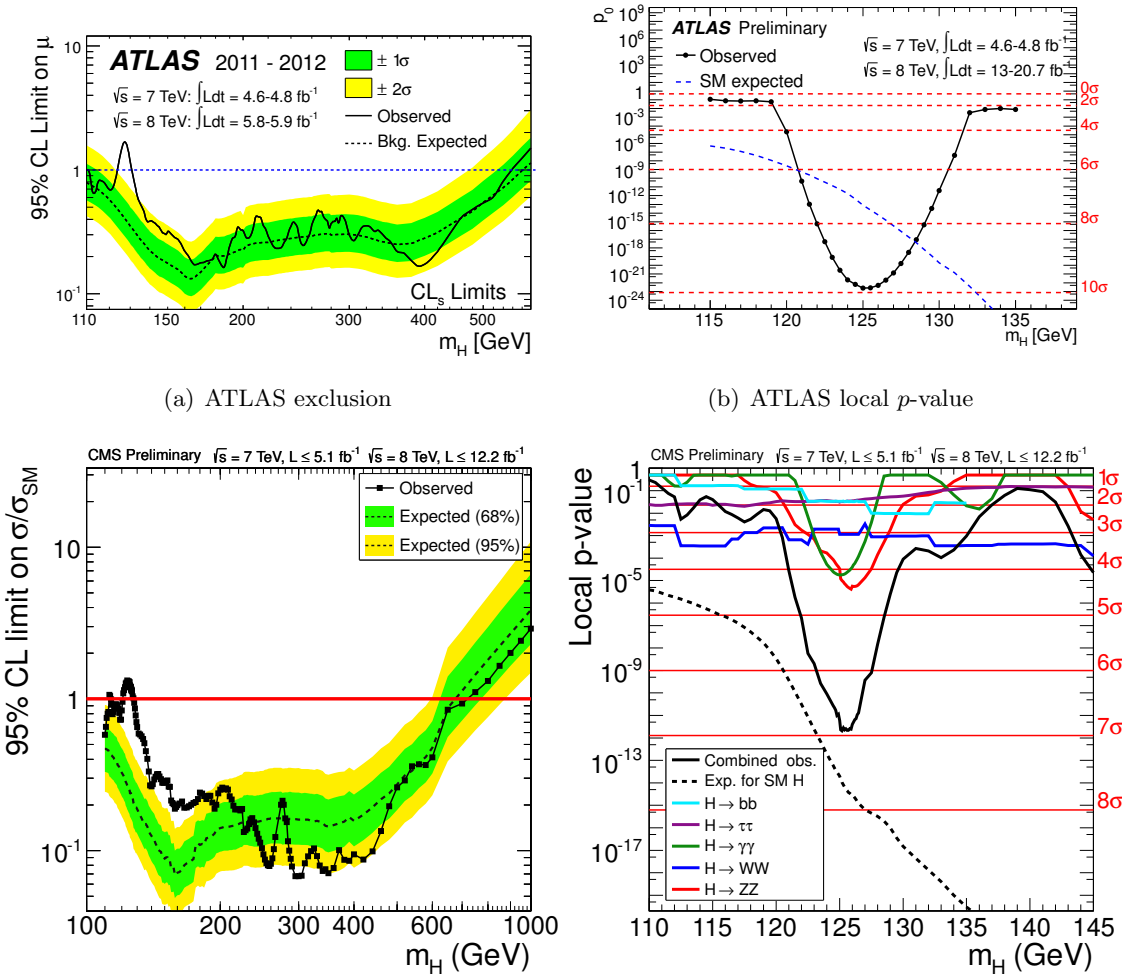

(a) ATLAS exclusion

(b) ATLAS local p-value

(c) CMS exclusion

(d) CMS local p-value

Figure 2.13.: Results of statistical combinations of ATLAS searches (top row) and CMS searches (bottom row) for a SM Higgs boson. The exclusion limits for the signal cross-section for the SM Higgs boson mass for ATLAS [6] and CMS [95] are shown in the left Figures. The right Figures show the local p-value as a function of the SM Higgs boson mass for ATLAS [96] and CMS [95]. For the determination of the local p-value, ATLAS used the same decay channels as CMS.

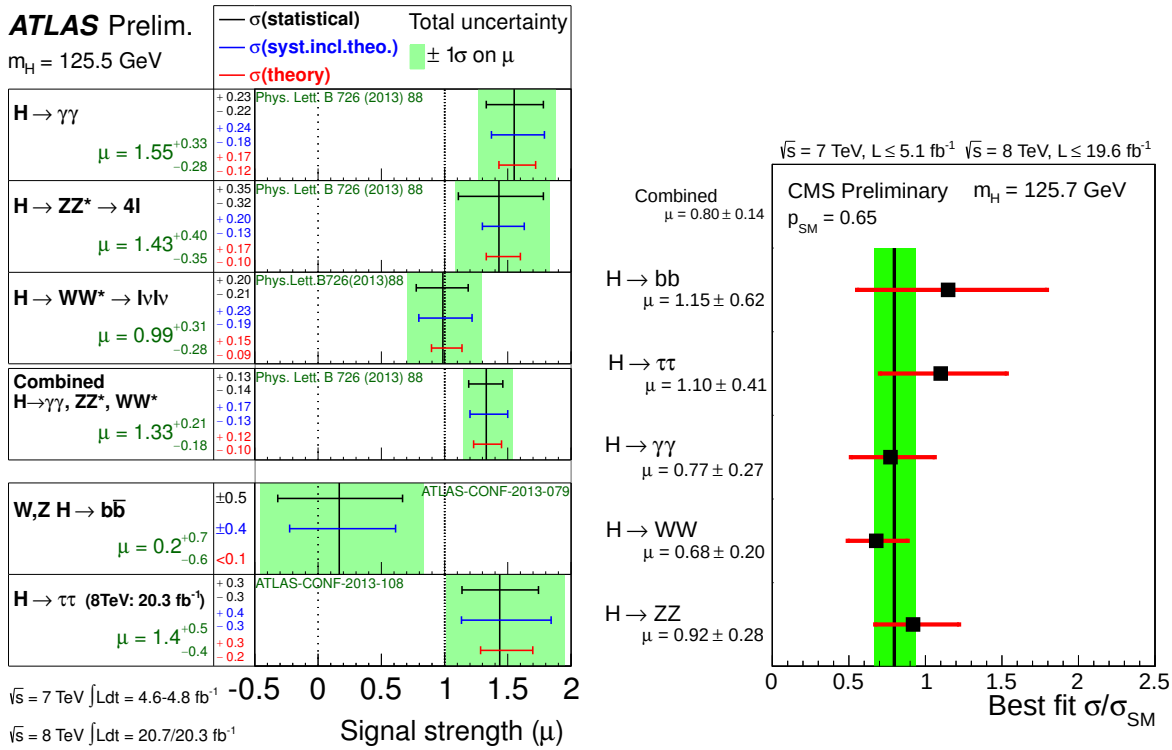

(a) ATLAS (b) CMS

Figure 2.14.: Best fit values by ATLAS [97] (left) and CMS [98] (right) for the measured signal cross-sections of the examined Higgs boson decay modes, relative to the SM expectation for the Higgs boson mass with the largest observed signal significance.

bosons. Further studies of the spin and the parity of the Higgs boson [99, 100] support the SM prediction of a spin-0 scalar particle ($J^P = 0^+$), while excluding the $J^P = 2^+$ hypothesis at more than 97.8 % CL [99].

2.3.2. MSSM Interpretation

2.3.2.1. Theoretical Constraints

In the MSSM, the tree-level parameter $\tan\beta$ is constrained by the requirement that the couplings of the Higgs bosons to fermions should remain perturbative. Requiring that the Yukawa coupling to the third-generation quarks is smaller than $\sqrt{4\pi}$ leads to a rather weak constraint for the general MSSM case [17]:

$$0.3 \lesssim \tan\beta \lesssim 150.$$

In the cMSSM (see Subsection 2.2.2), however, the universal boundary conditions at the GUT scale further restrict this range, as demonstrated in Ref. [101]:

$$1 \lesssim \tan\beta \lesssim m_t/m_b \approx 60.$$

Because the CP-odd Higgs boson has no coupling to W bosons and the respective coupling of the heavier CP-even Higgs boson also vanishes in the decoupling limit, no upper bound on their mass follows from the requirement of perturbative unitarity [16]. Also, the trilinear

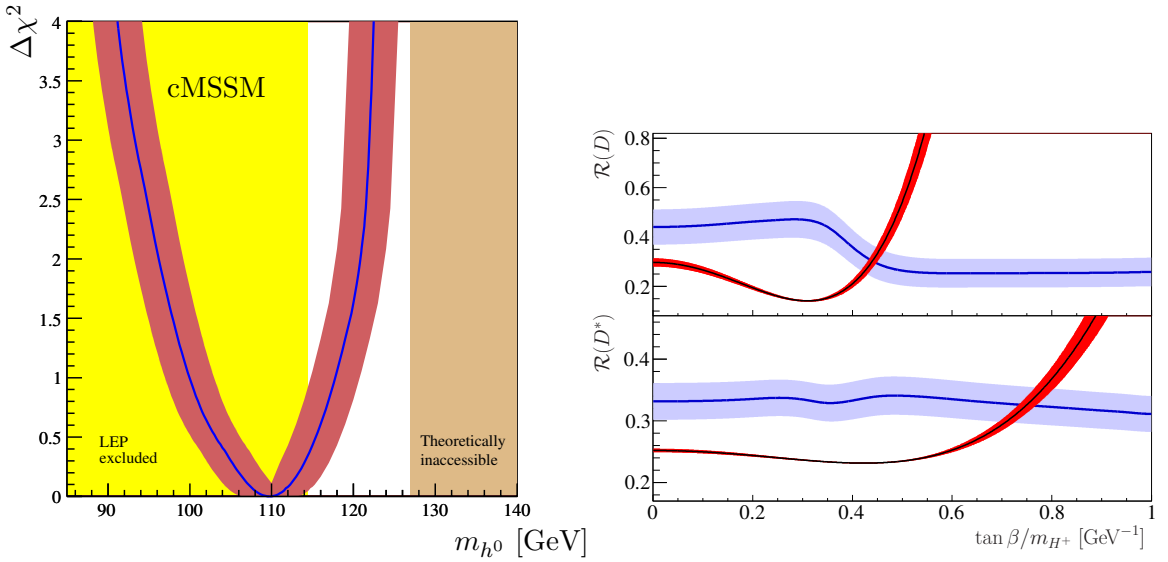

(a) $\chi^2 - \chi^2_{\text{min}}$ for the cMSSM (b) Measured and expected $\mathcal{R}(D^{(*)})$

Figure 2.15.: Global $\chi^2 - \chi^2_{\text{min}}$ value of the MSSM fit to constraints from precision measurements as a function of m_{h^0} [102] (left). The LEP lower limit assumes SM-like couplings of the lighter CP-even Higgs boson to gauge bosons. The right plot shows a comparison of the measured ratios $\mathcal{R}(D^{(*)}) = \text{BR}\left(\bar{B} \to D^{(*)}\tau^-\bar{\nu}_\tau\right)/\text{BR}\left(\bar{B} \to D^{(*)}\ell^-\bar{\nu}_\ell\right)$ (blue) and the prediction for type-II 2HDMs (red) [103].

and quartic Higgs boson couplings are proportional to the gauge couplings in the MSSM and thus do not impose a lower bound on the Higgs boson masses.

As mentioned before, the lightest neutral Higgs boson can be heavier than the Z boson only by virtue of loop corrections. In the case of the cMSSM, the mass of the lighter CP-even Higgs boson is constrained even more tightly than in the general case of Eq. (2.42) [102]:

$$m_{h^0}^{\text{cMSSM}} < 127\,\text{GeV}.$$

2.3.2.2. Constraints on the MSSM Higgs Sector from Precision Measurements

Precision measurements of SM observables [83] and the density of cold dark matter [104] (discussed in Refs. [105]) can be used to compute indirect constraints [106] on the MSSM parameters. Model-sensitive parameters, such as the branching ratio $\text{BR}\,(b \to s\gamma)$, rare decays $B_s \to \mu^+\mu^-$, the anomalous magnetic moment of the muon, and the abundance of cold dark matter, are used to constrain the MSSM parameters, as detailed in Ref. [102]. Figure 2.15(a) shows the goodness of the MSSM fit to electroweak precision variables as a function of m_{h^0}[11]. The resulting prediction for the mass of the lighter CP-even Higgs boson in the MSSM is:

$$m_{h^0}^{\text{MSSM}} = \left(110\,^{+8}_{-10}\,(\text{exp.}) \pm 3\,(\text{theo.})\right)\text{GeV}.$$

The LEP exclusion range shown in Figure 2.15(a) relies on SM-like couplings of the lighter CP-even Higgs boson to gauge bosons, which is true only for a part of the non-excluded parameter space.

[11] Note that this cMSSM differs from the mSUGRA model introduced above.

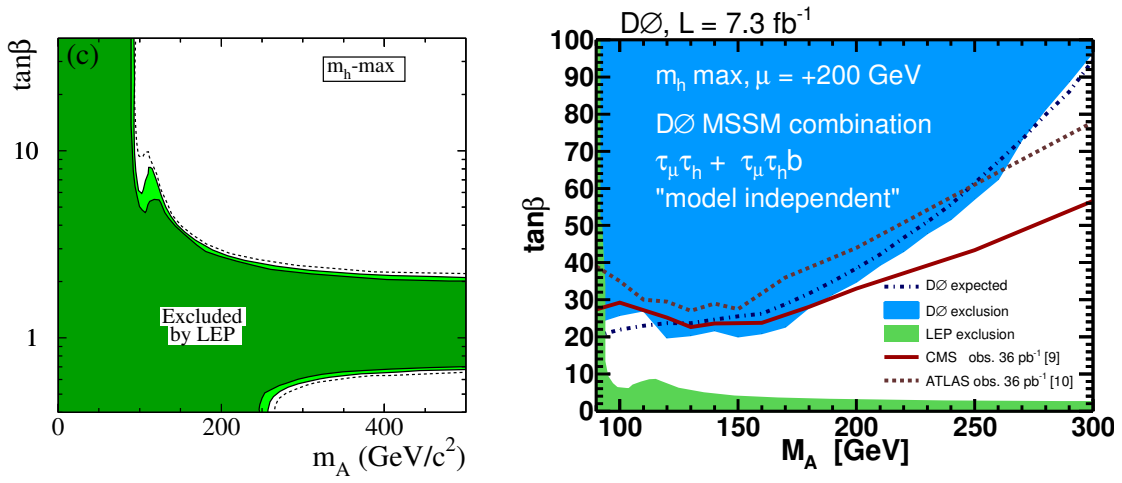

(a) Combined LEP limit

(b) DØ limit

Figure 2.16.: Exclusion limits in the $m_{h^0}^{\text{max}}$ scenario. The left plot shows the areas excluded at 95 % CL (light green) and at 99.7 % CL (dark green) as well as the expected exclusion contour at 95 % CL (dashed line) [71]. The right Figure compares this exclusion to the expected and observed upper limits from the searches by DØ [110]. The comparison to LHC results is discussed in Chapter 10.

Another test of the SM and the MSSM can be inferred from a combination of branching ratios of B mesons for decays involving either τ leptons or light leptons [103]. In a recent measurement by BaBar [103], the ratios $\mathcal{R}(D) = \text{BR}\left(\bar{B} \to D\tau^-\bar{\nu}_\tau\right)/\text{BR}\left(\bar{B} \to D\ell^-\bar{\nu}_\ell\right)$ and $\mathcal{R}(D^*) = \text{BR}\left(\bar{B} \to D^*\tau^-\bar{\nu}_\tau\right)/\text{BR}\left(\bar{B} \to D^*\ell^-\bar{\nu}_\ell\right)$ deviate from the SM expectation with a combined significance of 3.4σ. These ratios have been shown to be sensitive to the presence of charged Higgs bosons [107,108]. Their dependence on $\frac{\tan\beta}{m_{H^+}}$ has been calculated for the general case of a type-II model with two Higgs fields (*type-II 2HDM*, as in the MSSM) [107, 109]. Figure 2.15(b) shows a comparison of the results by BaBar and the predicted values for type-II 2HDMs. The ranges of agreement between prediction and measurement $(\tan\beta/m_{H^+})_{\mathcal{R}(D)} = (0.44\pm0.02)\,\text{GeV}^{-1}$ and $(\tan\beta/m_{H^+})_{\mathcal{R}(D^*)} = (0.75\pm0.04)\,\text{GeV}^{-1}$ do not overlap. The observed disagreement has a significance of 3.1σ for type-II 2HDM models—almost as much as for the SM prediction [103].

2.3.2.3. Direct Searches for Higgs Bosons in the MSSM

The LEP experiments have performed direct searches for Higgs bosons produced in Higgs-strahlung and Higgs boson pair production. The Higgs-strahlung process dominates the combined sensitivity for $\tan\beta \lesssim 5$. The Higgs boson pair production process dominates for larger values of $\tan\beta$ and allows to exclude $m_{A^0}, m_{h^0} < 93\,\text{GeV}$ in the $m_{h^0}^{\text{max}}$ scenario. No neutral Higgs bosons were found, and parts of the parameter space could be excluded, as shown in Figure 2.16(a) for the $m_{h^0}^{\text{max}}$ scenario [71]. The upper $\tan\beta$ boundary of the excluded region is a consequence of the decrease in coupling strength for larger values of $\tan\beta$, reducing the cross-section of Higgs boson pair production, and of kinematics. The lower boundary for $m_{A^0} \gtrsim 250\,\text{GeV}$ results from the limited center–of–mass energy. The LEP collaborations have also published and combined search results concerning charged Higgs bosons (Higgs boson pair production), excluding $m_{H^+} < 80\,\text{GeV}$ at 95 % CL [111].

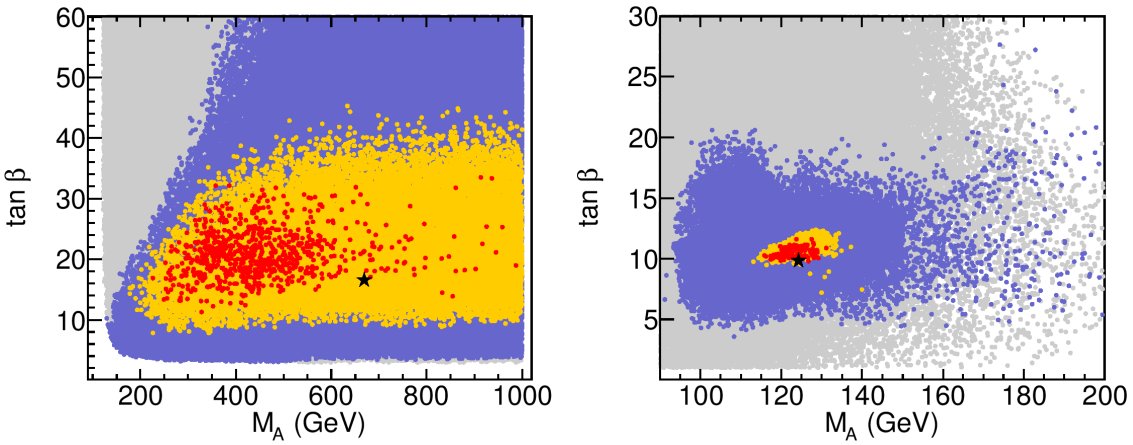

(a) h^0 interpretation (b) H^0 interpretation

Figure 2.17.: pMSSM-7 parameter sets of the light-Higgs case (left) and the heavy-Higgs case (right) in the m_{A^0}–$\tan\beta$ plane, color-coded by the goodness of their fit to data: Points that fail the constraints from the direct Higgs boson searches are shown in gray, others in blue, unless their χ^2 value is below thresholds of 5.99 (yellow) or 2.3 (red). The best-fitting parameter sets $\Delta\chi^2$ are shown as black asterisks (★) [118].

The Tevatron experiments searched for neutral MSSM Higgs bosons with subsequent decays to τ lepton pairs. The CDF and DØ collaborations have taken into account the gluon fusion production mode and b-associated Higgs boson production. DØ presented the most stringent limit in the m_{A^0}–$\tan\beta$ plane for the $m_{h^0}^{\text{max}}$ scenario of the MSSM derived at the Tevatron (see Figure 2.16(b)), using $7.3\,\text{fb}^{-1}$ of collision data [110]. DØ [110, 112] and CDF [112] also took Higgs boson decays to b-quark pairs into account, but the sensitivity of this channel is significantly worse than those involving decays to τ lepton pairs. Upper limits on the production cross-section were previously combined with CDF results and published, using $1.8 - 2.2\,\text{fb}^{-1}$ [113]. The results in the m_{A^0}–$\tan\beta$ plane are compared to the results from ATLAS and CMS in Chapter 10. CDF and DØ have also performed searches for charged Higgs bosons, resulting in upper limits on the branching fraction of t-quark decays involving Higgs bosons [114].

ATLAS and CMS have performed searches for neutral MSSM Higgs bosons in the gluon fusion and b-associated Higgs boson production modes with decays to pairs of τ leptons and muon pairs (ATLAS: $\tau_e\tau_\mu$ in this thesis and a combined search in Ref. [10] with other channels) or only pairs of τ leptons (CMS [115], see comparison in Section 9.4). Searches for charged Higgs bosons yielded improved limits for $\text{BR}(t \to H^+b)$ for both ATLAS [116] and CMS [117].

The analysis presented within this thesis improves the sensitivity (primarily) to light neutral Higgs bosons of the MSSM by evaluating $4.7\,\text{fb}^{-1}$ of ATLAS data containing leptonically decaying τ lepton pairs in two regions. These regions are designed to provide sensitivity to signal events from gluon fusion and from b-associated production. The results are statistically combined with similar regions aimed at different decay modes in a joint publication [10].

Interpretation of the Discovery of a Higgs Boson Within the MSSM

The observation of a Higgs boson [6, 7] constrains the Higgs sector of the MSSM strongly by requiring to interpret it as either the h^0 particle (*light-Higgs case*) or the H^0 particle (*heavy-Higgs case*). Both cases have been evaluated [118] by probing a seven-dimensional parameter subspace (*pMSSM-7*) of the MSSM, containing the parameters most relevant to the Higgs sector: m_{A^0}, $\tan\beta$, μ, $m_{\tilde{b}_L} = m_{\tilde{t}_L} = m_{\tilde{b}_R} = m_{\tilde{t}_R}$, $m_{\tilde{\tau}_L} = m_{\tilde{\nu}_L} = m_{\tilde{\tau}_R}$, $A_t = A_b = A_\tau$, and M_2. For each set of parameters, a fit to the individually measured signal strengths of the search channels in Refs. [6,7] as well as the measurements from the LEP and the Tevatron and a set of low-energy observables has been performed. The measured value of the anomalous magnetic moment of the muon drives the χ^2 value of the SM fit, while it can be accommodated well by the pMSSM-7. In order to avoid that this effect dominates the comparison of the goodness of the SM and pMSSM-7 fits, the mass of the second-generation sleptons have been fixed in the pMSSM-7 fit. The parameter sets are displayed in Figure 2.17, color-coded according to the difference of their χ^2 values ($\Delta\chi^2$) to the best-fitting parameter sets. In the Gaussian limit, the thresholds of $\Delta\chi^2 = 2.3$ and $\Delta\chi^2 = 5.99$ correspond to the 68 and 95 % CL contours for two degrees of freedom, respectively. Areas in parameter space with very good agreement with data exist for both cases. However, the respective area for the light-Higgs case is larger and features a better χ^2 value at the optimum than that of the heavy-Higgs case. The measured signal strengths of the various channels considered by ATLAS and CMS in up to $18\,\text{fb}^{-1}$ [95, 119] can be accommodated well within present uncertainties for either case. The two cases differ strongly in their phenomenological implications: The light-Higgs case fits best with the tree-level parameter values $m_{A^0} = 669\,\text{GeV}, \tan\beta = 16.5$. It is therefore similar to the decoupling limit (see Section 2.2), featuring one light and two significantly heavier Higgs bosons. The heavy-Higgs case with the preferred values $m_{A^0} = 124.2\,\text{GeV}, \tan\beta = 9.8$ implies the presence of a light Higgs boson with a mass of $m_{h^0} = 65.3\,\text{GeV}$. This value is well below the LEP lower limit, but the couplings to vector bosons are sufficiently reduced to be consistent with exclusion limits from the LEP experiments. On the other hand, the observed resonance would need to consist of two nearly mass-degenerate Higgs bosons A^0 and H^0 (with $m_{H^0} = 125.8\,\text{GeV}$) of different couplings [118].

3 The ATLAS Experiment at the Large Hadron Collider

Designed to exploit the discovery potential of the Large Hadron Collider (LHC), A Toroidal LHC Apparatus (ATLAS) records events at unprecedented center–of–mass energies ($\sqrt{s} = 1 - 14\,\text{TeV}$ in proton (pp) collisions) and interaction rates (up to $10^9\,\text{Hz}$) [8].

This Chapter briefly introduces the key features and proton collision performance of the LHC in Section 3.1. Section 3.2 first provides an overview of the detector design and then details the features with the greatest relevance to this thesis.

3.1. The Large Hadron Collider

The LHC is today's most powerful hadron collider. It is located in the circular tunnel of the decommissioned Large Electron–Positron Collider (LEP), which has a circumference of 26 660 m, at the European Laboratory for Particle Physics (CERN).

The luminosity of the LHC is given by [120]:

$$\mathcal{L} = \frac{N_b^2 n_b \nu_{\text{rev}} \gamma}{4\pi \varepsilon_n \beta^\star} F \tag{3.1}$$

with

$$F = \left(1 + \left(\frac{\theta_c \sigma_z}{2\sigma^\star}\right)^2\right)^{-1/2}. \tag{3.2}$$

The design luminosity of $\mathcal{L} = 10^{34}\,\text{cm}^{-2}\text{s}^{-1}$ is achieved with the following values for $\sqrt{s} = 14\,\text{GeV}$ [120]: $N_b = 1.15 \times 10^{11}$ denotes the number of protons (with relativistic gamma factor $\gamma = 7461$) per bunch, $n_b = 2808$ the number of bunches in a beam, $\nu_{\text{rev}} = 11\,245\,\text{Hz}$ the revolution frequency, $\varepsilon_n = 3.75\,\mu\text{m rad}$ the normalized transverse beam emittance, and $\beta^\star = 0.55\,\text{m}$ the beta function at the interaction point (IP). $F = 0.84$ models the impact of the finite crossing angle between the beams: $\theta_c = 285\,\mu\text{rad}$ is the crossing angle, $\sigma_z = 7.55\,\text{cm}$ the root mean square (RMS) of the longitudinal bunch profile, and $\sigma^\star = 16.7\,\mu\text{m}$ the RMS of the transverse bunch profile.

Relativistic proton beams consisting of up to 2808 bunches can be injected in opposite directions into the two LHC beam pipes at 450 GeV from a chain of smaller accelerators (see Figure 3.1) [120]. The LHC provides hadron collisions at four IPs, which are each equipped with a large experiment (see Figure 3.2). The beam setup provides the largest luminosity values at the IPs of the ATLAS and Compact Muon Solenoid (CMS) experiments, whose physics programs overlap and benefit most from high luminosities. The research programs of A Large Ion Collider Experiment (ALICE) and the LHCb experiment focus mainly on heavy ion collisions and the physics of b-hadrons, respectively, so they require lower instantaneous luminosities. In order to achieve different instantaneous luminosities at different IPs, the beam profile is not as strongly focused in the IPs of ALICE and LHCb as in those of ATLAS

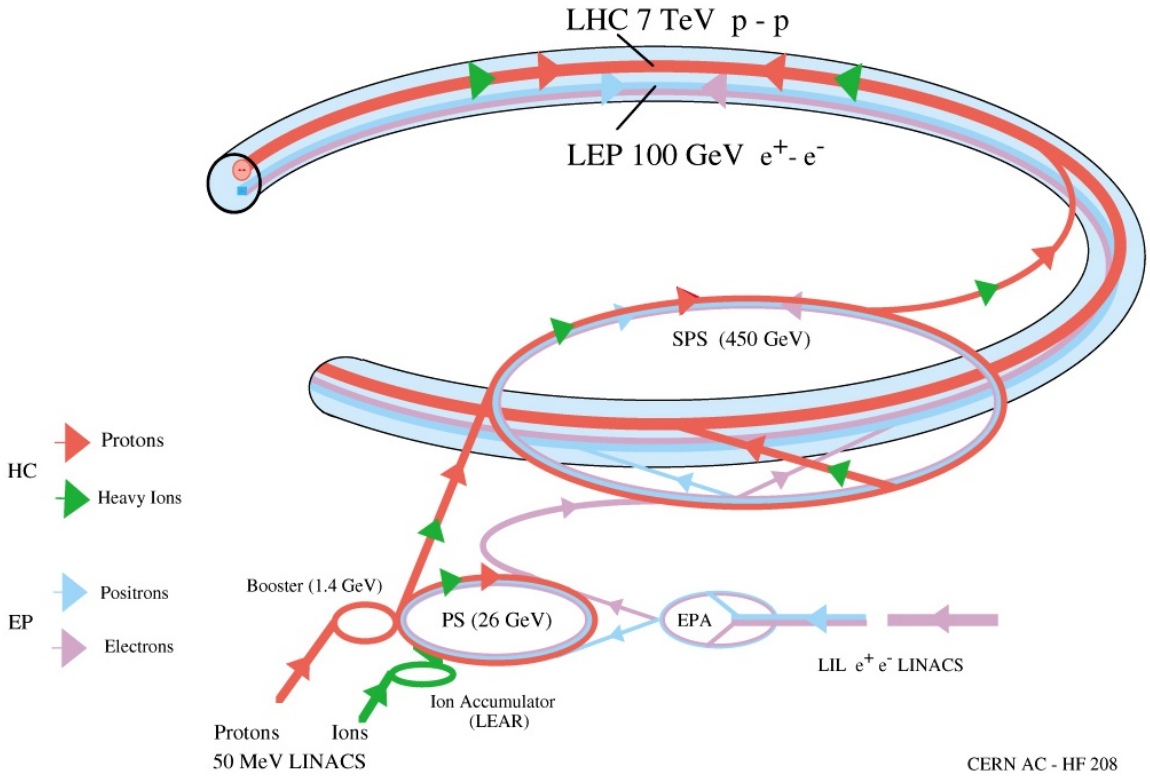

Figure 3.1.: Overview of the LHC injection chain (not to scale) [121].

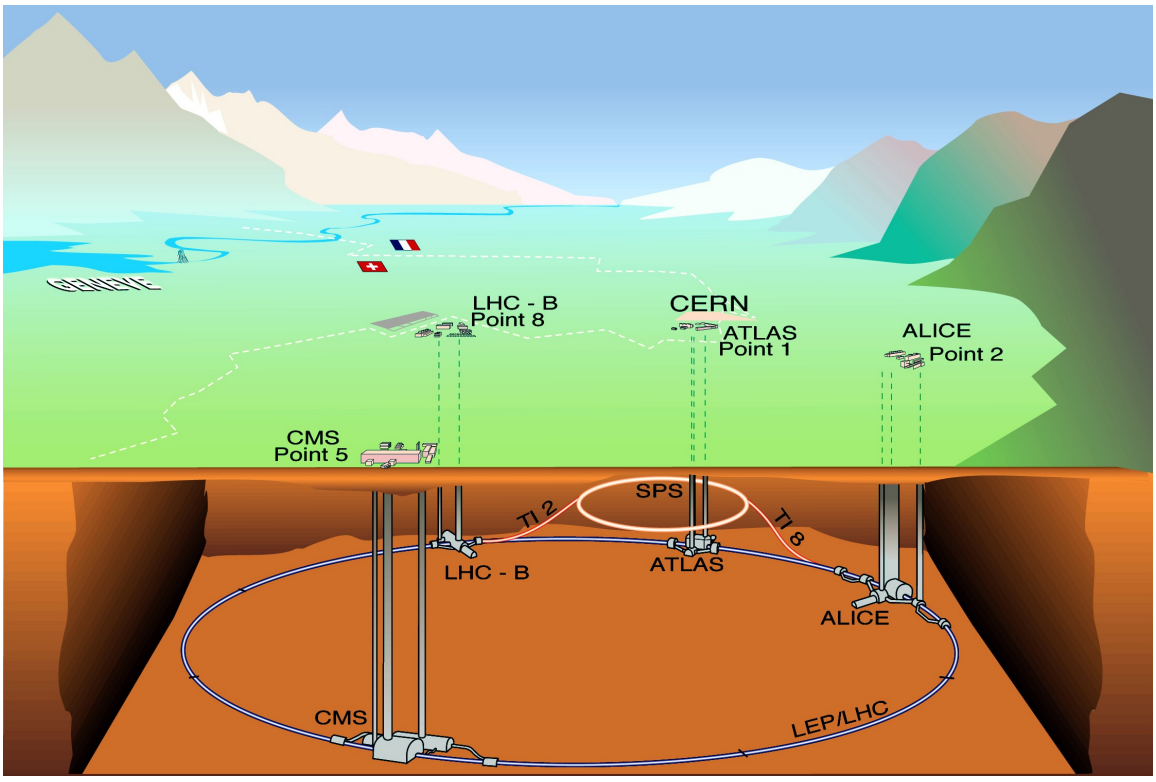

Figure 3.2.: Schematic view of the LHC and the large experiments at its IPs and its location between the Jura mountains (right) and the lake of Geneva (not to scale) [122].

and the CMS experiment. This mitigates the problem of *pileup*, which can refer to two related circumstances: *In-time pileup* refers to concurrent interactions, i.e., multiple interactions during the same bunch crossing. *Out-of-time pileup* refers to remnant signals from previous interactions, which plays a role when the time resolution of a sub-detector is comparable to or worse than the time between bunch crossings.

The specialized ALICE and LHCb experiments are not discussed in this thesis. ATLAS and the CMS are general-purpose experiments, whose strengths and weaknesses complement each other.

The ATLAS detectors are summarized in Section 3.2, which draws many details from Ref. [8]. A thorough description of the CMS can be found in Ref. [9].

The super-conducting dipole magnets of the synchrotron are designed to provide a nominal bending field of up to 8.33 T, corresponding to a center–of–mass energy of up to 14 TeV [120]. Due to safety concerns after the failure of an electric connection, the center–of–mass energy was limited to 7 (8) TeV in the first (second) year of operation before upgrading the quench protection systems in 2013/14.

The LHC can also accelerate heavy ions at energies up to the design value of 2.76 TeV/nucleon for lead nuclei at a luminosity of up to $\mathcal{L} = 10^{27}\,\mathrm{cm}^{-2}\mathrm{s}^{-1}$ [120]. Collisions of heavy ions produce lower parton momenta and a larger event complexity, so heavy ion runs are irrelevant to this thesis.

3.1.1. LHC Performance Evolution and ATLAS Data Acquisition

The data-taking in 2010 was dominated by the constraints of machine commissioning and only about $48\,\mathrm{pb}^{-1}$ were delivered to ATLAS at $\sqrt{s} = 7\,\mathrm{TeV}$. In 2011, peak instantaneous luminosity was ramped up gradually to about $3.65 \times 10^{33}\,\mathrm{cm}^{-2}\mathrm{s}^{-1}$, and an integrated luminosity of $5.61\,\mathrm{fb}^{-1}$ was delivered to ATLAS. In 2012, the center–of–mass energy was increased to $\sqrt{s} = 8\,\mathrm{TeV}$, and the instantaneous luminosity was again increased, so an integrated luminosity of about $22.8\,\mathrm{fb}^{-1}$ was delivered to ATLAS and CMS [123].

The mean number of interactions (μ) can be calculated in data from the measured instantaneous luminosity ($\mathcal{L}$, see Subsection 3.2.6), the total inelastic cross-section (σ_{inel}), the number of colliding bunches (n_b), and the revolution frequency (ν_{rev}) [124]:

$$\mu = \frac{\mathcal{L}\sigma_{\mathrm{inel}}}{n_b \nu_{\mathrm{rev}}}. \tag{3.3}$$

The 2011 proton run has been divided into data-taking periods of comparable conditions for data taking at ATLAS (denoted as `A`–`M`), of which only those with nominal magnetic fields in the detector and a center–of–mass energy of 7 TeV (`B`,`D`–`M`) have been used for this thesis. The performance of all sub-detectors was monitored throughout the run. Requiring those of relevance for this thesis to be operational leaves a dataset that corresponds to an integrated luminosity of $(4.66 \pm 0.18)\,\mathrm{fb}^{-1}$ [125, 126].

As shown in Figure 3.3, comparable amounts of data were taken with configurations including values of the optical β function (at the IP) of 1.5 m (`B`,`D`–`K`) and then 1.0 m (`L`–`M`) [127].

While the instantaneous luminosity reached only a fraction of its design value of $10^{34}\,\mathrm{cm}^{-2}\mathrm{s}^{-1}$, the corresponding number of mean interactions per bunch crossing (23) has already been approached during the last runs of the year. Apart from the $\beta^\star$ value, the bunch spacing can account for the difference in luminosity: A bunch spacing of 50 ns[1] was used rather than the design value of 25 ns [127].

[1] with the exception of 75 ns used during data-taking period `B`

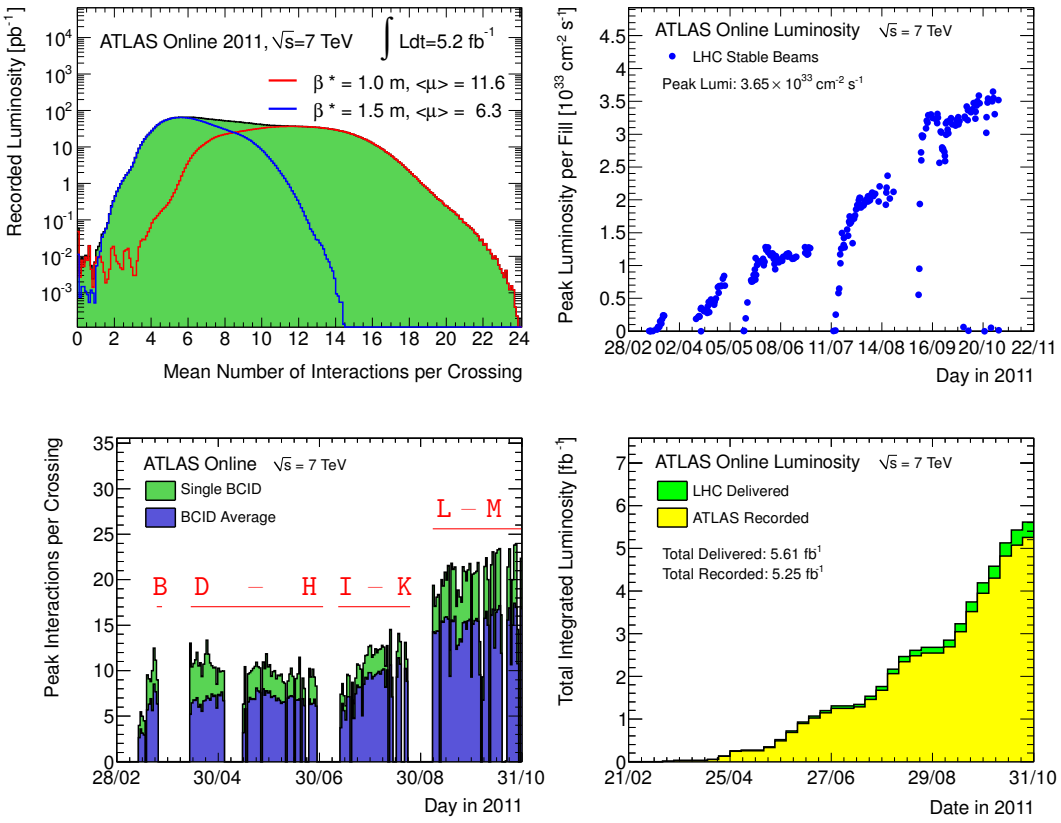

Figure 3.3.: Evolution of the performance of the LHC in 2011 [127]. The top left Figure shows the distribution of the mean number of interactions per bunch crossing for all recorded data, highlighting the difference between data-taking periods with $\beta^\star$ values of 1.5 m (data-taking periods B–K) and 1.0 m (L–M). The top right Figure shows the gradual increase in peak instantaneous luminosity throughout 2011. The bottom left Figure shows the evolution of the mean ("BCID Average") and largest observed ("Single BCID") interaction multiplicities at peak luminosity throughout 2011. The data-taking period names (B–M) have been overlaid. The bottom right Figure shows the cumulated integrated luminosity delivered to and recorded by ATLAS.

The overlay of several interactions in a single event poses a challenge to the LHC experiments. The experiments must therefore exploit differences between "interesting" and "common" interactions as well as resolve individual interactions: During 2011, the transverse beam profile at the ATLAS IP was characterized by the RMS values $\sigma_x = 15.7\,\mu$m, $\sigma_y = 13.5\,\mu$m, $\sigma_z = 56.8\,$mm at $\sqrt{s} = 7\,$TeV [128]. As shown in Subsection 3.2.2, the tracking information can be used to match charged particles and associated objects, such as jets, to individual interactions. Subsection 3.2.7 discusses how the ATLAS experiment deals with the large event rate it receives from LHC collisions, using a sophisticated trigger and data acquisition (TDAQ) system.

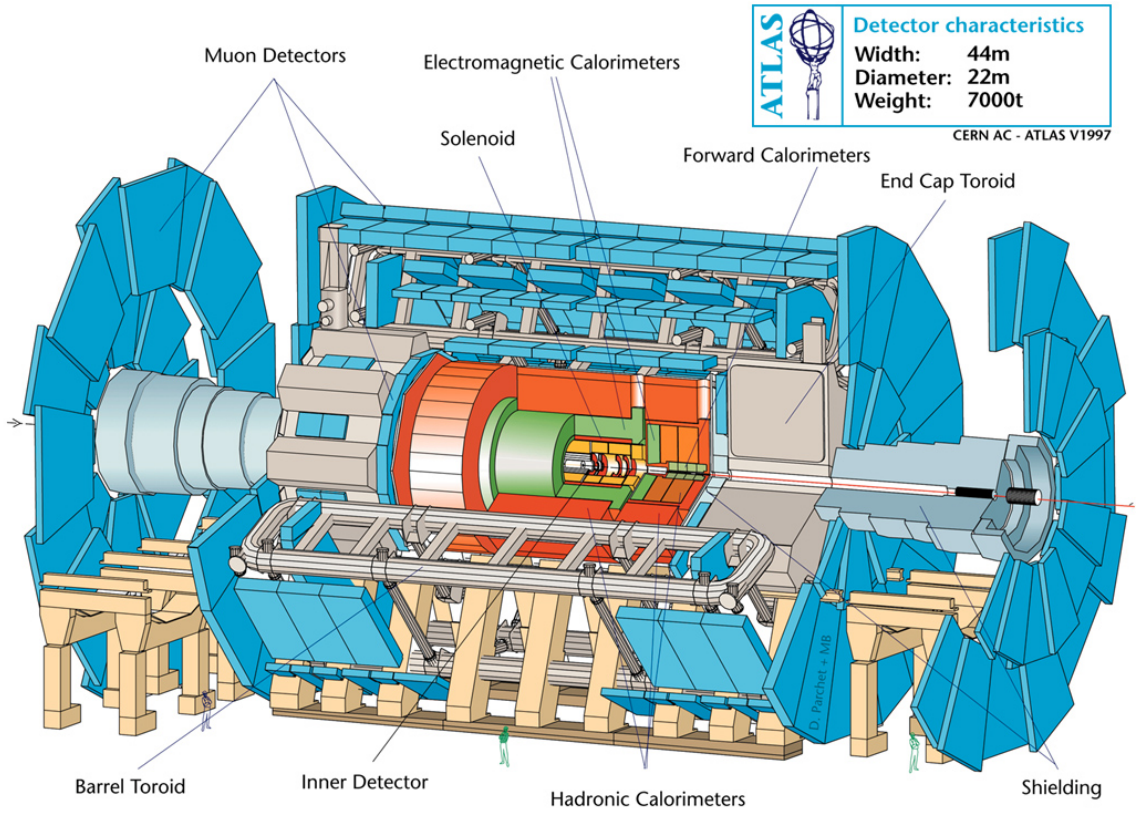

Figure 3.4.: Schematic view of the ATLAS detector, including the main detector components and overall dimensions [129].

3.2. Key Features of the ATLAS Experiment

The ATLAS detector has been conceived [130] as a general-purpose experiment at the LHC with a main focus on analyzing proton collisions at a luminosity of up to $\mathcal{L} = 10^{34}\,\mathrm{cm}^{-2}\mathrm{s}^{-1}$. Its name means A Toroidal LHC Apparatus, conveying the prominent use of large air-core toroid magnets in the muon spectrometer, as shown in Figure 3.4.

The sub-detectors are all designed to cover the largest possible fraction of the solid angle around the IP. This is reflected by their layout of concentric cylinders (*barrels*) and matching disk-shaped *endcaps*, which are assembled along the beampipe.

In order to detect particles originating from the IP, the inner tracking detectors, the calorimetry, and the muon spectrometer are placed, in that order, from the IP outwards. For the measurement of momenta, a solenoidal magnetic field of 2 T pervades the inner tracking detectors, and a toroidal field with a local field strength of up to 3.5 T is generated in the muon spectrometer [8].

3.2.1. The ATLAS Coordinate System

A right-handed spherical coordinate system [8] is employed within this thesis. The Cartesian (x, y, z) and spherical (r, ϕ, θ) coordinates pertain to the reconstructed IP—with the exception of the *nominal* coordinates, whose origin is located at the geometrical center of the detector. The x-, y-, and z-axes point to the center of the LHC, upwards, and along the direction of the counter-clockwise beam (when viewed from above), respectively. The beams cross

(vertically) in the y–z plane. With respect to the axis of symmetry of the detector, the beam direction differs by a rotation of 0.5 mrad about the y-axis and 0.08 mrad about the x-axis. Consequently, the coordinate system has been rotated about the y-axis to compensate for this [131]. From the polar angle (θ), the pseudo-rapidity (η) is derived:

$$\eta = -\ln \tan \frac{\theta}{2}. \tag{3.4}$$

The pseudo-rapidity of a massless particle is equal to its rapidity (y). Because the pseudo-rapidity is good approximation of the rapidity for relativistic particles, rapidity differences are invariant under Lorentz transformations along the beam direction. The pseudo-rapidities of particles are therefore very useful in describing hadron collisions in a lab frame due to the fact that parton momenta are statistically distributed, resulting in an unknown z-component of the velocity of the center–of–mass system. By choosing the coefficient of $\frac{1}{2}$ for the polar angle in Eq. (3.4), dimensions are preserved in the central detector area, $\left|\frac{d\eta}{d\theta}(\theta = \frac{\pi}{2})\right| = 1$, so the pseudo-rapidity is also used in the definition of opening angles (ΔR) of two vectors (r_1, ϕ_1, θ_1) and (r_2, ϕ_2, θ_2):

$$\Delta R = \sqrt{(\Delta\phi)^2 + (\Delta\eta)^2}, \tag{3.5}$$

where $\Delta\phi$ is the transverse opening angle and $\Delta\eta$ is the difference in η of the two vectors.

When assessing the compatibility of a track and a vertex position, the track is extrapolated[2] to find the point of closest approach (PCA) to the vertex in the transverse projection. The difference of the z-coordinates of the PCA and the vertex is the longitudinal impact parameter (z_0). The transverse distance of the PCA and the vertex is the transverse impact parameter (d_0), which is defined to be positive (negative) if the momentum of the particle at the PCA has a clockwise (counter-clockwise) direction in the transverse plane.

3.2.2. The Inner Detector

In order to reconstruct decay vertices, measure the momenta of charged particles, and to distinguish particles from different interactions occurring during the same bunch crossing (*in–time pileup*), space-points of tracks of charged particles must be precisely measured as close as possible to the IP. This task is accomplished with the Inner Detector, which consists of three sub-detectors (see Figure 3.5):

- The Pixel detector is located closest to the IP and consists of three layers of identical silicon pixel modules both in the barrel and in the endcaps. These modules are segmented into rectangles of $50\,\mu\text{m} \times 400\,\mu\text{m}$ for 90 % of the active surface and $50\,\mu\text{m} \times 600\,\mu\text{m}$ for the remaining 10 %. The modules are oriented to have the direction of higher granularity in the tangent direction to the barrels, coinciding with the bending plane of charged particles. The layer closest to the IP is called the B-layer [8].

- The semi-conductor tracker (SCT) surrounds the Pixel detector. It consists of silicon modules that each contain two layers of sensitive strips with a strip pitch of 80 μm, which draw an angle of 40 mrad. The barrel region contains four such concentric double layers, which each contain one layer with a strip orientation parallel to the beam axis. The forward region is covered by nine discs with radial strip orientation on each side of the IP [8].

[2] taking into account magnetic fields within the detector

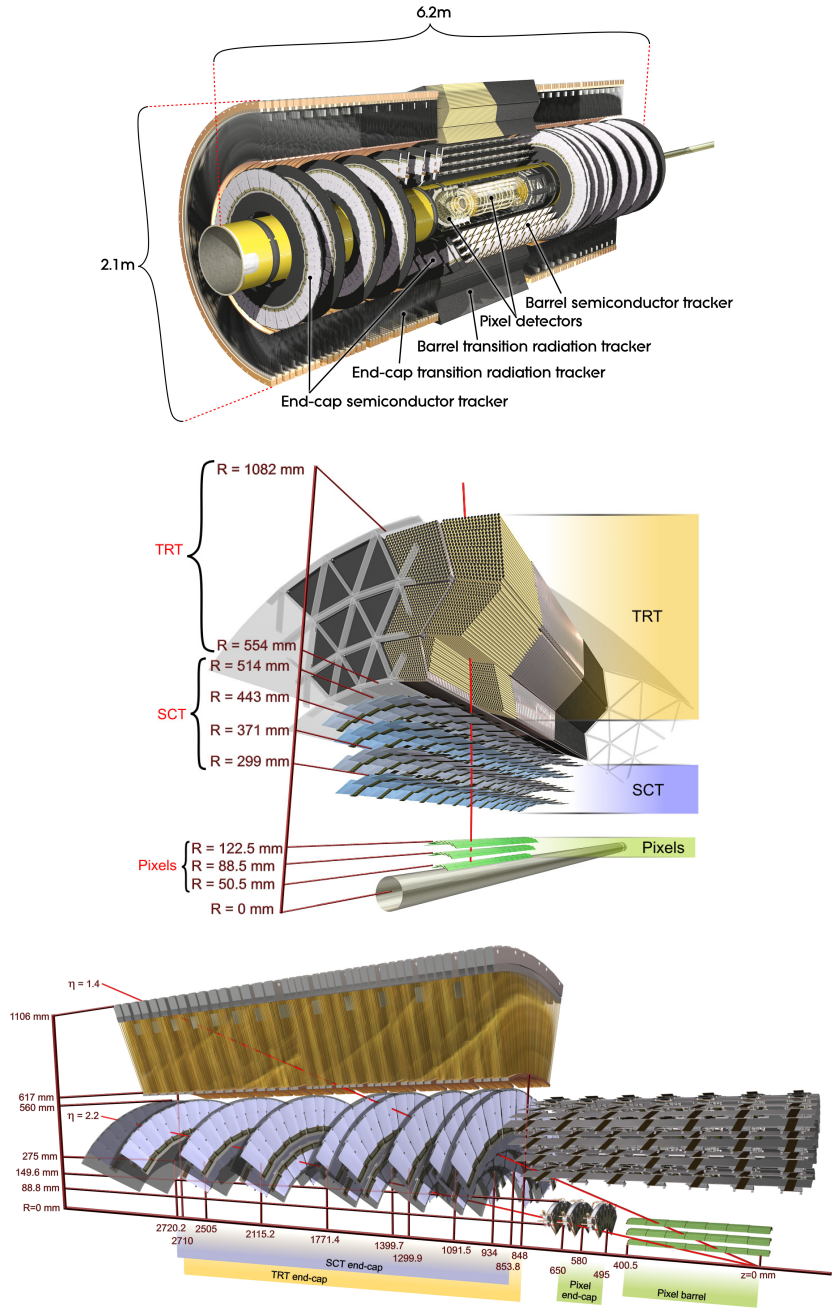

Figure 3.5.: Overview of the inner tracking detectors (top) and dimensioned cross-section view of a sector of the barrel region (middle) and a sideways view of one endcap region (bottom) [8].

- The transition radiation tracker (TRT) is a gaseous straw-tube detector, whose barrel and end-caps are shaped like hollow cylinders, which radially envelope the Pixel and SCT detectors. It consists of 73 layers of tubes in the barrel region and 160 layers in the endcaps, each measuring 4 mm in diameter. The layers are interleaved with transition radiation material [8]. The TRT registers ionizations from charged particles. The transition radiation material provides an additional means of distinguishing between electrons and pions: The former induce transition radiation, which leads to a larger signal in the TRT tubes [132].

This combination of three different sub-detectors has been chosen to address the challenge of providing high-precision tracking in the high-occupancy environment close to the IP. The Pixel detector is located 50.5 to 122.5 mm from the nominal beam axis[3], so it contributes the space points closest to the IP. The Pixel detector therefore dominates the resolution of the reconstruction of impact parameters and vertices. For $t\bar{t}$ events, a vertex resolution with a RMS of 11 μm in the transverse and 40 μm in the longitudinal direction is achieved. The resolution of a track parameter X depends on the transverse momentum of the track as follows [8]:

$$\sigma_X(p_\mathrm{T}) = \sigma_X(p_\mathrm{T} \to \infty)\sqrt{1 + \left(\frac{p_X}{p_\mathrm{T}}\right)^2}. \tag{3.6}$$

The impact parameter resolution of pions with large momenta has been determined to be $\sigma_{d_0}(p_\mathrm{T} \to \infty) = 10\,\mu$m (12 μm) in the transverse and $\sigma_{z_0\times\sin\theta}(p_\mathrm{T} \to \infty) = 91\,\mu$m (71 μm) in the longitudinal directions for the pseudo-rapidity range $0.25 < |\eta| < 0.50$ ($1.50 < |\eta| < 1.75$) [8]. While the amount of material in the Inner Detector is approximately minimal for $0.25 < |\eta| < 0.50$, particles in the range $1.50 < |\eta| < 1.75$ pass through the most material. For muons, the p_T value for which the uncertainty on the measured transverse momentum equals the contribution from multiple scattering ranges from $p_{p_\mathrm{T}} = 44 - 80$ GeV and results in a relative transverse momentum uncertainty of $1.5 - 1.9$ % for muons with $p_\mathrm{T} = 10$ GeV, underlining the importance of material budgeting in the Inner Detector [8]. As shown for electrons and pions in Ref. [8], the track reconstruction efficiency of non-minimally ionizing particles is sensitive to additional material, leading to a degradation of the performance in the forward regions.

In order to minimize the amount of passive material while maintaining a high granularity in the transverse plane, silicon strips are used in the SCT. The small angle of 40 mrad between the two strip layers of a SCT module serves two purposes: They provide a good spatial separation of ghost hits, i.e., ambiguities that arise from coinciding particles traversing the same module, and improve the resolution in the transverse plane. Besides the advantage of improved discrimination of electrons and pions, the 73 (160) straw planes of the TRT in the barrel (endcap) add typically 36 space points per track, improving the resolution of ambiguities from ghost and noise hits as well as the accuracy of track extrapolation into the calorimeters and the muon spectrometer. The TRT only covers the pseudo-rapidity range $|\eta| < 2.0$, while the Pixel and SCT detector extend to $|\eta| = 2.5$ [8].

The pattern finding algorithms of the Inner Detector can be used to reconstruct tracks of charged particles down to a p_T threshold of 0.1 GeV for performance studies. For other measurements, a threshold of 0.5 GeV is typically applied to select tracks for vertexing. A track reconstruction efficiency of more than 99 % is achieved for muons with a transverse momentum of 5 GeV, except in the regions with $2.25 < |\eta| < 2.5$, where it degrades to 98 % [8].

[3] up to 149.6 mm in the endcap region

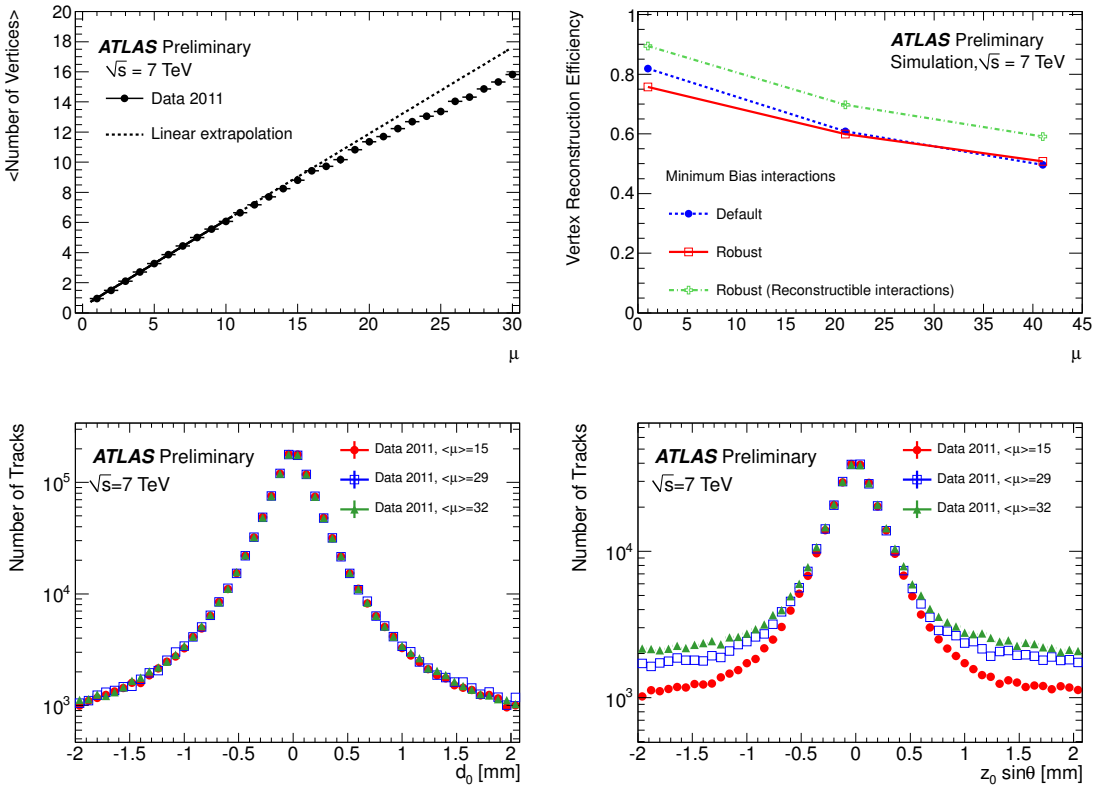

Figure 3.6.: Impact of pileup conditions on the tracking performance [124]. The number of reconstructed vertices is shown as a function of the mean number of proton interactions (top left), which is calculated with Eq. (3.3). For the total inelastic cross-section, the value $\sigma_{\text{inel}} = 71.5\,\text{mb}$ from Pythia [133] has been used. The decreasing slope corresponds to a declining vertexing efficiency for large numbers of proton interactions, as shown in simulation in the top right Figure. This decline is shown both for the default track requirements and for tighter requirements on the number of tracker hits (`robust`). The `robust` requirement has also been evaluated with respect to only interactions with at least two generated particles with $|\eta| < 2.5$ that satisfy the track p_{T} cut $p_{\text{T}} > 400\,\text{MeV}$. The bottom Figures show the transverse (left) and longitudinal (right) impact parameter distributions of tracks in data that pass the `robust` requirement.

Tracks originating in the luminous region are used to seed primary vertex candidates. These are evaluated using an adaptive vertex fitting algorithm [134], which is based on Kalman filtering [135]. Figure 3.6 shows the dependence of the efficiency of reconstructing the primary vertex of an interaction on the mean number of concurrent interactions in the event and the associated impact parameter distributions. At least three compatible tracks are required for a good vertex candidate. The tails of the longitudinal impact parameter distribution are more pronounced for larger interaction multiplicities because tracks are associated to the most compatible vertex if insufficient separation prevents the reconstruction of close vertices as additional vertices. This simultaneously leads to a decline in the primary vertex reconstruction efficiency. While the transverse bunch dimension is of the order of the d_0 resolution, such additional tracks enter the tail regions of the $z_0 \sin\theta$ distribution.

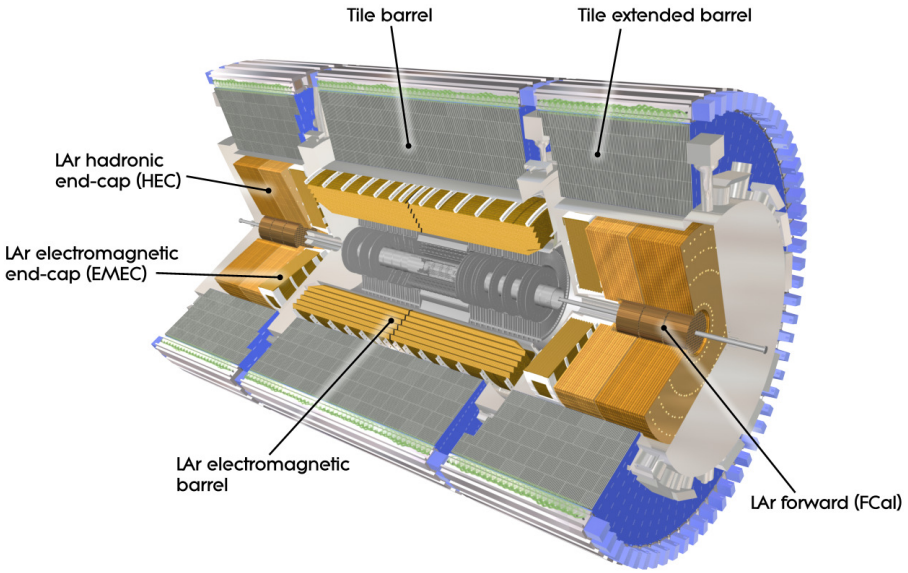

Figure 3.7.: Overview of the calorimetry [8].

3.2.3. Calorimetry

The electromagnetic and hadronic calorimeters (see Figure 3.7) surround the central solenoid, which encloses the Inner Detector.

The pseudo-rapidity range $|\eta| < 3.2$ is covered by a combination of a presampler, an electromagnetic calorimeter, and a hadronic calorimeter; each is a combination of barrel and endcap parts. The presampler is a thin liquid Argon (LAr) calorimeter layer that records the transverse profile of the shower at the entry into the calorimetry, so the previous energy loss from showering can be taken into account. It is deployed in the range $|\eta| < 1.8$, covering the region with the largest variations in the amount of material before the calorimeters. The adjoining LAr calorimeter consists of zig-zag-bent structures (combining lead absorbers and kapton electrodes) in two to three layers, designed to obtain symmetry in the azimuthal direction and leading to the name accordion calorimeter (see Figure 3.8). In the pseudo-rapidity range (almost) coinciding with the coverage by the Inner Detector ($|\eta| < 2.4$), its cells have a size of 0.025×0.1 in $\eta \times \phi$, and they are further sub-divided into strips in η. The second layer is also segmented into finer cells for $|\eta| < 2.5$ (0.025×0.025 in $\eta \times \phi$), where a third layer (0.05×0.025 in $\eta \times \phi$) exists for better resolution of the longitudinal shower shape, and the second layer has coarser sub-divisions for $2.5 < |\eta| < 3.2$ (0.1×0.1 in $\eta \times \phi$).

The region up to $|\eta| = 3.2$ is covered by dedicated hadronic calorimeters: a scintillator tile sampling calorimeter with steel absorbers (consisting of a three-layered barrel) covers the region with $|\eta| < 1.7$, and a LAr hadronic calorimeter with copper plates, the regions with $1.5 < |\eta| < 3.2$. Because of space constraints, the use of separate electromagnetic and hadronic calorimeters is not feasible in the very forward regions, so a combined, three-layered LAr forward calorimeter (FCal) is deployed in the regions with $3.1 < |\eta| < 4.9$. The first layer again uses copper as absorber material and is optimized for measuring electromagnetic showers, while the other two layers use tungsten [8].

Because showers induced by electrons and photons are attenuated more easily by interactions with matter than those induced by hadrons, the column density of the total material between the interaction point and the entry point into the electromagnetic calorimeter plays

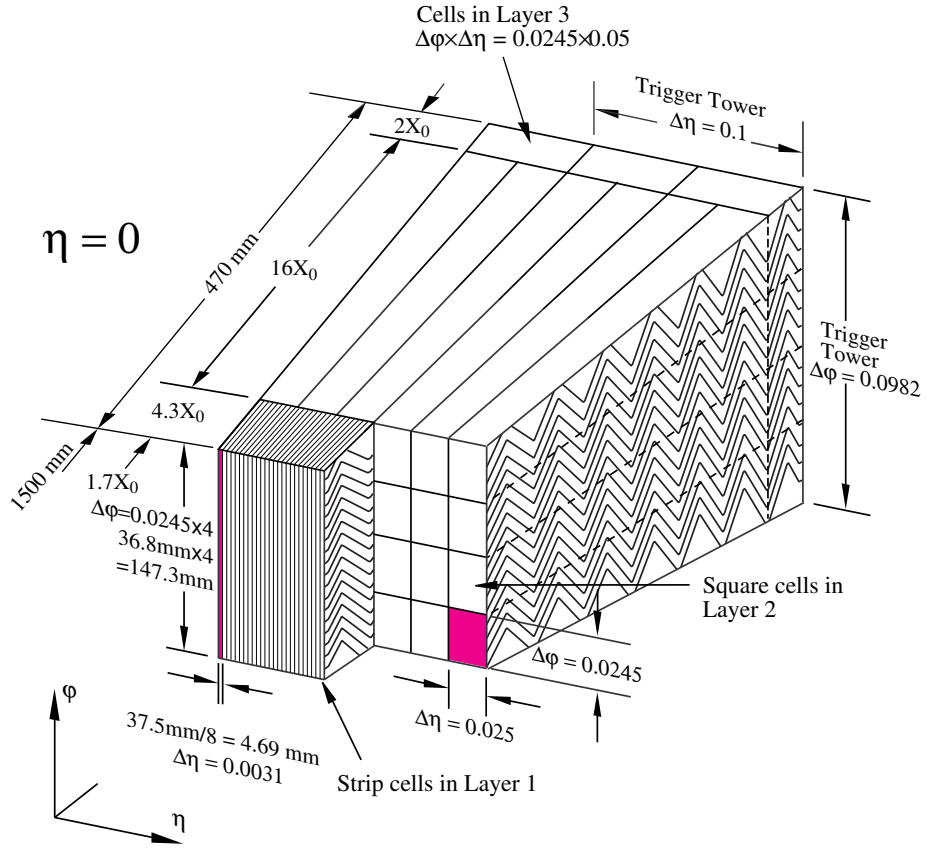

Figure 3.8.: Schematic view of the three layers of the electromagnetic calorimeter in the central detector region [8]. The dimension of depth is labeled both in units of length and in radiation lengths.

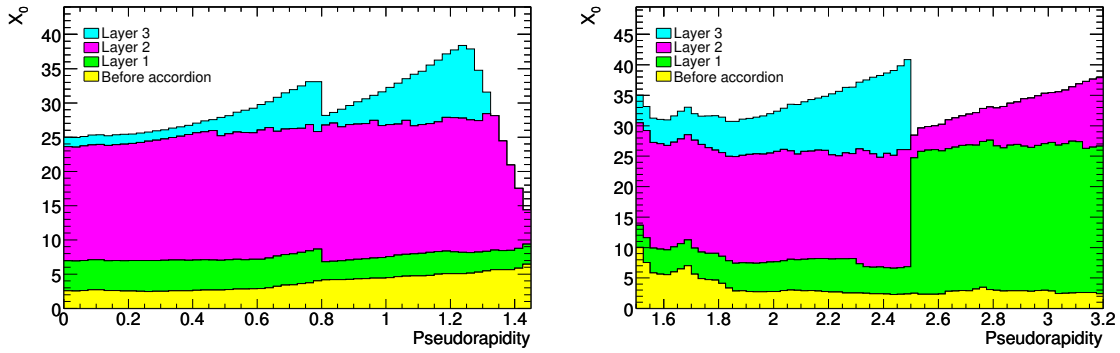

Figure 3.9.: Material before and in the electromagnetic accordion calorimeter, given in units of radiation lengths (X_0). The left Figure shows the barrel region, the right Figure, the endcap. [8].

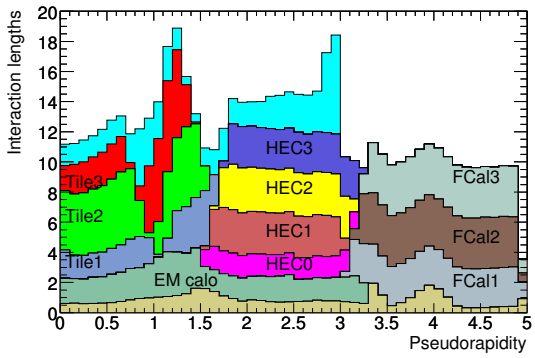

Figure 3.10.: Material before muon spectrometer, normalized to the hadronic interaction length. The first and last stacked contributions pertain to material before entry into the calorimetry and that between the hadronic calorimeters and the first sensitive layer of the Muon Spectrometer [8].

an important role in the design of the Inner Detector and central solenoid. The amount of material before the accordion calorimeter is shown in Figure 3.9 in units of the radiation length (X_0). The amount of material varies between about $2X_0$ and $10X_0$, depending on the pseudo-rapidity. For precision measurements of electromagnetic showers, the total column density before the hadronic calorimeter corresponds to between about $25X_0$ and $40X_0$, with the exception of the ends of the barrel ($1.3 < |\eta| < 1.5$), where the equivalent column density declines to about $14X_0$, while the amount before the accordion calorimeter increases to about $6X_0$. Besides limiting the amount of material before the calorimetry, it is important to contain showers within the hadronic calorimeter in order to avoid a loss in accuracy of the energy measurement and to attenuate the shower before the muon spectrometer. The hadronic calorimeters and the FCal provide at least the equivalent of ten hadronic interaction lengths in front of the muon spectrometer for pseudo-rapidities up to $|\eta| < 4.9$ (see Figure 3.10) [8].

The electromagnetic calorimeter and the Inner Detector allow the reconstruction of electrons with transverse momentum values between 20 and 50 GeV at an efficiency of more than 98 % throughout the tracker coverage (see Figure 3.11) [136]. Depending on the transverse momentum and pseudo-rapidity of the electron, the identification efficiency varies between 72 and 86 % for the *tight* electron identification criteria (see Subsection 6.1.2). The electron reconstruction is designed to provide an energy resolution of 1 to 4 %, depending on the transverse momentum and pseudo-rapidity of the electron (see Figure 3.12) [8]. Because precision and efficiency are drastically reduced in the transition region $1.37 < |\eta| < 1.52$, electron candidates from these regions are not considered for the analysis presented in this thesis. The uncertainty of the energy scale calibration varies from $0.5 - 1$ % in the central detector region to $0.8 - 1.6$ % near the barrel–endcap transition region (see Figure 3.13) [136].

The amount of calorimeter activity in LHC collisions at ATLAS favors the use of anti-k_T jets for the good performance in splitting overlapping jet candidates of this algorithm (see Subsection 4.1.3). The ratio of the reconstructed energy deposits to the energy of the incident parton (jet response at electromagnetic scale) for quark-induced k_T jets depends strongly on the transverse energy and the pseudo-rapidity of the jet (see Figure 3.14). The jet energy scale has been determined from simulation and calibrated to match the performance in collision data within $1 - 3$ % in the central detector region (with uncertainties up to 6 % in the forward regions). Depending on the topology of the event and the flavor of the incident parton, additional uncertainties of typically 0.5 to 3 % apply [137].

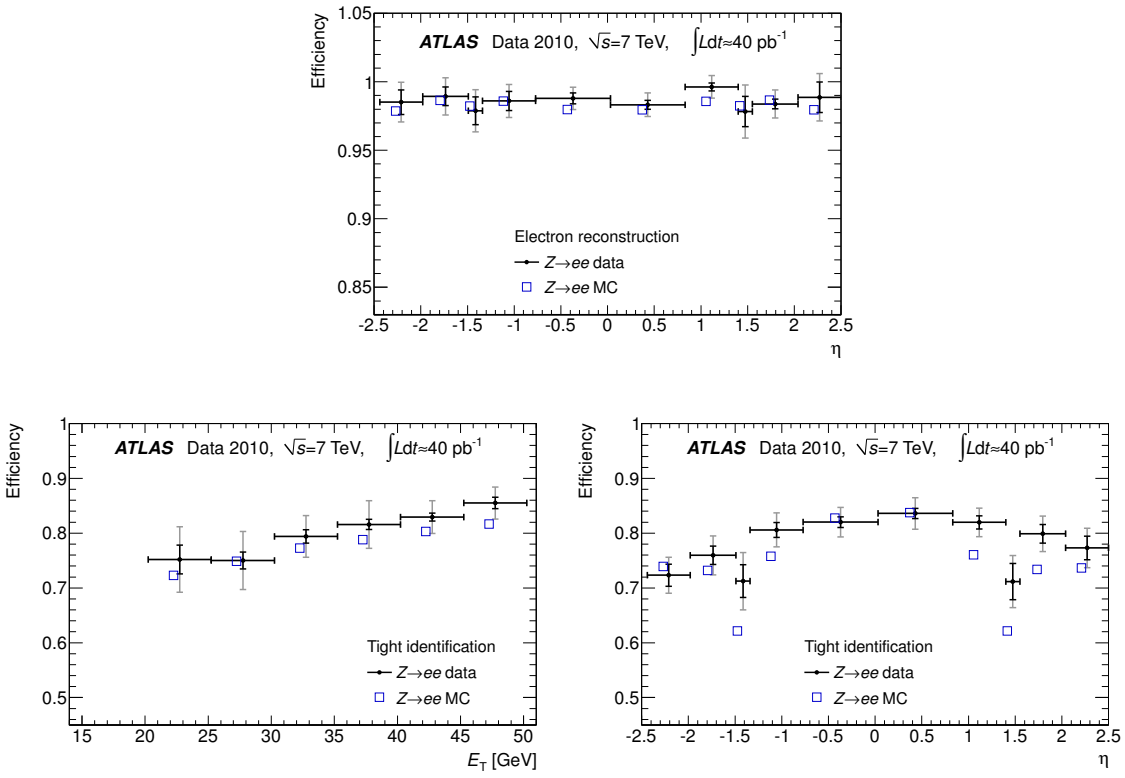

Figure 3.11.: Electron reconstruction efficiency across the relevant pseudo-rapidity range (top) and efficiency of the *tight* electron identification criteria as a function of the transverse energy (left) and the pseudo-rapidity (right), obtained from $Z/\gamma^* \rightarrow ee$ decays recorded in 2010 [136].

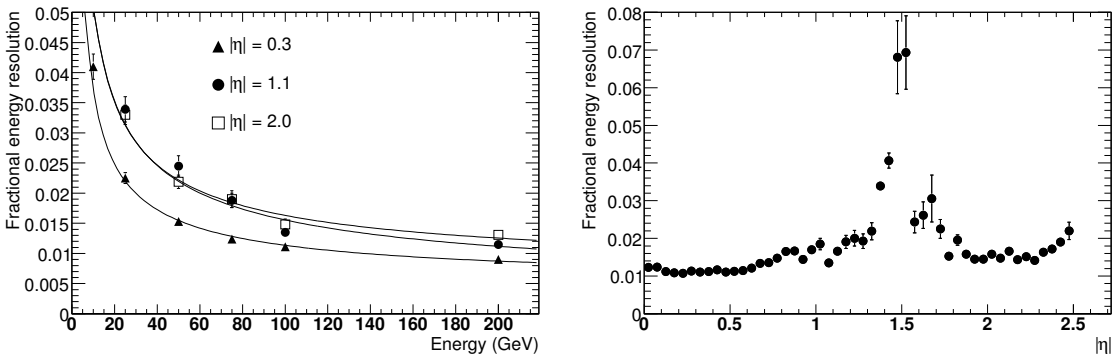

Figure 3.12.: Fractional energy resolution for electrons as a function of the energy (left, shown for three different pseudo-rapidities) and the pseudo-rapidity (right, shown for an electron energy of 100 GeV), taken from simulation [8].

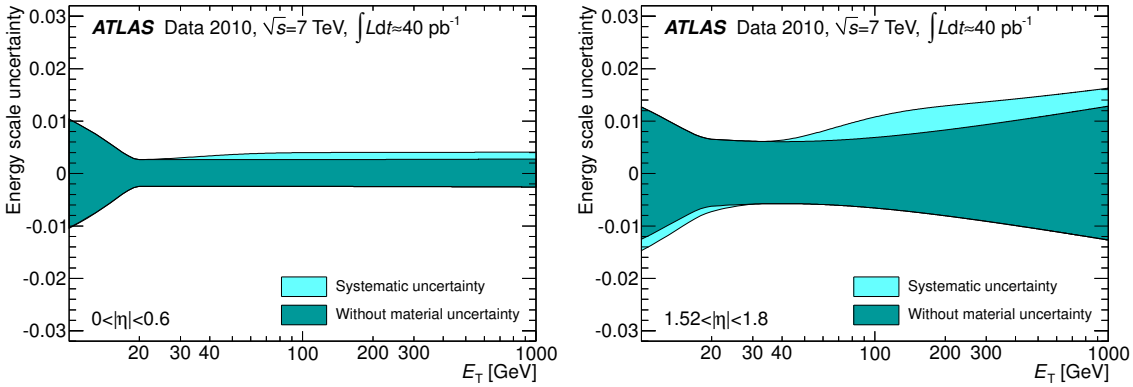

Figure 3.13.: Electron energy scale uncertainty in two pseudo-rapidity ranges in 2010 data-taking, showing the impact of the uncertainties of the material distribution. The range $0 < |\eta| < 0.6$ (left) has the smallest energy scale uncertainty, the range $1.52 < |\eta| < 1.8$ (right), the largest [136].

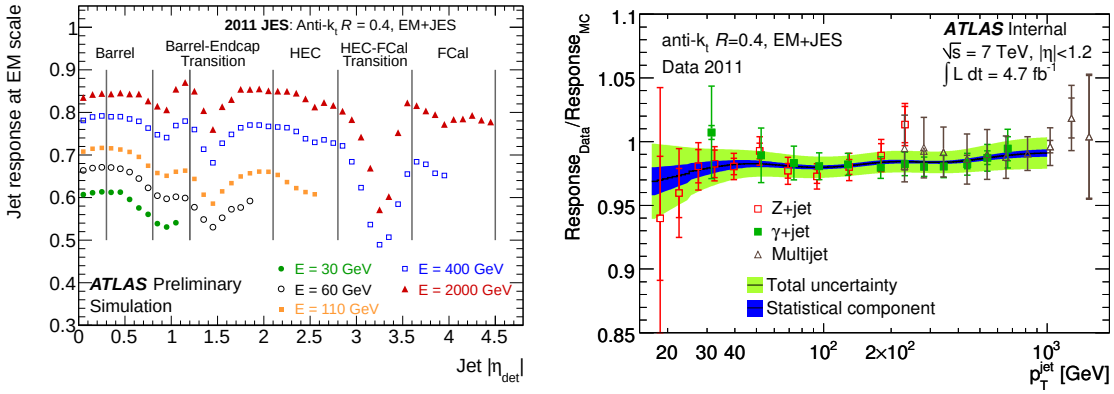

Figure 3.14.: Jet response at the electromagnetic scale as a function of pseudo-rapidity are compared for $|\eta| < 1.2$ in the right Figure, citing the statistical and total uncertainty [137].

3.2.4. The Muon Spectrometer

The Muon Spectrometer with its toroid magnets (see Figure 3.15) defines the overall dimensions of the detector. The various detector components used in the Muon Spectrometer are planar, so they are assembled in alternating smaller and larger overlapping segments to accommodate the toroid coils in the barrel region. Because of services from the Inner Detector and the central solenoid, a gap exists between the two half-barrels of the Muon Spectrometer for $|\eta| < 0.1$. The magnetic field is created by an air-core toroid in the barrel region and two endcap toroids, so the impact of multiple scattering on the momentum resolution is mitigated. The detector components are placed in three stations in the barrel, at radii of approximately 5, 7.5, and 10 m. The endcaps are realized as discs, one in front of and two behind the endcap toroid (from the IP), the outermost endcaps placed at $z = \pm 23$ m [8].

While the Muon Spectrometer measures the sagitta of the track in the toroid field in the barrel, the measurement in the endcap relies on determining the change in direction after the traversal of an endcap toroid.

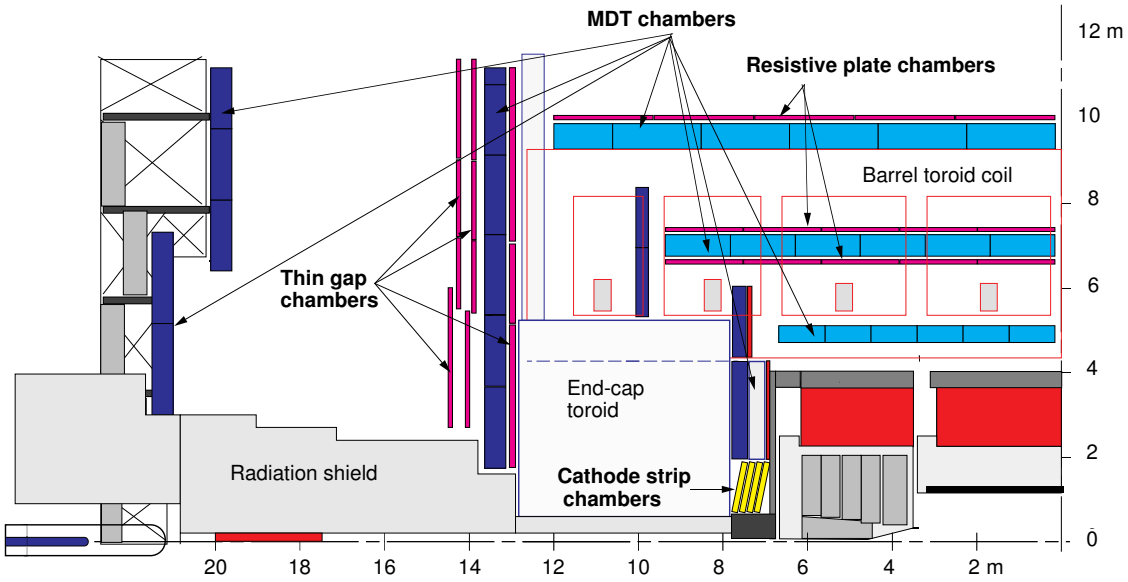

Figure 3.15.: Quarter section of the Muon Spectrometer in the y–z plane [138].

The low particle multiplicities in the Muon Spectrometer enable its use for triggering. Subsection 3.2.7 describes how a trigger decision can be reached within 2.5 μs, thus avoiding an overflow of the buffers which temporarily store all events. The design goal of 10 % accuracy in measurements of the transverse momentum of muons with up to 1 TeV requires a sagitta measurement with an uncertainty below 50 μm. This cannot be achieved with fast chambers, so most stations are equipped with separate chambers for precise (monitored drift tubes (MDTs) in the barrel, MDTs and cathode strip chambers (CSCs) in the endcaps) and for fast measurements (resistive plate chambers (RPCs) in the barrel, thin gap chambers (TGCs) in the endcaps[4], see Figure 3.15). The resolution of the azimuthal coordinate is irrelevant for measuring the sagitta, so only the first barrel station uses precision chambers to measure it, while the ϕ measurement relies on the fast chambers in the other stations[5]. Because of the size of the Muon Spectrometer, the position of the precision (MDT) chambers is constantly monitored to avoid systematic uncertainties from detector deformations. They are used in all barrel and endcap stations, covering the pseudo-rapidity range $|\eta| < 2.7$, except in the innermost endcap, where they are substituted by CSCs in the range $2.0 < |\eta| < 2.7$ because they can manage higher expected muon rates and offer a better time resolution [8].

The MDT chambers deliver an accuracy of 35 μm in the direction perpendicular to the tubes at a maximum drift time of 700 ns, while the CSCs have a resolution of 40 μm at a maximum drift time of 40 ns [8].

By combining the Inner Detector and Muon Spectrometer measurements, the transverse momentum resolution for muons with low transverse momenta can be drastically improved with respect to a stand-alone reconstruction in the Muon Spectrometer (see Figure 3.16) [8]. A di-muon mass resolution of $1.6 - 2.8$ % can be achieved for $Z/\gamma^* \to \mu\mu$ events (see Figure 3.17). The combined and stand-alone measurements rely on Muon Spectrometer hits, so the efficiency for $\eta \approx 0$ is degraded because services (such as cooling, power supply, read-out connections, and detector control connections) for the Inner Detector and for the central

[4]The signal spread of 15–25 ns of the trigger chambers is sufficient for identifying individual bunch crossings, as exploited by the TDAQ system (see Subsection 3.2.7) [8].
[5]The cathode strip chambers offer a resolution of 5 mm in this direction.

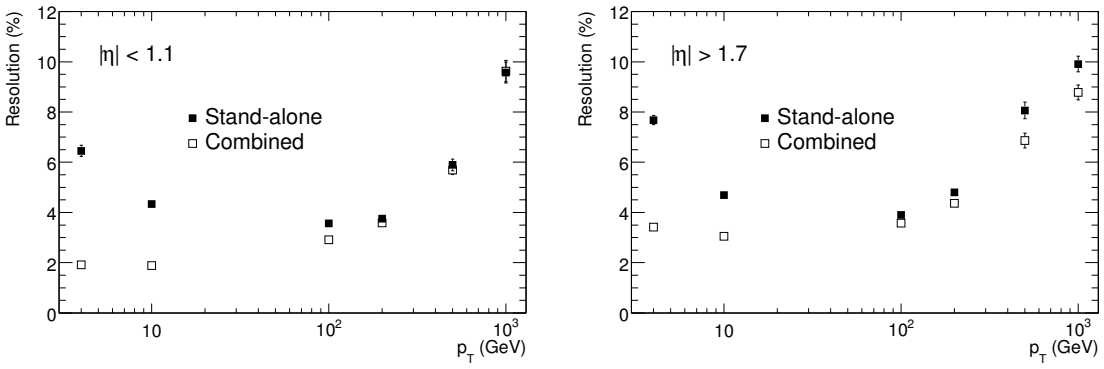

Figure 3.16.: Comparison of the transverse momentum resolutions for muons in the barrel (left) and endcap (right) regions as a function of the transverse momentum, taken from simulation [8]. "Stand-alone" muons are reconstructed only from Muon Spectrometer information, while "combined" muons use Muon Spectrometer and Inner Detector information.

solenoid prevent the placement of muon chambers there [139]. Muon candidates which are reconstructed from their Inner Detector track and minimal ionization in the calorimeters ("calomuons") show a smaller efficiency loss in the central detector region.

3.2.5. Missing Transverse Energy

While the longitudinal component of the momentum of the center–of–mass system is unknown in pp collision events, momenta of final-state particles are balanced in the transverse plane. Given the great detector coverage (up to $|\eta| = 4.9$), the momentum vectors of all detected objects are added[6], and any significant imbalance is attributed to non-interacting particles. Because calorimeter-based measurements dominate the overall uncertainty, the resolutions of the x- and y-components are proportional to the square root of the scalar transverse energy sum ($\sum E_{\mathrm{T}}$):

$$\sigma_{E^{\mathrm{miss}}_{\mathrm{T},x/y}} = \alpha\sqrt{\frac{\sum E_{\mathrm{T}}}{\mathrm{GeV}}} \tag{3.7}$$

with a coefficient $\alpha = 0.7\,\mathrm{GeV}$ in $Z/\gamma^* \to \mu\mu$ events (see Figure 3.18). The resolution is worse for simulated $W \to e\nu$ decays than for $Z/\gamma^* \to \mu\mu$ events by about 1 GeV. In both Z boson and W boson decays, the impact of pileup can be significantly mitigated by using tracking information: Calorimeter clusters which do not belong to any reconstructed objects are neglected, unless a track from the primary interaction points to the respective calorimeter region (drawing an angle of less than $\Delta R < 0.3$). This use of pileup suppression limits the variation of the resolution coefficient to about $\Delta\alpha = 0.02\,\mathrm{GeV}$ between $\mu = 8$ and $\mu = 40$ in $Z/\gamma^* \to \mu\mu$ events and reduces the resolution degradation by about half in $W \to e\nu$ events. Missing transverse energy can thus be exploited even under high-pileup conditions [140]. A good missing transverse energy resolution is crucial for the analysis presented within this thesis.

[6] More details about the computation of missing transverse energy are summarized in Subsection 6.1.6.

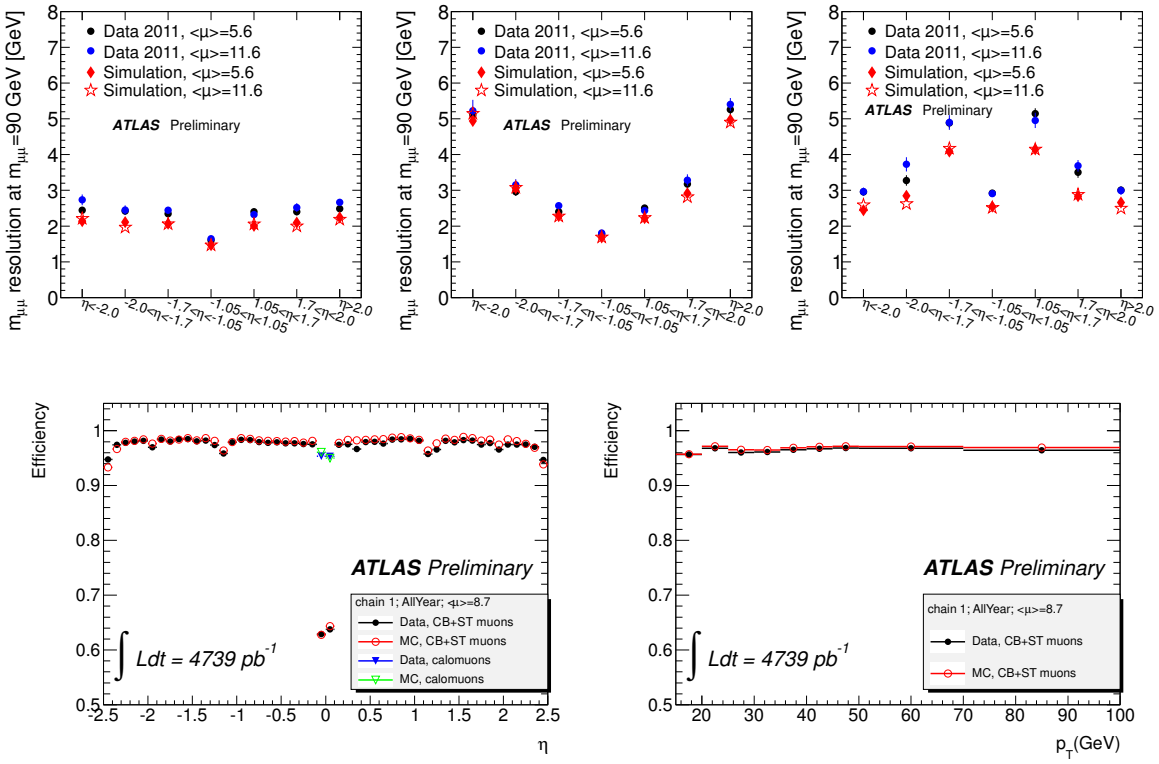

Figure 3.17.: Measured di-muon mass resolution for $Z/\gamma^* \to \mu\mu$ events (top row). The combined measurement (top left) profits from the strengths of the Inner Detector measurement (top center) in the central region and those of the Muon Spectrometer in the forward regions (top right). The bottom row shows the reconstruction efficiency for muons as a function of the pseudo-rapidity (bottom left) and the transverse momentum (bottom right) of the candidate [139]. The bottom left plot also compares the efficiency of reconstructing the same muon either from matching the Inner Detector track to a Muon Spectrometer track segment or by combining the full Muon Spectrometer and Inner Detector track measurements ("CB+ST muons") to the efficiency of reconstructing the muon from Inner Detector and calorimeter information ("calomuons").

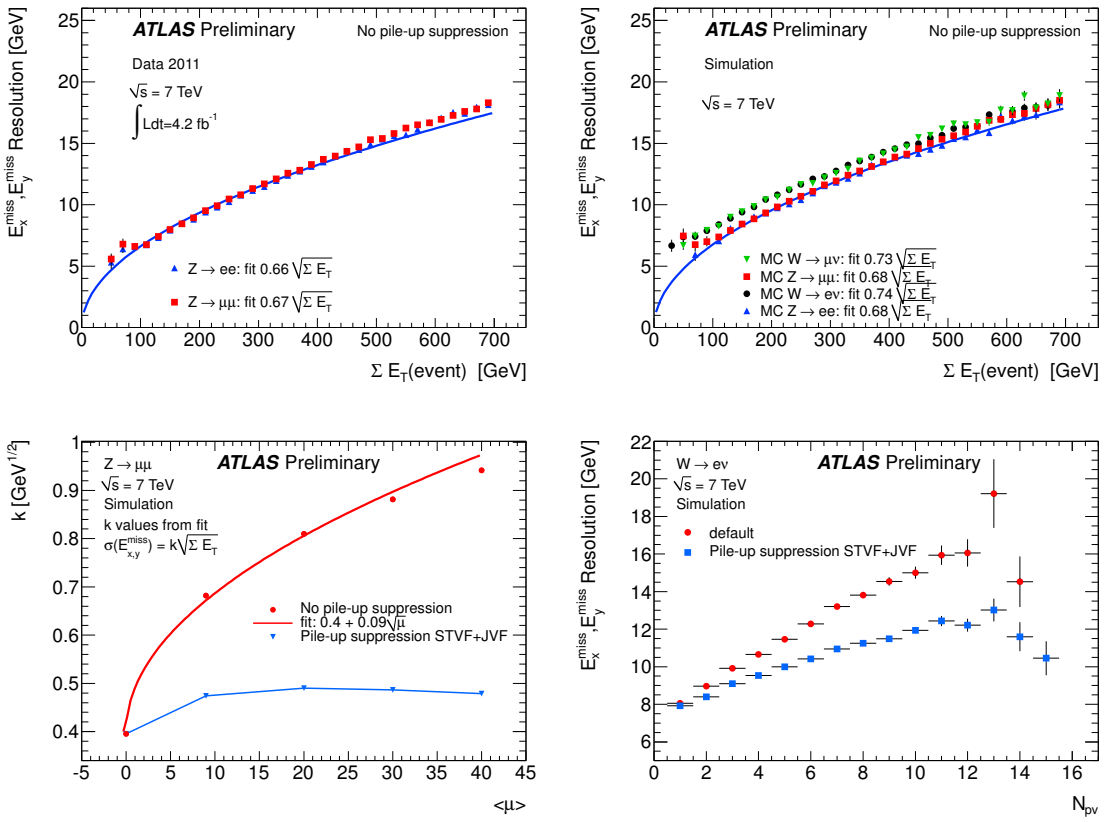

Figure 3.18.: Measured missing transverse energy resolution for events containing Z boson decays to electron and muon pairs as a function of $\sum E_{\mathrm{T}}$ (top left). The performance agrees well with simulation (top right); the simulated resolution is lower for W boson decays. The lower left-hand Figure shows the degradation of the expected missing transverse energy resolution for larger mean numbers of interactions per bunch-crossing (μ) without and with tracker-based pileup suppression for $Z/\gamma^* \rightarrow \mu\mu$ events. The lower right-hand Figure shows the dependence of the missing transverse energy resolution on the number of reconstructed primary vertices in simulated $W \rightarrow e\nu$ events with and without pileup correction [140].

3.2.6. Forward Detectors and Luminosity Measurement

The experimental site of the ATLAS detector is equipped with additional detectors that extend into regions of very high pseudo-rapidities: The beam conditions monitor (BCM) is an integral part of the ATLAS TDAQ system which supplies fast feedback on beam conditions, emitting a beam-abort signal in case of impending beam loss into the detector. It consists of two pairs of diamond sensors on each side of the IP at $z = \pm 184\,\mathrm{cm}, |\eta| = 4.2$, each featuring a very fast signal rise time of 1 ns [8].

The luminosity measurement using Cerenkov integrating detector (LUCID) uses sensors located at $z = \pm 17\,\mathrm{m}, 5.6 < |\eta| < 6.0$ and provides a luminosity measurement by registering collision remnants after bunch crossings, which can also be obtained from the BCM [8]. This method requires a calibration using *van der Meer scans* [141] to determine the transverse beam size at the IP ($\sigma^\star$ in Eq. (3.2)). In a horizontal and a vertical scan, the focus of two beams is offset from the center of the nominal luminous area, so their overlap in the transverse plane as a function of the offset is probed. By continuously monitoring the rate change of bunch crossings without reconstructible vertices, the RMS of the transverse bunch structure can be inferred in each scan direction. Consequently, the absolute value of the luminosity can be calculated with Eq. (3.2) if the number of protons per bunch is known. As an alternative, the integrated luminosity per bunch crossing during the van der Meer scans can be normalized by using the total inelastic *pp* cross-section.

The zero-degree calorimeter (ZDC) is located at $z = \pm 140\,\mathrm{m}$ in the LHC tunnel. Its main use is the detection of neutrons with pseudo-rapidities above $|\eta| = 8.3$ to determine the centrality of heavy ion collisions [8].

The absolute luminosity for ATLAS (ALFA) detectors are placed at $z = \pm 240\,\mathrm{m}$ from the ATLAS IP. Its scintillating-fiber trackers measure elastic scattering to infer the luminosity [8].

The BCM, LUCID, and ALFA detectors as well as the Inner Detector can be used alone or in various logical combinations to register bunch crossings without interactions. Taking the mean number of interactions from Inner Detector data, the luminosity results from the evaluated algorithms agree within 2 %. The logical disjunction of the BCM detectors has been selected as baseline luminosity measurement [125], and a corresponding uncertainty of 3.9 % is assigned to the dataset used within this thesis.

3.2.7. Trigger, Data Acquisition, Computing Model

The ATLAS subdetectors together offer more than 87.7 million readout channels. Per collision event, about 1300 kBytes of detector data are produced, leading to an unmanageable amount of (mostly irrelevant) data [8]. A three-staged trigger system selects events at a sustainable rate of about 400 Hz [142, 143], requiring the persistification and reconstruction of about 500 MBytes/s of raw ATLAS data.

The detector is fully read out into buffers by 932 readout drivers (RODs), with a buffer depth corresponding to 2.5 μs of collisions at a bunch spacing of 25 ns, defining the maximum L1 trigger latency. This is achieved by using specialized hardware relying on lookup tables rather than sophisticated reconstruction software, so the L1 trigger cannot use Inner Detector data, must limit the granularity from the calorimetry, and relies on the faster (but less precise) RPCs and TGCs of the Muon Spectrometer. This step is illustrated in Figure 3.19. The later stages of the trigger selection (level 2 (L2) trigger and Event Filter (EF), together known as high-level trigger (HLT)) can use data from all subsystems.

The L1 trigger processes Muon Spectrometer hits using coincidence-matrix boards, starting from hits in the middle station of the barrel or the outermost trigger station in the endcap region. These boards can be programmed with coincidence matrices for three low transverse

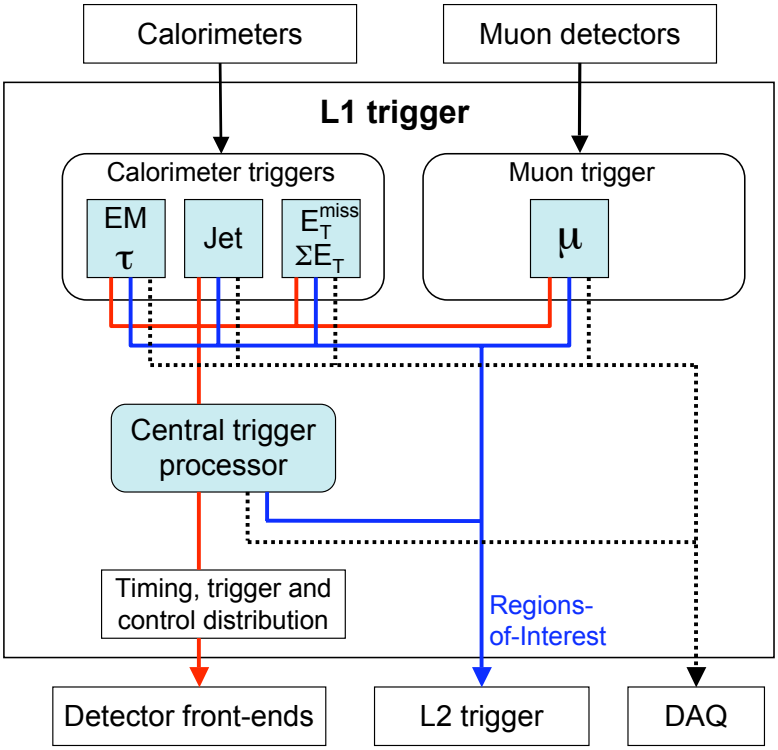

Figure 3.19.: Schematic representation of the L1 trigger [8].

momentum thresholds (up to 10 GeV) and three high transverse momentum thresholds, requiring coinciding hits from two and three stations, respectively. In order to evaluate jet triggers, signatures of electrons or photons, hadronic τ lepton decay triggers, and triggers on large $\sum E_{\mathrm{T}}$ or $E_{\mathrm{T}}^{\mathrm{miss}}$ values within the allowed L1 latency, calorimeter cells are merged to form *trigger towers* with a granularity of no more than 0.1×0.1 in $\eta \times \phi$ (see Figure 3.8). These are then subjected to a sliding-window seed search, and lookup tables are used to match the signature to predefined patterns [8].

Whenever a pattern from the trigger menu stored in the central trigger processor (CTP) is recognized, the CTP emits a L1 accept signal and the full detector response from the region surrounding it (region of interest (RoI)) is passed to the RoI builder (about 2 % of the full event data), unless the rejection of a fixed fraction of passing events has been set (*prescaling*). The full event data are passed to the data acquisition (DAQ) system. The DAQ and RoI builder systems are designed to handle L1 accept rates up to 75–100 kHz [8]. In 2011, the L1 accept rate has been kept below 60 kHz to limit HLT computing demands [142].

The RoIs are subsequently input to the L2 trigger, which applies the appropriate feature extraction algorithms, whose output is used to test L2 hypotheses. The L2 trigger has a mean latency of 40 ms and reduces the event rate to approximately 3.5 kHz (design value, [8]) or 5 kHz (value in 2011, [142]).

The event is then fully reconstructed from the buffered detector data, employing the same algorithms that are used in the offline analysis. According to the L2 hypotheses the event passes, it is then subjected to the feature extraction and hypothesis algorithms of the EF, which require an average processing time of about 4 s [8]. The sequential application of L1 signatures and matching L2 and EF hypotheses is called a *trigger chain*. The choice of trigger conditions in the various chains has to match both the available computing power of the

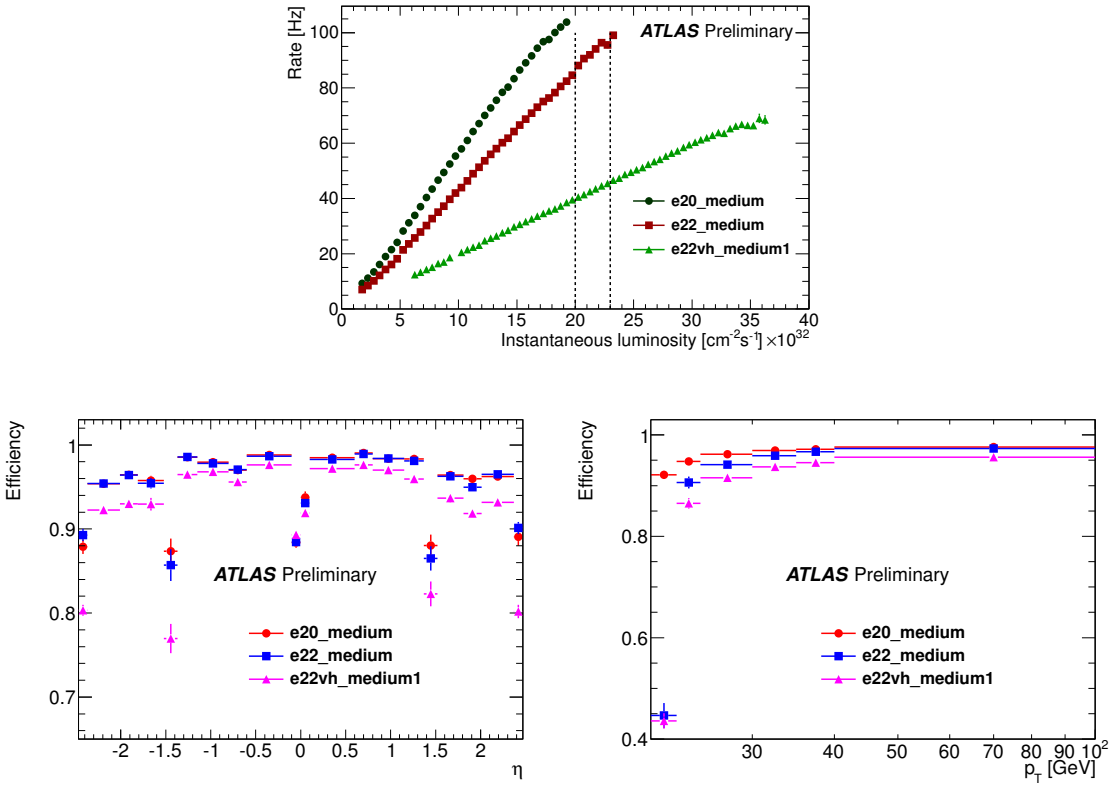

Figure 3.20.: Trigger bandwidth used by the single-electron trigger signatures used as a function of the instantaneous luminosity (top). The dashed lines mark the thresholds until which the corresponding trigger was available without prescaling. The p_{T} thresholds (20 and 22 GeV) are cited, and "vh_medium1" pertains to the tighter track criteria and additional hadronic leakage requirement. The bottom row shows the trigger efficiency in data with respect to offline reconstructed medium electrons (using looser quality requirements than the event selection, see Subsection 6.1.2) as a function of the pseudo-rapidity (left) and of the transverse momentum (right) of the electron [142].

HLT computing farm and the available trigger bandwidth of, on average, 400 Hz [142, 143]. Furthermore, the menu must be balanced across the various chains to enable as broad a physics program as possible.

The performance of the single-electron trigger used within this thesis is summarized in Figure 3.20. The rise in instantaneous luminosity throughout 2011 data-taking required the tightening of the p_{T} threshold and identification criteria to limit the usage of trigger bandwidth: A p_{T} threshold of 20 GeV for single electrons was used for $\mathcal{L} < 2 \cdot 10^{33}\,\mathrm{cm}^{-2}\mathrm{s}^{-1}$, and a threshold of 22 GeV, for higher luminosities. For $\mathcal{L} > 2.3 \cdot 10^{33}\,\mathrm{cm}^{-2}\mathrm{s}^{-1}$, track quality criteria were tightened and a threshold to the amount of energy leaking into the hadronic calorimeter was set. A plateau value of $95 - 97\,\%$ efficiency is achieved for electrons with a transverse momentum of more than 40 GeV. The central detector region, where services from the Inner Detector and the central solenoid are led out of the detector, as well as the regions at $|\eta| \approx 1.5$, which include the crack between the barrel and endcaps of the electromagnetic calorimeter, exhibit a reduced trigger efficiency. Electrons from the crack regions are removed in the analysis (see Subsection 6.1.2) because they carry larger systematic uncertainties [142].

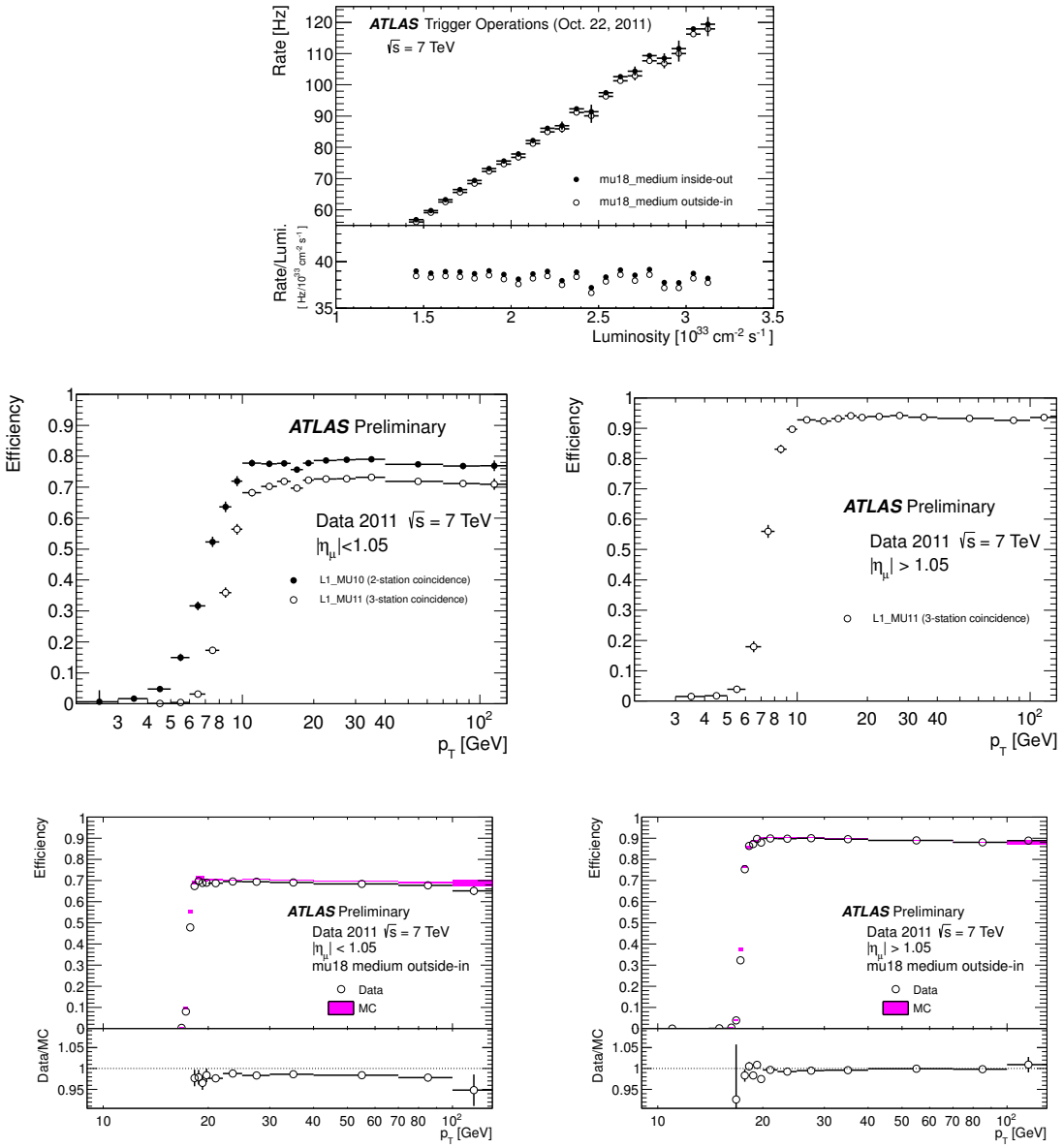

Figure 3.21.: Trigger bandwidth used by the single-muon trigger signatures used as a function of the instantaneous luminosity (top). The middle (bottom) row shows the L1 (EF) trigger efficiency with respect to offline reconstructed muons as a function of the transverse momentum of the muon, distinguishing the central (left) and forward (right) regions [143].

The performance of the single-muon trigger is summarized in Figure 3.21. Besides the introduction of medium quality cuts in muon identification in period `I`, the same trigger threshold of 18 GeV in the HLT could be used, limiting the acceptance rate to 120 Hz. The L1 trigger requirement was tightened in the barrel region to a three-station coincidence at a threshold of 11 GeV in period `I`, leading to an efficiency loss of about 6 % in the barrel for muons with a transverse momentum of more than 20 GeV. The L1 muon trigger offers an efficiency of about 72 % (93 %) for the barrel (endcap) three-station coincidence at a p_{T} threshold of 11 GeV. The value in the barrel region is reduced by the Muon Spectrometer gap at $z = 0$ and the support structures. For both regions, the rising flank of the efficiency curve ranges from $6 - 10$ GeV, while the HLT efficiency rises within a few GeV, justifying the offset of 7 GeV in p_{T} thresholds between the L1 trigger and the HLT [142]. The HLT reconstructs muons both starting from Muon Spectrometer tracks (outside-in) and from Inner Detector tracks (inside-out), at similar efficiencies, to optimize the total reconstruction efficiency.

The electron and muon triggers are also used to form combined signatures, such as the electron–muon trigger used within this thesis (see Subsection 6.1.3 for the contributions of the individual triggers to the overall signal acceptance).

3.2.8. The World-Wide Large Hadron Collider Computing Grid

ATLAS and the other LHC experiments require the persistification of huge amounts of data (500 MBytes/s by ATLAS alone), which must constantly be available for calibration and analysis. In order to avoid reliance of every data-related activity on a single computing center, a hierarchical system of computing centers distributed around the world, the World-Wide Large Hadron Collider Computing Grid (WLCG) [144], has been set up. The central system at CERN (*Tier-0* facility) receives the raw data from all events that the experiments select for analysis. A copy is created in persistent storage, and event reconstruction is performed with a given calibration. Consequently, the reconstructed events are exported to eleven computing centers serving ATLAS (*Tier-1* sites), which each have multiple adjoined computing centers, collectively referred to as *clouds*. The Tier-0 center as well as most Tier-1 sites are exempt from executing physics analyses, which are executed at lower-Tier Grid sites. The Tier-1 and lower-Tier Grid sites are also used for storing a copy of the raw data, reconstructing it again when new calibration data is available, and for the generation and simulation of Monte Carlo (MC) data.

4 Characterization of Physics Processes and Event Simulation

In the generation of simulated events, a combination of analytical and phenomenological methods is used to model the proton collisions and subsequent interactions, which produce the final-state particles. The final-state particles interact with the matter around them, and the detector response to energy deposits in active detector regions is simulated. The various classes of signal and background processes impose different challenges to the generators, so different programs are used for the individual processes.

Section 4.1 introduces the various aspects of proton interactions that are simulated and describes the jet definition used within this thesis. Section 4.2 summarizes how these elements are combined to model complete Large Hadron Collider (LHC) events and how the detector response is simulated.

4.1. Elements of Proton Collision Events

The description of proton collisions requires the simulation of three main stages: The parton distribution functions (PDFs) model the probabilities of finding a certain parton flavor at a certain momentum fraction of the incoming proton ($x_{1,2}$). The hard interaction is governed by the interaction Lagrangian at an energy scale (Q). The transition matrix element (ME) can be calculated perturbatively up to an arbitrary order of the coupling strengths ($\alpha_{\text{ew}}, \alpha_s$), achieving ever smaller associated uncertainties at each order (see below).

The transition to the lower scale of the outgoing particles is modeled in two steps: A parton shower (PS) models the emission of quantum chromodynamics (QCD) radiation, which iteratively reduces the energy of the partons while α_s grows. Eventually, an energy scale is reached where a phenomenological model can be applied to simulate the formation of hadrons (called *hadronization process*). This process results in jets of color-neutral particles (*confinement*, see Subsections 4.1.2 and 4.1.3). According to the *factorization theorem*, the overall cross-section (σ) can be factorized into the hard interaction, QCD-induced showers (connecting the hard process with both the initial-state partons and the (final-state) hadronization process), and the PDFs:

$$\sigma = \sum_{\substack{\text{parton pair} \\ ij}} \int_0^1 \int_0^1 dx_1 dx_2 \sigma_{ij}^{\text{ME,PS}}(x_1, x_2, \mu_{\text{F}}^2, \mu_{\text{R}}^2) f_i(x_1, \mu_{\text{F}}^2) f_j(x_2, \mu_{\text{F}}^2). \tag{4.1}$$

This separates the two domains of scales where perturbation theory holds ($Q > \mu_F$) and where non-perturbative processes dominate ($Q < \mu_F$). The factor $\sigma_{ij}^{\text{ME,PS}}$ depends on the sampled parton momenta x_i and describes the hard interaction and QCD-induced showers, based on perturbation theory. The ME calculation also depends on the scale choice in the renormalization (μ_R), which is performed to avoid large logarithmic terms in fixed-order calculations. The PDFs (f_i, f_j) provide a phenomenological description of the non-perturbative processes in the protons. The scale dependences are unphysical, and the cross-section is evaluated for

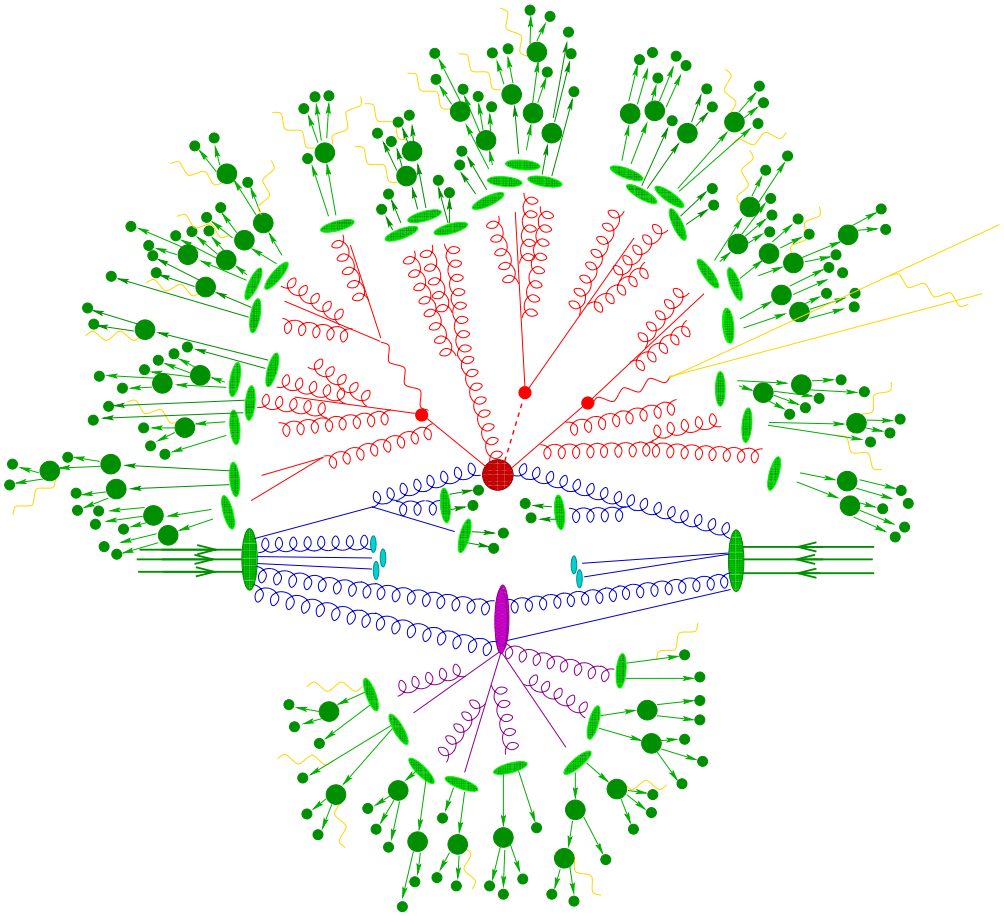

Figure 4.1.: Visualization of a simulated proton collision involving the t-quark-associated production of the lightest neutral Higgs boson [145]. The ISR before the main interaction (dark red dot) is shown. While the Higgs boson (dotted line) decays into two quarks, the t-quarks undergo FSR (red lines). The left t-quark decays hadronically and the right one, leptonically. The light red dots mark the decay vertices. A second interaction from other partons is shown in purple. The stage of hadronization is shown in light green, the decay of the hadrons in dark green. Yellow lines indicate final-state leptons and photons.

different values of μ_R and μ_F to estimate the systematic uncertainty (see Subsection 8.1.1) associated to the scale choices.

To illustrate these stages, a proton collision event is shown in Figure 4.1. Partons from both initial-state protons, which are both symbolized by three incoming valence quarks, produce initial-state radiation (ISR), and some of the resulting quarks and gluons interact. The main interaction, in this illustration t-quark-associated production of the lightest neutral Higgs boson, is evaluated at the electroweak scale. The outgoing partons (including the Higgs boson decay products) emit final-state radiation (FSR) and then hadronize. The unstable particles finally decay in one or more steps to form the final-state particles.

Particles from additional parton interactions and the proton remnants of a pp collision are collectively referred to as underlying event (UE).

4.1.1. Modeling of Parton Distribution Functions

The PDFs cannot be directly derived from theory, but they can be measured, e.g., in electron–proton collisions. Even though such collisions involve much lower center–of–mass energy values, the *Dokshitzer–Gribov–Lipatov–Altarelli–Parisi (DGLAP) evolution equations* can be used to infer the scale dependence of the PDFs and hence a prediction at LHC energies [146]:

$$\frac{df_i(x_i,Q^2)}{d\log Q^2} = \frac{\alpha_s}{2\pi}\int_{x_i}^{1}\frac{dy}{y}\left(f_i(y,Q^2)P_{qq}\left(\frac{x_i}{y}\right)+g(y,Q^2)P_{qg}\left(\frac{x_i}{y}\right)\right) \tag{4.2}$$

$$\frac{dg(x_i,Q^2)}{d\log Q^2} = \frac{\alpha_s}{2\pi}\int_{x_i}^{1}\frac{dy}{y}\left(f_i(y,Q^2)P_{gq}\left(\frac{x_i}{y}\right)+g(y,Q^2)P_{gg}\left(\frac{x_i}{y}\right)\right). \tag{4.3}$$

The parton emission probability (P_{XY}) gives the probability for a parton Y to split, producing a parton X with a momentum fraction z:

$$P_{qq}(z) = \frac{4}{3}\left(\frac{1+z^2}{1-z}\right) \tag{4.4}$$

$$P_{qg}(z) = \frac{1}{2}\left(z^2+(1-z)^2\right) \tag{4.5}$$

$$P_{gq}(z) = \frac{4}{3}\left(\frac{1+(1-z)^2}{z}\right) \tag{4.6}$$

$$P_{gg}(z) = 6\left(\frac{1-z}{z}+\frac{z}{1-z}+z(1-z)\right). \tag{4.7}$$

The singularities in Eqs. (4.4), (4.6), and (4.7) are connected to the emission of soft gluons and lead to infrared divergences that cancel with virtual corrections.

Eqs. (4.2) and (4.3) relate the scale dependence of the PDFs for quarks (f_i) and gluons (g) to the circumstance that the respective particle is a daughter particle of a harder (momentum share $y > x$) quark (f_i terms) or gluon (g terms). Therefore, each term carries the appropriate splitting probability ((4.4) through (4.7)) as a factor.

PDFs are supplied as sets that contain the central values and the error eigenvectors associated to the 68 % CL intervals. For the analysis presented within this thesis, the MSTW2008 [147] PDF set has been used for the computation of next–to–next–to–leading order (NNLO) cross-sections. The set contains PDFs at leading order (LO), next–to–leading order (NLO), and NNLO, which are selected to match the order in α_s that is used for the ME calculation. The Pythia [133] and AcerMC [148] samples use the MRST2007 LO**[1] PDF set [149], CT10 [150] is used for MC@NLO [151], and CTEQ6L1 [152] for Alpgen [153], Herwig [154], and Sherpa [145].

4.1.2. Modeling of QCD Radiation and Bremsstrahlung

In the collision of two hadrons, QCD radiation occurs at two stages: before the hard interaction (ISR) and afterwards (FSR). In either case, a PS arises from splitting vertices and provides a transition between different energy scales: The total energy is shared among more and more particles. Given the energy scale of the main interaction, the energy scales after ISR

[1] The ** notation refers to a modification introduced to better reproduce higher-order results with LO generators, while maintaining a similar value of α_s as in LO PDFs.

and before FSR are fixed. FSR is therefore simulated as sequential splittings, starting from the scale of the hard interaction. ISR modeling must perform the same evolution backwards from the scale of the hard interaction to the momentum of the incident partons.

QED-bremsstrahlung is simulated with PHOTOS [155], except for Sherpa, which uses the built-in PHOTONS++ program.

4.1.3. Jet Algorithms

The process of separating quarks or gluons is accompanied by a sharp increase in potential energy, which culminates in the creation of additional quark–anti-quark pairs. During hadronization, these[2] recombine with the original quarks to form color-neutral objects, such as mesons (consisting a quark–anti-quark pair) or baryons (consisting of three quarks (or three anti-quarks) of different color). Owing to the momentum of the original parton and high probabilities for the emission of soft and collinear gluons, the final-state particles form a more or less collimated jet of particles. However, for this analysis, the momenta of the outgoing partons (of the hard interaction) are of interest—rather than those of the final-state hadrons. This is reflected in the reconstruction of jets, which are ideally reconstructed as a single object per outgoing parton.

In order to minimize the adverse impact of detector noise and pileup, information from neighboring calorimeter cells is merged into topological clusters, and jets are then reconstructed from the clusters. Topological clusters require the energy measured by a seed cell to exceed a threshold that is significantly higher than the noise level (by a factor of $4-6$ [156]). Due to the large multiplicities of soft particles from minimum-bias interactions in LHC collisions, noise and pileup contributions are considered in the energy calibration of the calorimeter cells.

The reconstruction of jets from calorimeter clusters can be performed in different ways, which offer different levels of robustness against pileup influences. As laid out in the *Snowmass accord* [157], an acceptable jet definition should be simple to relate to theoretical and experimental quantities and result in finite cross-sections at any order of perturbation theory. The latter feature is known as infrared safety and implies that infinite terms from soft and collinear emissions cancel with virtual corrections. The cross-section prediction should depend only weakly on how partons recombine during the hadronization process.

A simple ansatz for the reconstruction of jets is given by *cone algorithms*, which search for local maxima in the calorimeter activity within a cone of fixed opening angle ΔR. However, such algorithms lack infrared safety and perform poorly in events with overlapping jets because the opening angle between the jet axis and a calorimeter cluster does not take the properties of QCD radiation into account.

Sequential algorithms therefore use opening angles and cluster energies to determine a quantity which takes QCD properties into account, such as the *Durham distance measure* (y_{ij}) [158] in electron–positron collisions:

$$y_{ij} = 2\frac{\min(E_i^2, E_j^2)}{s}(1-\cos\theta_{ij}). \tag{4.8}$$

i and j name two clusters with energies E_i and E_j, and $\sqrt{s}$ is the center–of–mass energy.

For hadron collisions, the geometric opening angle θ_{ij} is replaced by ΔR_{ij}[3], $\sqrt{s}$ is replaced

[2] and partons from final-state radiation (FSR)

[3] using the same definition as in Eq. (3.5)

by the distance parameter R, and only the transverse component of the energies is used [159]:

$$d_{ij} = \frac{\min(E_{\mathrm{t},i}^{2p}, E_{\mathrm{t},j}^{2p})}{R^2}(\Delta R_{ij})^2. \tag{4.9}$$

The use of ΔR_{ij} maintains approximate Lorentz invariance of the distance measure. As shown in the following, the exponent $2p$ determines the order in which clusters are merged and R is the maximal opening angle between the jet axis and any associated cluster.

For each cluster and combination of two clusters, the distance measure is computed, using

$$d_i = E_{\mathrm{t},i}^{2p} \tag{4.10}$$

for a single cluster. The smallest of the d_i and d_{ij} results is considered: If one of the two–cluster combinations d_{ij} yields the minimum, they are merged by adding their corresponding four-vectors. Otherwise, the respective cluster is accepted as a jet candidate and both it and the associated d_{ij} values are removed from the list of clusters to be merged. From the structure of Eqs. (4.9) and (4.10), it is clear that one of the (single-cluster) values d_i or d_j is always smaller than the corresponding d_{ij} value if $\Delta R_{ij} > R$.

The case $p = 1$ is known as the k_t algorithm, $p = 0$ is called Cambridge–Aachen algorithm, and $p = -1$ corresponds to anti-k_t jets, which are used within this thesis.

The resulting jet candidates are compared for the three cases in Figure 4.2, using a distance parameter value of $R = 1$, which is larger than the optimized[4] value of 0.4 used within this thesis to illustrate how clusters are split among overlapping jets. The main difference lies in the way energy deposits located in between two jet candidates are attributed: While the Cambridge–Aachen algorithm splits such areas evenly, the k_t algorithm attributes clusters to the softer seed, and the anti-k_t algorithms, to the harder seed. For all three types of jet algorithms, the number of jets above a given threshold is infrared-safe. An important advantage of the anti-k_t algorithms lies in the fact that jets have a circular shape in the η–ϕ plane even in the presence of a soft seed, given that the hard seeds are not too close together. The distance measure R is then directly proportional to the size of the jet area, which is beneficial to the calibration against noise and soft energy deposits from pileup.

4.1.4. Main Interaction

The main interaction occurs at a large energy scale $\mathcal{O}(100\,\mathrm{GeV})$, so $\alpha_s \ll 1$ enables a precise prediction of the cross-section by considering a finite perturbative expansion up to NLO or NNLO in α_s.

Each cross-section contribution can be computed by applying the appropriate Feynman rules. Soft and collinear divergences cancel when taking virtual corrections into account.

Soft and collinear emissions are modeled by PSs, which are simulated with Herwig or Pythia [133][5]. Because higher-order corrections in the ME calculation and emissions within the PS both describe the same process, the combined use of the ME and PS methods results in double counting. A distance measure, such as d_{ij} in the sequential algorithms mentioned above, is therefore used to separate emissions into the "hard" domain (described by the ME) or the "soft" domain (treated by the PS).

One such scheme is *CKKW matching*[6] [162], which is used within Sherpa. This scheme correctly treats the no–emission probability within the parton shower already within the event generation step by reweighting events with the analytical Sudakov form factor [163].

[4] The resolution degradation from energy deposits outside the jet area and from energy deposits of the underlying event (UE) are minimal for $R \approx 0.4$ at a center–of–mass energy of 7 TeV [161].

[5] Sherpa does not use an external shower Monte Carlo (MC) program—see below.

[6] named for the original authors

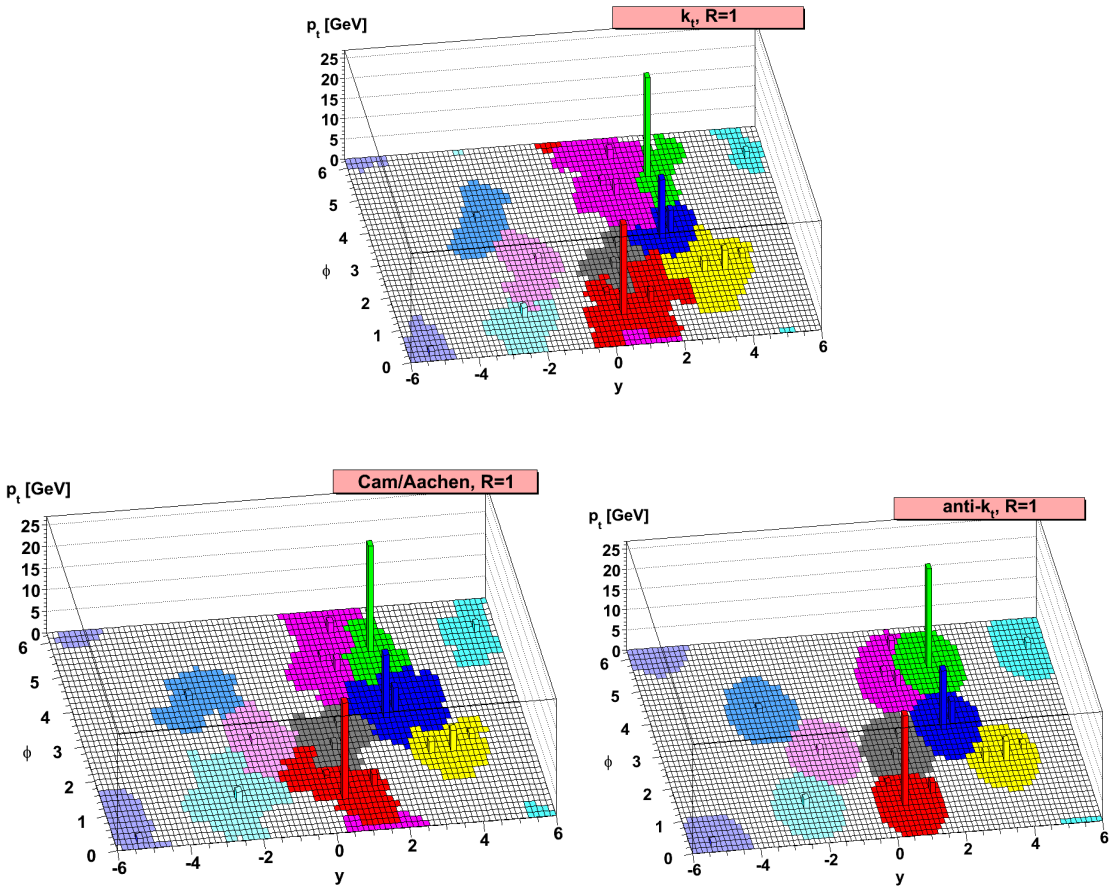

Figure 4.2.: Outcome of three sequential algorithms applied to a generic simulated event (using Herwig) overlaid with randomly distributed soft deposits [160]. The energy deposits are shown in the η–ϕ plane, and colors indicate to which jet candidate clusters are associated. The top Figure shows the result of the k_t algorithm, the bottom Figures show the results of the Cambridge–Aachen algorithm (left) and of the anti-k_t algorithm (right).

If different programs are used for calculating the ME and for simulating the PS, the Sudakov suppression has to be applied after the PS simulation and before simulating the hadronization step, as in the *MLM matching* scheme[7] [164]. For the given use case, it carries the advantage of requiring neither a veto on jets that fall into the domain of the ME corrections nor knowledge of the analytical form of the Sudakov factor used by the PS simulation. In contrast to CKKW matching, the retention or rejection of events is decided only after the simulation of the parton shower, while MC generators using CKKW matching do not need to discard events after the generation step.

The simulation of the hard interaction and the PSs require substantially less computing power per event than the simulation of subsequent interactions with the detector. In the presence of cuts at the reconstruction or analysis steps and taking the limit solid angle coverage of tracking and calorimetry into account, many generated events do not require the detector simulation step because their kinematic properties render them ineligible. A

[7] named for the original author

generator event filter (GEF) can be used to reject such events. By taking the filter efficiency into account, the cross-section of the resulting dataset can be computed from the inclusive cross-section value.

The decay of τ leptons produced in the hard process is simulated in TAUOLA [165] for the gluon fusion and $Z/\gamma^* \to \tau\tau$ processes, to take spin correlations into account. τ lepton decays in b-associated Higgs boson production (including spin correlations) are simulated by Sherpa itself.

The production cross-sections of the signal processes are discussed in Subsection 2.2.3. The production cross-sections of the background processes whose event yields are taken from simulation are listed in Table 8.1.

b-Associated Production

b-associated Higgs boson production ($bb\phi$) is the most promising signal process for the given analysis. As shown later in Figure 6.3, the transverse momentum spectra of the final-state leptons contain a large fraction which is either too soft or outside the detector coverage. In order to reduce the statistical uncertainty for the selected events, the `2LepEF` GEF is applied after the event generation step, requiring the presence of two light leptons that each fulfill a pseudo-rapidity cut of $|\eta| < 3$ and have a minimum transverse momentum value of 5(10) GeV for muons (electrons).

The process is modeled at LO by Sherpa[8], and the PDFs from MSTW2008 at LO have been used. Only the CP-odd boson is simulated[9], and the $\tan\beta$ value is not varied for the different scenarios examined within this thesis because the differences in the shapes of distributions are negligible. Therefore, one to three A^0 templates for different m_{A^0} values are combined and the event yields are appropriately scaled to reproduce the Minimal Supersymmetric Standard Model (MSSM) scenario to be probed. As mentioned in Subsection 2.2.2, the one-loop and most important two-loop corrections are taken into account for the prediction of the production cross-section.

The Santander matching scheme [166] is used for combining two ways of treating the incident b-quarks in the calculation of the production cross-section: The five-flavor scheme (5FS) takes the incident b-quarks from a b-quark PDF, while the four-flavor scheme (4FS) prediction includes the b-quark production in the signal process. For larger Higgs boson masses, the 4FS suffers from large logarithms. The 5FS (σ^{5FS}) prediction at NNLO from bbH@NNLO [79] and the 4FS prediction (σ^{4FS}) from Ref. [80] at NLO are therefore weighted by a factor w according to the Higgs boson mass (m_H):

$$\sigma^{\text{Santander}} = \frac{\sigma^{\text{4FS}} + w\sigma^{\text{5FS}}}{1+w} \qquad w = \ln\frac{m_\phi}{m_b} - 2. \tag{4.11}$$

Gluon Fusion

The Higgs boson production from gluon fusion ($gg \to \phi$) exhibits a softer Higgs boson transverse momentum spectrum than b-associated Higgs boson production because there are no recoiling objects at leading order. POWHEG [167, 168] is used for the ME calculation at NLO, and Pythia, for the PS. POWHEG uses modified shower generators that always consider the hardest emission first (p_{T} ordering). The matching scheme therefore does not

[8] with up to three additional partons

[9] The b-quarks are treated as massless quarks for the central cross-section value, so the couplings are identical for scalar and pseudo-scalar Higgs bosons. The difference between the results for massless and massive b-quarks is small, as shown in Subsection 8.1.2.

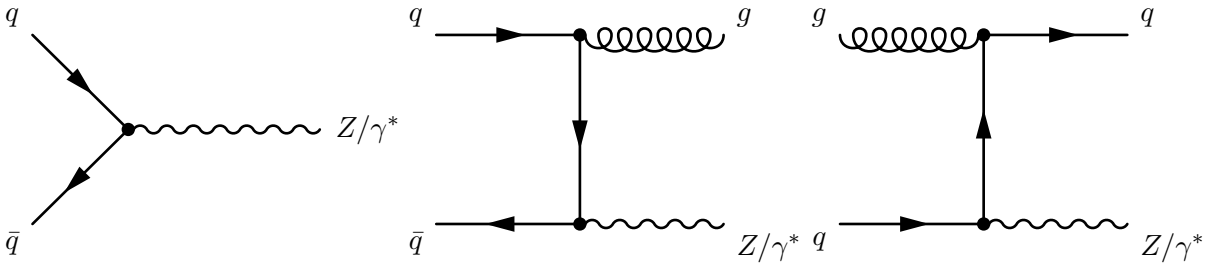

Figure 4.3.: Dominant tree-level processes for Z/γ^* boson production at the LHC.

need to consider other emissions, and negative event weights are avoided. In contrast to the CKKW matching method, color connections in soft emissions are respected [167].

The Higgs boson transverse momentum spectrum is subject to sizable higher-order corrections. A reweighting technique is therefore used to reproduce the spectrum to NNLO+next–to–next–to–leading logarithm (NNLL) accuracy, obtained from HqT [169]. Squark loops are neglected. The NNLO cross-section is approximated by scaling the Standard Model (SM) cross-section contributions from the t-quark and the b-quark loops and their interference term by the appropriate coupling modifications for the MSSM at NLO from HIGLU [77]. For the t-quark loop contribution, the NNLO corrections from ggH@NNLO [78] have also been taken into account [29].

In preparation of an update to Ref. [29], the contributions from third-generation squark loops, NNLO contributions involving t-quarks, and the supersymmetric correction to the light-quark contribution have been calculated for the $m_{h^0}^{\text{max}}$ scenario. The evaluation was performed [170] with the POWHEG-Box framework [171], based on POWHEG, and SusHi [172] at a center–of–mass energy of 8 TeV. For the lightest CP-even Higgs boson, the contributions from squarks and electroweak corrections have an effect of at most 2 % on the production cross-section for $110\,\text{GeV} < m_{A^0} < 1000\,\text{GeV}$, while the impact on the heavier CP-even Higgs boson grows to about 5 % for small values of $\tan\beta \approx 5$. The variations are for a center–of–mass energy of 7 TeV are expected to be similar, so they are covered by the cross-section uncertainties assumed in Subsection 8.1.1.

Z/γ^*+Jets

The production of Z/γ^* bosons with or without additional jets is the most important background to the search channel investigated within this thesis. The dominant production modes are shown in Figure 4.3. The $Z/\gamma^* \to ee$ and $Z/\gamma^* \to \mu\mu$ processes can be efficiently rejected by selecting only events with exactly one electron and one muon that pass the identification criteria or by requiring a large amount of missing transverse energy. As described later, the $Z/\gamma^* \to \tau\tau$ background represents an irreducible background, which can only be discriminated against by reconstructing the invariant di-τ mass ($m_{\tau\tau}$) and by exploiting the different flavor composition of the associated jets in b-associated Higgs boson production.

While the natural width of the Z boson is $(2.4952 \pm 0.0023)\,\text{GeV}$ [21] and the lepton p_{T} resolutions are $1.5 - 3\,\%$, the presence of neutrinos from τ lepton decays increases the reconstructed width of the Z boson resonance, so the corresponding root mean square (RMS) is about 25 GeV (see Section 5.3). Because the $m_{\tau\tau}$ mass resolution degrades with increasing boson masses, the separation of neutral Higgs bosons and Z bosons improves slowly with the hypothetical Higgs boson mass.

Both a Pythia dataset and a dataset with ME calculation from Alpgen and PS simulation from Herwig (shower) in conjunction with Jimmy [173] (hadronization and UE)[10] have

[10] henceforth referred to as Herwig+Jimmy

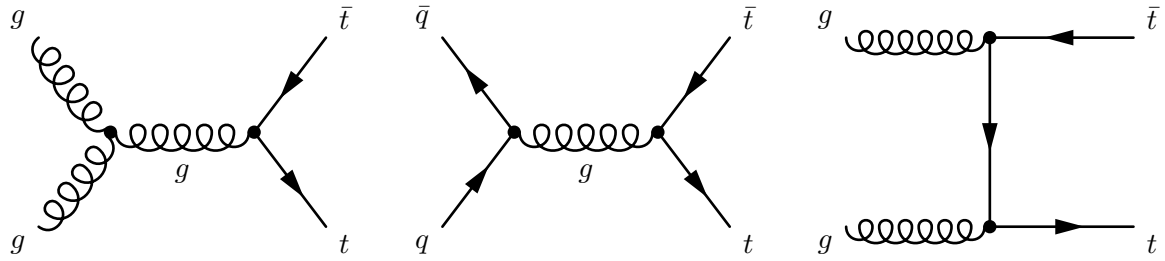

Figure 4.4.: Dominant tree-level production modes for t-quark pairs at the LHC.

been used. The overlap between additional emissions in the ME and the PS is removed, using the MLM matching scheme. Previous studies have concluded that both generators are equally reliable in predicting the p_{T} spectrum of the Z boson, but that Alpgen can predict the properties of additional (hard) jets more accurately. The ME is calculated at NLO in Alpgen, while the ME calculation at LO in Pythia is reweighted to NLO.

t-Quark Pair Production

t-Quark pairs are mainly produced in the processes shown at tree level in Figure 4.4. In the search for b-associated Higgs boson production, $t\bar{t}$ production constitutes an important background when selecting events with a b-jet. t-quarks have only been observed to decay in the $t \to qW^+$ modes, whose dominant contribution with $(91 \pm 4)\,\%$ is the process $t \to bW^+$ [21].

The b-quarks in the final state can be used for for discrimination against other processes. A large mean jet multiplicity (also the decays of the W bosons) and hard spectra of the jets and leptons dominate the detector signature. As the final-state leptons do not originate from a di-τ resonance, the $m_{\tau\tau}$ spectrum of $t\bar{t}$ events is flat.

In the analysis presented within this thesis, $t\bar{t}$ events are generated with two NLO generators: MC@NLO in conjunction with Herwig+Jimmy for the simulation of the ME and PS, UE, and hadronization, respectively, while POWHEG with Herwig+Jimmy is used to assess the theoretical uncertainty related to the description of kinematic distributions in the generation step (see Subsection 8.2.3). A GEF requiring at least one of the W bosons to decay via $W^- \to l\bar{\nu}_l$ is applied in order to enhance the fraction of events with isolated leptons, which are required by the analysis (see Section 6.1).

MC@NLO uses a modified subtraction scheme [151], which performs a resummation of large logarithmic terms in the generation which is consistent with the resummation used in the PS generator. This procedure results in events with positive and negative weights, so a larger dataset is required to achieve the same level of statistical uncertainty when compared to event generation with equal weights.

Single t-Quark Production

The production of single t-quarks contributes significantly to samples requiring the presence of an identified b-jet. Like in $t\bar{t}$ events, the reconstructed objects in single t-quark production exhibit large momenta and lead to a rather flat shape of the contribution to the $m_{\tau\tau}$ distribution.

Three tree-level processes contribute to the production of single t-quarks (see Figure 4.5): the exchange of a W boson in the s- (3.9 pb at NLO [151]) and t-channels (58.7 pb at NLO [151]) and the production in association with a W boson (Wt, 13.1 pb at NLO [151]). The latter constitutes the largest contribution to the selected single t-quark production events in this thesis (96.7 % in a sample without b-jets and 99.5 % for exactly one tagged b-jet) for

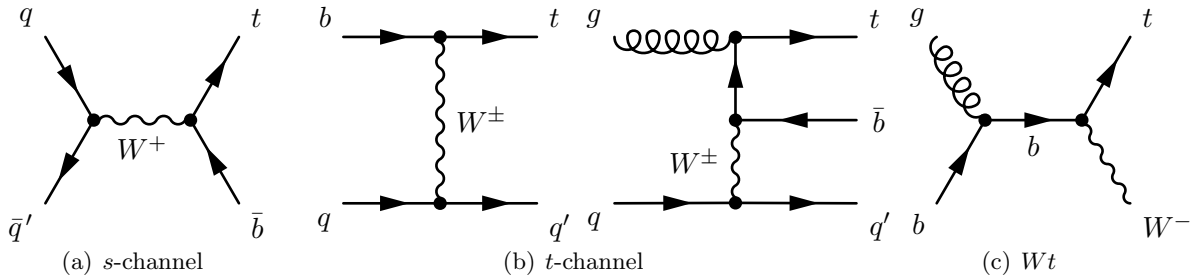

(a) s-channel (b) t-channel (c) Wt

Figure 4.5.: Dominant tree-level Feynman diagrams for single t-quark production.

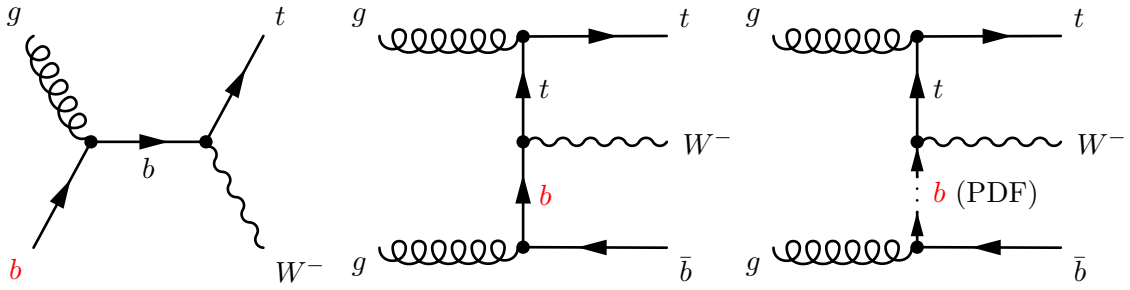

Figure 4.6.: Contributing Feynman diagrams of Wt processes, differing in the role of the incident b-quark (b). While heavy flavor production is unambiguous at LO (left), the matching scheme [174] used in AcerMC is needed to avoid the double-counting of flavor production processes from gluon splitting in the NLO diagram (middle) and the b-quark PDF (right).

two reasons: This process contains one strong vertex in addition to the Wtb vertex, rather than another electroweak vertex. Furthermore, the abundance of energetic gluons in reactions with soft b-quarks enables the production of t-quarks despite their large mass.

When using a NLO ME calculation, the b-quark in the initial states of the t-channel and Wt processes can be viewed as either an initial-state parton or as stemming from an energetic gluon splitting into a b-quark pair (see Figure 4.6). The latter case is indistinct from the emission of ISR, so a matching scheme [174] is derived from the DGLAP evolution equations (see Subsection 4.1.1) to remove the overlap, again leading to a fraction of events which are assigned negative weights. This scheme is implemented in AcerMC, which is used for the generation of all single t-quark production processes.

Di-Boson Production

Because of their decay modes involving leptons and also heavy quarks, gauge boson pairs also contribute to the di-lepton samples analyzed within this thesis. The corresponding $m_{\tau\tau}$ distribution is rather flat in shape for lack of particles decaying to a pair of vector bosons.

While all gauge boson combinations with a total charge of zero or one elementary charge can be produced in quark pair annihilation (see leading-order contributions in Figure 4.7), W boson pairs and Z boson pairs can also be produced from gluon pairs (see Figure 4.8). For the case of W boson pairs, this contribution makes up 2.9 % of the total cross-section [175], while the loop-induced production of Z boson pairs is negligible. For the analysis of the sample without b-tagged jets, quark-induced processes are simulated in MC@NLO, while `GG2WW` [176] has been used for gluon-induced production. The same UE and hadronization configuration as in the production of $t\bar{t}$ events with MC@NLO is used for both programs. The PDF CT10 is used for the MC@NLO datasets, CTEQ6m for the `GG2WW` datasets, and MRST2007 LO**

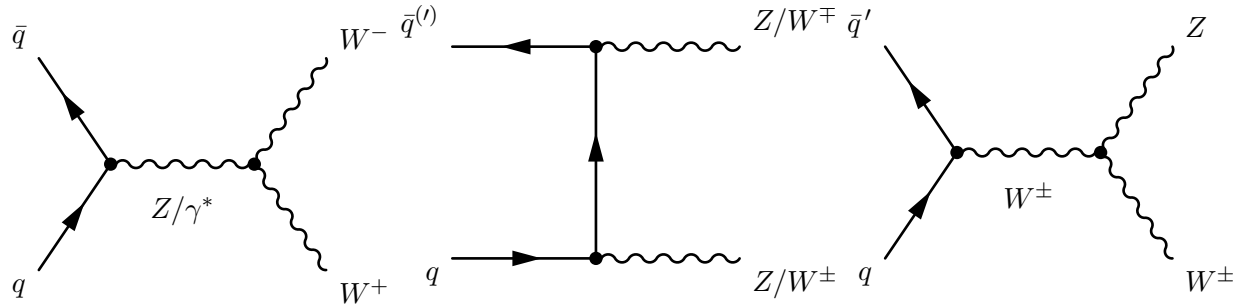

Figure 4.7.: Dominant tree-level Feynman diagrams for di-boson production.

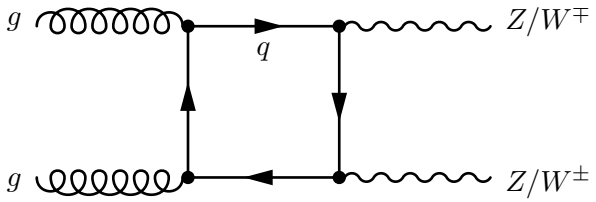

Figure 4.8.: 1-loop Feynman diagram for ZZ/WW production.

for the Herwig datasets. These datasets provide a more accurate description of di-boson backgrounds than the Herwig datasets used for the sample with one b-tagged jet.[11]

A GEF is applied to the `GG2WW` (Herwig) datasets, requiring at least one lepton with a transverse momentum above 10 GeV within the pseudo-rapidity range $|\eta| < 2.7(2.8)$.

W+Jets

W bosons are produced in similar processes as Z bosons, and the same Alpgen configuration is used as for the $Z/\gamma^* +$ Jets background. Despite the large production cross-section, this background plays a minor role: Only single leptons are produced by W boson decays, so either another lepton must be produced in the decay of a heavy quark or another object be misidentified as a lepton. Because of a strong rejection of non-isolated muons and other objects producing similar detector signatures (see Section 6.1), the $W(\rightarrow \mu\nu_\mu) +$ jets process dominates. In order to describe W boson production in association with jets, Alpgen is used.

Multi-Jet Background

The large production cross-section ($\mathcal{O}(100\,\text{mb})$) makes multi-jet events another important background—despite a very low acceptance for lepton candidates from multi-jet events and a good suppression by the consequent analysis cuts.

This combination leads to large uncertainties when estimating the multi-jet background from a MC dataset of a realistic size. The present analysis therefore uses a purely data-driven approach for the multi-jet contribution.

4.2. Detector Simulation, Pileup, Underlying Event

In order to imitate real collision events, the hadronization step is followed by simulating the interactions of all particles with the detector. In order to reflect the concurrent interactions

[11] The decision for Herwig in the sample with one b-tagged jet had already been finalized when the use of the MC@NLO and `GG2WW` was proposed for the sample without b-tagged jets. The difference in the sample with one b-tagged jet kinematics is negligible because of its low acceptance of di-boson events.

(in the same as well as in previous bunch crossings), the energy deposits from multiple interactions are overlaid. The resulting event takes the proton remnants and other backgrounds into account.

The complete set of energy deposits is then passed through the hit digitization, whose output is of the same format as the real detector output. The various reconstruction and identification algorithms are then applied to the event using the Athena framework [177], which is based on the Gaudi framework [178].

The following Subsections represent only a rough overview. More details can be found in Ref. [179].

4.2.1. Detector Simulation

In order to accurately reproduce the detector response, a detailed detector model exists [179] for use with Geant4 [180]. All active and passive material is included, and the placement inaccuracies of the various components (*misalignment*) are taken into account.

Geant4 thus models the interactions of particles from *pp* collisions and other sources with the detector. This step consumes about 95 % of the simulation time per event [179]. The detector response is then simulated in the digitization step (see Subsection 4.2.4).

4.2.2. Pileup

As mentioned in Section 3.1, the interaction rate is much larger than the bunch crossing rate, and the time between bunch crossings is smaller than the time resolution of several sub-detectors. Both aspects are taken into account by simulating additional, overlapping interactions whose signals are synchronous (*in–time*) with those from the primary interaction or shifted (*out–of–time*) after digitization.

4.2.3. Underlying Event

The particles from the UE undergo non-perturbative interactions, whose impact is parameterized within Jimmy and within Pythia. The parameters are fixed in the AUET2B LO** [181] and Perugia 2011 [182] tunes—the former is used as default.

Additional contributions from background radiation and beam–gas interactions are also considered before the digitization step.

4.2.4. Digitization, Reconstruction

Given the thorough knowledge of the real detector response from performance studies, the simulated energy deposits can be translated into a detector response, which can then be subjected to the downstream processing of raw data: The reconstruction and identification procedures are identical for collision data and simulated events.

Both steps exhibit significant dependencies on the run conditions present during the represented data-taking period. In-time and out–of–time pileup affect the performance in various ways. Tolerable detector defects, which do not require vetoing all events from the respective data-taking period, mainly impact efficiency and resolution values. Simulated data must therefore reproduce the fraction of collision-data events taken at a given instantaneous luminosity and detector status as accurately as possible. Residual discrepancies can then be compensated by weighting simulated events according to various kinematic properties (see Section 6.1).

5 Analysis Overview

The searches for Minimal Supersymmetric Standard Model (MSSM) Higgs bosons using $4.7\,\text{fb}^{-1}$ to $4.8\,\text{fb}^{-1}$ of ATLAS data, including the analysis detailed within this thesis, have been combined and published [10]. Section 5.1 summarizes these searches, and Section 5.2 presents an overview over the analysis strategy followed within this thesis for $e\mu$ final states. Section 5.3 explains the mass reconstruction technique employed by this analysis, which allows for the discrimination of events according to the reconstructed Higgs boson candidate mass.

5.1. Searches for Neutral Higgs Bosons in the MSSM with ATLAS

As outlined in Subsection 2.2.3, Higgs boson production in association with b-quarks or from gluon fusion offer the largest discovery potential in the MSSM with $\tan\beta$ values significantly larger than 1 (as well as in other type-II models with two Higgs fields and enhanced Higgs boson couplings to down-type fermions). Subsequent decays to τ lepton pairs, which have a very clean detector signature, are also enhanced, making their observation feasible. Final states with only hadronic ($\tau_{\text{had}}\tau_{\text{had}}$ *channel*), one leptonic in combination with one hadronic ($\tau_{\text{lep}}\tau_{\text{had}}$ *channel*), and only leptonic ($\tau_{\text{lep}}\tau_{\text{lep}}$ *channel*) charged decay products are considered separately. This strategy allows to account for the different background compositions of the channels in $4.7\,\text{fb}^{-1}$ of ATLAS data. In order to better select events with b-associated Higgs boson production and with gluon fusion, each channel is divided into a *b-tagged* and a *b-vetoed* sample according to the jet content of the respective events. The event selection of the $\tau_{\text{had}}\tau_{\text{had}}$ ($\tau_{\text{lep}}\tau_{\text{had}}$) channels contain a veto against events with one (two) light leptons in the final state to avoid double-counting of events across channels. Higgs boson decays to muon pairs have also been considered ($\mu\mu$ *channel*), again with separate *b-tagged* and *b-vetoed* selections and $4.8\,\text{fb}^{-1}$ of collision data. Because of the good mass resolution for muon pairs, the $\mu\mu$ channel contributes to the combined sensitivity—despite the much larger coupling of Higgs bosons to τ leptons.

The $\tau_{\text{lep}}\tau_{\text{lep}}$ and $\tau_{\text{lep}}\tau_{\text{had}}$ selections have been optimized with respect to the expected exclusion for Higgs boson masses near $m_{A^0} = 120\,\text{GeV}$ ($m_{A^0} = 130\,\text{GeV}$ for the $\mu\mu$ channel), while the $\tau_{\text{had}}\tau_{\text{had}}$ selection has been optimized for $m_{A^0} = 300\,\text{GeV}$. Low p_{T} thresholds on electrons and muons (compared to τ_{had} candidates) matter most for low Higgs boson masses, so the $\tau_{\text{lep}}\tau_{\text{lep}}$ contributes most significantly in this region.

The event selections of the other channels and their contributions to the combined sensitivity are discussed in more detain in Section 9.4.

As no significant excess of signal-like events has been observed across the mass range $90\,\text{GeV} < m_\phi < 500\,\text{GeV}$, the results have been combined to obtain 95 % CL upper limits on $\tan\beta$ in the $m_{h^0}^{\text{max}}$ scenario of the MSSM and on the four combinations of production cross-section times branching fraction $\sigma(bb\phi \text{ or } gg \to \phi) \times \text{BR}\,(\phi \to \tau\tau \text{ or } \mu\mu)$ (see Section 9.4).

5.2. The $\tau_{\text{lep}}\tau_{\text{lep}}$ Channel

Among the $\tau_{\text{lep}}\tau_{\text{lep}}$ decay modes, both the *same-flavor modes* ($\phi \to \tau_e\tau_e/\tau_\mu\tau_\mu$) and the *different-flavor modes* have initially been taken into account. Even though same-flavor signal events are as abundant as different-flavor signal events, the contribution from the $Z/\gamma^* \to ee/\mu\mu$ backgrounds is considerable and hard to suppress for these decay modes, spoiling the signal–to–background ratio and, ultimately, the sensitivity. Therefore, only the $\tau_e\tau_\mu$ final state is considered within this thesis.

An event preselection is applied, requiring exactly one electron and muon (see Section 6.1 for details), whose electric charges must add up to zero and whose invariant mass must be at least 30 GeV. This cut has been adopted from the Standard Model (SM) Higgs boson search [183]. It removes the flank of the Drell-Yan continuum and several low-mass resonances.

A cut-based selection has been optimized with respect to the MSSM signal hypothesis $m_{A^0} = 120\,\text{GeV}$, $\tan\beta = 20$, assuming the $m_{h^0}^{\text{max}}$ scenario. This hypothesis corresponds to a total signal cross-section[1] of about 3.3 pb and $m_{A^0} \approx m_{h^0} = 118.2\,\text{GeV}, m_{H^0} = 132.0\,\text{GeV}$. 58 % of the signal cross-section pertain to b-associated production, where the contributions of the h^0 and A^0 bosons dominate (about 96 % of $bb\phi \to \tau\tau \to \ell\ell$). For gluon fusion, the cross-section share of the h^0 and A^0 bosons is about 80 %.

The expected significance values ($\mathcal{S}_i$) are calculated from the expected signal yields S_i and background yields B_i in two samples (i):

$$\mathcal{S}_i = 2\left((S_i + B_i)\ln\left(1 + \frac{S_i}{B_i}\right) - S_i\right), \tag{5.1}$$

and the expected significance values are added in quadrature.

The samples are defined by the jet content[2] of the respective events as either events with exactly one tagged b-jet (called b-tagged events) or events without tagged b-jet (called b-vetoed events), according to the flavor tagging algorithm `MV1` [184], which is explained in Subsection 6.1.4.

Figure 5.1 shows the kinematic properties of b-jets in simulated events with b-associated Higgs boson production. A looser set of cuts[3] is applied on particle-level (compared to the preselection of the analysis) in order to illustrate the soft transverse momentum spectra. The p_{T} spectrum requires the selection of soft b-jets to maintain a high selection efficiency for such events. Because of the p_{T} threshold ($p_{\text{T},b\text{-jet}} > 20\,\text{GeV}$) applied to jets and the limited tracker coverage of $|\eta| < 2.5$, at most 15 % of events with b-associated Higgs boson production can be expected to contain detectable b-jets. Only a minuscule fraction of gluon fusion events is expected in the b-tagged sample because of a low b-jet multiplicity and a good rejection of light jets (see Subsection 6.1.4).

The following discriminating variables have been considered for the selection:

- the transverse momentum of the di-lepton system ($p_T(e\mu)$),
- the scalar sum of the transverse momenta of jets $H_T = \sum_{\text{jet } i} p_{\text{T},i}$,
- the scalar sum of the transverse momenta of the leptons and the missing transverse energy ($E_{\text{T}}^{\text{miss}} + p_{\text{T},e} + p_{\text{T},\mu}$),

[1] including the decay branching ratios $\phi \to \tau\tau \to \ell\ell$

[2] taking into account jets with transverse momenta $p_{\text{T,jet}} > 20\,\text{GeV}$ and pseudo-rapidity values in the range $|\eta_{\text{jet}}| < 2.5$

[3] requiring an electron and a muon of opposite charge and with $p_{\text{T},\ell} > 2\,\text{GeV}$, a jet p_{T} threshold of 10 GeV, and a minimal separation of electrons, muons, and jets of $\Delta R > 0.2$

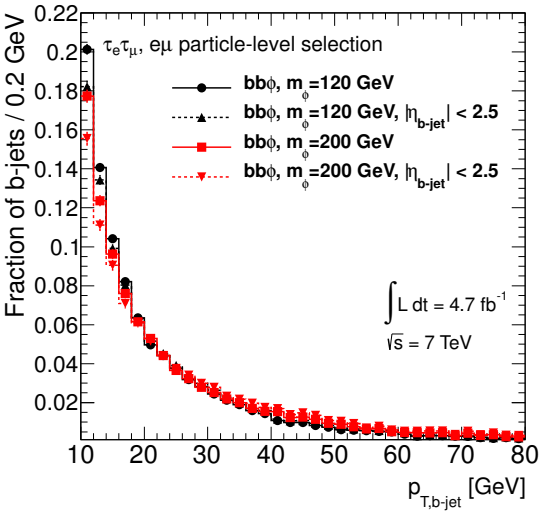

(a) Transverse momenta of all b-jets and of central b-jets ($|\eta| < 2.5$)

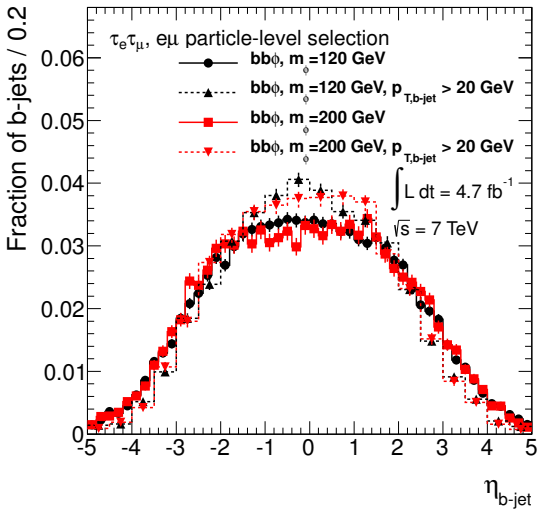

(b) Pseudo-rapidity of all b-jets in signal events and of b-jets with $p_{\text{T},b\text{-jet}} > 20\,\text{GeV}$

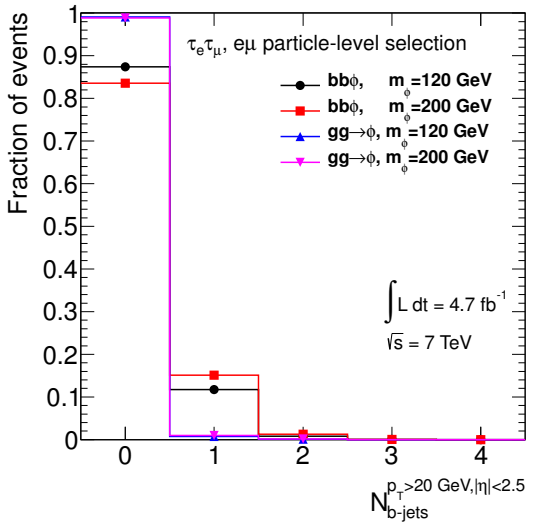

(c) Number of central b-jets with $p_{\text{T}} > 20\,\text{GeV}$

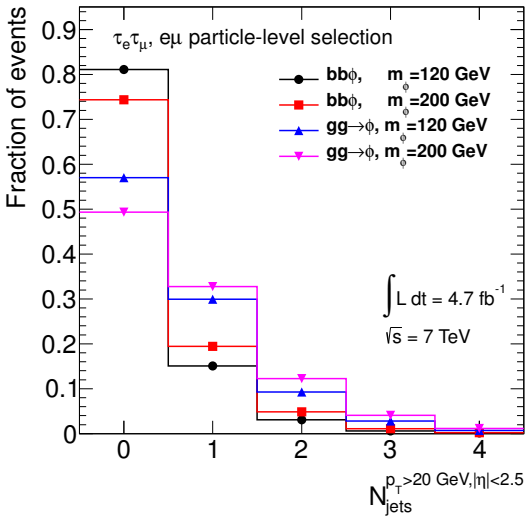

(d) Number of central jets with $p_{\text{T}} > 20\,\text{GeV}$

Figure 5.1.: Jet properties in signal events with b-associated Higgs boson production and gluon fusion after the $e\mu$ particle-level selection, normalized to unity. The Figures pertain to anti-k_t jets with $R = 0.4$, reconstructed from the hadrons in simulated events.

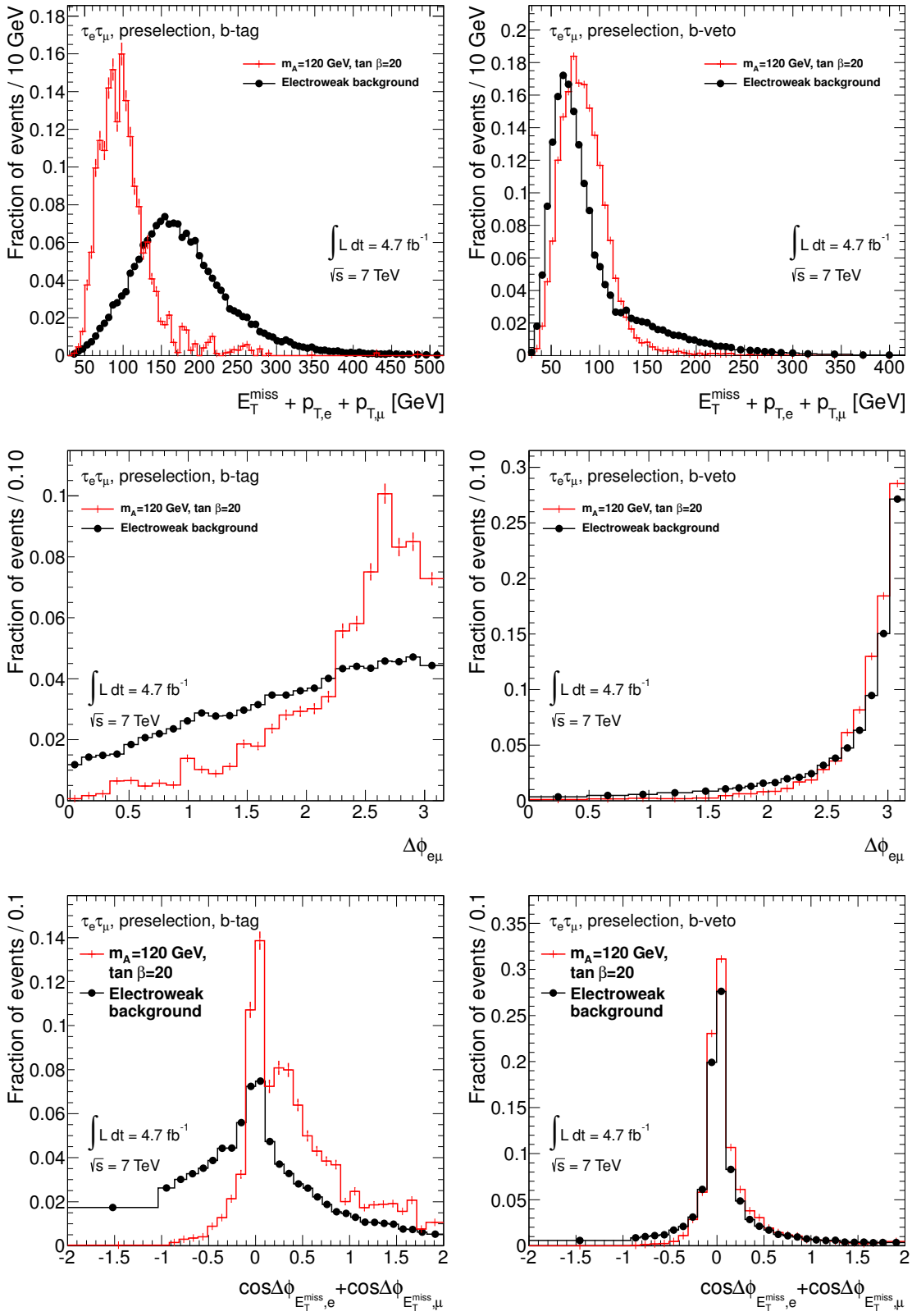

Figure 5.2.: Normalized distributions of the variables used within the selection, drawn after the preselection for the b-tagged and b-vetoed samples.

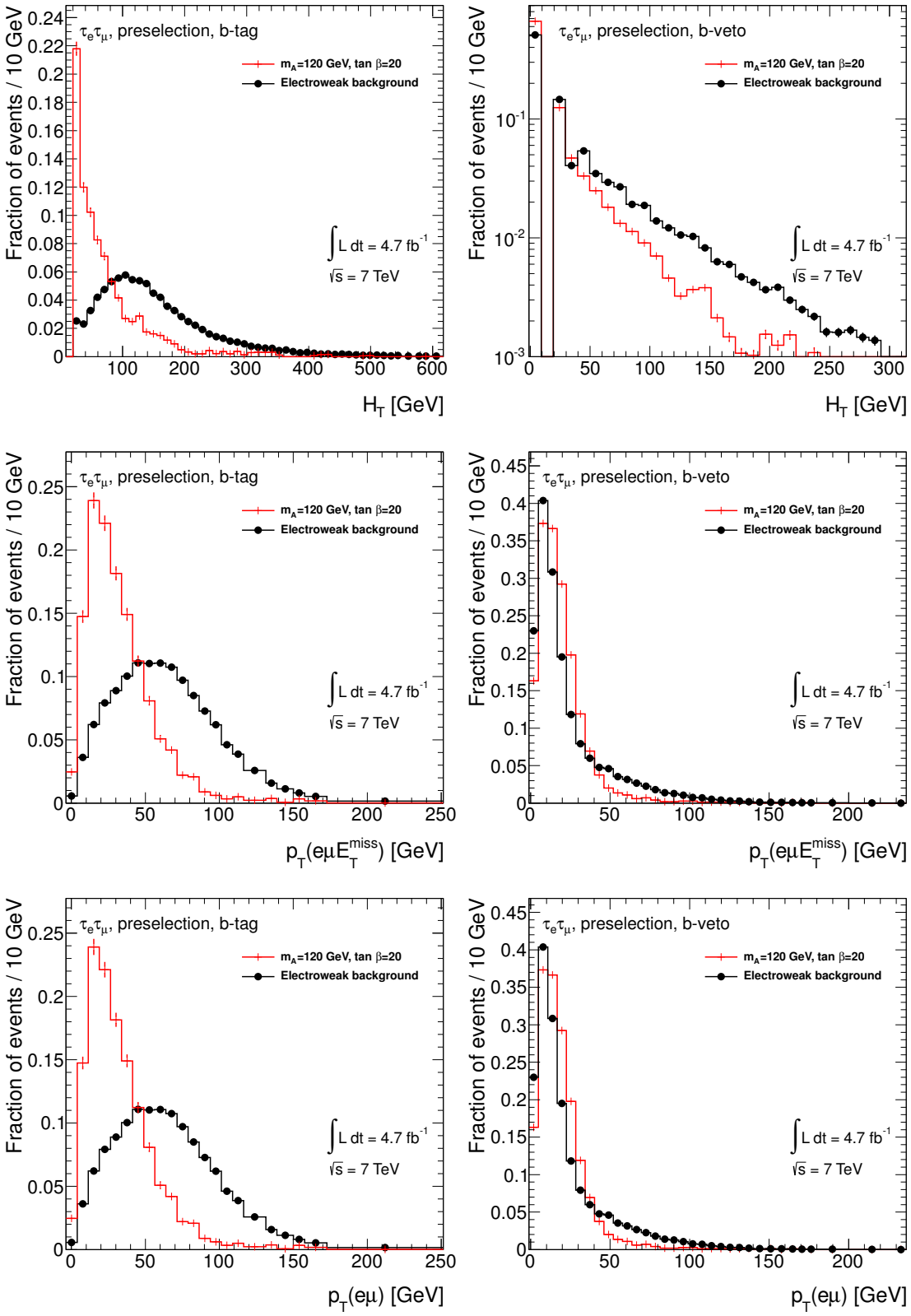

Figure 5.3.: Normalized distributions of the variables used within the selection (top line) and additional variables (bottom two lines), drawn after the preselection for the b-tagged and b-vetoed samples.

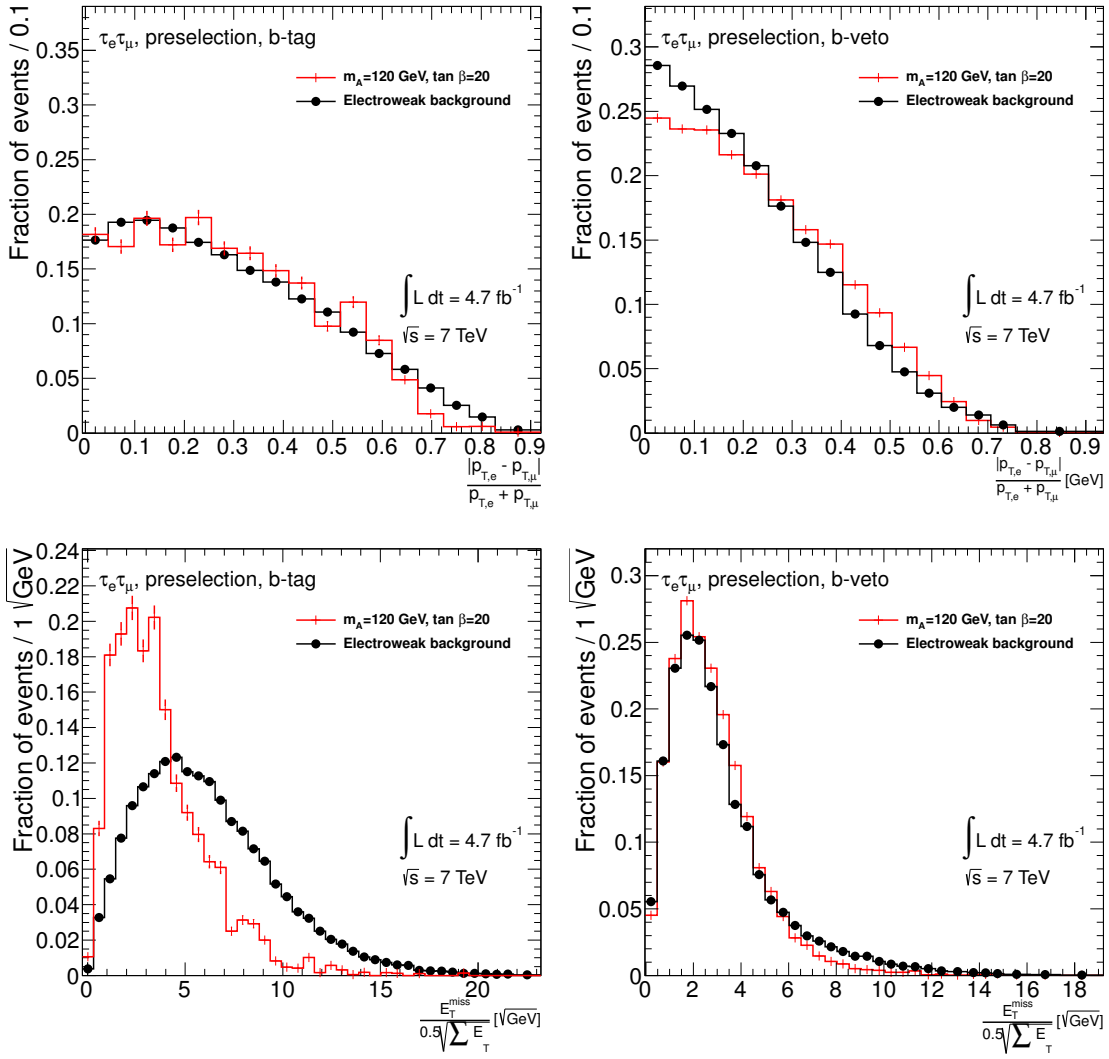

Figure 5.4.: Normalized distributions of additional variables, drawn after the preselection for the b-tagged and b-vetoed samples.

- the transverse opening angle between the leptons ($\Delta\phi_{e\mu}$),
- the combination of the transverse opening angles between the lepton directions and the direction of the missing transverse energy $\left(\sum_{\ell=e,\mu} \cos\Delta\phi_{E_{\mathrm{T}}^{\mathrm{miss}},\ell}\right)$,
- the asymmetry between the scalar transverse momenta of the leptons $\left(\frac{|p_{\mathrm{T}}^{e}-p_{\mathrm{T}}^{\mu}|}{p_{\mathrm{T}}^{e}+p_{\mathrm{T}}^{\mu}}\right)$,
- the $E_{\mathrm{T}}^{\mathrm{miss}}$ *significance* with respect to all calibrated objects (see Subsection 6.1.6) of the event for the b-vetoed selection $\left(\frac{E_{\mathrm{T}}^{\mathrm{miss}}}{0.5\cdot\sqrt{\sum_{\text{calibrated object } i} E_{\mathrm{T},i}}} \text{ with energy values in GeV}\right)$, and
- the transverse momentum of the Higgs boson candidate $\left(p_{\mathrm{T}}(e\mu E_{\mathrm{T}}^{\mathrm{miss}}) = \left(\vec{p}_e + \vec{p}_\mu + \vec{p}_{\mathrm{T}}^{\mathrm{miss}}\right)_{\mathrm{T}}\right)$ for the b-vetoed selection.

The di-lepton invariant mass has not been considered because of strong correlations with the Higgs boson candidate mass ($m_{\tau\tau}^{\mathrm{MMC}}$). The shapes of the distributions of the reconstructed variables are shown in Figures 5.2 through 5.5 to illustrate their discriminating power against other electroweak backgrounds[4]. As a preselection, exactly one electron and one muon of opposite charge and with an invariant mass ($m_{e\mu}$) of more than 30 GeV are required (see Subsection 6.2.1) in addition to a b-jet veto or the presence of exactly one b-jet.

The distributions for signal and background events are much more similar in shape for the b-vetoed sample than for the b-tagged sample—a consequence of the different flavor content of the various backgrounds: Events containing t-quark decays are produced at a much higher rate than signal events and are very likely to have b-tagged jets. Therefore, they dominate the b-tagged sample at the preselection stage (92 % of all expected background events[5]). In the b-vetoed sample, $Z/\gamma^* \to \tau\tau$ events contribute 68 % of the expected background events at the preselection stage. The selection detailed in Chapter 6 therefore consists of effective cuts against events with t-quarks for the b-tagged sample, while a high selection efficiency for signal events is favored for the selection applied to the b-vetoed sample because $t\bar{t}$ and di-boson backgrounds play a smaller role (and the only good discriminant against the $Z/\gamma^* \to \tau\tau$ background is the di-τ invariant mass). The selection cuts (see Chapter 6) are also optimal for the expected limit[6] for $m_{A^0} = 120\,\mathrm{GeV}$, $\tan\beta = 20$ as figure of merit.

Among the selection variables, $E_{\mathrm{T}}^{\mathrm{miss}} + p_{\mathrm{T},e} + p_{\mathrm{T},\mu}$ (see Figure 5.2) plays a special role: An upper cut is imposed, which is very efficient only in selecting signal events with low Higgs boson masses, while the decay of heavy Higgs bosons produces significantly harder lepton (and thus $E_{\mathrm{T}}^{\mathrm{miss}} + p_{\mathrm{T},e} + p_{\mathrm{T},\mu}$) spectra (see Figure 6.10 as well as Tables 6.7 and 6.9). Because no other selection variables can substitute its discriminating power and because this analysis contributes most for low Higgs boson masses (compared to the $\tau_{\mathrm{lep}}\tau_{\mathrm{had}}$ and $\tau_{\mathrm{had}}\tau_{\mathrm{had}}$ channels), this inefficiency is unavoidable.

It is possible to restrict the jet definition in H_{T} to rely only on central jets ($|\eta| < 2.4$), whose original interaction can be identified using the technique described in Subsection 6.1.4. The resulting variable ($H_{\mathrm{T}}^{\mathrm{JVF}}$) is shown in Figure 5.5. However, the optimization favors the more general definition used in H_{T}, and the large H_{T} threshold effectively mitigates the influence of additional jets from pileup interactions.

5.3. Reconstruction of Di-τ Invariant Mass

In the presence of the irreducible $Z/\gamma^* \to \tau\tau$ background, the di-τ-invariant mass ($m_{\tau\tau}$) is the logical choice as final discriminant because it corresponds to the (unknown) Higgs boson mass(es). In order to investigate the presence of one or more narrow di-τ resonances on top of the various backgrounds, an accurate $m_{\tau\tau}$ reconstruction is crucial for the sensitivity.

Because each τ lepton decay involves one (for hadronic decays) or two (for leptonic decays) neutrinos, which cannot be directly detected, an unambiguous $m_{\tau\tau}$ reconstruction requires additional assumptions. The primary assumption states that sources of missing transverse momentum other than the momenta of the neutrinos from the τ lepton decays are negligible. In this case, the missing transverse momentum can be interpreted as the vectorial sum of the transverse momenta of the neutrinos. The following discussion assumes the case of two

[4] dominated at this stage by $Z/\gamma^* \to \tau\tau$ ($t\bar{t}$) in the b-vetoed (b-tagged) sample; the composition at the various stages of the selection is discussed in Section 6.2

[5] including the multi-jet background

[6] the factor by which the predicted cross-section has to be scaled to obtain an expected exclusion at a CL of 95 %

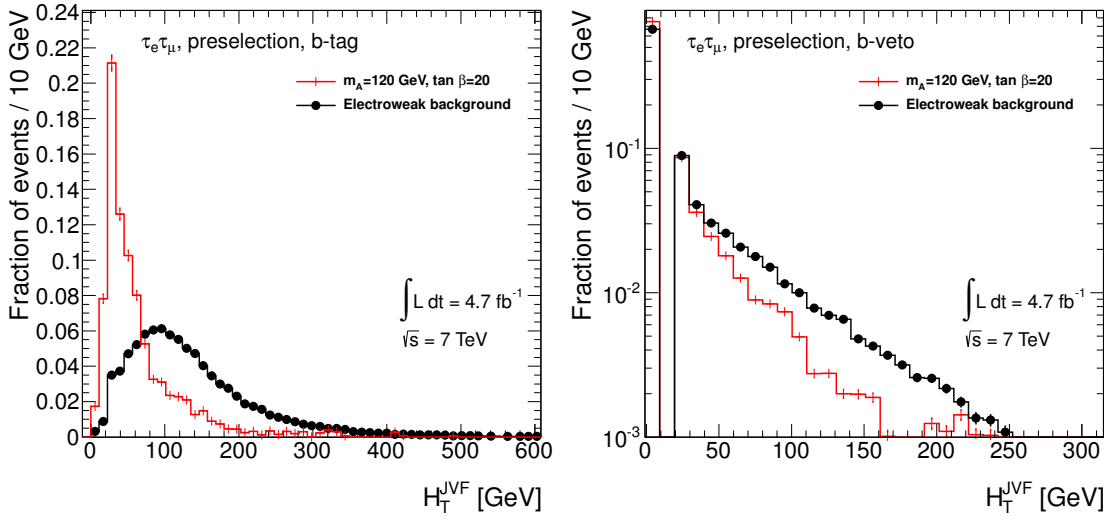

Figure 5.5.: Normalized distributions of additional variables, drawn after the preselection for the b-tagged and b-vetoed samples.

(different-flavor) final state leptons ($\tau_e\tau_\mu$). $m_{\tau\tau}$ can be calculated in similar ways for $\tau_{\text{lep}}\tau_{\text{had}}$ and $\tau_{\text{had}}\tau_{\text{had}}$ decays.

Neglecting the invariant mass ($m^{\nu_\tau\nu_e\nu_\tau\nu_\mu}$) and z-component of the momentum ($p_z^{\nu_\tau\nu_e\nu_\tau\nu_\mu}$) of the neutrino system defines the *effective mass* ($m_{\tau\tau}^{\text{eff}}$). The effective mass is thus calculated as the invariant mass of the sum of the missing transverse momentum four-vector and the lepton four-vectors. Though this mass reconstruction technique yields a result for any preselected event, the resulting $m_{\tau\tau}^{\text{eff}}$ value depends on the momentum of the Higgs boson and how this momentum is distributed among the final state particles. The neglected terms $p_z^{\nu_\tau\nu_e\nu_\tau\nu_\mu}$ and $m^{\nu_\tau\nu_e\nu_\tau\nu_\mu}$ lead to lower results for $m_{\tau\tau}^{\text{eff}}$ than the true di-τ invariant mass $m_{\tau\tau}^{\text{true}}$—even for perfectly well-measured lepton and neutrino momenta. It has been used as final discriminant in the predecessor [13] to the present analysis.

Instead of assuming $m^{\nu_\tau\nu_e\nu_\tau\nu_\mu} = p_z^{\nu_\tau\nu_e\nu_\tau\nu_\mu} = 0$, the *collinear mass* ($m_{\tau\tau}^{\text{coll}}$) [185] exploits the large momenta of the τ leptons, which result from $m_{\tau\tau}^{\text{true}} \gg m_\tau$ for Z bosons and Higgs bosons. In consequence, the momenta of each τ lepton and its invisible decay products are assumed to be collinear with that of the charged lepton in the final state, as depicted in Figure 5.6. This assumption is called the *collinear approximation*.

This method decomposes the missing transverse momentum vector into two components along the directions of the lepton momenta, so the mass resolution deteriorates if the transverse opening angle between the two final state leptons gets close to either 0 or π. In general, the collinear mass reconstruction performs best when the di-τ resonance recoils against other objects, such as additional jets in the event.

The di-τ invariant mass in the collinear approximation can be reconstructed from the invariant mass of the sum of the four-momenta of the electron and the muon ($m_{e\mu}$) as:

$$m_{\tau\tau}^{\text{coll}} = \frac{m_{e\mu}}{\sqrt{x_1 x_2}}. \tag{5.2}$$

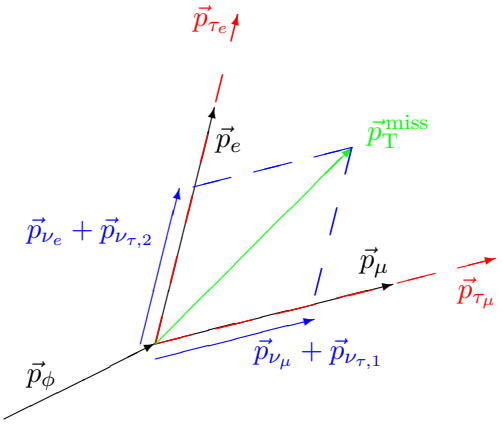

Figure 5.6.: Illustration of the collinear mass reconstruction (not to scale). The Higgs boson (momentum $\vec{p}_\phi$) decays to two (much lighter) τ leptons with momenta $\vec{p}_{\tau_e}$ and $\vec{p}_{\tau_\mu}$, whose directions coincide with those of their (even lighter) daughter particles ($\vec{p}_e, \vec{p}_\mu, \vec{p}_{\nu_\mu}, \vec{p}_{\nu_e}, \vec{p}_{\nu_{\tau,1}}, \vec{p}_{\nu_{\tau,2}}$). If the τ lepton momenta draw an angle significantly different from 0 and π, the missing transverse energy vector ($\vec{p}_{\mathrm{T}}^{\,\mathrm{miss}}$) can be unambiguously decomposed into components parallel to the measured directions of the electron ($\vec{p}_e$) and the muon ($\vec{p}_\mu$).

The visible momentum fractions (x_i) of the of the τ leptons are:

$$x_1 = \frac{p_{\mathrm{T},\mu}}{p_{\mathrm{T},\tau,1}} = \frac{p_{\mu,x}p_{e,y} - p_{\mu,y}p_{e,x}}{p_{\mu,x}p_{e,y} + p_x^{\mathrm{miss}}p_{e,y} - p_{\mu,y}p_{e,x} - p_y^{\mathrm{miss}}p_{e,x}} \tag{5.3}$$

$$x_2 = \frac{p_{\mathrm{T},e}}{p_{\mathrm{T},\tau,2}} = \frac{p_{\mu,x}p_{e,y} - p_{\mu,y}p_{e,x}}{p_{\mu,x}p_{e,y} - p_x^{\mathrm{miss}}p_{\mu,y} - p_{\mu,y}p_{e,x} + p_y^{\mathrm{miss}}p_{\mu,x}}. \tag{5.4}$$

In cases where $x_1 x_2 < 0$, the collinear mass is undefined, leading to an inefficiency of the mass reconstruction. This inefficiency and the di-τ mass resolution depend on the true invariant di-τ mass and the transverse momentum of the di-τ system.

It is, however, also possible to drop the assumption of collinearity by use of the *missing mass calculator (MMC) technique* [186]: This introduces three degrees of freedom[7] per leptonically decaying τ lepton (index $i = 1, 2$; mass m_τ): The spatial direction ($\phi_{\nu\nu,i}, \theta_{\nu\nu,i}$) and the invariant mass $m_{\nu\nu,i}$ of each $\nu_\tau\nu_\ell$ system. A full reconstruction of the event therefore involves solving a set of four equations for eight unknowns:

$$E_x^{\mathrm{miss}} = p_{\nu\nu,1}\sin\theta_{\nu\nu,1}\cos\phi_{\nu\nu,1} + p_{\nu\nu,2}\sin\theta_{\nu\nu,2}\cos\phi_{\nu\nu,2} \tag{5.5}$$

$$E_y^{\mathrm{miss}} = p_{\nu\nu,1}\sin\theta_{\nu\nu,1}\sin\phi_{\nu\nu,1} + p_{\nu\nu,2}\sin\theta_{\nu\nu,2}\sin\phi_{\nu\nu,2} \tag{5.6}$$

$$\begin{aligned} m_\tau^2 =& m_{\nu\nu,1}^2 + m_{\ell,1}^2 + 2\sqrt{p_{\ell,1}^2 + m_{\ell,1}^2}\sqrt{p_{\nu\nu,1}^2 + m_{\nu\nu,1}^2} \\ & - 2p_{\ell,1}p_{\nu\nu,1}\cos\Delta\theta_{(\nu\nu,\ell),1} \end{aligned} \tag{5.7}$$

$$\begin{aligned} m_\tau^2 =& m_{\nu\nu,2}^2 + m_{\ell,2}^2 + 2\sqrt{p_{\ell,2}^2 + m_{\ell,2}^2}\sqrt{p_{\nu\nu,2}^2 + m_{\nu\nu,2}^2} \\ & - 2p_{\ell,2}p_{\nu\nu,2}\cos\Delta\theta_{(\nu\nu,\ell),2}. \end{aligned} \tag{5.8}$$

E_x^{miss} and E_y^{miss} are the measured x- and y-components of $E_{\mathrm{T}}^{\mathrm{miss}}$. $\Delta\theta_{(\nu\nu,\ell),i}$ are the opening

[7] in addition to the momentum of the di-ν system ($p_{\nu\nu,i}$)

angles between $p_{\nu\nu,i}$ and $p_{\ell,i}$ in the rest systems of the τ leptons. They can be calculated from the values in the lab frame by a Lorentz transformation.

This system of equations is under-constrained, but subject to well-known three-body decay kinematics, assuming unpolarized τ leptons. A probability is thus assigned, and the $m_{\tau\tau}$ value of the solution that best fulfills[8] Eqs. (5.5) to (5.8) is registered in a histogram with equidistant binning, using the probability as a weight. The mass bin with the largest sum of weights is then taken as MMC mass ($m_{\tau\tau}^{\mathrm{MMC}}$).

The MMC implementation used within this thesis, described in detail in Ref. [187], extends this procedure to better take into account the $E_{\mathrm{T}}^{\mathrm{miss}}$ resolution as largest source of uncertainty in the $m_{\tau\tau}^{\mathrm{MMC}}$ computation. The above procedure is repeated for a grid of $(E_x^{\mathrm{miss}}, E_y^{\mathrm{miss}})$ pairs that lie within three standard deviations of the measured $E_{\mathrm{T}}^{\mathrm{miss}}$ vector before selecting the best $m_{\tau\tau}^{\mathrm{MMC}}$ value.

The three $m_{\tau\tau}$ definitions are compared for three Higgs boson mass hypotheses in Figure 5.7 for the b-tagged sample and in Figure 5.8 for the b-vetoed sample. The mean and RMS values of the distributions are summarized in Table 5.1 along with the efficiency of the mass reconstruction after the selection[9]. The distributions in the b-tagged sample are narrower than those in the b-vetoed sample, and the reconstruction efficiencies for $m_{\tau\tau}^{\mathrm{MMC}}$ and $m_{\tau\tau}^{\mathrm{coll}}$ are larger in the b-tagged sample. In each case, the mean values follow $m_{\tau\tau}^{\mathrm{eff}} < m_{\tau\tau}^{\mathrm{MMC}} < m_{\tau\tau}^{\mathrm{coll}}$, and the mean value for the collinear mass is significantly higher than the true Higgs boson mass. Also, the $m_{\tau\tau}^{\mathrm{coll}}$ distributions have large tails, which are associated to a low efficiency of reconstructing a mass in the range from 0 to 480 GeV. Note that the analysis is not optimized for best separation and reconstruction efficiency of the collinear mass.

Taking into account the reconstruction efficiency and the separation between different Higgs boson masses in the crucial mass range between 90 and 150 GeV[10], the MMC constitutes the best available $m_{\tau\tau}$ definition.

[8] to account for numerical imprecision

[9] An upper cut of 480 GeV is also included in this number to remove the extended tail of the $m_{\tau\tau}^{\mathrm{coll}}$ distributions.

[10] where the signal and the $Z/\gamma^* \to \tau\tau$ backgrounds have a large overlap in all $m_{\tau\tau}$ distributions

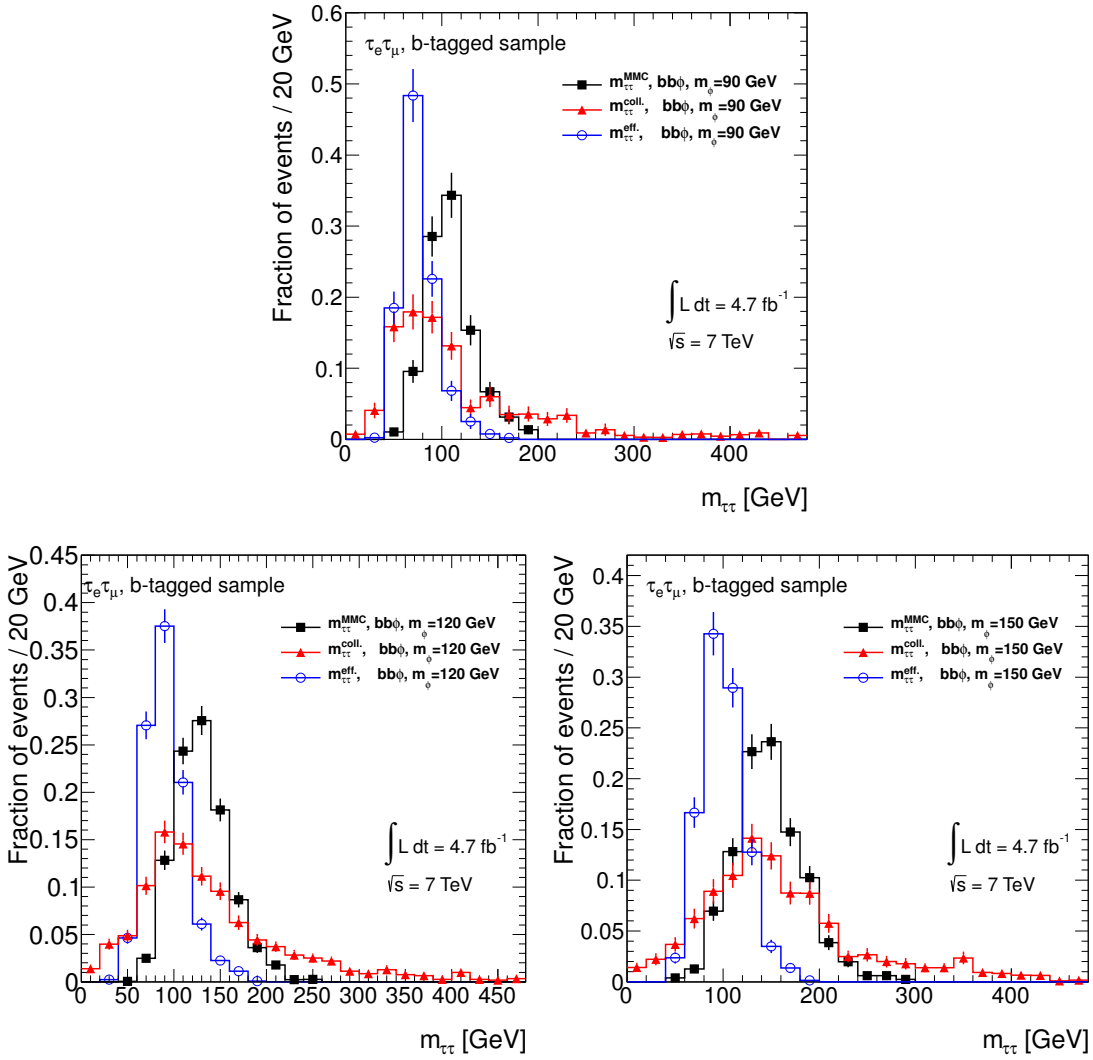

Figure 5.7.: Comparison of $m_{\tau\tau}$ distributions after the b-tagged selection (excluding the requirement that a solution was found for $m_{\tau\tau}^{\mathrm{MMC}}$) for the three definitions considered in the text, given for b-associated Higgs boson production, using three different mass hypotheses. The events for which a mass reconstruction technique fails (underflow) or yields a result above 480 GeV (overflow) are also considered in the normalization.

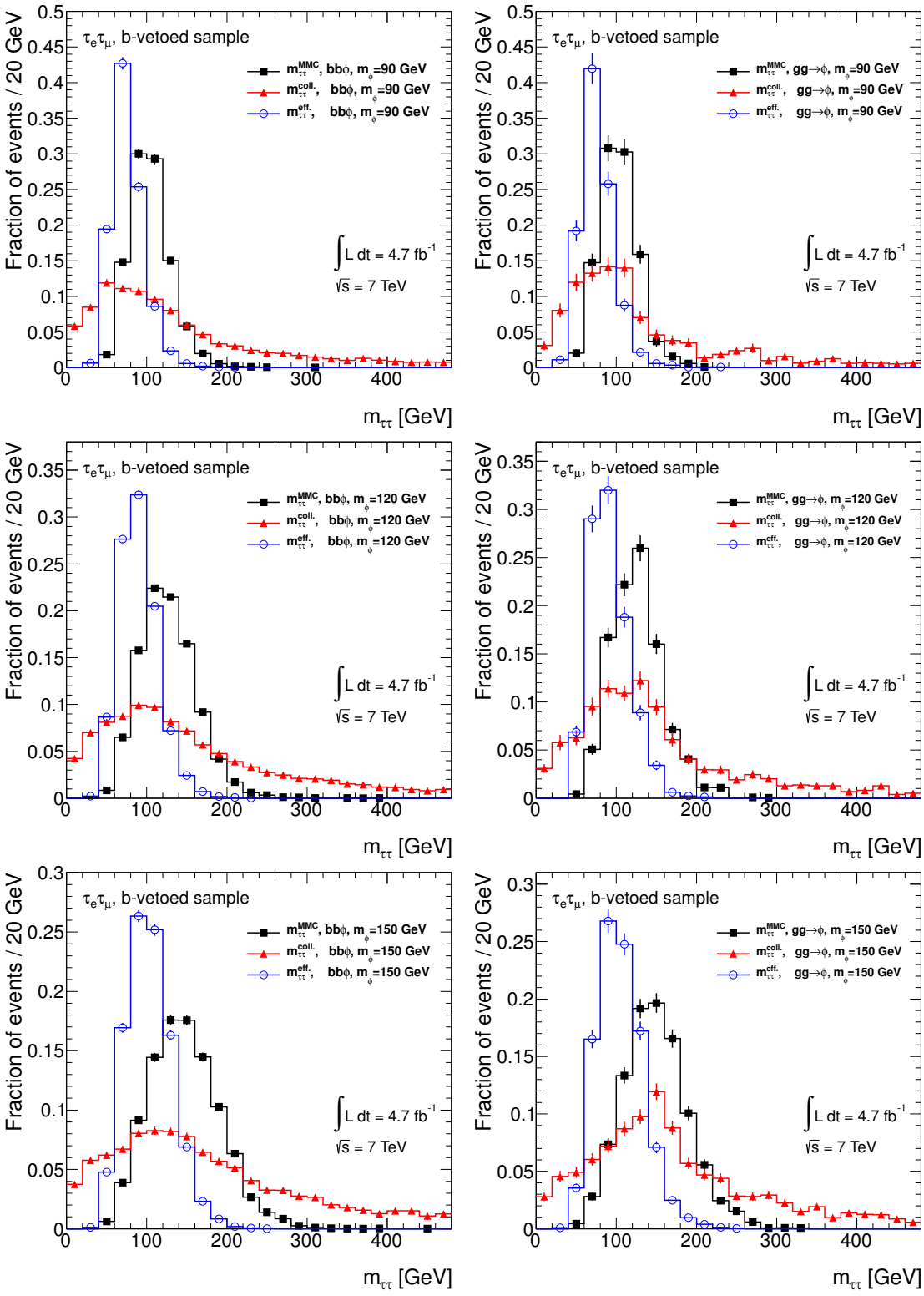

Figure 5.8.: Comparison of $m_{\tau\tau}$ distributions after the b-vetoed selection (excluding the requirement that a solution was found for $m_{\tau\tau}^{\mathrm{MMC}}$) for the three definitions considered in the text, given for b-associated Higgs boson production (left) and for gluon fusion (right), using three different mass hypotheses. The events for which a mass reconstruction technique fails (underflow) or yields a result above 480 GeV (overflow) are also considered in the normalization.

Table 5.1.: Mean and RMS values of the $m_{\tau\tau}$ distributions for the MMC, the collinear mass, and the effective mass after the application of all selection cuts (excluding the requirement that a solution was found for $m_{\tau\tau}^{\mathrm{MMC}}$). The efficiency of $m_{\tau\tau}^{\mathrm{eff}}$ is exactly 1, as denoted by an asterisk (*).

	m_ϕ	$m_{\tau\tau}$	Mean [GeV]	RMS [GeV]	$\varepsilon_{m_{\tau\tau}}$ in range $0\,\mathrm{GeV} < m_{\tau\tau} < 480\,\mathrm{GeV}$
b-tagged sample					
$bb\phi$	90	$m_{\tau\tau}^{\mathrm{MMC}}$	108.4 ±1.3	25.1 ±1.0	1.000
		$m_{\tau\tau}^{\mathrm{coll}}$	119 ±5	83 ±3	0.890
		$m_{\tau\tau}^{\mathrm{eff}}$	76.3 ±1.0	19.3 ±0.7	$1^{(\star)}$
	120	$m_{\tau\tau}^{\mathrm{MMC}}$	129.8 ±0.8	29.7 ±0.6	0.999
		$m_{\tau\tau}^{\mathrm{coll}}$	139 ±2	81.3 ±1.7	0.883
		$m_{\tau\tau}^{\mathrm{eff}}$	91.6 ±0.6	22.5 ±0.5	$1^{(\star)}$
	150	$m_{\tau\tau}^{\mathrm{MMC}}$	147.3 ±1.3	36.0 ±0.9	1.000
		$m_{\tau\tau}^{\mathrm{coll}}$	160 ±3	85 ±2	0.891
		$m_{\tau\tau}^{\mathrm{eff}}$	99.6 ±0.8	23.3 ±0.6	$1^{(\star)}$
b-vetoed sample					
$bb\phi$	90	$m_{\tau\tau}^{\mathrm{MMC}}$	104.2 ±0.3	25.8 ±0.2	0.996
		$m_{\tau\tau}^{\mathrm{coll}}$	132.7 ±1.5	103.6 ±1.1	0.818
		$m_{\tau\tau}^{\mathrm{eff}}$	76.6 ±0.3	20.2 ±0.2	$1^{(\star)}$
	120	$m_{\tau\tau}^{\mathrm{MMC}}$	126.8 ±0.3	34.98±0.19	0.997
		$m_{\tau\tau}^{\mathrm{coll}}$	152.5 ±0.9	107.4 ±0.7	0.782
		$m_{\tau\tau}^{\mathrm{eff}}$	90.21±0.18	24.13±0.13	$1^{(\star)}$
	150	$m_{\tau\tau}^{\mathrm{MMC}}$	147.6 ±0.4	43.7 ±0.3	0.997
		$m_{\tau\tau}^{\mathrm{coll}}$	170.9 ±1.3	111.8 ±0.9	0.754
		$m_{\tau\tau}^{\mathrm{eff}}$	103.3 ±0.3	28.7 ±0.2	$1^{(\star)}$
$gg \to \phi$	90	$m_{\tau\tau}^{\mathrm{MMC}}$	103.1 ±0.8	23.8 ±0.6	0.996
		$m_{\tau\tau}^{\mathrm{coll}}$	126 ±3	95 ±2	0.846
		$m_{\tau\tau}^{\mathrm{eff}}$	76.5 ±0.7	20.7 ±0.5	$1^{(\star)}$
	120	$m_{\tau\tau}^{\mathrm{MMC}}$	126.2 ±0.8	32.6 ±0.6	0.999
		$m_{\tau\tau}^{\mathrm{coll}}$	146 ±3	96.4 ±1.9	0.817
		$m_{\tau\tau}^{\mathrm{eff}}$	91.7 ±0.6	24.9 ±0.5	$1^{(\star)}$
	150	$m_{\tau\tau}^{\mathrm{MMC}}$	149.0 ±0.8	40.2 ±0.6	0.997
		$m_{\tau\tau}^{\mathrm{coll}}$	169 ±2	101.3 ±1.5	0.811
		$m_{\tau\tau}^{\mathrm{eff}}$	105.2 ±0.6	29.1 ±0.4	$1^{(\star)}$

6 Event Selection

This Chapter first summarizes the definitions of the detector signatures used within this thesis (Section 6.1) and then details the event preselection and the selection applied to the b-tagged and b-vetoed samples (Section 6.2).

6.1. Object Reconstruction

The analysis presented within this thesis relies on a thorough understanding of the reconstruction and identification of leptons, jets (including the identification of b-jets), and missing transverse energy in order to correctly estimate selection efficiencies and uncertainties of quantities derived from these objects, such as the final discriminant ($m_{\tau\tau}^{\mathrm{MMC}}$).

In order to achieve a more accurate description of collision data by simulation, simulated events are weighted according to performance parameters, such as the average number of interactions that were simulated per bunch crossing, and to kinematic properties of reconstructed objects.

To adjust the simulated distribution of the average number of interactions per bunch crossing, which is crucial for the simulation of pileup, an event weight with a mean value of 1 and a root mean square (RMS) of 11.9 % is applied. The weights are calculated in such a way that they also correct the fractions of simulated events pertaining to four groups of data-taking periods[1] to match collision data. This is particularly important for the trigger simulation because the trigger menu changes according to the data-taking period. These second-order corrections allow a further reduction of systematic uncertainties related to simulation.

The performance of the measurements of the various detector signatures are summarized in Section 3.2.

6.1.1. Muons

For the reconstruction and identification of muons, input from the Inner Detector and from the Muon Spectrometer is used. Additional data from the calorimetry and the Inner Detector allows for the discrimination of *isolated* muon candidates: By imposing upper limits on the surrounding activity (tracks and energy deposits in the calorimeters), muons originating from hadron decays can be suppressed further.

Tracks from the Inner Detector and the Muon Spectrometer are combined in pairs, and a χ^2 matching procedure selects the most likely combination, based on the track momentum vectors from the Inner Detector and from the Muon Spectrometer, taking into account the prevalent magnetic fields within the detector. The varying precision of the individual space points is considered by the algorithm, resulting in *Statistically Combined (STACO)* combined muon candidates [188].

The direction of the muon candidate is taken from the combined track as reconstructed, while the momentum and the energy are "smeared" with a Gaussian distribution for simulated muons, according to the individual and combined momentum and direction measurements

[1] The data-taking conditions are similar for each of these four groups: `A−D`, `E−H`, `I−K`, and `L−M`.

by the Inner Detector and Muon Spectrometer [189]. This correction slightly degrades the momentum resolution in simulation (which is set to a value slightly better than the expected performance), so the resolution of corrected muons better resembles the resolution measured in collision data. The reconstruction efficiency is corrected by applying an event weight that depends on the pseudo-rapidity and the azimuthal angle of the muon momentum. The reconstruction efficiency from simulation is thus corrected by on average $-1.6\,\%$[2] with a RMS of $2.0\,\%$. The efficiency of the isolation cuts has been verified in the context of Ref. [183].

The muon objects are chosen from the STACO data collection by application of the following cuts on the object properties:

- The transverse momentum of the muon candidate must exceed 10 GeV.
- The pseudo-rapidity of the combined track must be within the tracker coverage ($|\eta| < 2.5$).
- The candidate must have an Inner Detector and a Muon Spectrometer track associated to it.
- In order to suppress muons from cosmic radiation further, the z-component of the point of closest approach between the Inner Detector track of the muon and the proton beam must not differ by more than 1 cm from that of the primary vertex position.

Muon candidates are then subjected to a set of cuts that apply to the Inner Detector track [189]:

- To guarantee correct vertex association and facilitate the removal of muons from cosmic rays, at least one hit must come from the Pixel B-layer if a hit is expected.
- There must be hits (or the respective sensors registered as non-operational) from at least two Pixel layers and six semi-conductor tracker (SCT) sensor layers.
- There must be at most two layers of silicon sensors not registering a matching hit.
- The requirement on transition radiation tracker (TRT) hits depends on the pseudo-rapidity of the combined track:
  - *In the central TRT region* ($|\eta| < 1.9$), there need to be at least six TRT hits that are rated *good* or *outlier*[3], with the latter group representing less than 10 % of the TRT hits.
  - *In the forward TRT region* ($|\eta| > 1.9$), there must be at most five TRT hits or outliers, or the outliers are required to represent less than 10 % of the TRT hits.

Muons are called isolated or anti-isolated according to tracking and calorimetry information pertaining to cones around the muon direction: If the scalar sum of the transverse momenta of tracks not matched to the muon candidate does not exceed 6 % of the transverse momentum of the candidate (*track isolation fraction*) and other energy deposits in the calorimeters do not exceed 4 % (*calorimeter isolation fraction*), the muon candidate is called isolated. Cone radii of $\Delta R = 0.2$ (0.4) are used for calorimetric (track) isolation. Figure 6.1 shows a comparison of the distributions of the isolation variables in signal events and collision data

[2] evaluated in $bb\phi, m_\phi = 120\,\text{GeV}$ and $t\bar{t}$ events

[3] TRT hits from within the correct corridor through the TRT whose inclusion in the combined track fit would lead to an unacceptable χ^2 value [188].

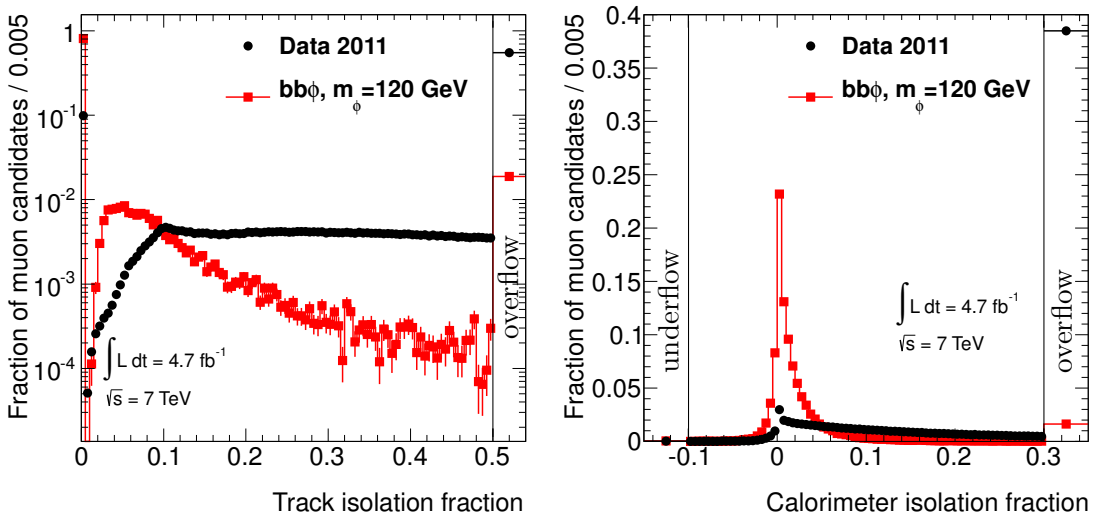

Figure 6.1.: Track (left) and calorimeter (right) isolation variables for muons that pass the identification cuts in the $bb\phi$, $m_\phi = 120\,\text{GeV}$ signal dataset and in collision data. Because the calorimeter calibration takes the mean noise and pileup levels into account, negative cell energy values (and thus negative calorimeter isolation fraction values) can arise.

Table 6.1.: Pileup offset per reconstructed primary vertex (a) for the three relevant pseudo-rapidity ranges [190]. Because the calorimeter calibration takes the mean noise and pileup levels into account, negative cell energy values (and thus negative calorimeter isolation fraction values) can arise.

Pseudo-rapidity range	a[MeV]
$\lvert\eta\rvert < 1.05$	45.49 ± 0.33
$1.05 < \lvert\eta\rvert < 2.0$	38.70 ± 0.41
$2.0 < \lvert\eta\rvert < 2.5$	34.18 ± 0.54

before the application of the preselection cuts. Only muon candidates that pass all above criteria are considered, so the isolation criteria play an important role in the rejection of muons with large surrounding activity, such as muons from the multi-jet background, whose contribution is estimated by inverting the isolation criteria (see Subsection 7.1.2). Pileup effects are taken into special account for calorimetric isolation by subtracting an offset value $\Delta E_{\text{T}}^{\text{cone20}} = a(\eta) \cdot N_{\text{PV}}$, according to the number of reconstructed primary vertices[4] N_{PV} and the pseudo-rapidity of the muon candidate (see Table 6.1) [190].

6.1.2. Electrons

Electron candidates are reconstructed from calorimeter clusters and matching Inner Detector tracks (*cluster-based reconstruction*). Discrimination against jets and hadronically decaying τ leptons is achieved by exploiting differences in the shower evolution and by isolation requirements to avoid misidentified electron candidates. Sets of cuts with different prioritizations of reconstruction efficiency and rejection of misreconstructed electrons have been introduced

[4] with at least two associated tracks

before Large Hadron Collider (LHC) collision data was available [188] and tuned based on the measured performance in collision data [136, 191]. In the present analysis, an electron object definition that emphasizes the rejection of misreconstructed electrons[5] is used without modification to the identification criteria (see Ref. [192] for a summary). The reconstruction and identification efficiencies are corrected by applying the product of two event weights that each depend on the pseudo-rapidity and the transverse momentum of the electron candidate. The reconstruction efficiency from simulation is thus corrected by on average $-1.7\,\%$ in $bb\phi, m_\phi = 120\,\text{GeV}$ events, and no mean correction results for $t\bar{t}$ events. The RMS of of the associated scale factor is $2.7\,\%$ for $bb\phi, m_\phi = 120\,\text{GeV}$ events and $2.2\,\%$ for $t\bar{t}$ events. The efficiency of the isolation cuts has been verified in the context of Ref. [183].

The four-momentum of an electron candidate uses the precision of the directional measurement of the Inner Detector and the calorimetric energy measurement. The transverse momentum p_T is calculated from the pseudo-rapidity η and the total energy E:

$$p_\text{T} = \frac{E}{\cosh \eta}.$$

The total energy is then corrected, according to the recipe described in Ref. [193]:

- The energy is calibrated for electron candidates from collision data by a factor that depends on the energy and on the nominal pseudo-rapidity and azimuthal angle of the point at which the electron enters the calorimeter, accounting for an inhomogeneous detector response.
- The energy for electrons from simulation and from collision data with nominal pseudorapidities in the range $1.42 < |\eta| < 1.55$ is corrected upwards by $5 - 10\,\%$. Because electrons from the core of the barrel–endcap transition region of the electromagnetic calorimeter are not taken into account (see below), the correction is effective only in the range $1.52 < |\eta| < 1.55$.
- For electron candidates from simulation, the energy is additionally "smeared" with a Gaussian distribution to reproduce the energy resolution in collision data.

Subsequently, the following selection cuts are applied to the electron candidates:

- The transverse momentum of the electron candidate must exceed $15\,\text{GeV}$.
- The pseudo-rapidity of the track must be within the tracker coverage $|\eta| < 2.47$.
- Electrons from the barrel–endcap transition region of the electromagnetic calorimeter (with nominal pseudo-rapidities in the range $1.37 < |\eta| < 1.52$) are rejected.
- The object quality bit mask is checked for intolerable defects[6] of the electromagnetic calorimeter near the electron candidate [194].

Electron isolation criteria are again defined in terms of cones around the track direction: If the scalar sum of the transverse momenta of tracks not matched to the electron candidate does not exceed $6\,\%$ of the transverse momentum of the candidate (*track isolation fraction*) and other energy deposits in the calorimeters do not exceed $8\,\%$ of the transverse momentum of the candidate (*calorimeter isolation fraction*), the electron candidate is called isolated. Cone radii of $\Delta R = 0.2$ (0.4) are used for calorimetric (track) isolation. Figure 6.2 shows

[5] called tightPP

[6] leading to a level of uncertainty which is not covered by the nominal uncertainty

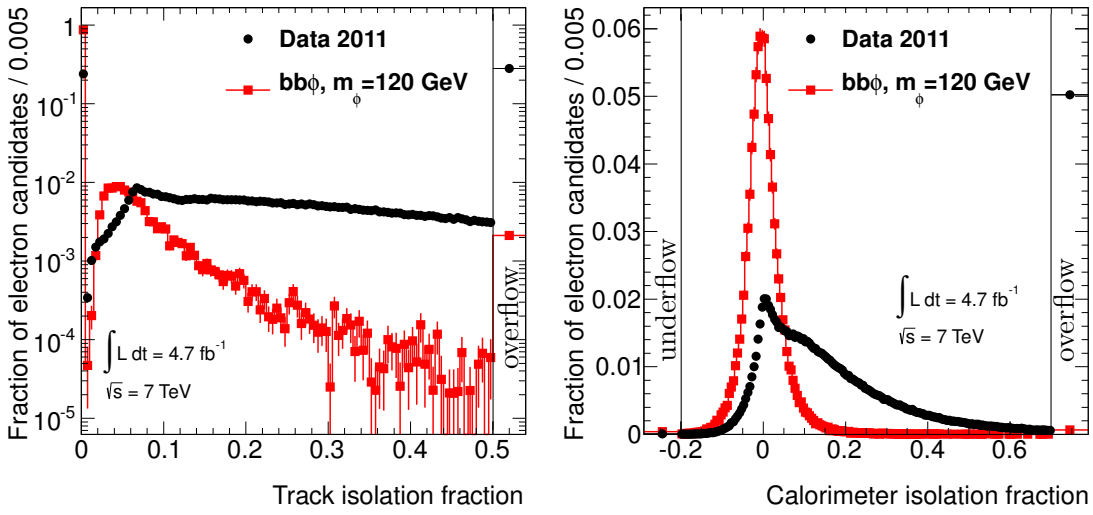

Figure 6.2.: Track (left) and calorimeter (right) isolation variables for electrons that pass the identification cuts in the $bb\phi$, $m_\phi = 120\,\text{GeV}$ signal dataset and in collision data. Because the calorimeter calibration takes the mean noise and pileup levels into account, negative cell energy values (and thus negative calorimeter isolation fraction values) can arise.

a comparison of the distributions of the isolation variables in signal events and collision data before the application of the preselection cuts. Only electron candidates that pass all above criteria are considered. The calorimetric isolation value $E_{\text{T}}^{\text{cone20}}$ is corrected for pileup[7] and calibrated to account for the shape of the shower, the electron candidate energy for subtraction, and the nominal pseudo-rapidity. For simulated electrons, the $E_{\text{T}}^{\text{cone20}}$ value is additionally "smeared" to reproduce the $E_{\text{T}}^{\text{cone20}}$ energy resolution determined from collision data [195].

6.1.3. Lepton Triggers

The two final state leptons present the opportunity to perform the analysis on the data streams dedicated to events with muons and events with electrons or photons as a part of their trigger signature.

As discussed in Subsection 3.2.7, the repeated increases in the instantaneous luminosity at the beginning of a fill of the accelerator (see Subsection 3.1.1) made it necessary to tighten the loosest trigger conditions between data-taking periods in 2011. An inclusive disjunction (denoted by ||) of a single-electron, a single-muon, and an electron–muon trigger (see p_{T} thresholds in Table 6.2) was used to maximize the recorded number of signal events. In order to limit the impact of the uncertainty from the trigger efficiencies, the p_{T} cuts on reconstructed analysis objects restrict the transverse momenta to ranges where the trigger efficiencies are approximately constant with respect to p_{T} (*plateau regions*).

The trigger efficiencies in simulated events ($\varepsilon_\mu^{\text{MC}}(\eta_\mu, \phi_\mu), \varepsilon_e^{\text{MC}}(\eta_e, p_{\text{T},e})$) and collision data ($\varepsilon_\mu^{\text{data}}(\eta_\mu, \phi_\mu), \varepsilon_e^{\text{data}}(\eta_e, p_{\text{T},e})$) for the single-muon and single-electron triggers are available from Ref. [196]. The performance of the electron–muon trigger has been studied in the context of Ref. [183], finding that the difference of the efficiencies of the electron signature

[7] according to the number of reconstructed primary vertices with at least two associated tracks

Table 6.2.: Evolution of the lepton p_{T} thresholds used within the trigger and within the analysis for the three types of trigger signatures used within the preselection.

Trigger Object	Electron		Muon	Electron + Muon
Data-Taking Periods	B–H	I–M	B–M	B–M
Corresponding Integrated Luminosity $\mathcal{L}$ [fb^{-1}]	1.2	3.5	4.7	4.7
$p_{\mathrm{T},e}^{\mathrm{trigger}}$[GeV]	20	22	–	10
$p_{\mathrm{T},e}^{\mathrm{analysis}}$[GeV]	24	24	15	15
$p_{\mathrm{T},\mu}^{\mathrm{trigger}}$[GeV]	–	–	18	6
$p_{\mathrm{T},\mu}^{\mathrm{analysis}}$[GeV]	10	10	20	10

in data and in simulation is negligible. The efficiency of the muon signature is correctly reproduced by simulation for muons with pseudo-rapidities of $|\eta| > 1$ and has to be corrected by $-2\,\%$ ($+4\,\%$) for $0 < \eta < 1$ ($-1 < \eta < 0$). The efficiency for collision data taken in 2011 was $90\,\%$ ($75\,\%$) for $|\eta| > 1$ ($|\eta| < 1$) for the electron–muon trigger with respect to the reconstruction and identification of an electron–muon pair as described above.

The correct assessment of trigger efficiencies relies on correctly determining the correspondence between objects reconstructed by the trigger and the lepton candidates of the analysis. For electrons, this matching procedure looks for an Event Filter (EF) object from the same trigger chain[8] within a cone of $\Delta R < 0.15$ around the track. Because muon trigger objects are not grouped by trigger chain, the presence of both a level 2 (L2) object and an EF object are verified within a cone of $\Delta R < 0.1$ around the combined track. Subsequently, the p_{T} of the EF object is checked. For the electron–muon trigger, the presence of an EF electron object from the same trigger chain alongside a L2 and an EF muon object is verified, using the same cone sizes as for the single-lepton triggers.

The assumption that the three triggers are uncorrelated leads to a good description of the overall trigger efficiency [183] by event reweighting: The event reweighting factor (SF) is then simply the product of the scale factors (SFs) per trigger $i = e, \mu, e\mu$:

$$\mathrm{SF} = \frac{\varepsilon^{\mathrm{data}}_{e||\mu||e\mu}(\eta_\ell, \phi_\ell, p_{\mathrm{T},\ell})}{\varepsilon^{\mathrm{MC}}_{e||\mu||e\mu}(\eta_\ell, \phi_\ell, p_{\mathrm{T},\ell})} = \prod_{i=e,\mu,e\mu} \mathrm{SF}_i \tag{6.1}$$

with

$$\mathrm{SF}_i = \begin{cases} \frac{\varepsilon_i^{\mathrm{data}}}{\varepsilon_i^{\mathrm{MC}}} & \text{if } i \text{ passed} \\ \frac{1-\varepsilon_i^{\mathrm{data}}}{1-\varepsilon_i^{\mathrm{MC}}} & \text{if } i \text{ failed} \\ 1 & \text{if no matching lepton(s) for } i. \end{cases} \tag{6.2}$$

The calculation of the inefficiency SF (i failed) relies on the fact that the probabilities that a trigger is passed or failed add up to unity.

Figure 6.3 shows a particle-level comparison of the p_{T} spectra and η distributions for the Higgs boson mass hypotheses 120 GeV (for b-associated Higgs boson production and gluon fusion) and 200 GeV (for b-associated Higgs boson production only)[9], highlighting the trigger-based analysis-level p_{T} thresholds. A looser set of cuts is applied on particle level (compared

[8] see Subsection 3.2.7

[9] These datasets were also used for the particle-level assessment of systematic errors from Monte Carlo (MC) event simulation (see Section 8.1).

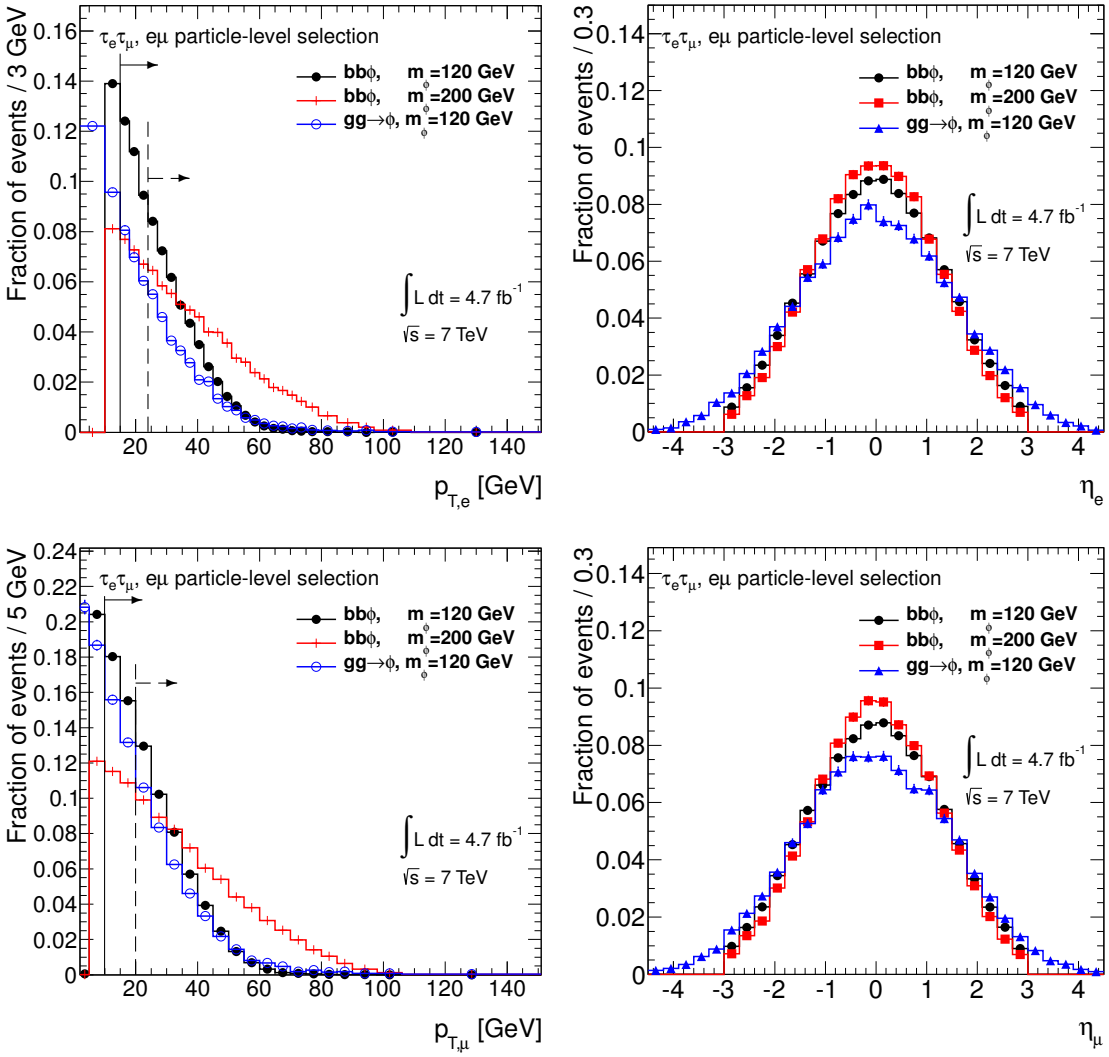

Figure 6.3.: Normalized p_T and η distributions for electrons and muons from a parton-level simulation for the production mechanisms of gluon fusion and b-associated Higgs boson production. A comparison of the distributions for the mass hypotheses 120 GeV and 200 GeV is shown. The p_T thresholds of the analysis for events from the respective single-lepton and from the di-lepton signature are shown as dashed and solid lines, respectively.

Table 6.3.: Total trigger efficiency of the logical disjunction (denoted by ||) of all three triggers ($e||\mu||e\mu$) with respect to all $bb\phi, m_\phi = 120\,\text{GeV}$ events passing the kinematic selection of either the b-tagged or the b-vetoed sample (first data column, in percent). The fractions of events (with respect to $e||\mu||e\mu$, in percent) that are selected by using only the single-electron, single-muon, or the electron–muon triggers as well as combinations of two triggers are given also given. The efficiencies are taken from simulation and distinguish between the data-taking periods `D`, `G`, `I`, and `L`, which represent the various data-taking conditions and versions of the trigger menu employed in 2011.

Data-Taking Period	Total Trigger Efficiency [%]	Relative Single-Trigger Efficiency [%]			Relative Dual-Trigger Efficiency [%]		
	$e\|\|\mu\|\|e\mu$	e	μ	$e\mu$	$\mu\|\|e\mu$	$e\|\|e\mu$	$e\|\|\mu$
`D`	76.4	80.0	60.5	82.7	83.7	99.7	100.0
`G`	80.2	78.9	60.2	82.9	83.3	99.6	100.0
`I`	92.9	68.1	55.2	84.7	85.9	98.8	89.0
`L`	94.6	69.5	55.3	85.2	85.7	99.6	89.2

to the preselection of the analysis) in order to illustrate the soft transverse momentum spectra. The impact of the `2LepEF` generator event filter (GEF) cut, introduced in Subsection 4.1.4, can be seen in the p_T spectra and η distributions of the two $bb\phi$ samples.

Due to inefficiencies in the lepton triggers (see Figures 3.20 and 3.21), the best signal selection efficiency is achieved by an inclusive disjunction of the single-electron, the single-muon, and the combined electron–muon triggers ($e||\mu||e\mu$): About $76 - 95\,\%$—depending on data-taking conditions—of events passing the kinematic selection are selected by the $e||\mu||e\mu$ trigger condition. For the signal scenario $\phi = 120\,\text{GeV}$, the combined electron–muon trigger is the most efficient individual trigger, and the extension by single-electron and single-muon triggers increases the signal acceptance by approximately $18\,\%$ after the selection of an oppositely charged electron–muon pair. Table 6.3 shows the total trigger efficiency of the $e||\mu||e\mu$ trigger condition and the fractions of all triggered signal events from the b-tagged and b-vetoed samples (using $e||\mu||e\mu$ as reference) that single triggers and disjunctions of two triggers select. The inefficiency introduced into the complete selection by requiring the $e||\mu||e\mu$ trigger condition rather than only requiring the reconstruction of an electron–muon pair decreases for the later data-taking periods[10]. The single-electron trigger cuts, which have been progressively tightened with increasing instantaneous luminosity, enhance the relative contribution of the electron–muon trigger in data-taking periods `I` to `M`.

6.1.4. Jets, Flavor Tagging

As jets play an important role in the event selection, jet observables must be defined in a way that ensures robustness against theoretical and experimental uncertainties. In order to mitigate the effects of detector noise, jet objects are reconstructed from topological clusters [156], which use known noise levels to select only calorimeter cells with significant energy deposits. The overlap of jets poses an important challenge at high interaction rates. The performance of simple sliding-window algorithms deteriorates faster in such environments than that of sequential recombination jet finding algorithms, such as the anti-k_T algorithm [160, 197] used

[10] Note that this quantity depends on the efficiency of the selection cuts.

for jet finding within this thesis (distance parameter $R = 0.4$).

In order to limit the impact of pileup and the overall size of systematic uncertainties, a lower p_{T} cut of 20 GeV is imposed. Energy deposits are reconstructed at the electromagnetic scale and corrected to reflect the approximate energy of the initial parton [137]. Jets with nominal pseudo-rapidities $|\eta| < 4.5$ are used. For jet pseudo-rapidities in the range $|\eta| < 2.4$, Inner Detector tracks are matched to overlapping jets by extrapolating the tracks to the calorimetry boundary and selecting the jet whose axis encloses the smallest angle ΔR with the track impact point. Jets can thus be assigned p_{T} contributions associated to any of the reconstructed vertices [198]. Jets with $|\eta| < 2.4$ are accepted if more than 75 % of the total track p_{T} sum is associated to the main interaction vertex. This measure is known as *jet vertex fraction (JVF)*. The vertex belonging to the main interaction is selected by finding the vertex candidate with the largest squared track p_{T} sum $\left(\sum_{\text{track } i}^{N} p_{\mathrm{T},i}^2\right)$, where N is the number of associated tracks.

The flavor of the initial parton is determined for each jet with a nominal pseudo-rapidity within the tracker coverage $|\eta| < 2.5$ (*flavor tagging*), which can be exploited for the search for neutral Higgs bosons produced in association with b-quarks. Jets originating from b-quarks show a set of characteristics that can be used to discriminate against jets from light quarks or gluons: b-quarks form b-hadrons during hadronization, such as the B^0 meson, which have significant mean decay lengths ($c\tau_{B^0} = (0.455 \pm 0.002)\,\mathrm{mm}$, relativistically enhanced in the lab frame) and masses ($m_{B^0} = (5279.58 \pm 0.17)\,\mathrm{MeV}$ [21]). b-hadron decays frequently involve other hadrons with significant lifetimes, such as D mesons. As a result, b-jets can be identified by searching for tracks within the jet that show a significant offset (impact parameter) from the closest reconstructed primary vertex candidate (used by *impact parameter taggers*). Another method involves quantifying the significance of the separation between a primary and a secondary vertex (*secondary vertex taggers*). The `Jet Fitter` tagger [199] considers various b-hadron decay chains and attempts to reconstruct a b-hadron and a c-hadron decay vertex along the jet axis.

These three types of flavor tagging algorithms use complementary sets of input information. As a result, a combination of tagger outputs leads to a better performance (see Figure 6.4 and Table 6.4): Of the tagging algorithms considered in the original optimization, the `IP3D+JetFitter` [202] algorithm performs best. It uses an artificial neural network (ANN) which combines the outputs from `Jet Fitter` and the `IP3D` impact parameter tagger. It was then superseded as best performing flavor tagging algorithm by the `MV1` tagger [184], which uses another ANN to combine the `IP3D+JetFitter` result with the secondary vertex tagger `SV1`. The working points are summarized in Table 6.4. The result of `MV1` is used as flavor tagging observable in this analysis. A working point corresponding to $\varepsilon_b^{p_{\mathrm{T}}>15\,\mathrm{GeV}} = 74.6\,\%$ tagging efficiency in simulated $t\bar{t}$ events [200] (using jets with $p_{\mathrm{T}} > 15\,\mathrm{GeV}$ and $|\eta| < 2.5$) has been chosen: The optimization described in Section 5.2 had been executed for all calibrated working points of the flavor tagging algorithms `SV0`, `IP3D+SV1`, and `IP3D+JetFitter`[11]. The sum of the squared significance values favored the 69.5 % efficient `IP3D+JetFitter` working point and showed a strong dependence on $\varepsilon_b^{p_{\mathrm{T}}>15\,\mathrm{GeV}}$. Furthermore, the larger $\varepsilon_b^{p_{\mathrm{T}}>15\,\mathrm{GeV}}$ value allows for a better rejection of t-quark backgrounds and a more efficient selection of a $t\bar{t}$ control sample, justifying the working point selection for `MV1`.

The performance has been evaluated with b-jets from collision data, selecting a $t\bar{t}$ sample [184]. Mistag rates have been measured with two independent methods for light jets [203] and with a sample of events containing $D^{\star\pm}$ decays for the c-jet rejection factor [204].

[11] The `MV1` tagger was not available at the time the optimization was performed. The choice of the cut values was later verified with the `MV1` tagger.

Table 6.4.: Flavor tagging working points used within the optimization of the event selection and the working points of the `MV1` tagger. The efficiency for b-jets above 15 GeV ($\varepsilon_b^{p_T>15\,\mathrm{GeV}}$) and inverse efficiencies for light jets ($R_{\mathrm{light}}^{p_T>15\,\mathrm{GeV}}$), c-jets ($R_c^{p_T>15\,\mathrm{GeV}}$), and τ_{had}-induced jet candidates ($R_{\tau_{\mathrm{had}}}^{p_T>15\,\mathrm{GeV}}$) are given. A simulated $t\bar{t}$ dataset has been used to obtain these numbers [200]. The optimal `IP3D+JetFitter` working point and the `MV1` working point chosen for this analysis are highlighted in boldface.

Flavor Tagging Algorithm	$\varepsilon_b^{p_T>15\,\mathrm{GeV}}$	$R_{\mathrm{light}}^{p_T>15\,\mathrm{GeV}}$	$R_c^{p_T>15\,\mathrm{GeV}}$	$R_{\tau_{\mathrm{had}}}^{p_T>15\,\mathrm{GeV}}$
`SV0`	49.6	384	9	32
`IP3D+SV1`	59.4	373	7	24
	69.4	71	5	8
	79.8	13	3	3
`IP3D+JetFitter`	59.4	422	8	25
	69.5	**92**	**5**	**11**
	79.6	16	3	4
`MV1`	59.6	635	8	27
	69.6	134	5	13
	74.6	**58**	**4**	**9**
	84.7	9	2	3

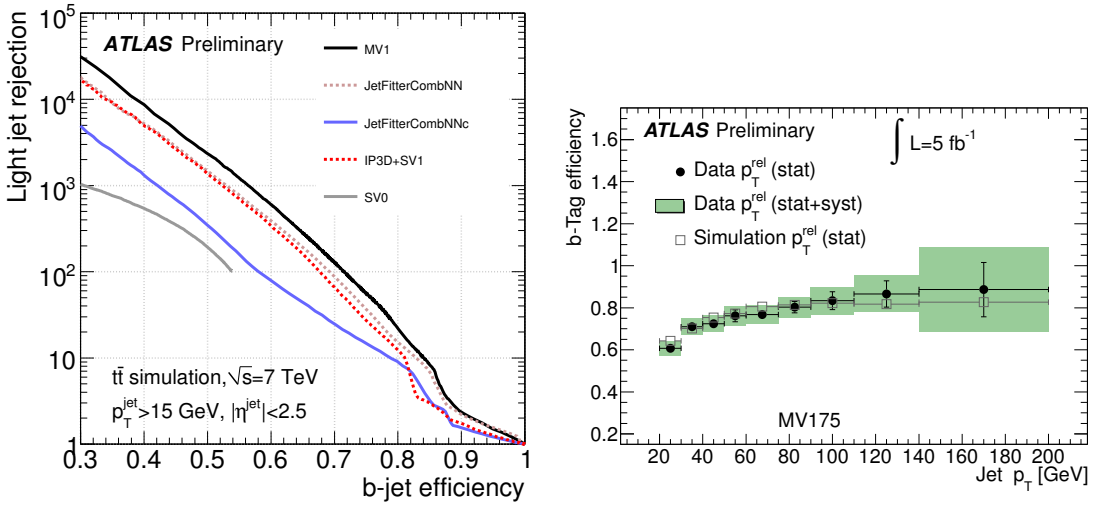

Figure 6.4.: Inverse probability to incorrectly tag a jet from a light quark or gluon as a b-jet (light jet rejection), drawn in dependence of the efficiency for true b-jets for various tagging algorithms (left). The right Figure shows the tagging efficiency for a b-jet as a function of its transverse momentum for the working point used within this thesis [201].

Events with simulated flavor tagging response can be corrected by application of an event weight [205]: For best discrimination against $t\bar{t}$ events, this analysis takes flavor tagging results from all jets satisfying $p_{\mathrm{T}} > 20\,\mathrm{GeV}$ and $|\eta| < 2.5$ into account. The per-event correction factor w_{event} is therefore calculated as the product of the per-jet correction factors w_i [205]:

$$w_{\mathrm{event}} = \prod_{\text{jet } i} w_i. \tag{6.3}$$

The per-jet correction factors (w_i) are the ratios of probabilities in simulated and in collision data for the tagger result (tagger response above or below threshold) that was found in the simulated event. It can be expressed in terms of the flavor-dependent[12] tagging probabilities $\varepsilon^{\mathrm{data}}_{\mathrm{flavor}}$ and $\varepsilon^{\mathrm{MC}}_{\mathrm{flavor}}$, which depend on the transverse momentum $p_{\mathrm{T},i}$ and the pseudo-rapidity η_i of the jet:

$$w_i = \begin{cases} \frac{\varepsilon^{\mathrm{data}}_{\mathrm{flavor}}(p_{\mathrm{T},i},\eta_i)}{\varepsilon^{\mathrm{MC}}_{\mathrm{flavor}}(p_{\mathrm{T},i},\eta_i)} & \text{if the jet } i \text{ passes as } b\text{-jet} \\ \frac{1-\varepsilon^{\mathrm{data}}_{\mathrm{flavor}}(p_{\mathrm{T},i},\eta_i)}{1-\varepsilon^{\mathrm{MC}}_{\mathrm{flavor}}(p_{\mathrm{T},i},\eta_i)} & \text{if the jet } i \text{ fails } b\text{-jet requirement.} \end{cases} \tag{6.4}$$

In principle, the flavor tagging efficiencies ($\varepsilon^{\mathrm{MC}}_{\mathrm{flavor}}(p_{\mathrm{T},i},\eta_i)$) depend on the topology of the simulated event. The efficiency values for $t\bar{t}$ events are available from Ref. [184]. It has been verified for signal events from b-associated production ($m_{A^0} = 120\,\mathrm{GeV}$, $\tan\beta = 20$) that the values of $\varepsilon^{\mathrm{MC}}_{\mathrm{flavor}}(p_{\mathrm{T},i},\eta_i)$ agree with those for $t\bar{t}$ within 1 %, and the estimation of the other main backgrounds does not rely on simulated jets. Therefore, the values from $t\bar{t}$ can be used for all events with simulated jets without loss of accuracy. The per-event correction factor is—by construction—close to 1 on average in inclusive samples. The RMS is 4.1 % in $bb\phi, m_\phi = 120\,\mathrm{GeV}$ events, while it is substantially larger in $t\bar{t}$ events (11.4 %) because of the larger jet multiplicities.

6.1.5. Overlap removal

As the various types of physics objects are reconstructed independently, electrons, muons, and jets may overlap geometrically[13]. If the opening angle between two objects (ΔR) is smaller than 0.2, only one object is accepted, following the prioritization (in descending order):

1. muon candidates,
2. electron candidates, and
3. jets.

This order has been chosen to reflect the good rejection against electrons and jets in reconstructed muons and the fact that electrons are also valid seeds for jet finding. Note that lepton isolation requirements are taken into account along with the other quality criteria. As a consequence, a jet with an overlapping muon will be considered a jet in an "isolated" sample because the muon fails the isolation cut. On the other hand, it will be considered a muon in an "anti-isolated" sample because of the above prioritization.

[12] distinguishing b-, c-, and light jets

[13] This includes the possibility that objects of the same type overlap, though lepton isolation and electron quality cuts reject the majority of such candidates.

6.1.6. Missing Transverse Energy

The transverse energy sum ($\sum E_{\mathrm{T}}$) and the missing transverse energy vector are reconstructed from all mutually exclusive objects in the event [206]:

- muon candidates with $|\eta_\mu| < 2.7$, including candidates which are reconstructed only from the Inner Detector (to compensate insensitive areas in the Muon Spectrometer, which are occupied by detector support structures and cables),
- electron candidates, following the calibration scheme outlined in Ref. [136],
- photon candidates at the electromagnetic scale,
- τ lepton candidates, using the local hadronic calibration (LCW) [207],
- jets, using the LCW scheme for transverse momentum values in the range $10\,\mathrm{GeV} < p_{\mathrm{T,jet}} < 20\,\mathrm{GeV}$ and the LCW scheme in conjunction with the jet energy scale (JES) calibration above 20 GeV [207],
- tracks not associated to another object, and
- calorimeter topoclusters with $|\eta_{\mathrm{cluster}}| < 4.9$ that are not associated to any jet or lepton candidate, using the LCW calibration.

In events without non-interacting final-state particles, the x- and y-components of the vectorial sum of the above contributions should vanish (within the uncertainties) because of momentum balance. The x- and y-components of the missing transverse energy vector are therefore introduced to absorb any imbalance:

$$0 \equiv \sum_{\text{contribution } i} E_{x/y,i} + E^{\mathrm{miss}}_{\mathrm{T},x/y}. \tag{6.5}$$

In case that the missing transverse energy $E^{\mathrm{miss}}_{\mathrm{T}} = \sqrt{\left(E^{\mathrm{miss}}_{\mathrm{T},x}\right)^2 + \left(E^{\mathrm{miss}}_{\mathrm{T},x}\right)^2}$ is significantly larger than zero, it is attributed to non-interacting particles escaping the detector.

6.2. Event Selection

The event selection consists of the preselection of a sample with an electron and a muon candidate and the subsequent application of kinematic cuts to improve the sensitivity of the search for the signal processes in a b-tagged and a b-vetoed sample.

6.2.1. Preselection

The data streams dedicated to events with muons and events either electrons or photons as a part of their trigger signature are filtered by application of a *Good Runs List*, which removes events that were recorded during times of degraded detector performance and leaves a dataset corresponding to an integrated luminosity of $(4.66 \pm 0.18)\,\mathrm{fb}^{-1}$.

Reconstructed events from good runs are then checked for the presence of at least one good vertex with at least three associated Inner Detector tracks. All jets with transverse momenta above 20 GeV that do not overlap with a preselected electron or muon are required to pass the `looser bad` set of quality cuts defined in Ref. [208]. These cuts remove events with calorimeter clusters of bad accuracy from the hadronic endcap calorimeter, from coherent noise in the

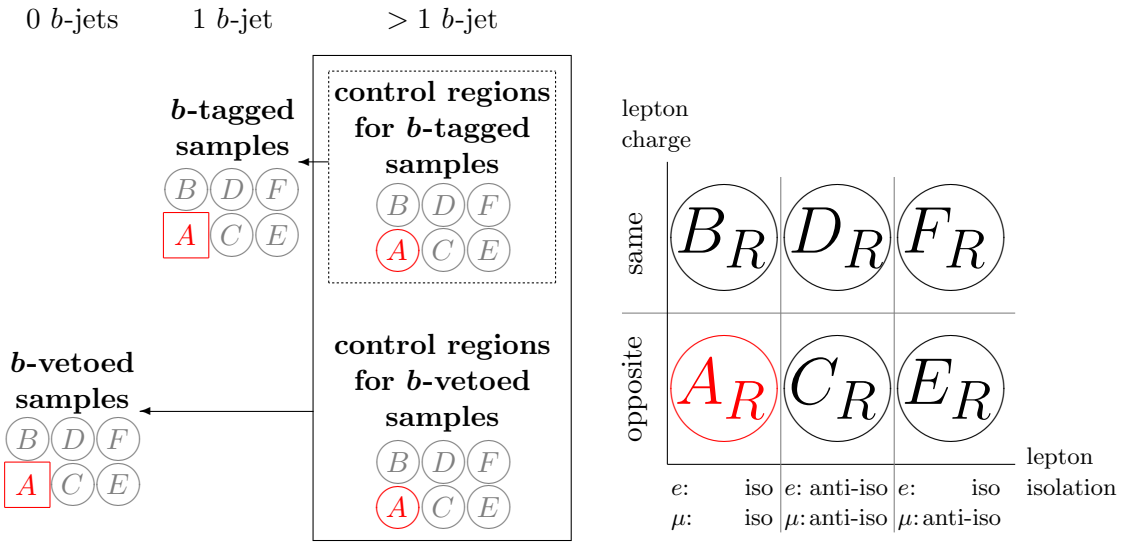

(a) Jet binning of the 24 signal and control regions.

(b) Multi-jet background estimation for a region (R) with the $ABCD$ method.

Figure 6.5.: Signal A and control regions used within this thesis (left). The control regions for multi-jet backgrounds are illustrated on the right.

electromagnetic calorimeter as well as backgrounds from non-collision backgrounds, such as cosmic rays.

In data-taking periods E–H, a tolerable defect of several front-end boards affected the read-out of a part of the liquid-argon calorimeter. This defect has been reproduced in simulation, so its effects are accurately modeled. However, in case of significant energy deposits in the affected region—which can be detected by the functional calorimeter parts that surround the defect—the energy measurement of the associated object and the overall $E_{\mathrm{T}}^{\mathrm{miss}}$ measurement would be degraded to an unacceptable extent. Consequently, such events from data-taking periods E–H are rejected if they contain at least one jet with a p_{T} value[14] of more than 20 GeV and with the reconstructed jet axis in the affected region ($-0.2 < \eta < 1.65$ and $-0.988 < \phi < -0.392$). Events with electron candidates ($p_{\mathrm{T}} > 15$ GeV) in a smaller region[15] ($-0.1 < \eta < 1.55$ and $-0.888 < \phi < -0.492$) are also rejected [208]. The object quality cuts and overlap removal procedure are not applied to these electron candidates in the veto decision.

Only events with exactly one electron (satisfying the criteria in Subsection 6.1.2) and one muon (satisfying the criteria in Subsection 6.1.1) whose invariant mass ($m_{e\mu}$) must be at least 30 GeV (see Section 5.2) are taken into account, so $Z/\gamma^* \to \ell\ell$ and W+jets events are strongly suppressed. Events are then split into signal and control regions, according to the properties of the leptons (isolation variables and relative charge) and b-jet content (see Figure 6.5): Events without tagged b-jets with $p_{\mathrm{T}} > 20$ GeV enter the b-vetoed sample. Exactly one b-tagged jet is required in the b-tagged sample. Events with two or more b-tagged jets are collected in control samples to estimate the contribution by $t\bar{t}$ events. Each of these samples is sub-divided into six regions (R) to estimate the contribution from multi-jet events:

[14] after approximate correction for the impact of the defect
[15] The lateral energy deposition profile of electrons is generally smaller than that of jets.

$\boldsymbol{A_R}$ Events with exactly one isolated electron and exactly one isolated muon of opposite electric charge enter the signal regions (A_R with zero or one b-jet(s)) and the $t\bar{t}$ control regions (A_R with two b-jets).

$\boldsymbol{B_R}$ Events with exactly one isolated electron and exactly one isolated muon of *the same* electric charge enter regions B_R.

$\boldsymbol{C_R}$ Events with exactly one *anti-isolated* electron and exactly one *anti-isolated* muon of opposite electric charge enter regions C_R.

$\boldsymbol{D_R}$ Events with exactly one *anti-isolated* electron and exactly one *anti-isolated* muon of *the same* electric charge enter regions D_R.

$\boldsymbol{E_R}$ Events with exactly one isolated electron and exactly one *anti-isolated* muon of opposite electric charge enter regions E_R.

$\boldsymbol{F_R}$ Events with exactly one isolated electron and exactly one *anti-isolated* muon of *the same* electric charge enter regions F_R.

The background estimation techniques that use the above control regions are described in Subsections 7.1.2 and 7.1.3. The efficiencies for the preselection of regions A_R are summarized in Table 6.5 for all signal datasets along with the fractions of preselected events entering the b-vetoed, b-tagged, and $t\bar{t}$ control samples. The fact that at most 14 % of $bb\phi$ events enter the b-tagged sample is a consequence of the soft b-jet spectrum (see Section 5.2).

6.2.2. Selection of b-Tagged Sample

As illustrated in Section 5.2 and Table 6.5, the requirement of exactly one b-tagged jet focuses sensitivity on the production of Higgs bosons in association with b-quarks. It leads to a background composed of 92 % events with t-quarks and 5 % events with Z boson decays at the preselection stage, evaluated with the background estimation techniques detailed in Chapter 7. As shown in Figures 5.2 and 5.3, the shapes of kinematic distributions (taken from simulation) after the preselection and b-jet requirement differ significantly between signal and electroweak background events. The resulting prediction, based on the background estimation techniques detailed in Chapter 7, is compared to the observation from collision data in Figures 6.6 and 6.7(a). The background contributions can be reduced by imposing a set of requirements, which optimize the sensitivity of the analysis (see Section 5.2):

The scalar sum of lepton transverse momenta and missing transverse energy can greatly reduce the contributions from events with t-quarks and di-bosons (see Figure 6.7(a)).

$$E_{\mathrm{T}}^{\mathrm{miss}} + p_{\mathrm{T},e} + p_{\mathrm{T},\mu} < 125\,\mathrm{GeV}$$

The large mass and the soft transverse momentum spectrum of Higgs bosons can be exploited to suppress events in which the ancestors of the final-state leptons have high transverse momenta and low invariant masses by selecting a back–to–back topology of the leptons (see Figure 6.7(b)).

$$\Delta\phi_{e\mu} > 2$$

Table 6.5.: Preselection efficiencies of the b-tagged and b-vetoed samples with isolated leptons for all signal datasets. The efficiency of the di-lepton requirement ($\varepsilon_{\text{presel.}}$) refers to the complete datasets (with the `2LepEF` requirement applied), while the other columns also take the `2LepEF` filter efficiency ($\varepsilon_{\texttt{2LepEF}}$) into account. The last three columns give the fractions of the preselected events entering the b-vetoed ($\varepsilon_{0\,b\text{-tags}}$), b-tagged ($\varepsilon_{1\,b\text{-tag}}$), and $t\bar{t}$ control samples ($\varepsilon_{>1\,b\text{-tags}}$).

	m_ϕ	$\varepsilon_{\text{presel.}}$	$\varepsilon_{\texttt{2LepEF}} \cdot \varepsilon_{\text{presel.}}$	Number of tagged b-jets		
	[GeV]	[10^{-3}]	[10^{-3}]	$\varepsilon_{0\,b\text{-tags}}$ [%]	$\varepsilon_{1\,b\text{-tag}}$ [%]	$\varepsilon_{>1\,b\text{-tags}}$ [%]
$bb\phi$	90	73.5	28.3	91.2	8.4	0.4
	100	85.9	36.5	90.8	8.8	0.4
	110	95.1	43.8	89.9	9.6	0.5
	120	107	52.8	90.2	9.3	0.5
	130	116	60.5	89.6	9.7	0.7
	140	124	67.5	89.2	10.2	0.6
	150	134	76.3	88.6	10.8	0.6
	170	144	87.6	87.7	11.4	0.8
	200	168	110	86.7	12.4	0.9
	250	134	no `2LepEF`	85.2	13.8	1.1
	300	154	no `2LepEF`	84.7	14.3	1.1
$gg \to \phi$	90	23.5	no `2LepEF`	98.3	1.6	0.1
	100	32.9	no `2LepEF`	98.1	1.8	0.1
	110	41.3	no `2LepEF`	97.1	2.6	0.2
	120	46.7	no `2LepEF`	97.0	2.9	0.1
	130	53.2	no `2LepEF`	96.5	3.3	0.1
	140	61.4	no `2LepEF`	96.5	3.4	0.1
	150	68.0	no `2LepEF`	96.7	3.2	0.1
	170	82.3	no `2LepEF`	97.0	2.9	0.1
	200	99.3	no `2LepEF`	96.8	3.0	0.2
	250	121	no `2LepEF`	96.0	3.7	0.3
	300	141	no `2LepEF`	96.0	3.7	0.3

The directions of the missing transverse energy vector and the lepton momenta in backgrounds involving t-quark production show no clear correlation. A combination of the transverse opening angles between the lepton directions and the direction of missing transverse energy can therefore be used to enhance events with $E_{\text{T}}^{\text{miss}}$ from di-τ decays by exploiting the flat distribution for such backgrounds (see Figure 6.7(c)).

$$\sum_{\ell=e,\mu} \cos \Delta\phi_{E_{\text{T}}^{\text{miss}},\ell} > -0.2$$

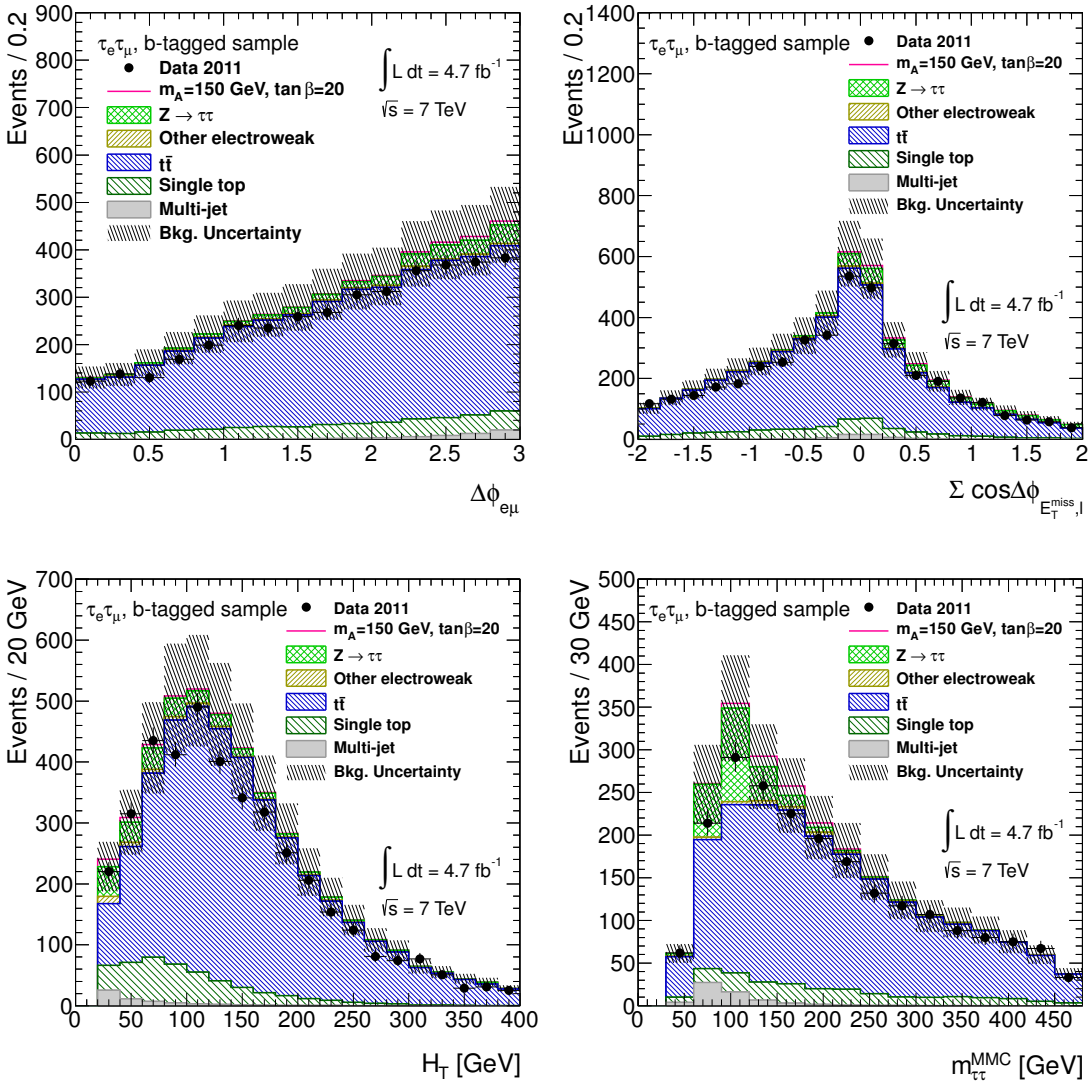

Figure 6.6.: Selection variables after the preselection of the b-tagged sample.

The scalar jet E_{T} sum exploits the higher mean jet multiplicity and harder spectrum of jets from background processes such as t-quark production (see Figure 6.7(d)).

$H_{\mathrm{T}} < 100\,\mathrm{GeV}$

The successful $m_{\tau\tau}$ reconstruction by the missing mass calculator (MMC) is required, which rejects configurations that are very unlikely for di-τ decays and is very efficient for signal events (failing in fewer than 1 % of the selected events for all signal hypotheses, see Table 5.1).

$m_{\tau\tau}^{\mathrm{MMC}}$ reconstructible

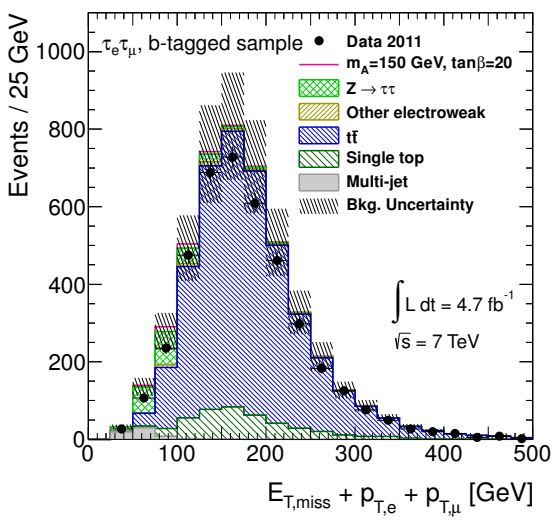

(a) $E_{\mathrm{T}}^{\mathrm{miss}} + p_{\mathrm{T},e} + p_{\mathrm{T},\mu}$ distribution after the requirement of exactly one b-tagged jet

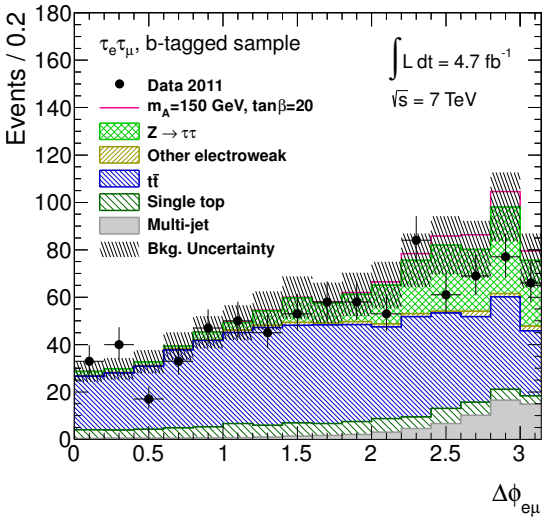

(b) $\Delta\phi_{e\mu}$ distribution after the $E_{\mathrm{T}}^{\mathrm{miss}} + p_{\mathrm{T},e} + p_{\mathrm{T},\mu}$ cut

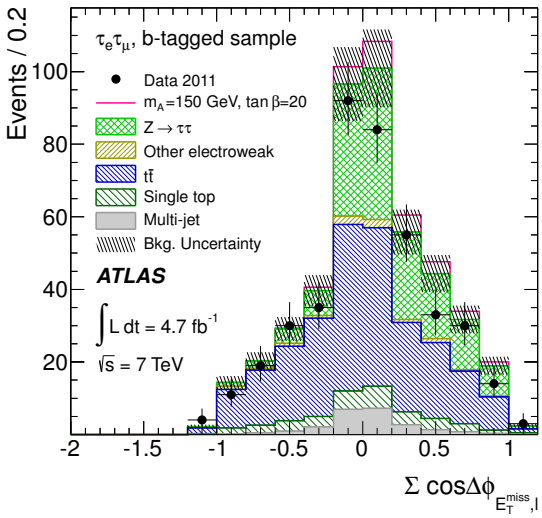

(c) $\sum_{\ell=e,\mu} \cos\Delta\phi_{E_{\mathrm{T}}^{\mathrm{miss}},\ell}$ distribution after the $\Delta\phi_{e\mu}$ cut

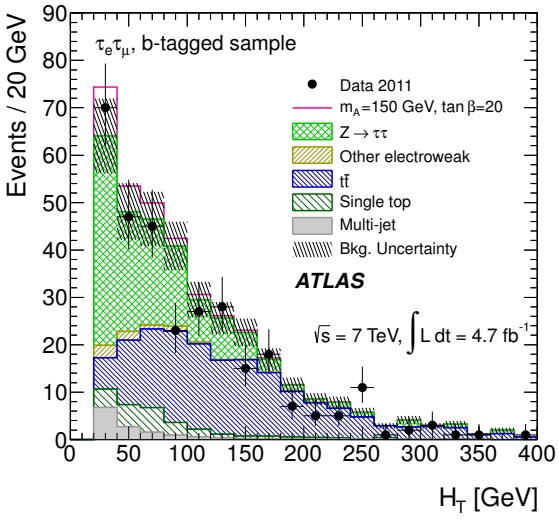

(d) H_{T} distribution after the $\sum_{\ell=e,\mu} \cos\Delta\phi_{E_{\mathrm{T}}^{\mathrm{miss}},\ell}$ cut

Figure 6.7.: Selection variables of the b-tagged sample.

The distributions of the selection variables are shown in Figures 6.7 and 6.8, using the background estimation techniques described in Chapter 7. The $m_{h^0}^{\mathrm{max}}$ scenario is used in these Figures with the tree-level parameter choice $m_{A^0} = 150\,\mathrm{GeV}$, $\tan\beta = 20$ for illustration. The MMC mass ($m_{\tau\tau}^{\mathrm{MMC}}$) is shown in Figure 6.8 along with the statistical and systematic uncertainties. The expected event yields with their statistical and systematic uncertainties (discussed in depth in Chapter 8) are summarized in Table 6.6. While t-quark production dominates the b-tagged sample after the preselection, its contributions ($t\bar{t}$ and single t-quark production) can be strongly suppressed, so $Z/\gamma^* \to \tau\tau$ events contribute about half the total background after the complete kinematic selection.

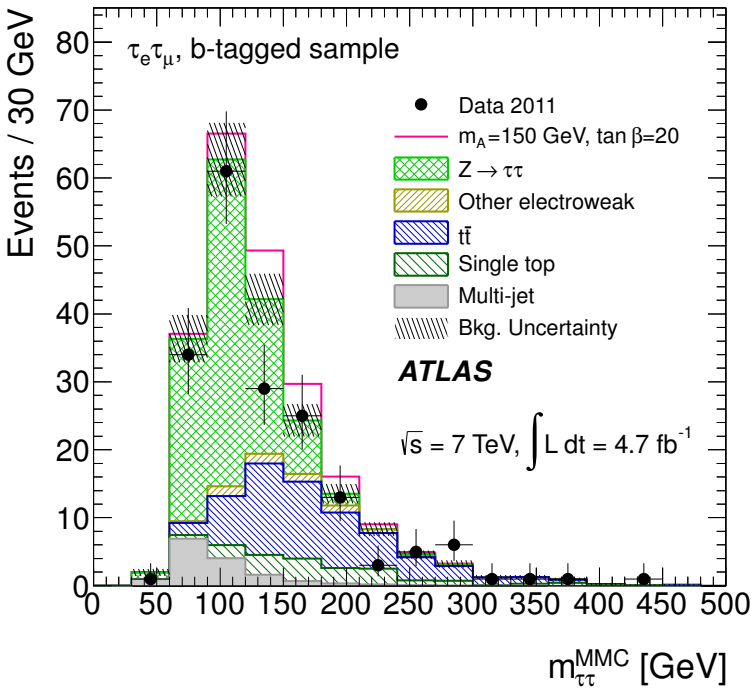

Figure 6.8.: $m_{\tau\tau}^{\mathrm{MMC}}$ distribution of the b-tagged sample after all selection cuts.

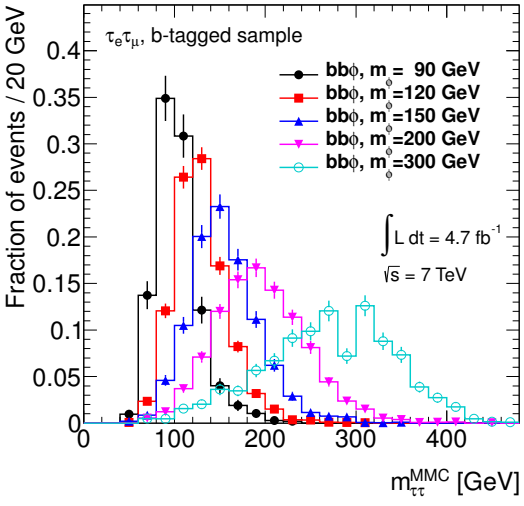

Figure 6.9.: $m_{\tau\tau}^{\mathrm{MMC}}$ distributions after all selection cuts for neutral Higgs bosons produced in association with b-quarks.

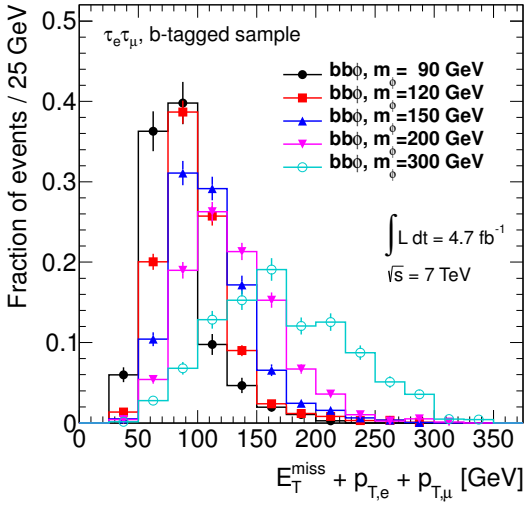

Figure 6.10.: $E_{\mathrm{T}}^{\mathrm{miss}} + p_{\mathrm{T},e} + p_{\mathrm{T},\mu}$ distributions after the requirement of exactly one b-tagged jet for neutral Higgs bosons produced in association with b-quarks.

Table 6.6.: Data event count and estimation of the sample composition (b-tagged sample) after each selection cut (format: central value ± statistical error ± systematic error). The statistical error reflects the event count and event weights of the respective dataset from which the distributions of kinematic variables are taken as well as auxiliary datasets used for normalization. All systematic uncertainties discussed in Chapter 8 are included. The percentages of all preselected $e^{\pm}\mu^{\mp}$ events entering the b-tagged sample is given in parentheses in red. The individual cut efficiencies per process are also given as percentages in parentheses in red, while the total selection efficiencies with respect to to preselected $e^{\pm}\mu^{\mp}$ events with exactly one b-jet are given as percentages in parentheses in green. For the signal processes, the $m_{h^0}^{\text{max}}$ scenario and $m_{A^0} = 150\,\text{GeV}$, $\tan\beta = 20$ have been assumed.

Selection step	Expected Event Yield										Data
	$bb\phi$	$gg \to \phi$	$Z/\gamma^* \to \tau\tau$	$t\bar{t}$	Single t	Di-Boson	$Z \to \ell\ell$	W + jets	Multi-Jet	ΣBG	
Preselection $e^{\pm}\mu^{\mp}$	310 $\pm 3^{+70}_{-74}$	164 $\pm 3^{+36}_{-34}$	11623 $\pm 64 \pm 1052$	8107 $\pm 161^{+1336}_{-1246}$	779 $\pm 9 \pm 108$	1858 $\pm 8 \pm 158$	252 $\pm 13 \pm 21$	285 $\pm 32^{+20}_{-22}$	1474 $\pm 93 \pm 336$	24379 $\pm 200^{+1744}_{-1676}$	24068
Exactly one b-jet	33.2 $\pm 0.9^{+8.3}_{-8.9}$ (10.7)	5.3 $\pm 0.5^{+1.2}_{-1.1}$ (3.2)	243 $\pm 8^{+30}_{-24}$ (2.1)	3814 $\pm 76^{+819}_{-801}$ (47.0)	428 $\pm 6^{+63}_{-62}$ (54.9)	34 $\pm 1 \pm 5$ (1.9)	3.0 $\pm 1.3^{+0.7}_{-0.4}$ (1.2)	7.5 $\pm 2.2^{+1.0}_{-0.9}$ (2.6)	61 $\pm 16 \pm 14$ (4.1)	4591 $\pm 79^{+822}_{-804}$ (18.8)	4148 (17.2)
$E_{\text{T}}^{\text{miss}} + p_{\text{T},e} + p_{\text{T},\mu}$ $< 125\,\text{GeV}$	23.8 $\pm 0.8^{+6.0}_{-6.4}$ (71.6)	3.1 $\pm 0.4 \pm 0.7$ (59.3)	204 $\pm 7^{+20}_{-22}$ (84.1)	637 $\pm 31^{+124}_{-120}$ (16.7)	78 $\pm 3^{+11}_{-12}$ (18.2)	11.9 $\pm 0.7^{+1.6}_{-1.8}$ (34.6)	1.6 $\pm 0.9 \pm 0.2$ (52.8)	2.5 $\pm 1.1^{+1.7}_{-0.3}$ (33.7)	50 $\pm 13 \pm 11$ (82.4)	986 $\pm 35^{+126}_{-123}$ (21.5)	844 (20.3)
$\Delta\phi_{e\mu} > 2$	22.0 $\pm 0.7^{+5.6}_{-5.9}$ (92.3/66.1)	2.8 $\pm 0.4 \pm 0.6$ (89.4/53)	157 $\pm 6 \pm 15$ (76.8/64.6)	235 $\pm 19^{+46}_{-44}$ (36.9/6.2)	31 $\pm 2 \pm 5$ (39.7/7.2)	7.5 $\pm 0.5 \pm 1.1$ (63.4/21.9)	1.1 $\pm 0.8^{+0.2}_{-0.1}$ (68.3/36.0)	1.6 $\pm 0.9^{+1.6}_{-0.2}$ (62.6/21.1)	23 $\pm 10 \pm 5$ (46.2/38.0)	456 $\pm 22^{+49}_{-47}$ (46.3/9.9)	410 (48.6/9.9)
$\sum_{\ell=e,\mu} \cos\Delta\phi_{E_{\text{T}}^{\text{miss}},\ell}$ > -0.2	20.8 $\pm 0.7^{+5.3}_{-5.5}$ (94.7/62.6)	2.7 $\pm 0.4 \pm 0.6$ (95.3/50.5)	143 $\pm 6 \pm 14$ (91.3/58.9)	163 $\pm 16^{+35}_{-34}$ (69.6/4.3)	21 $\pm 1^{+3}_{-4}$ (68.7/5.0)	4.9 $\pm 0.4 \pm 0.7$ (65.2/14.3)	1.1 $\pm 0.8^{+0.2}_{-0.1}$ (100/36.0)	1.2 $\pm 0.8^{+1.6}_{-0.2}$ (74.3/15.7)	14 $\pm 9 \pm 2$ (59.6/22.7)	349 $\pm 20^{+38}_{-37}$ (76.5/7.6)	311 (75.9/7.5)
$H_{\text{T}} < 100\,\text{GeV}$	18.4 $\pm 0.7^{+4.8}_{-4.9}$ (88.5/55.4)	2.3 $\pm 0.4 \pm 0.5$ (86.7/43.8)	109 $\pm 5^{+12}_{-11}$ (75.9/44.7)	57 $\pm 6^{+10}_{-7}$ (35/1.5)	16.3 $\pm 1.2^{+2.5}_{-3.8}$ (76.8/3.8)	4.1 $\pm 0.4 \pm 0.6$ (82.5/11.8)	1.1 $\pm 0.8^{+0.2}_{-0.1}$ (100/36.0)	1.2 $\pm 0.8^{+0.7}_{-0.2}$ (100/15.7)	15 $\pm 9 \pm 4$ (106.2/24.1)	203 $\pm 12^{+16}_{-14}$ (58.2/4.4)	185 (59.5/4.5)
$m_{\tau\tau}^{\text{MMC}}$ reconstructible	18.4 $\pm 0.7^{+4.4}_{-4.7}$ (100/55.4)	2.3 $\pm 0.4^{+0.6}_{-0.5}$ (100/43.8)	109 $\pm 5^{+12}_{-11}$ (100/44.7)	56 $\pm 6^{+9}_{-7}$ (97.4/1.5)	15.7 $\pm 1.2^{+2.4}_{-3.9}$ (95.8/3.7)	3.9 $\pm 0.4 \pm 0.6$ (96.3/11.3)	1.1 $\pm 0.8^{+0.2}_{-0.1}$ (100/36.0)	1.2 $\pm 0.8^{+0.7}_{-0.2}$ (100/15.7)	15 $\pm 9 \pm 4$ (99.9/24.1)	201 $\pm 12^{+15}_{-14}$ (98.9/4.4)	181 (97.8/4.4)

Table 6.7.: Total selection efficiencies of the b-tagged sample for all signal datasets. Values are given after the requirement of exactly one b-tagged jet ($\varepsilon_{b\text{-tag presel.}} = \varepsilon_{\texttt{2LepEF}} \cdot \varepsilon_{\text{presel.}} \cdot \varepsilon_{1\,b\text{-tag}}$, using the values from Table 6.5) and after the application of all topological cuts ($\varepsilon_{b\text{-tag sel.}} = \varepsilon_{b\text{-tag presel.}} \cdot \varepsilon_{b\text{-tag kin. sel.}}$). The impact of the relative efficiency of the $E_{\mathrm{T}}^{\mathrm{miss}} + p_{\mathrm{T},e} + p_{\mathrm{T},\mu}$ cut ($\varepsilon_{E_{\mathrm{T}}^{\mathrm{miss}}+p_{\mathrm{T},e}+p_{\mathrm{T},\mu}}$) on $\varepsilon_{b\text{-tag kin. sel.}}$ is shown in the final three columns.

	m_ϕ [GeV]	$\varepsilon_{b\text{-tag presel.}}$ [10^{-3}]	$\varepsilon_{b\text{-tag sel.}}$ [10^{-3}]	$\varepsilon_{b\text{-tag kin. sel.}}$ [%]	$\varepsilon_{E_{\mathrm{T}}^{\mathrm{miss}}+p_{\mathrm{T},e}+p_{\mathrm{T},\mu}}$ [%]	$\frac{\varepsilon_{b\text{-tag kin. sel.}}}{\varepsilon_{E_{\mathrm{T}}^{\mathrm{miss}}+p_{\mathrm{T},e}+p_{\mathrm{T},\mu}}}$ [%]
$bb\phi$	90	2.4	1.4	57	92	63
	100	3.2	2.0	63	91	69
	110	4.2	2.6	61	88	69
	120	4.9	3.1	63	86	73
	130	5.9	3.7	64	82	77
	140	6.9	4.1	60	78	77
	150	8.2	4.5	55	71	77
	170	10.0	5.3	53	63	84
	200	13.7	5.7	42	51	81
	250	18.5	4.4	24	29	83
	300	22.0	3.9	18	23	79
$gg \to \phi$	90	0.4	0.1	30	57	53
	100	0.6	0.2	40	62	63
	110	1.1	0.4	38	69	54
	120	1.4	0.5	37	57	65
	130	1.8	0.8	43	61	70
	140	2.1	1.0	50	72	70
	150	2.2	1.0	44	59	75
	170	2.4	1.0	42	52	81
	200	3.0	1.0	35	43	82
	250	4.4	0.9	21	24	86
	300	5.2	0.4	9	14	60

Besides the MMC mass (see Figure 6.9), the shape of the $E_{\mathrm{T}}^{\mathrm{miss}} + p_{\mathrm{T},e} + p_{\mathrm{T},\mu}$ distribution also shows a strong correlation with the Higgs boson mass hypothesis (see Figure 6.10). The $E_{\mathrm{T}}^{\mathrm{miss}} + p_{\mathrm{T},e} + p_{\mathrm{T},\mu}$ cut drives the dependence of the selection efficiency on the Higgs boson mass hypothesis (see Table 6.7). However, the $E_{\mathrm{T}}^{\mathrm{miss}} + p_{\mathrm{T},e} + p_{\mathrm{T},\mu}$ cut is crucial for the sensitivity for $m_\phi \approx 120\,\mathrm{GeV}$.

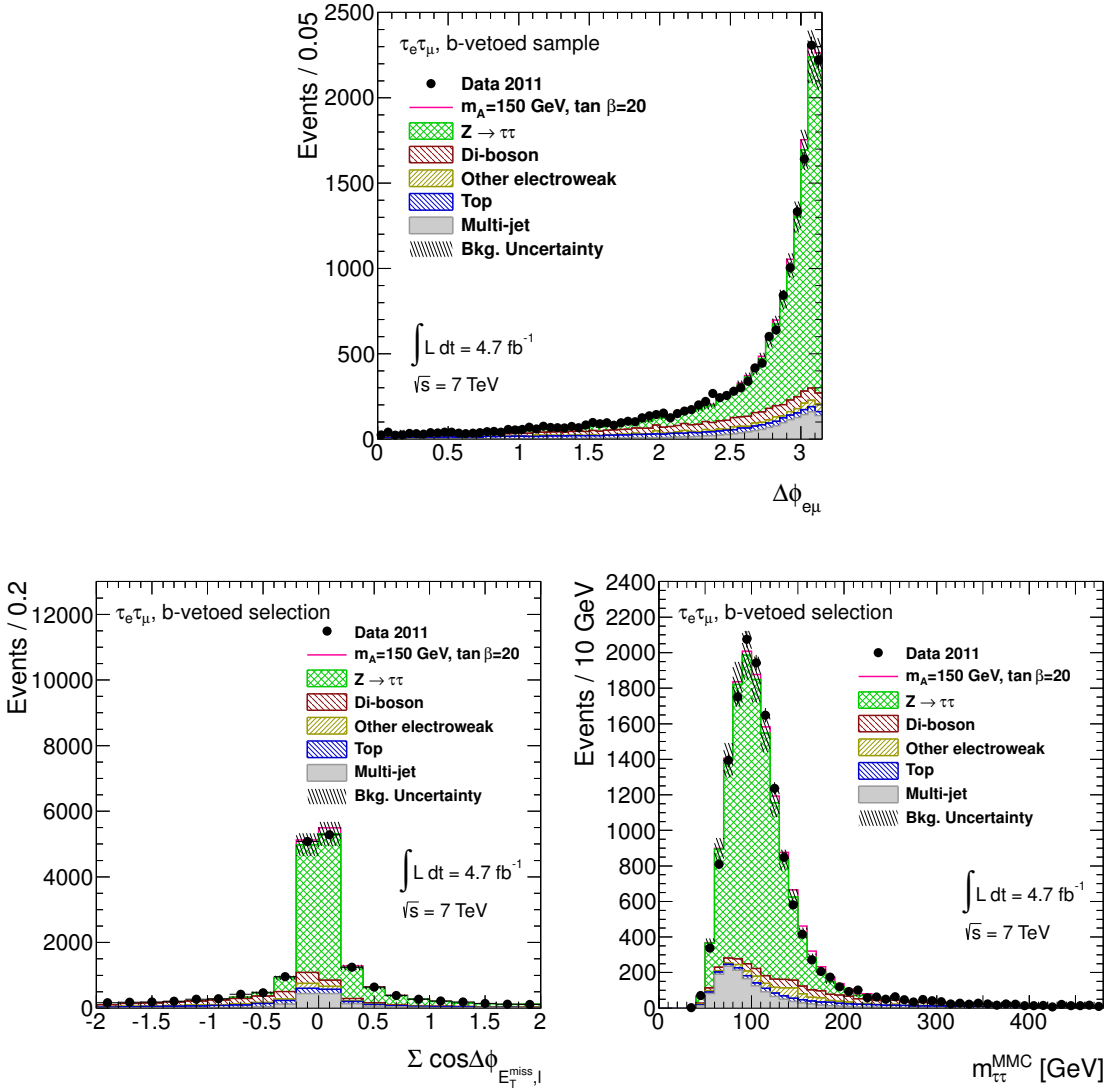

Figure 6.11.: Selection variables after the preselection of the b-vetoed sample.

6.2.3. Selection of b-Vetoed Sample

In contrast to the b-tagged sample, $Z/\gamma^* \to \tau\tau$ decays dominate the background composition already after requiring the absence of b-jets (about 68 % of the expected background). As shown in Figures 5.2 and 5.3, the kinematic variables (taken from simulation) at this stage are distributed similarly for signal and electroweak background events. The resulting prediction, based on the background estimation techniques detailed in Chapter 7, is compared to the observation from collision data in Figures 6.11 and 6.12(a). Because of this similarity in shape, only a small improvement of the signal–to–background ratio is possible in this sample by applying kinematic cuts, which optimize the sensitivity of the analysis (see Section 5.2):

A cut on the scalar sum of lepton transverse momenta and missing transverse energy is performed to reduce contributions from events with t-quarks and di-bosons (see Figure 6.12(a)).

$$E_{\mathrm{T}}^{\mathrm{miss}} + p_{\mathrm{T},e} + p_{\mathrm{T},\mu} < 150\,\mathrm{GeV}$$

The large mass and the soft transverse momentum spectrum of Higgs bosons can be exploited to suppress events in which the ancestors of the final-state leptons have high transverse momenta and low invariant masses by selecting a back–to–back topology of the leptons (see Figure 6.12(b)).

$$\Delta\phi_{e\mu} > 1.6$$

A cut on a combination of the transverse opening angles between the lepton directions and the direction of missing transverse energy can be used to enhance events with $E_{\mathrm{T}}^{\mathrm{miss}}$ from di-τ decays by exploiting the flat distribution in di-boson events (see Figure 6.12(c)).

$$\sum_{\ell=e,\mu} \cos\Delta\phi_{E_{\mathrm{T}}^{\mathrm{miss}},\ell} > -0.4$$

The successful $m_{\tau\tau}$ reconstruction by the MMC is required, which rejects configurations that are very unlikely for di-τ decays and is very efficient for signal events (failing in fewer than 1 % of the selected events for all signal hypotheses, see Table 5.1).

$$m_{\tau\tau}^{\mathrm{MMC}} \text{ reconstructible}$$

The distributions of the selection variables are shown in Figures 6.12 and 6.13, using the background estimation techniques described in Chapter 7. The $m_{h^0}^{\mathrm{max}}$ scenario is used in these Figures with the tree-level parameter choice $m_{A^0} = 150\,\mathrm{GeV}$, $\tan\beta = 20$ for illustration. The MMC mass ($m_{\tau\tau}^{\mathrm{MMC}}$) is shown in Figure 6.13 along with the statistical and systematic uncertainties. The expected event yields with their statistical and systematic uncertainties (discussed in depth in Chapter 8) are summarized in Table 6.8[16]. Because the irreducible $Z/\gamma^* \to \tau\tau$ contribution remains the dominant background throughout the selection, the optimization yielded a softer set of cuts than for the b-tagged sample. While the efficiency of the kinematic selection ranges from $42 - 57\,\%$ for $bb\phi, m_\phi = 90 - 200\,\mathrm{GeV}$ in the b-tagged sample (see Table 6.7), signal events from b-associated production and gluon fusion with $m_\phi = 90 - 200\,\mathrm{GeV}$ are selected with efficiencies between 77 and 95 % here (see Table 6.9).

As in the b-tagged sample, the MMC mass (see Figure 6.14) and the shape of the $E_{\mathrm{T}}^{\mathrm{miss}} + p_{\mathrm{T},e} + p_{\mathrm{T},\mu}$ distribution (see Figure 6.15) show a strong correlation with the Higgs boson mass hypothesis. The $E_{\mathrm{T}}^{\mathrm{miss}} + p_{\mathrm{T},e} + p_{\mathrm{T},\mu}$ cut drives the dependence of the selection efficiency on the Higgs boson mass hypothesis (see Table 6.9) and plays an important role in the reduction of the t-quark- and the di-boson-induced background contributions[17].

[16] Note that the expected di-boson contributions are estimated from different simulated datasets in the b-tagged (Table 6.6) and b-vetoed samples (Table 6.8). The two predictions agree within one standard deviation.

[17] Note that the optimized selection of the b-vetoed sample does not contain a cut on H_{T}.

Table 6.8.: Data event count and estimation of the sample composition (b-vetoed sample) after each selection cut (format: central value ± statistical error ± systematic error). The statistical error reflects the event count and event weights of the respective dataset from which the distributions of kinematic variables are taken as well as auxiliary datasets used for normalization. All systematic uncertainties discussed in Chapter 8 are included. The percentages of all preselected $e^{\pm}\mu^{\mp}$ events entering the b-vetoed sample is given in parentheses in red. The individual cut efficiencies per process are also given as percentages in parentheses in red, while the total selection efficiencies with respect to to preselected $e^{\pm}\mu^{\mp}$ events without b-jets are given as percentages in parentheses in green. For the signal processes, the $m_{h^0}^{\text{max}}$ scenario and $m_{A^0} = 150\,\text{GeV}$, $\tan\beta = 20$ have been assumed.

Selection step	Expected Event Yield										Data
	$bb\phi$	$gg \to \phi$	$Z/\gamma^* \to \tau\tau$	$t\bar{t}$	Single t	Di-Boson	$Z \to \ell\ell$	W + jets	Multi-Jet	ΣBG	
Preselection $e^{\pm}\mu^{\mp}$	310 $\pm 3^{+35}_{-44}$	164 $\pm 3^{+17}_{-16}$	11623 $\pm 64 \pm 1052$	8107 $\pm 158 \pm 689$	779 $\pm 9 \pm 98$	1968 $\pm 7 \pm 193$	252 $\pm 13 \pm 20$	285 $\pm 32 \pm 23$	1474 $\pm 93 \pm 336$	24488 $\pm 198 \pm 1315$	24068
No b-jets	275 $\pm 3^{+30}_{-37}$ (88.7)	159 $\pm 3^{+15}_{-14}$ (96.7)	11350 $\pm 63^{+1020}_{-1021}$ (97.6)	1292 $\pm 27^{+236}_{-235}$ (15.9)	274 $\pm 5 \pm 36$ (35.1)	1925 $\pm 7^{+199}_{-211}$ (97.8)	249 $\pm 13^{+23}_{-22}$ (98.8)	277 $\pm 32 \pm 25$ (97.4)	1411 $\pm 92 \pm 329$ (95.7)	16778 $\pm 120^{+1117}_{-1119}$ (68.5)	16816 (69.9)
$E_{\text{T}}^{\text{miss}} + p_{\text{T},e} + p_{\text{T},\mu}$ $< 150\,\text{GeV}$	269 $\pm 3^{+30}_{-37}$ (97.8)	147 $\pm 3^{+15}_{-14}$ (92.5)	11177 $\pm 63 \pm 1006$ (98.5)	453 $\pm 15^{+89}_{-87}$ (35.1)	102 $\pm 3 \pm 13$ (37.3)	1188 $\pm 6^{+124}_{-140}$ (61.7)	240 $\pm 13 \pm 22$ (96.1)	239 $\pm 31 \pm 22$ (86.0)	1328 $\pm 88 \pm 311$ (94.1)	14727 $\pm 114^{+1064}_{-1067}$ (87.8)	14974 (89.0)
$\Delta\phi_{e\mu} > 1.6$	267 $\pm 3^{+30}_{-37}$ (99.6/97.4)	144 $\pm 3^{+15}_{-14}$ (98.3/90.8)	10897 $\pm 62^{+981}_{-982}$ (97.5/96.0)	227 $\pm 11^{+46}_{-42}$ (50.1/17.6)	59 $\pm 2 \pm 8$ (58.4/21.7)	914 $\pm 5^{+95}_{-114}$ (76.9/47.5)	223 $\pm 13 \pm 20$ (93.1/89.4)	172 $\pm 25 \pm 16$ (72.1/62.0)	1163 $\pm 73 \pm 261$ (87.6/82.4)	13655 $\pm 100^{+1021}_{-1023}$ (92.7/81.4)	13938 (93.1/82.9)
$\sum_{\ell=e,\mu} \cos\Delta\phi_{E_{\text{T}}^{\text{miss}},\ell}$ > -0.4	266 $\pm 3^{+30}_{-37}$ (99.3/96.7)	143 $\pm 3^{+15}_{-14}$ (99.3/90.2)	10739 $\pm 61^{+967}_{-968}$ (98.6/94.6)	173 $\pm 10^{+42}_{-38}$ (76.2/13.4)	39.1 $\pm 1.9^{+5.2}_{-5.1}$ (65.7/14.3)	508 $\pm 4^{+53}_{-69}$ (55.6/26.4)	197 $\pm 12 \pm 18$ (88.3/78.9)	114 $\pm 20 \pm 10$ (66.3/41.1)	982 $\pm 61 \pm 224$ (84.4/69.6)	12752 $\pm 90^{+995}_{-997}$ (93.4/76.0)	13052 (93.6/77.6)
$m_{\tau\tau}^{\text{MMC}}$ reconstructible	265 $\pm 3^{+30}_{-37}$ (99.7/96.4)	143 $\pm 3^{+15}_{-14}$ (99.7/89.9)	10718 $\pm 61^{+965}_{-966}$ (99.8/94.4)	152 $\pm 9^{+43}_{-38}$ (87.9/11.8)	35.3 $\pm 1.8^{+4.7}_{-4.6}$ (90.3/12.9)	470 $\pm 4^{+49}_{-75}$ (92.5/24.4)	196 $\pm 12 \pm 18$ (99.5/78.5)	111 $\pm 20 \pm 10$ (97.8/40.2)	982 $\pm 60 \pm 225$ (100/69.6)	12664 $\pm 89^{+993}_{-996}$ (99.3/75.5)	12947 (99.2/77.0)

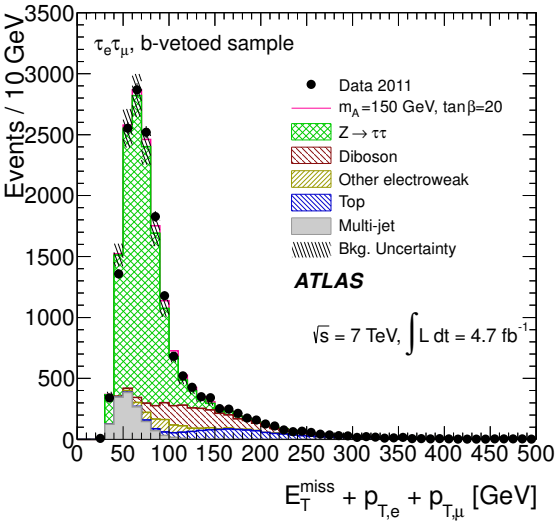

(a) $E_{\mathrm{T}}^{\mathrm{miss}} + p_{\mathrm{T},e} + p_{\mathrm{T},\mu}$ distribution after the veto on b-tagged jets

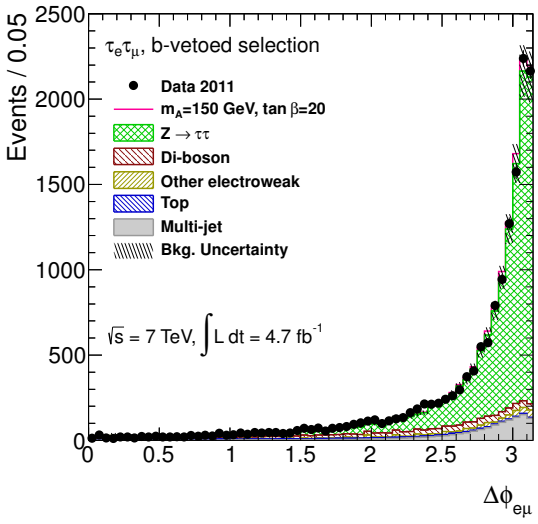

(b) $\Delta\phi_{e\mu}$ distribution after the $E_{\mathrm{T}}^{\mathrm{miss}} + p_{\mathrm{T},e} + p_{\mathrm{T},\mu}$ cut

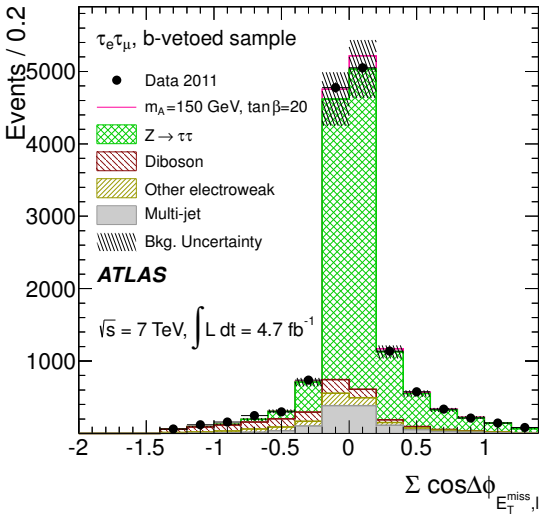

(c) $\sum_{\ell=e,\mu} \cos\Delta\phi_{E_{\mathrm{T}}^{\mathrm{miss}},\ell}$ distribution after the $\Delta\phi_{e\mu}$ cut

Figure 6.12.: Selection variables of the b-vetoed sample.

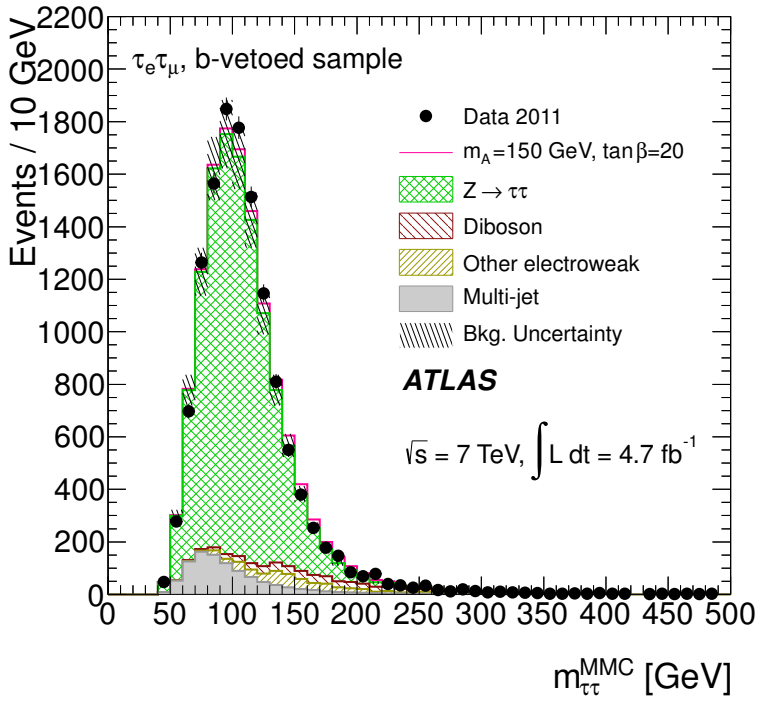

Figure 6.13.: $m_{\tau\tau}^{\mathrm{MMC}}$ distribution of the b-vetoed sample after selection cuts.

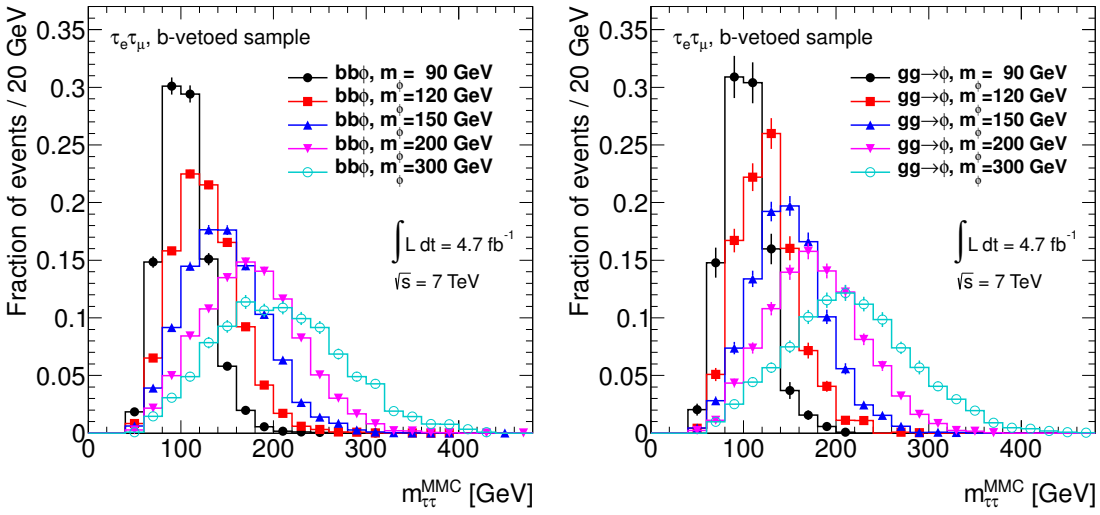

(a) b-associated production

(b) Production in gluon fusion

Figure 6.14.: $m_{\tau\tau}^{\mathrm{MMC}}$ distributions after all selection cuts for neutral Higgs bosons produced in association with b-quarks (left) and in gluon fusion (right).

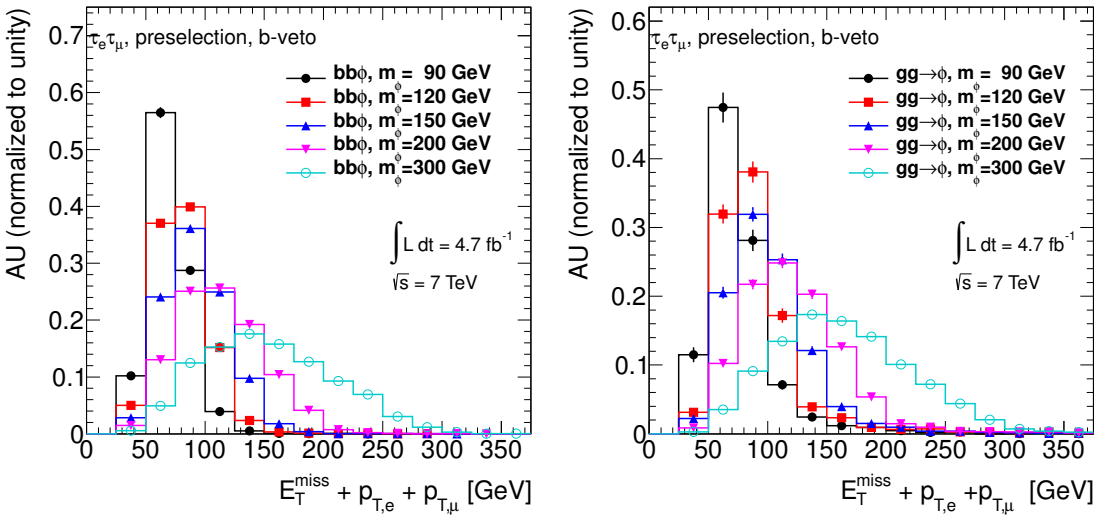

(a) b-associated production

(b) Production in gluon fusion

Figure 6.15.: $E_{\mathrm{T}}^{\mathrm{miss}} + p_{\mathrm{T},e} + p_{\mathrm{T},\mu}$ distributions after requiring the absence of b-tagged jets for neutral Higgs bosons produced in association with b-quarks (left) and in gluon fusion (right).

Table 6.9.: Total selection efficiencies of the b-vetoed sample for all signal datasets. Values are given after the b-jet veto ($\varepsilon_{b\text{-veto presel.}} = \varepsilon_{\texttt{2LepEF}} \cdot \varepsilon_{\text{presel.}} \cdot \varepsilon_{0\,b\text{-tags}}$, using the values from Table 6.5) and after the application of all topological cuts ($\varepsilon_{b\text{-veto sel.}} = \varepsilon_{b\text{-veto presel.}} \cdot \varepsilon_{b\text{-veto kin. sel.}}$). The impact of the relative efficiency of the $E_{\text{T}}^{\text{miss}} + p_{\text{T},e} + p_{\text{T},\mu}$ cut ($\varepsilon_{E_{\text{T}}^{\text{miss}}+p_{\text{T},e}+p_{\text{T},\mu}}$) on $\varepsilon_{b\text{-veto kin. sel.}}$ is shown in the final three columns.

	m_ϕ [GeV]	$\varepsilon_{b\text{-veto presel.}}$ [10^{-3}]	$\varepsilon_{b\text{-veto sel.}}$ [10^{-3}]	$\varepsilon_{b\text{-veto kin. sel.}}$ [%]	$\varepsilon_{E_{\text{T}}^{\text{miss}}+p_{\text{T},e}+p_{\text{T},\mu}}$ [%]	$\frac{\varepsilon_{b\text{-veto kin. sel.}}}{\varepsilon_{E_{\text{T}}^{\text{miss}}+p_{\text{T},e}+p_{\text{T},\mu}}}$ [%]
$bb\phi$	90	25.8	24.6	95	100	95
	100	33.2	31.8	96	100	96
	110	39.4	37.9	96	100	97
	120	47.6	46.3	97	99	98
	130	54.2	52.9	98	100	98
	140	60.2	58.5	97	99	98
	150	67.6	65.1	96	98	99
	170	76.8	71.2	93	94	99
	200	95.6	80.0	84	84	99
	250	115	74.7	65	66	99
	300	131	66.0	51	51	100
$gg \to \phi$	90	23.1	20.2	87	97	91
	100	32.3	29.0	90	96	93
	110	40.1	36.3	91	96	94
	120	45.4	41.3	91	94	97
	130	51.3	46.7	91	94	97
	140	59.3	53.9	91	94	97
	150	65.8	59.0	90	92	97
	170	79.8	69.2	87	88	98
	200	96.1	74.1	77	78	99
	250	116	66.8	57	58	99
	300	135	58.6	43	44	99

7 Background Estimation

The precise estimation of background contributions to the signal regions is crucial for the sensitivity and robustness of the analysis. Both the event yields and the shapes of the $m_{\tau\tau}^{\mathrm{MMC}}$ distributions have to be predicted at the lowest possible level of systematic uncertainty.

The main backgrounds are therefore estimated from data if possible (see Section 7.1), resulting in smaller systematic uncertainties than an estimation that is purely based on simulation. Other background contributions are sufficiently small, so the sensitivity of the analysis is hardly affected by the uncertainties introduced by the simulation of these processes (see Section 7.2).

7.1. Data-Driven Background Estimation Techniques

In order to reduce the level of systematic uncertainty within the background estimation, the $Z/\gamma^* \to \tau\tau$ background is estimated with the *embedding technique* [14] (see Subsection 7.1.1), which has been augmented for this thesis by the emulation of the lepton trigger. The cut efficiencies of all cuts after the preselection and the shape of all discriminating variables can thus be estimated from data.

The multi-jet background is estimated from sets of control regions with an extended *ABCD Method* (see Subsection 7.1.2), which enables the estimation of the event yields and the shape of the discriminating variables from data. The method employed within this thesis uses additional control regions to estimate systematic uncertainties from correlations on the event yield in the signal regions (as in Ref. [12]) and on the shape of the $m_{\tau\tau}^{\mathrm{MMC}}$ distributions.

The background contribution from t-quark pairs is estimated with a method developed for this thesis. It takes the event yield from control regions (see Subsection 7.1.3), while the shape of the discriminating variables is taken from simulation.

7.1.1. $Z/\gamma^* \to \tau\tau$ Background Estimation from Hybrid "Embedded" Events

As mentioned before, Z boson decays to τ lepton pairs constitute a background that is difficult to distinguish from the signal and is produced at a much larger cross-section than the signal. The suppression of this background relies on two factors: Depending on the Higgs boson mass hypothesis, the mass difference of the Higgs boson and the Z boson can be exploited by reconstructing the di-τ invariant mass. The mass of the Higgs boson candidates (reconstructed with the missing mass calculator (MMC) technique [186,187], see Section 5.3) is therefore taken as final discriminant, whose shape is used within the test statistic (see Section 9.1). Furthermore, the relatively lower b-jet multiplicity in Z boson decays (when compared to Higgs boson production in association with b-quarks) leads to a better ratio of the signal yield to the $Z/\gamma^* \to \tau\tau$ background yield in the b-tagged sample than in the b-vetoed sample.

It is challenging to accurately describe the jet content (including its flavor composition), the missing transverse energy (used within the $m_{\tau\tau}$ reconstruction)—especially the contributions from the underlying event (UE) and additional interactions from pileup—and the event kinematics in simulation. The resulting uncertainties can be avoided by estimating

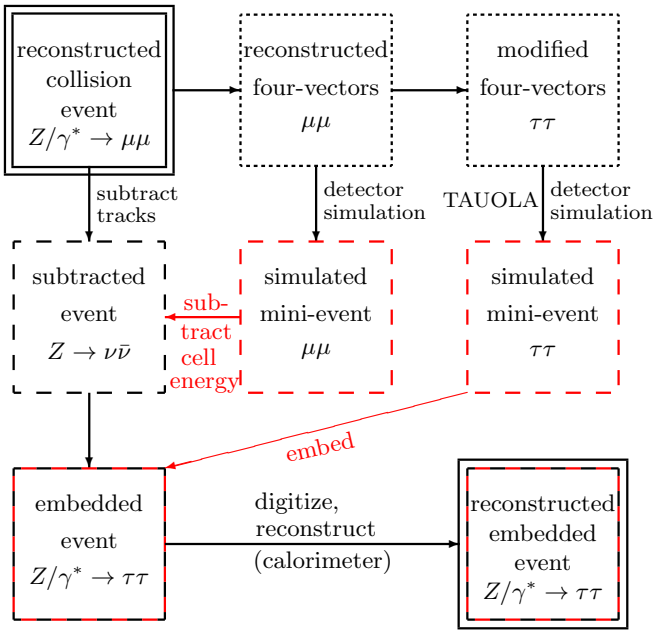

Figure 7.1.: Illustration of the embedding procedure. Solid lines symbolize whole events; broken lines, partial events. Black lines represent collision data used in the event; red lines, simulation. Alternating colors refer to hybrid events, i.e., events that contain objects from the original collision event as well as from simulation. The outer boxes represent reconstructed events, while the smaller boxes refer to tracks or energy deposits. Fine dashed lines symbolize a collection of two four-vectors only.

the $Z/\gamma^* \to \tau\tau$ background from data. However, no sufficiently signal-free control region is easily found for this process. A solution to this is the *embedding technique* [14], whose current implementation is described in Ref. [209]. This method produces "hybrid" events, i.e., events that combine detector signatures from collision data and from simulation. The procedure takes collision events with $Z/\gamma^* \to \mu\mu$ decays and replaces the reconstructed muons by simulated τ lepton decays (see Figure 7.1):

As a first step, a more than 99 % pure [210] sample of events containing Z boson decays into muon pairs is selected by requiring two muons with an invariant mass satisfying $m_{\mu\mu} > 40\,\text{GeV}$ from all runs in the Good Runs List also used for the signal region. This procedure ensures consistency of the data taking conditions, such as the instantaneous luminosity, in the embedded sample and the collision data evaluated for the analysis. Muon candidates must satisfy a cut on their transverse momenta ($p_{\text{T},\mu} > 15\,\text{GeV}$), have a pseudorapidity value of $|\eta| < 2.4$, and fulfill a track-based isolation criterion applying to a cone of $\Delta R < 0.2$ around the direction of the muon track: $p_{\text{T},\mu}^{\text{cone20}}/p_{\text{T},\mu} < 0.2$[1]. Due to the small coupling of Higgs bosons to muons, the signal contamination is negligible within this sample.

The reconstructed muon momenta are input into the detector simulation step to determine their expected energy deposits within the calorimeter cells. These deposits are subtracted from the original event, and the original tracks are subsequently removed, resulting in a simulated event resembling a $Z/\gamma^* \to \nu\bar{\nu}$ decay with kinematics and calorimeter objects from collision data.

The reconstructed muons are replaced by τ leptons with modified momenta

[1] This matches the definition of the track isolation fraction in Subsection 6.1.1.

$p_\tau = \sqrt{E_\mu^2 - m_\tau^2}$, thus taking into account the mass difference between muons and τ leptons. TAUOLA [165] is used to simulate τ lepton decays into electrons or muons; and PHOTOS [155] simulates the bremsstrahlung of the final state leptons.

The final state leptons are input into the detector simulation and the tracks and energy deposits in the calorimeter cells from the resulting *mini event* are superimposed on the quasi-$Z/\gamma^* \to \nu\bar{\nu}$ event. The digitization step is then run on the calorimeter information of the entire event—without the emulation of detector noise in order to avoid double-counting of noise contributions.

Because the τ lepton decay kinematics and interactions of electrons and muons with the detector can be modeled very accurately, the embedding technique provides a hybrid $Z/\gamma^* \to \tau\tau$ control sample with a very low associated systematic uncertainty (see Subsection 8.2.1). Each leptonic τ lepton decay involves two neutrinos, so the cut on the momentum of the original muon ($p_\mathrm{T} > 15\,\mathrm{GeV}$), which is then replaced by a τ lepton, translates to a lower cutoff value for the momentum distributions of the final state leptons. This fact strongly mitigates the impact on the muon transverse momentum spectrum (see Figure 7.3). The pseudo-rapidity and azimuthal angle distributions of leptons in the embedded sample follow the respective muon efficiencies for the triggering, the reconstruction, and the identification of the original muons. Because the reconstruction efficiency for muons varies significantly throughout the pseudo-rapidity range $|\eta| < 2.5$ and because a cut $|\eta_\mu| < 2.4$ is applied to the original muons, the kinematic properties of the final state leptons from the embedded sample differ from those of leptons from true $Z/\gamma^* \to \tau\tau$ events. However, the discriminating variables used within the kinematic selection do not directly depend on the lepton directions, and the impact of this bias is much smaller than the observed differences in the missing transverse energy and H_T distributions (see below).

The replacement procedure has been validated in the context of Ref. [183]: By simulating muons instead of decaying τ leptons, the $Z/\gamma^* \to \mu\mu$ hybrid events can be compared to the original $Z/\gamma^* \to \mu\mu$ events. Figure 7.2 shows three basic quantities: the transverse momenta of the muons, the missing transverse energy, and the sum of transverse energy contributions. The transverse mass of the $\mu\mu$–$E_\mathrm{T}^\mathrm{miss}$ system, which is calculated from missing transverse energy, the transverse momentum of the di-muon system ($p_{\mathrm{T},\mu\mu}$), and the transverse projection of the opening angle between the di-muon system and missing transverse energy ($\Delta\phi_{\mu\mu,E_\mathrm{T}^\mathrm{miss}}$), is also shown:

$$m_\mathrm{T} = \sqrt{2 p_{\mathrm{T},\mu\mu} E_\mathrm{T}^\mathrm{miss} (1 - \cos\Delta\phi_{\mu\mu,E_\mathrm{T}^\mathrm{miss}})}. \tag{7.1}$$

Only small differences occur in samples with $\mu\mu \to \mu\mu$ embedding, most noticeably in the $p_{\mathrm{T},\mu}$ and m_T distributions. The differences in these quantities can be attributed to the embedding technique, and the small differences that can be observed are covered by the systematic variations used in Subsection 8.2.1 to estimate the contribution to the systematic uncertainty.

Currently, the effect of the trigger cannot be simulated in embedded samples. To obtain the correct normalization, the event yield is determined from simulation at the preselection stage, which includes the trigger condition and the requirement that an electron–muon pair has been found, avoiding any larger dependence on simulated jets or missing transverse energy. The predicted event yields[2] are (11623 ± 64) events for Alpgen and (11663 ± 347) events for Pythia, so the predictions agree within the statistical uncertainties. The value from Alpgen is therefore taken as central prediction to determine the $Z/\gamma^* \to \tau\tau$ event yield after preselection.

[2] normalized to the production cross-section result of Refs. [175, 211, 211–213], see Table 8.1

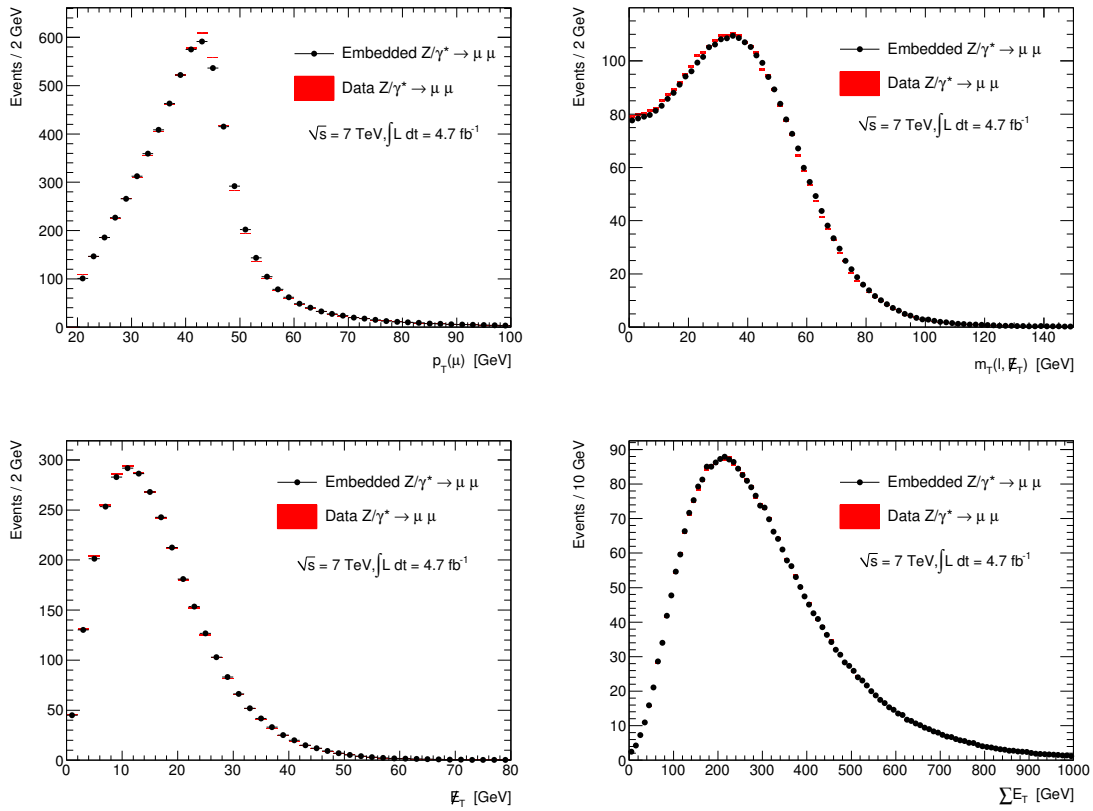

Figure 7.2.: Comparison of the transverse momentum (top left) [209], the transverse mass distribution (top right) [209], the missing transverse energy (bottom left) [183, 209], and the total transverse energy sum (bottom right) [209] from the selected data and the embedded $Z/\gamma^* \to \mu\mu$ sample. The embedded sample is normalized to the number of $Z/\gamma^* \to \mu\mu$ events in data.

Because of the lack of a proper trigger simulation in the embedded sample, differences in kinematic distributions between simulation and embedded $Z/\gamma^* \to \tau\tau$ events can arise. In particular, the various lepton p_{T} thresholds imposed by the trigger (see Table 6.2) change the lepton p_{T} distributions: Figure 7.3 shows the lepton p_{T} spectra in simulation (Alpgen) and those obtained from the embedded sample (`noTrig`). The comparison shows that a feature exists near the single-lepton trigger thresholds in simulation, but not in the embedded sample, which shows smooth falling flanks in the p_{T} spectra. In order to correctly reproduce this feature, which is also expected in data, in the embedded sample, a correction is applied to emulate the trigger efficiency. Three cases are discussed:

- All events are weighted equally, so no trigger emulation is performed (notated as `noTrig`).
- Events are reweighted[3], using the trigger efficiency obtained from data $\varepsilon^{\mathrm{data}}_{e||\mu||e\mu}$ from Refs. [183, 196] (see Subsection 6.1.3) applied as event weight (`trigReweighting`), or
- using factors of 0 or 1, based on the trigger emulation detailed below (`trigEmulation`).

[3]The normalization of the embedded sample is corrected according to the sum of weights.

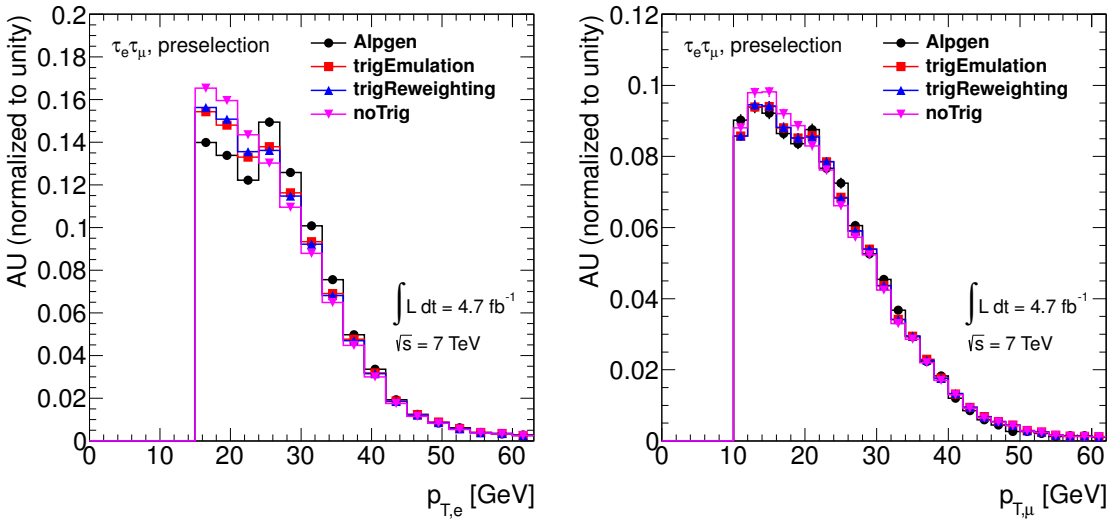

Figure 7.3.: Comparison of the electron (left) and muon (right) p_{T} spectra for $Z/\gamma^* \to \tau\tau$ events in the embedded sample and for Alpgen after the preselection (electron–muon pair of opposite charge, irrespective of the jet content).

The embedding trigger emulation (`trigEmulation`) provides a trigger decision, based on the trigger efficiencies of the single-lepton triggers obtained from data [196], by subsequently checking the three available triggers:

1. If the transverse momentum of the muon in the event fulfills $p_{\mathrm{T},\mu} > 20\,\mathrm{GeV}$, the event is accepted with a probability of $\varepsilon_\mu^{\mathrm{data}}(\eta_\mu, \phi_\mu)$ (emulating the single-muon trigger).

2. If the event is not accepted by the previous condition, the event is accepted with a probability of $\varepsilon_e^{\mathrm{data}}(\eta_e, p_{\mathrm{T},e})$ if the momentum of the electron in the event fulfills $p_{\mathrm{T},e} > 24\,\mathrm{GeV}$ (emulating the single-electron trigger).

3. Events not accepted by the previous conditions are accepted with a probability of $\varepsilon_\mu^{\mathrm{data}}(\eta_\mu, \phi_\mu)$ because the contribution by the muon trigger dominates the total inefficiency of the electron–muon trigger (emulating the electron–muon trigger).

The resulting kinematics of the three cases are compared to those obtained from simulation and two other weighting schemes for the embedded sample in Figures 7.3 through 7.5.

Of the three weighting methods, the embedding trigger emulation best reproduces the feature that the combination of the single-lepton and the electron–muon triggers introduces into the transverse momentum spectra of the final state leptons (see Figure 7.3), which is accurately described by simulation (see Subsection 3.2.7). Even though the feature cannot be perfectly modeled by the simple reweighting schemes detailed above, the associated uncertainty is reduced to the level of the other uncertainties (see Subsection 8.2.1). It can be modeled by comparing the distributions obtained using `trigEmulation` and `trigReweighting`.

Trigger emulation is therefore applied to the nominal $Z/\gamma^* \to \tau\tau$ prediction in the b-vetoed sample. In the b-tagged sample, the statistical uncertainties dominate, so all events are used with equal weights (`noTrig`) for the central $Z/\gamma^* \to \tau\tau$ prediction in the b-tagged sample[4].

[4] As the analysis of the b-tagged sample was finalized and preliminarily published [214] before this difference was discovered in the b-vetoed sample and it constitutes a subdominant effect, no trigger emulation was included in the analysis of the b-tagged sample.

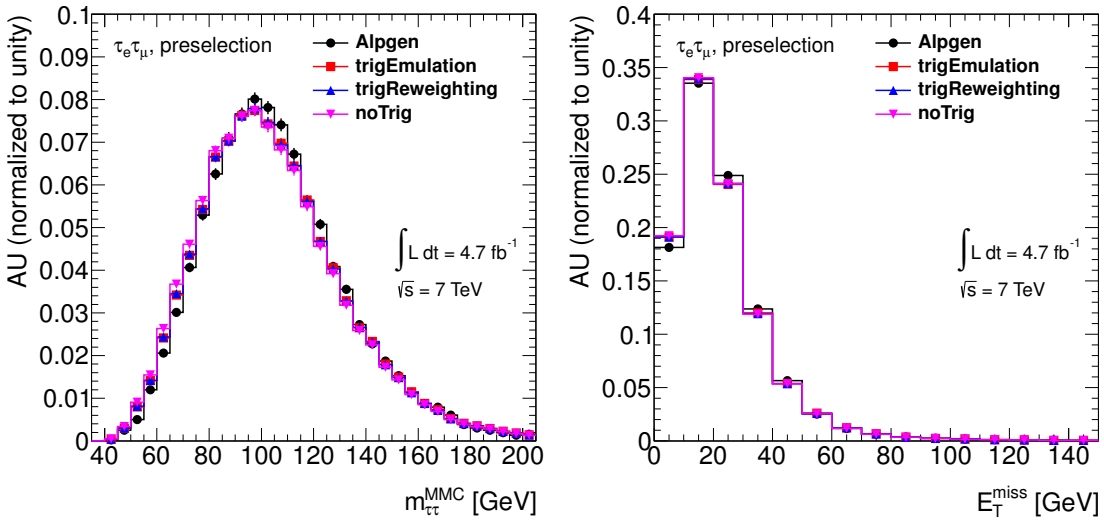

Figure 7.4.: Comparison of the $m_{\tau\tau}^{\mathrm{MMC}}$ (left) and $E_{\mathrm{T}}^{\mathrm{miss}}$ (right) distributions for $Z/\gamma^* \to \tau\tau$ events in the embedded sample and for Alpgen after the preselection (electron–muon pair of opposite charge, irrespective of the jet content).

While the three weighting methods produce different lepton p_{T} spectra, the effect on the reconstructed Higgs boson candidate mass ($m_{\tau\tau}^{\mathrm{MMC}}$) is only noticeable between values of about 50 and 85 GeV (see Figure 7.4). The predicted distribution from the corresponding Alpgen datasets, on the other hand, exhibits a systematic shift, which can be attributed to the $E_{\mathrm{T}}^{\mathrm{miss}}$ distribution, shown in the same Figure.

The distributions of the variables used within the kinematic selection (see Figure 7.5) show several differences: While the $\Delta\phi_{e\mu}$ and $\sum_{\ell=e,\mu} \cos\Delta\phi_{E_{\mathrm{T}}^{\mathrm{miss}},\ell}$ distributions agree well between all four predictions, the three different lepton trigger weighting scenarios in the embedded samples only significantly impact the $E_{\mathrm{T}}^{\mathrm{miss}} + p_{\mathrm{T},e} + p_{\mathrm{T},\mu}$ and $m_{\tau\tau}^{\mathrm{MMC}}$ distributions. The different predictions of the distributions of missing transverse energy and the lepton transverse momenta (see Figures 7.3 and 7.4) lead to differences in the $E_{\mathrm{T}}^{\mathrm{miss}} + p_{\mathrm{T},e} + p_{\mathrm{T},\mu}$ distribution below values of 100 GeV[5], and simulation shows a significantly larger fraction of events without valid jets ($H_{\mathrm{T}} = 0$). The estimation of missing transverse energy and jet-related quantities from data in $Z/\gamma^* \to \tau\tau$ events is therefore one of the most important advantages of the embedded sample (see Subsection 8.1.3).

Because the impact of the missing trigger simulation can be recovered with trigger emulation and many sources of systematic uncertainty can be eliminated by the data-driven approach, the embedded sample constitutes the most promising source for an accurate description of the $Z/\gamma^* \to \tau\tau$ background.

[5]Note that the lowest cut value is 125 GeV in the kinematic selection of the b-tagged sample, so these differences are irrelevant to the cut efficiencies.

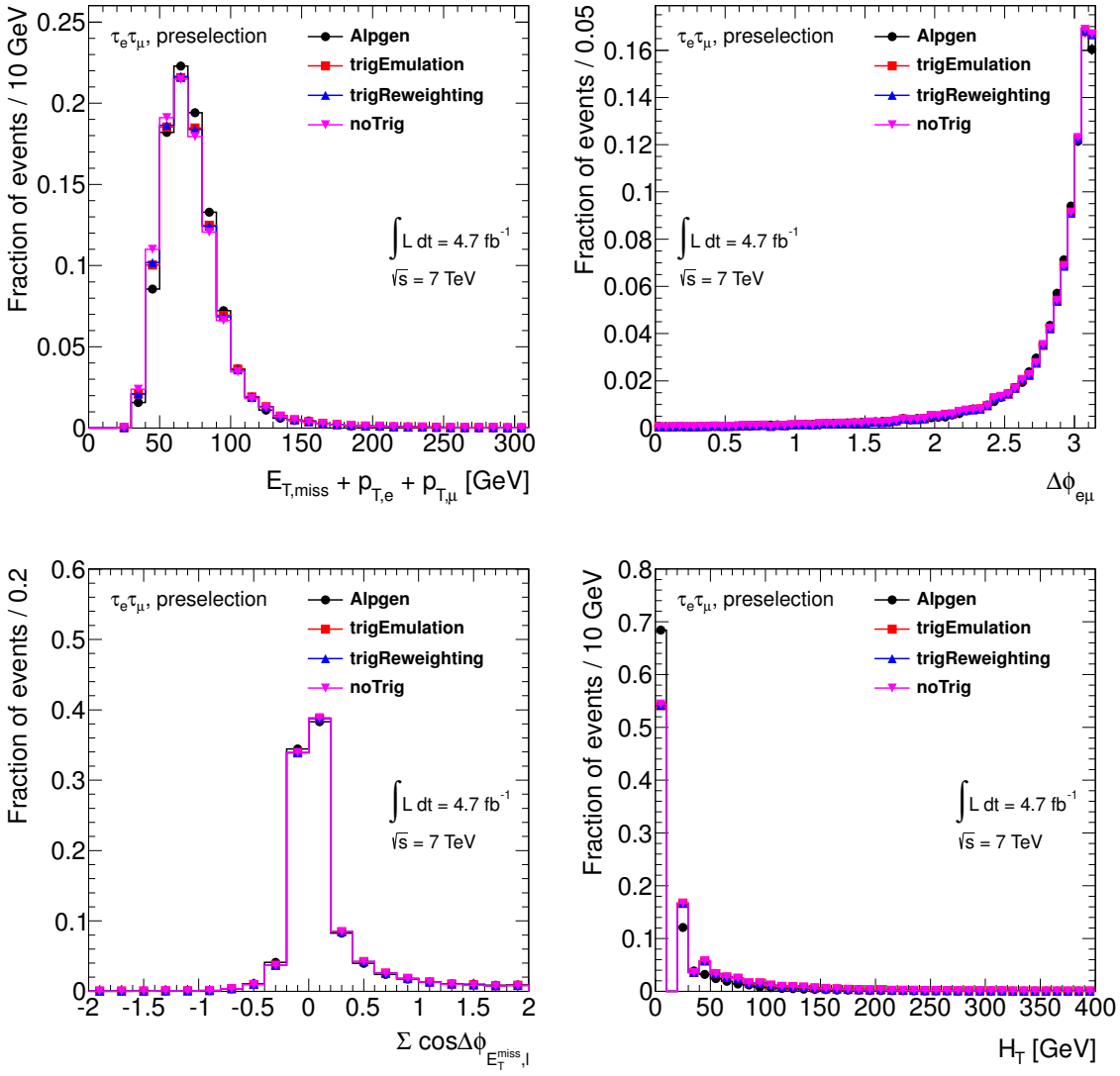

Figure 7.5.: Distributions of the variables used within the kinematic selection in simulation and embedded events at the preselection stage (electron–muon pair of opposite charge, irrespective of the jet content).

7.1.2. Multi-Jet Background Estimation from Control Regions

As shown in Ref. [15] for a previous analysis of the $\tau_{\text{lep}}\tau_{\text{had}}$ final states, the multi-jet contribution can be estimated with the so-called *ABCD method* by using a set of control regions (as mentioned in Subsection 6.2.1 and illustrated in Figure 6.5). The method uses two selection variables which must be uncorrelated with each other and with the final discriminant ($m_{\tau\tau}^{\text{MMC}}$) for the multi-jet background. The multi-jet contribution in a signal region can be computed from the event yields in the control regions, and the shape of the $m_{\tau\tau}^{\text{MMC}}$ distribution is obtained from a control region.

The control regions differ from the respective signal region A_R of the sample R[6] only by the isolation or charge requirements applied:

A_R Events with exactly one isolated electron and exactly one isolated muon of opposite electric charge enter the signal regions ($A_{b\text{-tag}}$, $A_{b\text{-veto}}$) and the $t\bar{t}$ control regions ($A_{\text{CR }b\text{-tag}}$, $A_{\text{CR }b\text{-veto}}$).

B_R Events with exactly one isolated electron and exactly one isolated muon of *the same* electric charge enter regions B_R.

C_R Events with exactly one *anti-isolated* electron and exactly one *anti-isolated* muon of opposite electric charge enter regions C_R. The shapes of distributions in the signal region are extracted from this region (see below).

D_R Events with exactly one *anti-isolated* electron and exactly one *anti-isolated* muon of *the same* electric charge enter regions D_R.

The *ABCD* method exploits the small correlations between these quantities and the final discriminant ($m_{\tau\tau}^{\text{MMC}}$) in order to obtain an estimate for the event yield as well as the shapes of distributions of kinematic variables from the control regions B_R, C_R, and D_R. In order to assess the impact of correlations, the method is extended by another set of isolation criteria, which introduce the additional control regions, E_R and F_R:

E_R Events with exactly one isolated electron and exactly one *anti-isolated* muon of opposite electric charge enter regions E_R.

F_R Events with exactly one isolated electron and exactly one *anti-isolated* muon of *the same* electric charge enter regions F_R.

By selecting one isolated electron and one anti-isolated muon in regions E_R and F_R, the good rejection against misreconstructed muons from the identification cuts is combined with the good rejection from the isolation cuts applied to electron candidates.

The multi-jet contribution in the signal regions can be estimated by first subtracting the electroweak contributions ($N_i^{\text{ew.}}$) from the yield in data (N_i^{data}) for all control regions $i = B_R, C_R, D_R, E_R, F_R$:

$$N_i^{\text{multi-jet}} = N_i^{\text{data}} - N_i^{\text{ew.}}. \tag{7.2}$$

The event yield is then extrapolated to the signal region: Assuming that the lepton isolation variables and the relative charge of the leptons are uncorrelated for multi-jet backgrounds, the ratio of yields is same for each set of regions with identical isolation requirements:

$$\frac{N_{A_R}^{\text{multi-jet}}}{N_{B_R}^{\text{multi-jet}}} = \frac{N_{C_R}^{\text{multi-jet}}}{N_{D_R}^{\text{multi-jet}}} = \frac{N_{E_R}^{\text{multi-jet}}}{N_{F_R}^{\text{multi-jet}}}. \tag{7.3}$$

[6] The region index R refers to the signal regions of the b-tagged or b-vetoed samples or the associated $t\bar{t}$ control regions (see Subsection 7.1.3).

The event yield for the signal regions can then be calculated using either regions C_R and D_R or E_R and F_R, which differ in the electron isolation requirement:

$$N_{A_R}^{\text{multi-jet}} = \frac{N_{C_R}^{\text{multi-jet}}}{N_{D_R}^{\text{multi-jet}}} \cdot N_{B_R}^{\text{multi-jet}} \tag{7.4}$$

or

$$N_{A_R}^{\text{multi-jet}} = \frac{N_{E_R}^{\text{multi-jet}}}{N_{F_R}^{\text{multi-jet}}} \cdot N_{B_R}^{\text{multi-jet}}. \tag{7.5}$$

In the present analysis, Eq. (7.4) is used for the central value of the multi-jet prediction, while the difference between the predictions from Eq. (7.4) and Eq. (7.5) is used as measure for the systematic uncertainty. The shape of the kinematic distributions in the regions A_R is taken from region C_R. The preference of regions C_R and D_R to obtain the central value of the prediction for the multi-jet background is founded in their purity and multi-jet event yields, which are better than those for regions E_R and F_R (see Table 7.1). A sufficient event yield is particularly important in the region from which the shapes of kinematic distributions are taken (see below). For each multi-jet control region, the individual electroweak contributions of all background classes and the event yield in collision data are given in Table 7.2. The expected signal contribution for the $m_{h^0}^{\text{max}}$ scenario and $m_{A^0} = 150\,\text{GeV}$, $\tan\beta = 20$ is below 1 % of the event yield in data for all control regions.

The $Z/\gamma^* \to \tau\tau$ contribution has been estimated from the Alpgen samples because the isolation variables are also taken from simulation in the embedded sample and carry an additional systematic uncertainty from the subtraction of energy deposits in calorimeter cells in the embedding procedure. The $t\bar{t}$ contribution has been estimated from the MC@NLO sample because of its small contribution to regions B_R through F_R (see Table 7.2), and the di-boson contribution from the Herwig samples. The uncertainty from the subtraction of electroweak backgrounds is neglected here, but it is taken into account as a normalization uncertainty in the calculation of exclusion limits.

As mentioned before, the shapes of distributions of kinematic variables can be obtained from the control regions. The shapes of the $m_{\tau\tau}^{\text{MMC}}$ distributions after the subtraction of electroweak background contributions for regions $B_{b\text{-tag}}$ to $F_{b\text{-tag}}$ and $B_{b\text{-veto}}$ to $F_{b\text{-veto}}$ are shown in Figure 7.6. The $m_{\tau\tau}^{\text{MMC}}$ distributions of the various control regions show significant shape differences when comparing control regions with different lepton isolation criteria. These differences are expected because of differences in the transverse momenta of the leptons (see Figure 7.7), which affect the reconstruction of $m_{\tau\tau}^{\text{MMC}}$. From this point of view, it would be preferable to take the shape from region B_R because the impact of the isolation variables on the $m_{\tau\tau}^{\text{MMC}}$ distributions is larger than those of the relative lepton charge. However, the low event yield in data would lead to unacceptable statistical uncertainties for the $m_{\tau\tau}^{\text{MMC}}$ shape prediction.

The resulting uncertainty on the shapes of the $m_{\tau\tau}^{\text{MMC}}$ distributions in the signal regions can be estimated from regions C_R and E_R: The nominal shape is taken from region C_R, while the difference to the shape from region E_R is taken as measure of the systematic uncertainty.

Table 7.1.: Multi-jet estimation for an integrated luminosity of $4.7\,\mathrm{fb}^{-1}$. Only the statistical component of the uncertainties is given for the numbers that refer to regions B_R through F_R. The second error component of the signal region estimate $N_{A_R}^{\text{multi-jet}}$ is the systematic error component, calculated from the difference of $\frac{N_{C_R}^{\text{multi-jet}}}{N_{D_R}^{\text{multi-jet}}}$ and $\frac{N_{E_R}^{\text{multi-jet}}}{N_{F_R}^{\text{multi-jet}}}$.

Selection step		Region B	Region C	Region D	$\frac{N_C^{\text{multi-jet}}}{N_D^{\text{multi-jet}}}$	Region E	Region F	$\frac{N_E^{\text{multi-jet}}}{N_F^{\text{multi-jet}}}$	$N_A^{\text{multi-jet}}$
b-tagged sample									
Preselection $e^{\pm}\mu^{\mp}$	Data	1252	166726	85436	1.951±0.008	37642	21531	1.507±0.024	1474±93±336
	ew. background	496±32	929±37	461±24		16083±135	7221±74		
Exactly one *b*-jet	Data	83	13102	7933	1.662±0.024	5146	3974	1.277±0.089	61±16± 14
	ew. background	46±4	203±5	171±16		3475±30	2665±26		
$E_{\mathrm{T}}^{\mathrm{miss}} + p_{\mathrm{T},e} + p_{\mathrm{T},\mu} < 125\,\mathrm{GeV}$	Data	49	12809	7715	1.669±0.025	2973	2324	1.306±0.086	50±13± 11
	ew. background	19±4	121±5	112±16		1572±26	1251±23		
$\Delta\phi_{e\mu} > 2$	Data	25	10999	6514	1.694±0.027	1930	1488	1.366±0.087	23±10± 5
	ew. background	11±3	62±2	56±2		772±17	640±15		
$\sum_{\ell=e,\mu} \cos\Delta\phi_{E_{\mathrm{T}}^{\mathrm{miss}},\ell} > -0.2$	Data	18	9203	5367	1.719±0.030	1431	1081	1.443±0.099	14± 9± 2
	ew. background	10±3	38±2	36±2		495±9	433±14		
$H_{\mathrm{T}} < 100\,\mathrm{GeV}$	Data	15	7953	4345	1.831±0.035	952	669	1.400±0.085	15± 9± 3
	ew. background	7±3	8.7±1.3	7.1±1.4		152±6	97±5		
$m_{\tau\tau}^{\mathrm{MMC}}$ reconstructible	Data	15	7944	4344	1.830±0.035	942	665	1.393±0.084	15± 9± 4
	ew. background	7.0±3.3	8.6±1.3	7.0±1.4		146±6	94±5		
b-vetoed sample									
Preselection $e^{\pm}\mu^{\mp}$	Data	1252	166726	85436	1.951±0.008	37642	21531	1.507±0.024	1474±93±336
	ew. background	496±32	929±37	461±24		16083±135	7221±74		
No *b*-jets	Data	1144	152998	76981	1.985±0.009	31417	17000	1.522±0.024	1411±92±329
	ew. background	433±32	659±37	250±18		11509±131	3922±69		
$E_{\mathrm{T}}^{\mathrm{miss}} + p_{\mathrm{T},e} + p_{\mathrm{T},\mu} < 150\,\mathrm{GeV}$	Data	1023	152537	76655	1.987±0.009	28896	15582	1.522±0.024	1328±88±311
	ew. background	355±30	602±37	208±18		9563±123	2880±65		
$\Delta\phi_{e\mu} > 1.6$	Data	843	145286	75157	1.983±0.009	26111	13856	1.539±0.024	1163±73±261
	ew. background	257±22	525±36	170±17		8244±116	2246±56		
$\sum_{\ell=e,\mu} \cos\Delta\phi_{E_{\mathrm{T}}^{\mathrm{miss}},\ell} > -0.4$	Data	686	136394	68263	1.995±0.009	21898	11876	1.540±0.025	982±61±224
	ew. background	194±15	399±33	107±11		6015±97	1565±46		
$m_{\tau\tau}^{\mathrm{MMC}}$ reconstructible	Data	679	136142	68126	1.996±0.009	21504	11711	1.539±0.024	982±60±225
	ew. background	187±15	378±33	99±11		5729±94	1460±45		

Table 7.2.: The contribution of non-multi-jet background to the multi-jet control regions (B_R through F_R) and the event yield in collision data after all topological selection criteria have been applied. The expected signal contribution for the $m_{h^0}^{\max}$ scenario and $m_{A^0} = 150\,\text{GeV}$, $\tan\beta = 20$ is below 1 % of the event yield in data for all control regions.

b-tagged sample							
	$Z/\gamma^* \to \tau\tau$	$t\bar{t}$	Single t	Diboson	$Z/\gamma^* \to \ell\ell$	W+jets	Data
$B_{b\text{-tag}}$	1.0± 0.6	0.2±0.1	0.6±0.2	0.4±0.2	0.6± 0.6	4 ± 3	15
$C_{b\text{-tag}}$	1.2± 0.5	4.7±0.6	1.1±0.4	0.2±0.1	0	1.3± 1.0	7944
$D_{b\text{-tag}}$	0	3.7±0.5	1.0±0.2	0	0	2.4± 1.3	4344
$E_{b\text{-tag}}$	21 ± 3	63 ±2	22.9±1.1	3.1±0.3	7.8± 2.3	28 ± 5	942
$F_{b\text{-tag}}$	1.8± 0.8	53.4±1.8	15.4±0.9	1.3±0.2	5.3± 2.0	17 ± 4	665
b-vetoed sample							
	$Z/\gamma^* \to \tau\tau$	$t\bar{t}$	Single t	Diboson	$Z/\gamma^* \to \ell\ell$	W+jets	Data
$B_{b\text{-veto}}$	58 ± 5	1.9±0.3	1.7±0.4	21.3±0.7	60 ± 6	44 ±13	679
$C_{b\text{-veto}}$	131 ± 7	40.1±1.5	15.9±1.0	4.3±0.4	22 ± 3	165 ±32	136142
$D_{b\text{-veto}}$	9.3± 1.7	32.6±1.3	9.1±0.7	1.3±0.2	15 ± 3	32 ±11	68126
$E_{b\text{-veto}}$	1480 ±23	339 ±4	240 ±4	69.9±1.5	246 ±12	3353 ±90	21504
$F_{b\text{-veto}}$	56 ± 5	336 ±4	139 ±3	14.1±0.6	237 ±11	677 ±43	11711

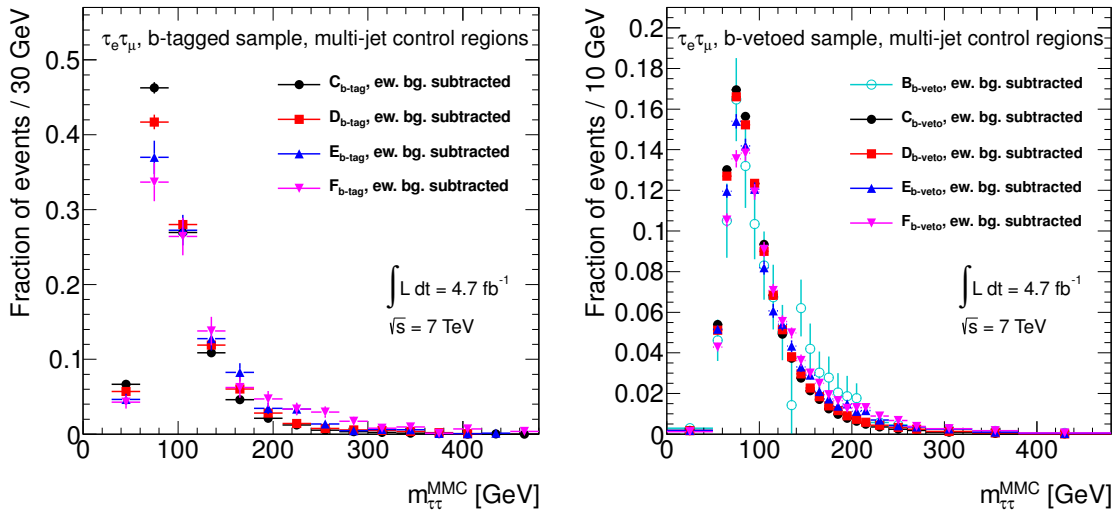

Figure 7.6.: Shapes of the $m_{\tau\tau}^{\text{MMC}}$ distributions from multi-jet control regions $B_{b\text{-tag}}$ through $F_{b\text{-tag}}$ (left) and $B_{b\text{-veto}}$ through $F_{b\text{-veto}}$ (right), after all topological cuts have been applied. Contributions from non-multi-jet processes have been subtracted from the distributions observed in data. The distribution from region $B_{b\text{-tag}}$ is not shown because of the low event yield in this region. The signal region estimate is taken from regions $C_{b\text{-tag}/b\text{-veto}}$.

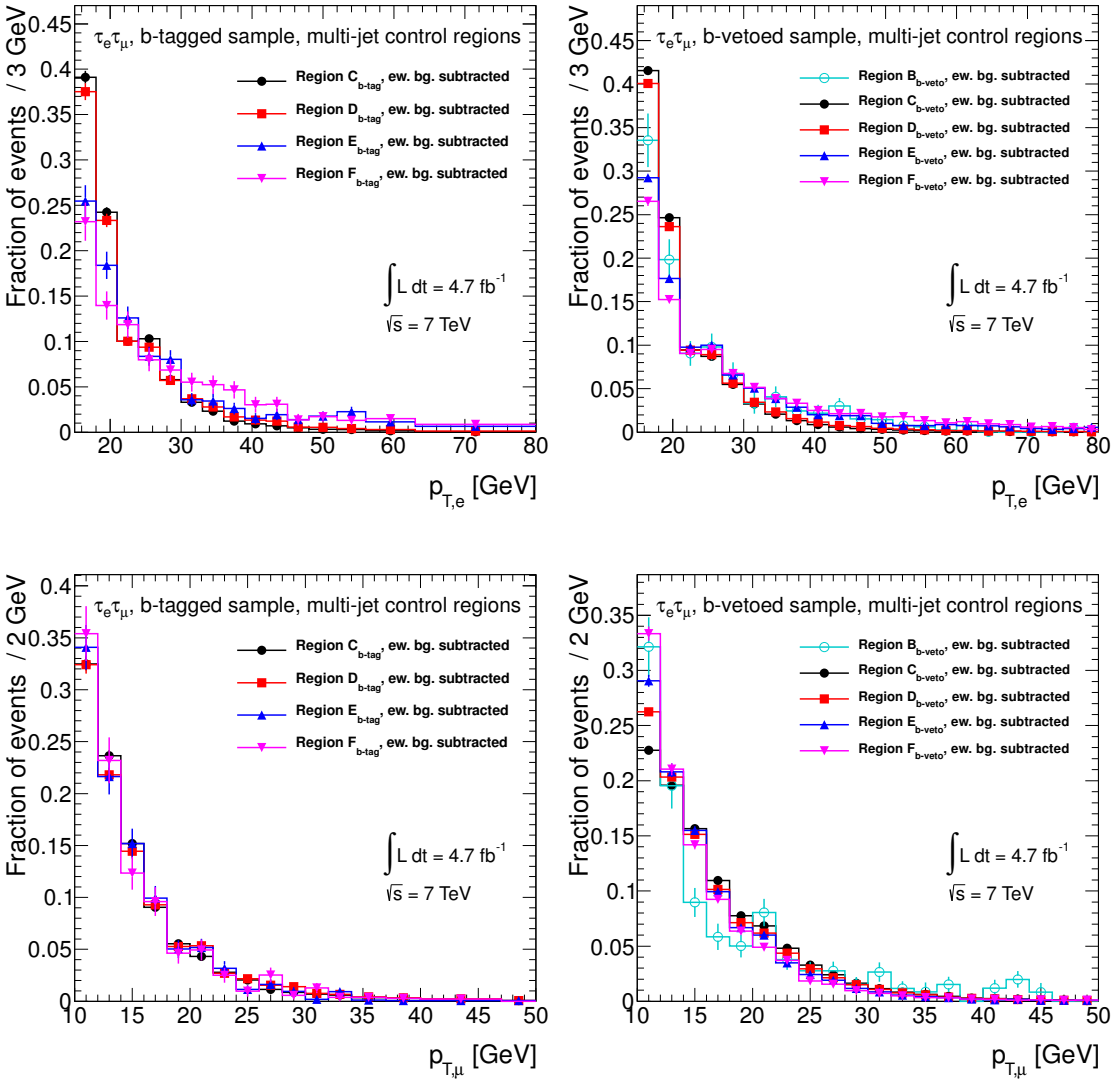

Figure 7.7.: Shapes of the lepton p_{T} distributions from multi-jet control regions B_R through F_R, after all topological cuts have been applied. Contributions from non-multi-jet processes have been subtracted from the distributions observed in data. The distribution from region $B_{b\text{-tag}}$ is not shown because of the low event yield in this region.

7.1.3. t-Quark Pair Background Estimation from Control Regions

t-quark pair production contributes significantly to the b-tagged sample with 28 % of the total background after the kinematic selection. In the b-vetoed sample, $t\bar{t}$ contributes only 1 % of the total background. In order to control systematic uncertainties from simulation, it should therefore also be estimated from data, especially in the b-tagged sample.

It has therefore been investigated whether the $t\bar{t}$ background can be estimated from data in a similar way as the multi-jet background by using an $ABCD$ method, taking different sets of variables into account:

- The impact parameters of the final-state leptons have initially been considered as discriminating variables, exploiting the fact that about 90 % of the $e\mu$ final states in $t\bar{t}$ decays originate from $t \to W(e/\mu + \nu)b$ decays. Leptonically decaying τ leptons in the signal and $Z/\gamma^* \to \tau\tau$ processes, however, have too small decay lengths to be separated sufficiently well, so they were not considered for the optimization of the event selection or the final $t\bar{t}$ estimation.

- For the b-tagged sample, an estimation with the variables $E_{\mathrm{T}}^{\mathrm{miss}} + p_{\mathrm{T},e} + p_{\mathrm{T},\mu}$ and H_{T} is possible (see Appendix A), but it requires the compensation of correlations from simulation. Because H_{T} (or an equally well-suited second discriminant against $t\bar{t}$ events) is not used in the kinematic selection of the b-vetoed sample, this method cannot be as easily adopted to the b-vetoed sample as the background estimation method detailed within this Subsection.

No set of variables has been found that offers negligible correlations of the variables to each other and to $m_{\tau\tau}^{\mathrm{MMC}}$, while also having sufficient event yields in the control regions.

In this analysis, the event yields of the $t\bar{t}$ background are obtained from a control region, using an extrapolation factor taken from simulation, and the shapes of the kinematic variables in the signal regions are also taken from simulation: While the b-tagged (b-vetoed) samples require exactly 1 (0) b-jets with transverse momenta above 20 GeV (at an efficiency of $\varepsilon_b = 75\,\%$ for b-jets with $p_{\mathrm{T}} > 15\,\mathrm{GeV}$ in simulated $t\bar{t}$ events), these control regions contain events with at least two tagged b-jets. The event yields in the signal regions in data $\left(N_{t\bar{t}}^{\text{SR } b\text{-tag}/b\text{-veto}}\right)$ can be obtained from the event yields in the control regions $\left(N_{t\bar{t}}^{\text{CR } b\text{-tag}/b\text{-veto}}\right)$, using extrapolation factors $\left(k_{\mathrm{MC}}^{b\text{-tag}/b\text{-veto}}\right)$ from simulation:

$$N_{t\bar{t}}^{\text{SR } b\text{-tag}/b\text{-veto}} = k_{\mathrm{MC}}^{b\text{-tag}/b\text{-veto}} \cdot N_{t\bar{t}}^{\text{CR } b\text{-tag}/b\text{-veto}}. \tag{7.6}$$

For the b-tagged sample, the H_{T} requirement is dropped in the control region to reduce the statistical uncertainties. Because of different b-jet multiplicities, the contribution from the production of single t-quarks cannot be estimated from the same control regions, so it is taken from simulation. The control regions for the b-tagged and the b-vetoed sample are both defined by the requirement of at least two b-tagged jets. The set of cuts applied to the control region for the b-tagged sample is tighter than that of the control region for the b-vetoed sample. Consequently, the former is a subset of the latter.

For simulated $t\bar{t}$ samples from MC@NLO and POWHEG+Jimmy, the event yields in the signal and control regions are determined, and their ratios give the extrapolation factors $k_{\mathrm{MC}}^{b\text{-tag}}$, $k_{\mathrm{MC}}^{b\text{-veto}}$ for each Monte Carlo (MC) event generator (see Table 7.3). For each sample, the predictions from the two simulated samples are weighted with their uncertainties. The weighted mean is used as central value for $k_{\mathrm{MC}}^{b\text{-tag}/b\text{-veto}}$, using half the difference of the two

Table 7.3.: Determination of the $t\bar{t}$ extrapolation factors $k^{b\text{-tag}/b\text{-veto}}_{\text{MC@NLO}}$ and $k^{b\text{-tag}/b\text{-veto}}_{\text{POWHEG+Jimmy}}$ for each stage of the selection of the b-tagged and b-vetoed samples.

b-tagged sample			
	MC@NLO		
	SR yield	CR yield	$k^{b\text{-tag}}_{\text{MC@NLO}}$
Preselection $e^{\pm}\mu^{\mp}$	6993±19	2545±11	2.748±0.014
Exactly one b-jet	3314±13	2545±11	1.302±0.008
$E_{\text{T}}^{\text{miss}} + p_{\text{T},e} + p_{\text{T},\mu} < 125\,\text{GeV}$	504±5	414±4	1.216±0.018
$\Delta\phi_{e\mu} > 2$	198±3	166±3	1.192±0.028
$\sum_{\ell=e,\mu} \cos\Delta\phi_{E_{\text{T}}^{\text{miss}},\ell} > -0.2$	135±3	110.1±2.3	1.222±0.035
$H_{\text{T}} < 100\,\text{GeV}$	46.3±1.5	110.1±2.3	0.420±0.016
$m_{\tau\tau}^{\text{MMC}}$ reconstructible	44.8±1.5	107.9±2.3	0.416±0.016
	PowHeg+Jimmy		
	SR yield	CR yield	$k^{b\text{-tag}}_{\text{POWHEG+Jimmy}}$
Preselection $e^{\pm}\mu^{\mp}$	6675±79	2881±52	2.317±0.050
Exactly one b-jet	2904±52	2881±52	1.008±0.026
$E_{\text{T}}^{\text{miss}} + p_{\text{T},e} + p_{\text{T},\mu} < 125\,\text{GeV}$	457±21	446±19	1.025±0.064
$\Delta\phi_{e\mu} > 2$	171±13	168±12	1.019±0.104
$\sum_{\ell=e,\mu} \cos\Delta\phi_{E_{\text{T}}^{\text{miss}},\ell} > -0.2$	118±10	122±10	0.963±0.115
$H_{\text{T}} < 100\,\text{GeV}$	51±7	122±10	0.413±0.063
$m_{\tau\tau}^{\text{MMC}}$ reconstructible	49±6	120±10	0.409±0.064
b-vetoed sample			
	MC@NLO		
	SR yield	CR yield	$k^{b\text{-veto}}_{\text{MC@NLO}}$
Preselection $e^{\pm}\mu^{\mp}$	6993±19	2545±11	2.748±0.014
No b-jets	1133.2±8.1	2545±11	0.445±0.004
$E_{\text{T}}^{\text{miss}} + p_{\text{T},e} + p_{\text{T},\mu} < 150\,\text{GeV}$	356.1±4.6	840.2±6.4	0.424±0.006
$\Delta\phi_{e\mu} > 1.6$	200.9±3.4	452.4±4.6	0.444±0.009
$\sum_{\ell=e,\mu} \cos\Delta\phi_{E_{\text{T}}^{\text{miss}},\ell} > -0.4$	140.2±2.8	324.3±4.0	0.432±0.011
$m_{\tau\tau}^{\text{MMC}}$ reconstructible	126.1±2.6	297.6±3.8	0.424±0.010
	POWHEG+Jimmy		
	SR yield	CR yield	$k^{b\text{-veto}}_{\text{POWHEG+Jimmy}}$
Preselection $e^{\pm}\mu^{\mp}$	6675±79	2881±52	2.317±0.050
No b-jets	890±29	2881±52	0.309±0.012
$E_{\text{T}}^{\text{miss}} + p_{\text{T},e} + p_{\text{T},\mu} < 150\,\text{GeV}$	295±17	928±28	0.318±0.021
$\Delta\phi_{e\mu} > 1.6$	158±12	477±20	0.331±0.029
$\sum_{\ell=e,\mu} \cos\Delta\phi_{E_{\text{T}}^{\text{miss}},\ell} > -0.4$	110±10	347±17	0.318±0.033
$m_{\tau\tau}^{\text{MMC}}$ reconstructible	97.5±9.4	325±17	0.300±0.033

Table 7.4.: $t\bar{t}$ extrapolation factors $k_{\mathrm{MC}}^{b\text{-tag}/b\text{-veto}}$ with systematic uncertainties included. Central values are obtained as weighted means, the systematic uncertainty reflects the difference between the values obtained from MC@NLO and POWHEG+Jimmy.

b-tagged sample	
	$k_{\mathrm{MC}}^{b\text{-tag}}$
Preselection $e^{\pm}\mu^{\mp}$	2.716±0.014±0.231
Exactly one b-jet	1.278±0.007±0.163
$E_{\mathrm{T}}^{\mathrm{miss}} + p_{\mathrm{T},e} + p_{\mathrm{T},\mu} < 125\,\mathrm{GeV}$	1.202±0.018±0.103
$\Delta\phi_{e\mu} > 2$	1.180±0.027±0.092
$\sum_{\ell=e,\mu} \cos\Delta\phi_{E_{\mathrm{T}}^{\mathrm{miss}},\ell} > -0.2$	1.199±0.034±0.143
$H_{\mathrm{T}} < 100\,\mathrm{GeV}$	0.420±0.016±0.004
$m_{\tau\tau}^{\mathrm{MMC}}$ reconstructible	0.415±0.016±0.004
b-vetoed sample	
	$k_{\mathrm{MC}}^{b\text{-veto}}$
Preselection $e^{\pm}\mu^{\mp}$	2.716±0.014±0.231
No b-jets	0.433±0.004±0.078
$E_{\mathrm{T}}^{\mathrm{miss}} + p_{\mathrm{T},e} + p_{\mathrm{T},\mu} < 150\,\mathrm{GeV}$	0.432±0.004±0.078
$\Delta\phi_{e\mu} > 1.6$	0.415±0.006±0.059
$\sum_{\ell=e,\mu} \cos\Delta\phi_{E_{\mathrm{T}}^{\mathrm{miss}},\ell} > -0.4$	0.434±0.008±0.063
$m_{\tau\tau}^{\mathrm{MMC}}$ reconstructible	0.412±0.010±0.070

single predictions as measure of the systematic uncertainty (see Table 7.4). This estimate assumes that the differences in the jet properties of the two samples are characteristic for the overall theoretical uncertainties. Because t-quark pairs are produced predominantly at low $|\eta|$, two central b-jets from the t-quark decays are expected for most events already at leading order. As a consequence, the b-jet multiplicity can be expected to be well-described by both generators. The $t\bar{t}$ control regions have a purity of 92 % (96 %) after the application of the selection cuts (with exception of the H_{T} cut, see above). Other contributions (predominantly events with $Z/\gamma^* \to \tau\tau$ or single t-quark decays) are estimated from simulation, except for the multi-jet background, which is estimated using an $ABCD$ method in the $t\bar{t}$ control regions as described in Subsection 7.1.2. Their contributions are subtracted from the number of observed events, and the result is scaled by k_{MC} to obtain the signal region prediction (see Table 7.5). A comparison of the signal region predictions by MC@NLO and the extrapolation method shows that the prediction from simulation is lower by 20 % (17 %) for the b-tagged (b-vetoed) sample. This is consistent with the observations of the Standard Model $H \to WW^{(*)} \to \ell\nu\ell\nu$ search [215].

Figure 7.8 shows the $t\bar{t}$ background and other contributions to the control regions of the b-tagged and b-vetoed samples. The $t\bar{t}$ background has been normalized to $N_{t\bar{t}}^{\mathrm{CR}\ b\text{-tag}/b\text{-veto}}$. Figure 7.9 shows a comparison of the $m_{\tau\tau}^{\mathrm{MMC}}$ shapes in the control regions (left) and the signal regions (right) after the application of all selection cuts. The signal region predictions of the two simulated datasets agree within statistical uncertainties, and the collision-data distributions in the control regions (with non-$t\bar{t}$ contributions subtracted) agree with simulation. This is supported by the high p-values obtained from KS tests between the simulated datasets[7], which are quoted in the figure. Therefore (and because of the agreement observed

[7]The p-value of a KS test for two sets of data that stem from the same underlying probability density function

Table 7.5.: Determination of event yields for different processes in the $t\bar{t}$ control regions, and the final signal region prediction. The second error quoted in the final column is derived from the systematic uncertainty of the extrapolation factor (cf. Table 7.4). The expected signal contamination for $m_{A^0} = 150\,\text{GeV}$, $\tan\beta = 20$ is below 1 %.

b-tagged sample								
	$N_{\text{data}}^{\text{CR}}$	$Z \to \tau\tau$	Single t	Di-boson	Multi-jet	$N_{\text{non-}t\bar{t}}^{\text{CR } b\text{-tag}}$	$N_{t\bar{t}}^{\text{CR } b\text{-tag}}$	$N_{t\bar{t}}^{\text{SR } b\text{-tag}}$
Preselection $e^{\pm}\mu^{\mp}$	3104	26.2±2.5	77.5±2.5	1.2±0.2	13.9±6.0	118.9±7.0	2985±57	8107±161±689
Exactly one b-jet	3104	26.2±2.5	77.5±2.5	1.2±0.2	13.9±6.0	118.9±7.0	2985±57	3814± 76±486
$E_{\text{T}}^{\text{miss}} + p_{\text{T},e} + p_{\text{T},\mu} < 125\,\text{GeV}$	561	14.8±1.9	10.6±0.9	0.5±0.1	5.0±3.2	30.9±3.8	530±25	637± 31± 54
$\Delta\phi_{e\mu} > 2$	214	9.0±1.5	3.9±0.5	0.3±0.1	1.7±2.1	14.9±2.6	199±15	235± 19± 18
$\sum_{\ell=e,\mu} \cos\Delta\phi_{E_{\text{T}}^{\text{miss}},\ell} > -0.2$	148	6.8±1.3	3.2±0.5	0.3±0.1	1.5±1.8	11.7±2.3	136±13	163± 16± 19
$H_{\text{T}} < 100\,\text{GeV}$	148	6.8±1.3	3.2±0.5	0.3±0.1	1.5±1.8	11.7±2.3	136±13	57.2± 5.8± 0.5
$m_{\tau\tau}^{\text{MMC}}$ reconstructible	146	6.8±1.3	3.2±0.5	0.3±0.1	1.5±1.8	11.7±2.3	134±13	55.7± 5.7± 0.5
b-vetoed sample								
	$N_{\text{data}}^{\text{CR}}$	$Z \to \tau\tau$	Single t	Di-boson	Multi-jet	$N_{\text{non-}t\bar{t}}^{\text{CR } b\text{-veto}}$	$N_{t\bar{t}}^{\text{CR } b\text{-veto}}$	$N_{t\bar{t}}^{\text{SR } b\text{-veto}}$
Preselection $e^{\pm}\mu^{\mp}$	3104	26.5±2.6	77.5±2.5	2.0±0.3	13.2±6.0	106.0±3.6	2985±56	8107±158±689
No b-jets	3104	26.5±2.6	77.5±2.5	2.0±0.3	13.2±6.0	106.0±3.6	2985±56	1292± 27±233
$E_{\text{T}}^{\text{miss}} + p_{\text{T},e} + p_{\text{T},\mu} < 150\,\text{GeV}$	1097	17.5±2.1	23.2±1.3	0.7±0.2	7.3±4.0	41.4±2.5	1048±33	453± 15± 82
$\Delta\phi_{e\mu} > 1.6$	578	11.5±1.7	12.6±1.0	0.5±0.2	5.8±3.4	24.6±2.0	548±24	227± 11± 32
$\sum_{\ell=e,\mu} \cos\Delta\phi_{E_{\text{T}}^{\text{miss}},\ell} > -0.4$	419	9.4±1.6	8.5±0.8	0.3±0.1	2.0±2.3	18.2±1.8	399±21	173± 10± 25
$m_{\tau\tau}^{\text{MMC}}$ reconstructible	386	9.1±1.5	7.6±0.8	0.3±0.1	1.0±2.1	17.0±1.7	368±20	152± 9± 26

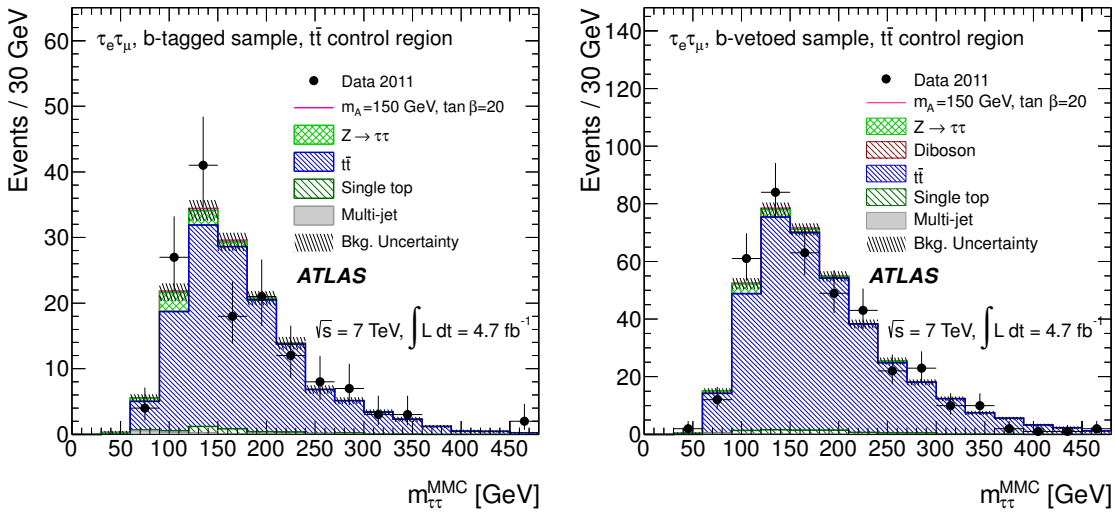

Figure 7.8.: Distributions of $m_{\tau\tau}^{\mathrm{MMC}}$ in the $t\bar{t}$ control regions of the b-tagged (left) and the b-vetoed sample (right) after the full selection. The $t\bar{t}$ distribution is taken from MC@NLO and rescaled from data. Good agreement between the shape of the MC prediction and data in this control region is observed.

in the alternative shape estimation in Chapter A), the $m_{\tau\tau}^{\mathrm{MMC}}$ shape in the signal region is taken from MC@NLO, which has lower statistical uncertainties than the predicted shape from data.

7.2. Background Estimation from Simulation

The single t-quark, di-boson, W+jets, and $Z/\gamma^* \to ll$ processes are estimated from simulation. Because the expected event yields are sufficiently low, the associated uncertainties have only a small impact on the sensitivity.

The production of single t-quarks constitutes about 8 % (0.3 %) of the b-tagged b-vetoed sample. It cannot be estimated from the $t\bar{t}$ control regions because the jets in single t-quark production exhibit different multiplicity distributions, flavor compositions, and spectra than those in $t\bar{t}$ events. In order to obtain the best description of additional jets in events with single t-quark production, AcerMC [148] is used.

Herwig has been used for the estimation of the di-boson background in the b-tagged sample, to which it contributes about 2 % of the background, and its corresponding control samples. MC@NLO has been used in the signal (about 4 % of the total background) and control regions of the b-vetoed sample.[8] This background is dominated by W boson pair production (95 % of the di-boson contribution).

The $Z/\gamma^* \to \ell\ell$ contribution is strongly suppressed by lepton identification. It is dominated by $Z/\gamma^* \to \mu\mu$ events (97 % of the $Z/\gamma^* \to \ell\ell$ backgrounds at the preselection stage) and contributes about 0.5 % (1.5 %) of the total background in the b-tagged (b-vetoed) sample. W boson production in association with jets also plays a minor role due to the requirement

is uniformly distributed between 0 and 1.

[8] The di-boson background plays a more important role in the b-vetoed sample. After the finalization of the analysis of the b-tagged sample, MC@NLO was adopted for the analysis of the b-vetoed sample for consistency with the analyses of the $\tau_{\mathrm{lep}}\tau_{\mathrm{had}}$ and $\tau_{\mathrm{had}}\tau_{\mathrm{had}}$ channels.

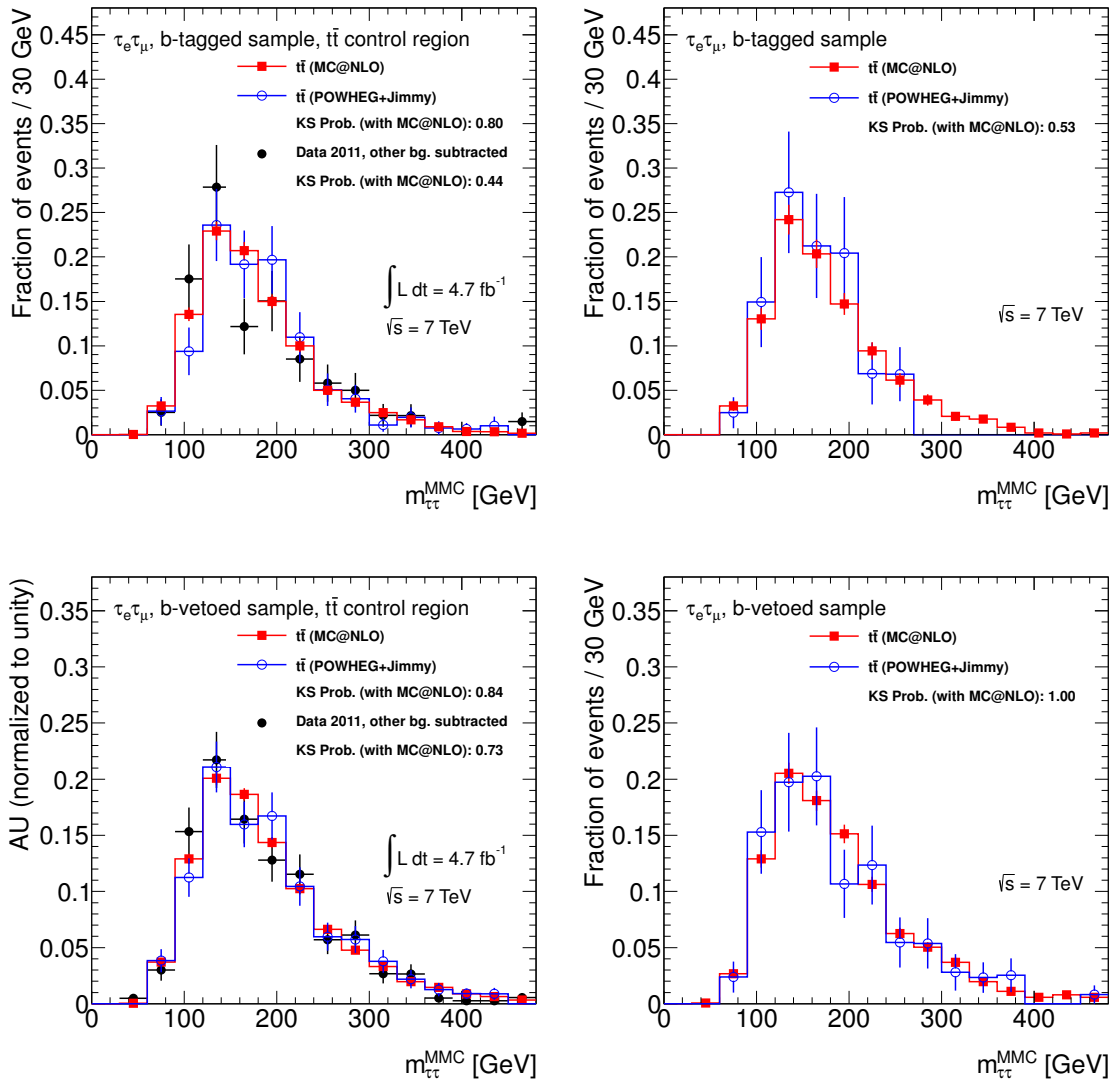

Figure 7.9.: Shape of reconstructed $m_{\tau\tau}$ (MMC) in the $t\bar{t}$ control regions (left) and in the signal regions (right) for the b-tagged (top) and the b-vetoed (bottom) samples after the full selection. Other background contributions have been subtracted from data in the control region. The results of KS tests that quantify the similarity of the $m_{\tau\tau}^{\mathrm{MMC}}$ shapes predicted by MC@NLO on one hand and POWHEG+Jimmy or data on the other hand are also given.

of two good leptons (0.6 % (0.9 %) of the total background in the b-tagged (b-vetoed) sample). Because of the importance of a good description of additional jets in the event, these backgrounds are estimated from simulated events produced with Alpgen. The simulation of $Z/\gamma^* \to \ell\ell$ and W boson production is supplemented by events with enhanced b-jet fractions to provide a more accurate estimate in the b-tagged sample.

8 Systematic Uncertainties

The presence of a signal in addition to the Standard Model (SM) background is assessed with a hypothesis test that is based on the predicted and observed $m_{\tau\tau}^{\mathrm{MMC}}$ distributions (see Chapter 9 for details). Therefore, uncertainties associated to the expected event yields (*normalization uncertainties*) have to be taken into account to quantify the sensitivity. Because the test statistic depends on the shapes of the $m_{\tau\tau}^{\mathrm{MMC}}$ distributions, *shape uncertainties* must also be estimated.

For each signal and background contribution, the normalization and shape uncertainties must be evaluated according to the estimation method used. The contributions that were estimated with simulated datasets are discussed in Section 8.1. The uncertainties of the data-driven background estimation techniques are described in Section 8.2.

The systematic uncertainties are summarized in Section 8.3.

8.1. Uncertainties of Event Simulation

The uncertainties associated to simulated events can be divided into three groups: The uncertainty of the production cross-section affects the normalization of the event sample.

The prediction of kinematic distributions of a given final state imposes another class of uncertainties in the presence of kinematic cuts, which are called *acceptance uncertainties*. This uncertainty is treated purely as a normalization uncertainty, so the contribution to the shape uncertainty is neglected.

The precision of the detector response, including reconstruction, identification, and isolation efficiencies as well as energy scales and resolutions, is determined by the kinematic properties of each event. The resulting $m_{\tau\tau}^{\mathrm{MMC}}$ distributions for variations of the detector response have been compared to the central estimate. In cases where a significantly different shape was observed, they were taken into account as shape and normalization uncertainties, otherwise, as pure normalization uncertainties.

8.1.1. Production Cross-Sections

The calculation of the cross-section values is described in Subsection 4.1.4. They take the one-loop and most important two-loop corrections into account. For the estimation of the cross-section uncertainties, variations of the parton distribution function (PDF) as well as of the factorization and renormalization scales must be considered. The total error is calculated from the error eigenvectors of the PDF MSTW2008 at next–to–next–to–leading order (NNLO) and variations of the factorization and renormalization scales by factors of two around the central value [147]: By assuming that the goodness of the global PDF fit (χ^2) is quadratic in the parameters of the PDF near the best fit value, variations can be expressed as a linear combination of eigenvectors[1] of the associated Hessian matrix [216].

The production cross-section is evaluated for the central value and variations by ± 1 times each of the 20 error eigenvectors, using the respective α_s value of the variation. Furthermore,

[1] each describing a variation of one standard deviation

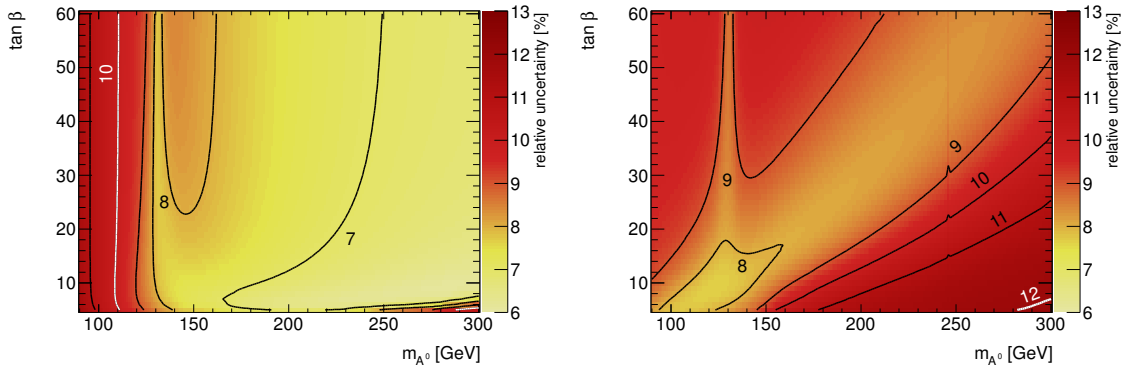

Figure 8.1.: Relative uncertainties of the total signal cross-sections for Higgs boson production in association with b-quarks (left) and for the gluon fusion production process (right), calculated with the recipe from Ref. [29], which uses Ref. [69,73,74,77–80]. The contributions of all three neutral Higgs bosons have been considered. To account for asymmetries, the mean values of the positive and negative errors are shown.

the cross-section is calculated for variations of the factorization and renormalization scales by factors of two and 1/2. After evaluating each set i of opposite variations from the error eigenvectors ($\uparrow$ and $\downarrow$), the larger positive and the larger negative (signed) variations ($V_\uparrow$ and $V_\downarrow$) from all sets are separately added in quadrature to find the uncertainty values of PDF and α_s in the positive (Σ_+) and negative (Σ_-) directions:

$$\Sigma_+ = \sqrt{\sum_i \left(\max(0, V_\uparrow, V_\downarrow)\right)^2} \tag{8.1}$$

$$\Sigma_- = \sqrt{\sum_i \left(\min(0, V_\uparrow, V_\downarrow)\right)^2}. \tag{8.2}$$

Finally, the error component from the variation of the factorization and renormalization scales is added linearly to the uncertainty of PDF and α_s to find the total cross-section uncertainty.

The uncertainty of the production cross-section is discussed in depth in Ref. [29] and ranges from $6-13\,\%$, depending on the choice of m_{A^0} and $\tan\beta$. The uncertainties of the total signal cross-sections are shown in Figure 8.1 for Higgs boson production in association with b-quarks and for the gluon fusion production process. The relative uncertainties of all three neutral Higgs bosons have been weighted with the respective cross-section contributions.

Except for the $t\bar{t}$ and multi-jet backgrounds, which are normalized with data-driven methods, all background predictions rely on theoretical predictions of the underlying production cross-section. These are calculated as perturbative series up to varying orders in α_s and α_{ew}, and the associated uncertainties have again been evaluated by varying the renormalization and factorization scales and repeatedly evaluating the cross-section for each of the error eigenvectors of the respective PDF. The results and the associated uncertainties are summarized in Table 8.1. For the di-boson contribution, the uncertainty for WZ production has been assumed for all three processes in the statistical combination with the other channels in Ref. [10] to simplify the background model.

Table 8.1.: Inclusive cross-sections used for background processes within the analysis. The highest order of perturbative corrections considered and the associated uncertainty are given along with the reference of the calculation. For the di-boson contribution, the uncertainty for WZ production has been assumed for all three processes in the statistical combination with the other channels [10]. The $t\bar{t}$ background is normalized from data within the analysis, so the production cross-section is only given for completeness.

Process	Central Value [pb]	Order	Relative Uncertainty [%]	Reference
$Z/\gamma^* \to ll$, $m_{ll} > 40\,\text{GeV}$ $Z/\gamma^* \to ll$, $10\,\text{GeV} < m_{ll} < 40\,\text{GeV}$	1070 3900	NNLO	5	[175, 211, 213] [175, 211–213]
Single t	58.7 (t-channel), 3.9 (s-channel), 13.1 (Wt)	NLO	13	[151]
Di-Boson	46.2 (WW), 18.0 (WZ), 5.6 (ZZ)	NLO	5/7 7/7 5/7	[175, 211, 213]/ [10]
W + jets	10460	NNLO	5	[175, 211, 213]
$t\bar{t}$	160.1	NNLL	$^{+8}_{-9}$	[217]

8.1.2. Acceptance Uncertainties

The accurate modeling of kinematic distributions in simulated samples is very challenging: Even though perturbation theory can, in principle, yield results at arbitrarily high precision, the input parameters still limit the precision of the resulting predictions. The PDF choice and generator settings impact the distributions of observables like momenta and pseudo-rapidities. The resulting normalization uncertainties are assumed to outweigh the accompanying shape uncertainties, which are neglected. This significantly simplifies the signal and background models.

Main Acceptance Uncertainty Contributions of Signal Processes

The signal samples for b-associated Higgs boson production have been produced using Sherpa [145]. The acceptance uncertainties are evaluated by implementing the analysis cuts on particle level and reweighting the events according to the flavor tagging efficiency obtained from data in Ref. [201]. The predicted event yields in the b-tagged and b-vetoed samples is determined for the following variations [218] of the bbA^0 samples with $m_{A^0} = 120\,\text{GeV}$ and $m_{A^0} = 200\,\text{GeV}$:

- The CKKW matching parameter Q_{cut} is by default set to a value of $\sqrt{20\,\text{GeV}/E_{\text{CMS}}}$, where E_{CMS} is the center–of–mass energy. The variations $\uparrow$ and $\downarrow$ refer to values of $\sqrt{30\,\text{GeV}/E_{\text{CMS}}}$ and $\sqrt{15\,\text{GeV}/E_{\text{CMS}}}$, respectively.
- The factorization scale is by default set to a value of $\mu_0 = \frac{m_{A^0}}{4}$ and has been varied to values of $2\mu_0$ ($\uparrow$) and $\frac{\mu_0}{2}$ ($\downarrow$).
- The renormalization scale is by default set to a value of $\mu_0 = m_{A^0}$. Because Sherpa uses the same scale for the simulation of parton showers, it is only varied up and down by 10 % by recommendation of the Sherpa authors [219].
- b-quarks are by default treated as massless particles. A varied sample simulates massive b-quarks to estimate the systematic uncertainty on this assumption. Only two

Table 8.2.: Relative changes in the signal event yield after selection cuts (evaluated on particle level) for the $bb\phi$ signal process. In the b-tagged sample, the observed change in the event yield for the alternative PDF choice has been inflated from $-6.2\,\%$ ($-6.5\,\%$) for $m_\phi = 120\,(200)\,\text{GeV}$ to $\pm 12\,\%$ because taking CTEQ6.6m as only available alternative PDF choice does not comply with the recommendations of the PDF4LHC Working Group [220].

	$m_\phi = 120\,\text{GeV}$	$m_\phi = 200\,\text{GeV}$
b-tagged sample		
CKKW matching parameter ↑ / ↓	$+13.9\,\%$ / $-12.4\,\%$	$+15.4\,\%$ / $-11.8\,\%$
Factorization scale ↑ / ↓	$-10.2\,\%$ / $-4.6\,\%$	$-4.8\,\%$ / $-6.5\,\%$
Renormalization scale ↑ / ↓	$-0.1\,\%$ / $+0.4\,\%$	$-0.4\,\%$ / $+1.8\,\%$
Massive b-quarks	$-4.7\,\%$	$+1.2\,\%$
PDF choice	$-6.2\,\% \rightarrow \pm 12\,\%$	$-6.5\,\% \rightarrow \pm 12\,\%$
UE activity ↑ / ↓	$+0.5\,\%$ / $+2.0\,\%$	$+0.4\,\%$ / $+0.3\,\%$
Total acceptance uncertainty	$+19\,\%$ / $-21\,\%$	$+20\,\%$ / $-18\,\%$
b-vetoed sample		
CKKW matching parameter ↑ / ↓	$-2.2\,\%$ / $+1.3\,\%$	$-1.6\,\%$ / $+2.8\,\%$
Factorization scale ↑ / ↓	$+1.6\,\%$ / $-0.9\,\%$	$+2.7\,\%$ / $+1.1\,\%$
Renormalization scale ↑ / ↓	$-0.2\,\%$ / $-0.2\,\%$	$+0.8\,\%$ / $+0.7\,\%$
Massive b-quarks	$+0.1\,\%$	$+0.6\,\%$
PDF choice	$-0.7\,\%$	$+0.2\,\%$
UE activity ↑ / ↓	$-1.1\,\%$ / $-0.1\,\%$	$+0.6\,\%$ / $+0.6\,\%$
Total acceptance uncertainty	$+2.1\,\%$ / $-2.9\,\%$	$+4.2\,\%$ / $-1.6\,\%$

additional partons can be considered in Sherpa when treating b-quarks as massive (rather than three for massless b-quarks). Samples with up to two additional partons are therefore compared to assess the impact of neglecting the b-quark mass.

- The default PDF (CTEQ6L1) has been replaced by CTEQ6.6m in one sample to assess the uncertainty from the PDF choice, following a recommendation of the Sherpa authors [219].

- The activity from the underlying event (UE) (measured in the transverse region) has been increased (↑) or decreased (↓) by 10 %, following a recommendation of the Sherpa authors [219].

The resulting relative uncertainties on the acceptance are summarized in Table 8.2. The total uncertainty is again calculated using Eqs. (8.1) and (8.2). In the b-tagged sample, the observed change in the event yield for the alternative PDF choice has been inflated from about $\pm 6\,\%$ to $\pm 12\,\%$ because taking CTEQ6.6m as only available alternative PDF choice does not comply with the recommendations of the PDF4LHC Working Group [220], but rather follows the recommendations of the Sherpa authors [219]. The uncertainties for the b-tagged sample are much larger than for the b-vetoed sample because of the tighter cuts of the kinematic selection. In both cases, the uncertainties from the variations of the CKKW matching parameter and the factorization scale contribute significantly. The inflation of the estimated uncertainty from the PDF choice in the b-tagged sample also results in a significant contribution.

Table 8.3.: Relative changes in the signal event yield in the b-vetoed samples after selection cuts (evaluated on particle level) for the $gg \to \phi$ signal process.

	$m_\phi = 120\,\text{GeV}$
b-VETOED SAMPLE	
Perugia 2011	+2.6 %
Final State Radiation ↑ / ↓	+2.0 % / +2.0 %
Initial State Radiation ↑ / ↓	+2.0 % / +2.3 %
Renormalisation/Factorisation Scale ↑ / ↓	+1.7 % / +1.4 %
Herwig Shower	+2.7 %
Total acceptance uncertainty	+5.1 % / −0 %

The gluon fusion signal process has been simulated with the POWHEG generator. The following variations of the default parameters have been evaluated:

- The default UE tune AUET2B LO** has been replaced by the Perugia underlying event tune of 2011 [182].
- The amount of final state radiation simulated by Pythia has been increased (↑) or decreased (↓) by varying the Λ value in running α_s for time-like showers by a factor of 2 or 1/2, respectively [133].
- The amount of initial state radiation simulated by Pythia has been increased (↑) or decreased (↓) by varying the space-like parton-shower evolution the squared transverse momentum evolution scale down by a factor of 1/4 or up by a factor of 4 and the scale of the hard interaction (and thus the maximum parton virtuality allowed in Q^2-ordered space-like showers) up by a factor of 1.5 or down by a factor of 1/8, respectively [133].
- Both the renormalization and factorization scales have been varied by a factor of 2 (↑) or 0.5 (↓) around the central value of m_{A^0}.
- Herwig instead of Pythia has been used to simulate the parton shower.

The resulting relative uncertainties on the acceptance are summarized in Table 8.3 for the b-vetoed sample. The total uncertainty is again calculated using Eqs. (8.1) and (8.2). The gluon fusion contribution to the signal event yield in the b-tagged sample is very small, so an explicit evaluation would introduce large statistical uncertainties because of the limited size of simulated samples. Instead, the same uncertainties as for b-associated Higgs boson production are assumed. The POWHEG samples cannot be reevaluated with other PDFs because the Bjorken scaling variables X_i are unavailable. The impact of the PDF choice is therefore neglected for the gluon fusion production mode.

These considerations motivate the estimate of the acceptance uncertainties used within Ref. [10], summarized in Table 8.4. For b-associated Higgs boson production, the uncertainties[2] for masses between 120 and 200 GeV have been determined by linear interpolation, while the values for $m_\phi < 120\,\text{GeV}$ and $m_\phi > 200\,\text{GeV}$ have been taken from the samples with 120 and 200 GeV, respectively. For gluon fusion, the same uncertainties have been assumed for the entire mass range.

[2] excluding the uncertainty stemming from the discrimination according to the number of tagged b-jets, see below

Table 8.4.: Relative signal acceptance uncertainty values from the main acceptance uncertainty contributions.

Signal Process		Signal Acceptance Uncertainty	
	m_ϕ [GeV]	b-tagged sample	b-vetoed sample
$bb\phi$	90	$+19\,\%\,/\,-21\,\%$	$+2.1\,\%\,/\,-2.9\,\%$
	100	$+19\,\%\,/\,-21\,\%$	$+2.1\,\%\,/\,-2.9\,\%$
	110	$+19\,\%\,/\,-21\,\%$	$+2.1\,\%\,/\,-2.9\,\%$
	120	$+19\,\%\,/\,-21\,\%$	$+2.1\,\%\,/\,-2.9\,\%$
	130	$+19\,\%\,/\,-21\,\%$	$+2.4\,\%\,/\,-2.7\,\%$
	140	$+19\,\%\,/\,-20\,\%$	$+2.6\,\%\,/\,-2.6\,\%$
	150	$+19\,\%\,/\,-20\,\%$	$+2.9\,\%\,/\,-2.4\,\%$
	170	$+20\,\%\,/\,-19\,\%$	$+3.4\,\%\,/\,-2.1\,\%$
	200	$+20\,\%\,/\,-18\,\%$	$+4.2\,\%\,/\,-1.6\,\%$
	250	$+20\,\%\,/\,-18\,\%$	$+4.2\,\%\,/\,-1.6\,\%$
	300	$+20\,\%\,/\,-18\,\%$	$+4.2\,\%\,/\,-1.6\,\%$
$gg \to \phi$	90	$+20\,\%\,/\,-20\,\%$	$+5.1\,\%\,/\,-0\;\,\%$
	100	$+20\,\%\,/\,-20\,\%$	$+5.1\,\%\,/\,-0\;\,\%$
	110	$+20\,\%\,/\,-20\,\%$	$+5.1\,\%\,/\,-0\;\,\%$
	120	$+20\,\%\,/\,-20\,\%$	$+5.1\,\%\,/\,-0\;\,\%$
	130	$+20\,\%\,/\,-20\,\%$	$+5.1\,\%\,/\,-0\;\,\%$
	140	$+20\,\%\,/\,-20\,\%$	$+5.1\,\%\,/\,-0\;\,\%$
	150	$+20\,\%\,/\,-20\,\%$	$+5.1\,\%\,/\,-0\;\,\%$
	170	$+20\,\%\,/\,-20\,\%$	$+5.1\,\%\,/\,-0\;\,\%$
	200	$+20\,\%\,/\,-20\,\%$	$+5.1\,\%\,/\,-0\;\,\%$
	250	$+20\,\%\,/\,-20\,\%$	$+5.1\,\%\,/\,-0\;\,\%$
	300	$+20\,\%\,/\,-20\,\%$	$+5.1\,\%\,/\,-0\;\,\%$

Flavor Tagging of Signal Events

The predicted multiplicity distribution of b-tagged jets also needs to be considered as a source of acceptance uncertainty of the $bb\phi$ and $gg \to \phi$ samples because the events are sorted into samples of different b-jet content. Such considerations lead to moderate uncertainties, which is shown explicitly for b-associated production in the following. However, as shown below, such considerations only have a small impact on the sensitivity of the analysis, so they are neglected in Ref. [10] and are taken into account only in this thesis. For gluon fusion, an estimate is given, justifying to neglect this contribution both in Ref. [10] and in this thesis.

Following a recipe from Ref. [221], the exclusive contributions with 0, 1, or 2 b-quarks with $p_\mathrm{T} > 20\,\mathrm{GeV}$, $|\eta| < 2.4$ ($\sigma^{\mathrm{NNLO}}_{0\,b\text{-quarks}}, \sigma^{\mathrm{NLO}}_{1\,b\text{-quark}}, \sigma^{\mathrm{LO}}_{2\,b\text{-quarks}}$) can be used to approximate the exclusive contributions with 0 or 1 b-tagged jets ($\sigma^{\mathrm{NNLO}}_{0\ b\text{-tagged jets}}, \sigma^{\mathrm{NLO}}_{1\ b\text{-tagged jet}}$) at the same order in α_s:

$$\sigma^{\mathrm{NNLO}}_{0\ b\text{-tagged jets}} = \sigma^{\mathrm{NNLO}}_{0\,b\text{-quarks}} + (1-\varepsilon_b)\sigma^{\mathrm{NLO}}_{1\,b\text{-quark}} + (1-\varepsilon_b)^2\sigma^{\mathrm{LO}}_{2\,b\text{-quarks}} \tag{8.3}$$

$$\sigma^{\mathrm{NLO}}_{1\ b\text{-tagged jet}} = \varepsilon_b\sigma^{\mathrm{NLO}}_{1\,b\text{-quark}} + 2\varepsilon_b(1-\varepsilon_b)\sigma^{\mathrm{LO}}_{2\,b\text{-quarks}}. \tag{8.4}$$

The efficiency ε_b at which true b-jets with $p_\mathrm{T} > 20\,\mathrm{GeV}$, $|\eta| < 2.5$ are tagged as b-jets has been determined for the selected flavor tagging working point from the simulated samples with Higgs boson masses of 100, 120, 160, 200, and 300 GeV (see Table 8.5) and is approximately 60 % for the five mass hypotheses. For other Higgs boson mass hypotheses, the value is

Table 8.5.: Exclusive and inclusive cross-sections and uncertainties for b-associated Higgs boson production of neutral Higgs bosons. The Yukawa coupling strengths predicted by the SM have been assumed. $\sigma^{\text{NNLO}}_{\text{total}}$, $\sigma^{\text{NNLO}}_{0\,b\text{-quarks}}$, $\sigma^{\text{NLO}}_{1\,b\text{-quark}}$, and $\sigma^{\text{LO}}_{2\,b\text{-quarks}}$ and the associated uncertainties have been taken from Ref. [221], except for the PDF, α_s uncertainty of $\sigma^{\text{NNLO}}_{\text{total}}$ [222].

m_ϕ	[GeV]	100	120	160	200	300
ε_b	[%]	59	61	62	63	62
$\sigma^{\text{NNLO}}_{\text{total}}$	[fb]	349	188	66.4	27.9	4.98
Scale uncertainty	[%]	$^{+2.9}_{-10}$	$^{+3.1}_{-9.1}$	$^{+3.2}_{-7.6}$	$^{+3.2}_{-6.9}$	$^{+3.0}_{-5.7}$
PDF, α_s uncertainty	[%]	$^{+3.4}_{-3.2}$	$^{+3.5}_{-3.3}$	$^{+3.9}_{-3.6}$	$^{+4.3}_{-4.0}$	$^{+5.6}_{-5.1}$
Total uncertainty	[%]	$^{+4.5}_{-10.5}$	$^{+4.7}_{-9.7}$	$^{+5.0}_{-8.4}$	$^{+5.3}_{-8.0}$	$^{+6.3}_{-7.6}$
$\sigma^{\text{NNLO}}_{0\,b\text{-quarks}}$	[fb]	239	124	41.2	16.5	2.71
Scale uncertainty	[%]	$^{+8.3}_{-15.9}$	$^{+8.6}_{-14.4}$	$^{+9.0}_{-11.7}$	$^{+9.1}_{-9.9}$	$^{+8.9}_{-8.2}$
PDF, α_s uncertainty	[%]	$^{+3.8}_{-3.2}$	$^{+3.7}_{-3.9}$	$^{+3.7}_{-4.8}$	$^{+4.3}_{-4.2}$	$^{+5.7}_{-5.4}$
Total uncertainty	[%]	$^{+9.1}_{-16.2}$	$^{+9.4}_{-14.9}$	$^{+9.7}_{-12.6}$	$^{+10.1}_{-10.8}$	$^{+10.6}_{-9.8}$
$\sigma^{\text{NLO}}_{1\,b\text{-quark}}$	[fb]	101	58.6	22.9	10.3	2.02
Scale uncertainty	[%]	$^{+4.1}_{-7.0}$	$^{+4.3}_{-7.0}$	$^{+4.7}_{-7.2}$	$^{+5.1}_{-8.5}$	$^{+5.7}_{-8.8}$
PDF, α_s uncertainty	[%]	$^{+3.4}_{-3.8}$	$^{+4.2}_{-3.5}$	$^{+5.4}_{-3.4}$	$^{+5.1}_{-4.4}$	$^{+5.3}_{-4.7}$
Total uncertainty	[%]	$^{+5.3}_{-8.0}$	$^{+6.0}_{-7.8}$	$^{+7.2}_{-8.0}$	$^{+7.2}_{-9.6}$	$^{+7.8}_{-10}$
$\sigma^{\text{LO}}_{2\,b\text{-quarks}}$	[fb]	12.0	7.20	2.97	1.39	0.29
Scale uncertainty	[%]	$^{+65}_{-35}$	$^{+62}_{-34}$	$^{+57}_{-32}$	$^{+54}_{-31}$	$^{+49}_{-30}$
PDF, α_s uncertainty	[%]	$^{+3}_{-3}$	$^{+2}_{-3}$	$^{+2}_{-3}$	$^{+3}_{-3}$	$^{+4}_{-4}$
Total uncertainty	[%]	$^{+65}_{-35}$	$^{+62}_{-34}$	$^{+57}_{-33}$	$^{+54}_{-31}$	$^{+49}_{-30}$
$\sigma^{\text{NLO}}_{1\,b\text{-tagged jet}}$	[fb]	65.4	39.2	15.6	7.14	1.39
Scale uncertainty	[%]	$^{+9.5}_{-9.5}$	$^{+9.3}_{-9.4}$	$^{+9.4}_{-9.5}$	$^{+9.5}_{-10.6}$	$^{+9.9}_{-10.8}$
PDF, α_s uncertainty	[%]	$^{+3.3}_{-3.7}$	$^{+4.0}_{-3.4}$	$^{+5.1}_{-3.4}$	$^{+4.9}_{-4.3}$	$^{+5.1}_{-4.6}$
Total uncertainty	[%]	$^{+10.6}_{-10.4}$	$^{+10.9}_{-10.1}$	$^{+11.6}_{-10.2}$	$^{+11.4}_{-11.6}$	$^{+11.8}_{-11.9}$
Acceptance uncertainty contribution	[%]	$^{+6.1}_{-0}$	$^{+6.2}_{-0.4}$	$^{+6.6}_{-1.8}$	$^{+6.1}_{-3.6}$	$^{+5.5}_{-4.3}$
$\sigma^{\text{NNLO}}_{0\,b\text{-tagged jets}}$	[fb]	282	148	50.3	20.5	3.52
Scale uncertainty	[%]	$^{+8.1}_{-14.7}$	$^{+8.3}_{-13.4}$	$^{+8.7}_{-11.1}$	$^{+8.8}_{-9.8}$	$^{+8.7}_{-8.6}$
PDF, α_s uncertainty	[%]	$^{+3.7}_{-3.3}$	$^{+3.8}_{-3.8}$	$^{+4.0}_{-4.5}$	$^{+4.4}_{-4.2}$	$^{+5.6}_{-5.2}$
Total uncertainty	[%]	$^{+9.0}_{-15.1}$	$^{+9.2}_{-14}$	$^{+9.7}_{-12}$	$^{+9.9}_{-10.7}$	$^{+10.4}_{-10.1}$
Acceptance uncertainty contribution	[%]	$^{+4.5}_{-4.6}$	$^{+4.5}_{-4.3}$	$^{+4.7}_{-3.6}$	$^{+4.6}_{-2.8}$	$^{+4.1}_{-2.5}$

obtained by linear interpolation, and the value for a Higgs boson mass of 100 GeV is also used at 90 GeV.

By comparison of the uncertainties of the inclusive cross-section and the sums in Eqs. (8.3) and (8.4), the additional acceptance uncertainty introduced by flavor tagging can be assessed.

The inclusive cross-section $\sigma^{\text{NNLO}}_{\text{total}}$ and the exclusive cross-sections $\sigma^{\text{NNLO}}_{0\,b\text{-quarks}}$, $\sigma^{\text{NLO}}_{1\,b\text{-quark}}$, $\sigma^{\text{LO}}_{2\,b\text{-quarks}}$ are given in Ref. [221] along with the uncertainties from PDF, α_s, and scale variations. The total uncertainty of the inclusive cross-section is compared to the total uncertainty of the sums in Eqs. (8.3) or (8.4), adding linearly the uncertainties of the exclusive contributions. The difference is taken as measure of the additional acceptance uncertainty from

the sorting into different samples. The calculation is shown in Table 8.5. The additional acceptance uncertainty reaches up to $^{+6}_{-4}$ % at $m_\phi = 200\,\text{GeV}$ for the b-tagged sample and up to $\pm 5\,\%$ at $m_\phi = 100\,\text{GeV}$. The double-counting of effects is avoided by considering only the difference of uncertainties: The scale, PDF, and α_s variations have been performed in a consistent manner between the inclusive and exclusive cross-sections.

While the acceptance uncertainty for $bb\phi$ arising from the selection of events with exactly one b-jet does not significantly contribute to the total acceptance uncertainty in the b-tagged sample, the effect exceeds the magnitude of the other sources of acceptance uncertainty in the b-vetoed sample.

The impact on the expected exclusion limits on the product of the production cross-section and the branching fraction to τ lepton pairs from the b-tagged (b-vetoed) sample is less than 0.8 % (0.5 %) across the examined mass range for b-associated production. Consequently, the published result from the combination with the other channels [10], which does not take this contribution into account, remains valid.

For signal events with Higgs boson production from gluon fusion, no explicit evaluation of the exclusive cross-sections is necessary: At next–to–leading order (NLO), such events on average only contain about 0.02 true b-jets on particle level at the preselection stage (see Figure 5.1(c)).

The acceptance of signal events with Higgs boson production from gluon fusion into the b-tagged sample relies on the mistagging of light jets. The selected flavor tagging algorithm offers a powerful rejection against light jets $R_{\text{light}}^{p_\text{T}>15\,\text{GeV}} \approx 58$ as other source of b-tagged jets. Given that no jets are expected at leading order (LO) and that the ratio of the NNLO and NLO cross-sections $\frac{\sigma_\text{NLO}}{\sigma_\text{LO}}$ is approximately 1.16 [223], a rough upper limit on the impact of flavor tagging uncertainties can be calculated:

Say that a fraction of events matching the relative cross-section difference of NLO and NNLO , which is approximately $\frac{1.16-1}{1.16} = 14\,\%$ in the mass range from 125 to 300 GeV [223], obtained an additional light jet when taking NNLO and higher-order corrections into account. This would lead to a $\frac{14\,\%}{R_{\text{light}}^{p_\text{T}>15\,\text{GeV}}} \approx 0.2\,\%$ change (with respect to the inclusive cross-section) from the b-vetoed sample into the b-tagged sample at the preselection stage. For gluon fusion in the b-vetoed sample, the expected limit on the product of the production cross-section and the branching fraction to τ lepton pairs changes by less than 0.2 % for all Higgs boson mass hypotheses when assuming an additional uncertainty of even 0.7 %. This contribution is therefore neglected.

The impact on the sensitivity for Minimal Supersymmetric Standard Model (MSSM) scenarios is also small: Even though 0.2 % of the gluon fusion cross-section at the preselection stage correspond to between 6 and 15 %[3] of the contribution from gluon fusion after the requirement of exactly one b-tagged jet, the resulting absolute uncertainty is dwarfed by the acceptance uncertainty and the cross-section uncertainties of the MSSM from the dominant process $bb\phi$.

The resulting total signal acceptance uncertainties are summarized in Table 8.6.

Acceptance Uncertainties of Background Processes

The use of data-driven background estimation techniques reduces the reliance on simulation for the background estimates, leading to an improved sensitivity of the analysis. The estimation of the dominant $Z/\gamma^* \to \tau\tau$ background mainly relies on an accurate description of the lepton p_T spectra in simulation (for obtaining the correct normalization factor for

[3] depending on the mass hypothesis, see Table 6.5

Table 8.6.: Relative signal acceptance uncertainty values, including the contribution from the selection of either no b-jets (b-vetoed sample) or exactly one b-jet (b-tagged sample).

Signal Process		Signal Acceptance Uncertainty	
	m_ϕ [GeV]	b-tagged sample	b-vetoed sample
$bb\phi$	90	$+20\,\%\,/\,-21\,\%$	$+5.0\,\%\,/\,-5.5\,\%$
	100	$+20\,\%\,/\,-21\,\%$	$+5.0\,\%\,/\,-5.5\,\%$
	110	$+20\,\%\,/\,-21\,\%$	$+5.0\,\%\,/\,-5.3\,\%$
	120	$+20\,\%\,/\,-21\,\%$	$+5.0\,\%\,/\,-5.2\,\%$
	130	$+20\,\%\,/\,-21\,\%$	$+5.2\,\%\,/\,-4.9\,\%$
	140	$+20\,\%\,/\,-20\,\%$	$+5.3\,\%\,/\,-4.7\,\%$
	150	$+20\,\%\,/\,-20\,\%$	$+5.5\,\%\,/\,-4.5\,\%$
	170	$+21\,\%\,/\,-19\,\%$	$+5.8\,\%\,/\,-4.0\,\%$
	200	$+21\,\%\,/\,-18\,\%$	$+6.2\,\%\,/\,-3.2\,\%$
	250	$+21\,\%\,/\,-18\,\%$	$+6.0\,\%\,/\,-3.1\,\%$
	300	$+21\,\%\,/\,-19\,\%$	$+5.9\,\%\,/\,-2.9\,\%$
$gg \to \phi$	90	$+20\,\%\,/\,-20\,\%$	$+5.1\,\%\,/\,-0\,\%$
	100	$+20\,\%\,/\,-20\,\%$	$+5.1\,\%\,/\,-0\,\%$
	110	$+20\,\%\,/\,-20\,\%$	$+5.1\,\%\,/\,-0\,\%$
	120	$+20\,\%\,/\,-20\,\%$	$+5.1\,\%\,/\,-0\,\%$
	130	$+20\,\%\,/\,-20\,\%$	$+5.1\,\%\,/\,-0\,\%$
	140	$+20\,\%\,/\,-20\,\%$	$+5.1\,\%\,/\,-0\,\%$
	150	$+20\,\%\,/\,-20\,\%$	$+5.1\,\%\,/\,-0\,\%$
	170	$+20\,\%\,/\,-20\,\%$	$+5.1\,\%\,/\,-0\,\%$
	200	$+20\,\%\,/\,-20\,\%$	$+5.1\,\%\,/\,-0\,\%$
	250	$+20\,\%\,/\,-20\,\%$	$+5.1\,\%\,/\,-0\,\%$
	300	$+20\,\%\,/\,-20\,\%$	$+5.1\,\%\,/\,-0\,\%$

the embedded sample after the preselection, see Subsection 7.1.1). An uncertainty of 5 % is assumed, based on a comparison to the results obtained with the CTEQ6.6 PDF and with different scale choices in Ref. [12].

The same uncertainty is assumed for the $Z/\gamma^* \to \ell\ell$ backgrounds, based on the almost identical kinematic properties of the daughter particles of the Z/γ^* boson.

As the $t\bar{t}$ sample is normalized from a control region, the acceptance uncertainty affects the extrapolation factor ($k_{\mathrm{MC}}^{b\text{-tag}/b\text{-veto}}$). The impact is estimated from $t\bar{t}$ samples of two different Monte Carlo (MC) event generators. The systematic uncertainties of this method are described in Subsection 8.2.3.

Because of their relatively low contribution to the selected samples, a value of 5 % has also been assumed for the acceptance uncertainty for the W + jets and di-boson samples without further studies.

8.1.3. Simulated Detector Response

In order to minimize and correctly assess the uncertainties of the detector response in simulation, a wide range of performance measurements have been performed with the ATLAS detector. The results were used to calibrate the simulated detector response to match the measured performance and to provide variations of the nominal performance which reflect the

uncertainty of the nominal performance and can be propagated through analyses to quantify the impact of each source of systematic uncertainty.

Because the detector response also depends on the data-taking conditions, a precise prediction first relies on a good description of their evolution in 2011 (see Subsection 3.1.1). The simulated performance of the detector sub-systems is then corrected to match the measured performance for the given data-taking conditions on an event–by–event basis.

The impact on the shapes of the $m_{\tau\tau}^{\mathrm{MMC}}$ distributions has been examined for all systematic variations, considering both the b-tagged and the b-vetoed sample, in order to determine which uncertainties can be treated as pure normalization uncertainties and whose impact on the shapes of the $m_{\tau\tau}^{\mathrm{MMC}}$ distributions must be taken into account for the final results. The shapes of $m_{\tau\tau}^{\mathrm{MMC}}$ distributions of variations not considered as shape uncertainties are collected in Appendix B.

Data-Taking Conditions

The relative systematic uncertainty of the integrated luminosity for the full set of collision data considered for this thesis was 3.9 % [125, 126] when the data was evaluated for publication [10]. Before finalizing the results, an improved luminosity measurement [224] with a relative uncertainty of 1.8 % became available. Because the impact on the sensitivity of the statistical combination of all channels has been determined to be marginal, the event yields and uncertainties have not been reevaluated for Ref. [10] or this thesis.

Muons

The momentum resolution for muons has been determined from collision data for the Inner Detector and the Muon Spectrometer [189, 225]. To reflect the uncertainty of this measurement, the calibration applied to the transverse momentum values obtained from the Inner Detector and the Muon Spectrometer (see Subsection 6.1.1) can be varied by one standard deviation ("μ ID track p_{T} ↑"/"μ ID track p_{T} ↓" and "μ MS track p_{T} ↑"/"μ MS track p_{T} ↓" in Tables 8.7 and 8.8). The impact on the shapes of the $m_{\tau\tau}^{\mathrm{MMC}}$ distributions is negligible (see Figures B.1 and B.2).

The combined efficiency of the reconstruction and identification in simulated data is also corrected by reweighting (see Subsection 6.1.1). The central value of the respective scale factor (SF) is distributed with a root mean square (RMS) of 0.02 around the central value of 0.98. The variations of the respective SF by one standard deviation are denoted as "μ recon./ID eff. ↑"/"μ recon./ID eff. ↓" in Tables 8.7 and 8.8. The impact on the shapes of the $m_{\tau\tau}^{\mathrm{MMC}}$ distributions is negligible (see Figure B.3).

The efficiency of the isolation requirements has been found to agree between simulation and collision data within the systematic uncertainties of the measurement. These have been estimated to be 4 % for transverse momenta between 10 and 20 GeV and 1 % for larger p_{T} values [183]. These variations are denoted as "μ iso. SF ↑"/"μ iso. SF ↓" in Tables 8.7 and 8.8. The impact on the shapes of the $m_{\tau\tau}^{\mathrm{MMC}}$ distributions is negligible (see Figure B.4).

The normalization uncertainty contribution from muon simulation is about 2 %.

Electrons

The energy scale and resolution for electrons has been measured, and the performance in simulation is corrected [136, 193]. The systematic uncertainties from these studies are reflected by the "e energy scale ↑"/"e energy scale ↓" and "e energy res. ↑"/"e energy res. ↓"

variations, respectively. The impact on the shapes of the $m_{\tau\tau}^{\mathrm{MMC}}$ distributions is negligible (see Figures B.5 and B.6).

The efficiencies of the reconstruction step (including the track quality cuts) and the identification step are also corrected by reweighting [136,191], resulting in a SF, which is distributed with a RMS of about 0.02 around the mean value of 1. The efficiency of the reconstruction and identification steps are varied by one standard deviation, denoted as "e recon./track qual. eff. ↑"/"e recon./track qual. eff. ↓" and "e ID ↑"/"e ID ↓" in Tables 8.7 and 8.8, respectively. The impact on the shapes of the $m_{\tau\tau}^{\mathrm{MMC}}$ distributions is negligible (see Figures B.7 and B.8).

Just as for muons, the efficiency of the electron isolation requirements has been found to agree between simulation and collision data. The uncertainties of the measurement are 4 % for transverse momenta between 15 and 20 GeV and 2 % for larger p_{T} values [183]. These variations are denoted as "e iso. SF ↑"/"e iso. SF ↓" in Tables 8.7 and 8.8. The impact on the shapes of the $m_{\tau\tau}^{\mathrm{MMC}}$ distributions is negligible (see Figure B.9).

The total normalization uncertainty contribution from electron simulation is about 3 %.

Trigger Efficiencies

A precise knowledge of the efficiencies of the electron, muon, and electron–muon triggers is very important for the overall uncertainties. In order to minimize the normalization uncertainty contribution related to the trigger and to avoid any bias in the kinematic distributions that rely on lepton properties, reconstructed leptons were matched to the relevant trigger signatures, and the transverse momenta were restricted to ranges above the trigger thresholds (see Subsection 6.1.3).

Events passing these requirements are reweighted to match the performance measured in collision data (see Subsection 6.1.3). The remaining uncertainty has been determined for the electron trigger (0.3 %) and the muon trigger (0.5 %) [196], so it is negligible in comparison to the lepton reconstruction, identification, and isolation efficiency uncertainties.

Jets, Flavor Tagging

The jet energy reconstruction has been calibrated and validated [226, 227], allowing for a calibration of the scale and the resolution of the reconstructed jet energy. The jet energy scale (JES) uncertainty consists of several components: The transverse momenta of jets carry an uncertainty of up to about 3 % for light-flavored jets, depending mainly on the transverse momentum [226]. This contribution also takes into account the number of reconstructed vertices and other jets in the event.

A flavor-dependent component is added quadratically for simulated b-jets to match the measured resolution increase with respect to light jets. It amounts to 2.5 % in the p_{T} range from 20 to 40 GeV and gradually declines to 0.76 % above 600 GeV [226].

The associated systematic uncertainties are propagated to the analysis by evaluating the variation by one standard deviation: "Jet energy scale ↑"/"Jet energy scale ↓" and "Jet energy resolution ↑". These are compared to the nominal distributions for $t\bar{t}$, simulated $Z/\gamma^* \to \tau\tau$, and signal events in Figures 8.2 and 8.3. For $t\bar{t}$ events in the b-vetoed sample and Higgs boson production by gluon fusion in the b-tagged sample, statistical uncertainties dominate.

These variations have a significant impact on the shapes of the $m_{\tau\tau}^{\mathrm{MMC}}$ distributions: Both the "Jet energy scale ↑" and "Jet energy resolution ↑" variations shift the $m_{\tau\tau}^{\mathrm{MMC}}$ distributions to higher values, while the "Jet energy scale ↓" variation shifts the $m_{\tau\tau}^{\mathrm{MMC}}$ distributions to lower values. The effect is more pronounced in the b-tagged than in the b-vetoed sample because of the larger jet multiplicity of the b-tagged sample and the larger p_{T} uncertainty for

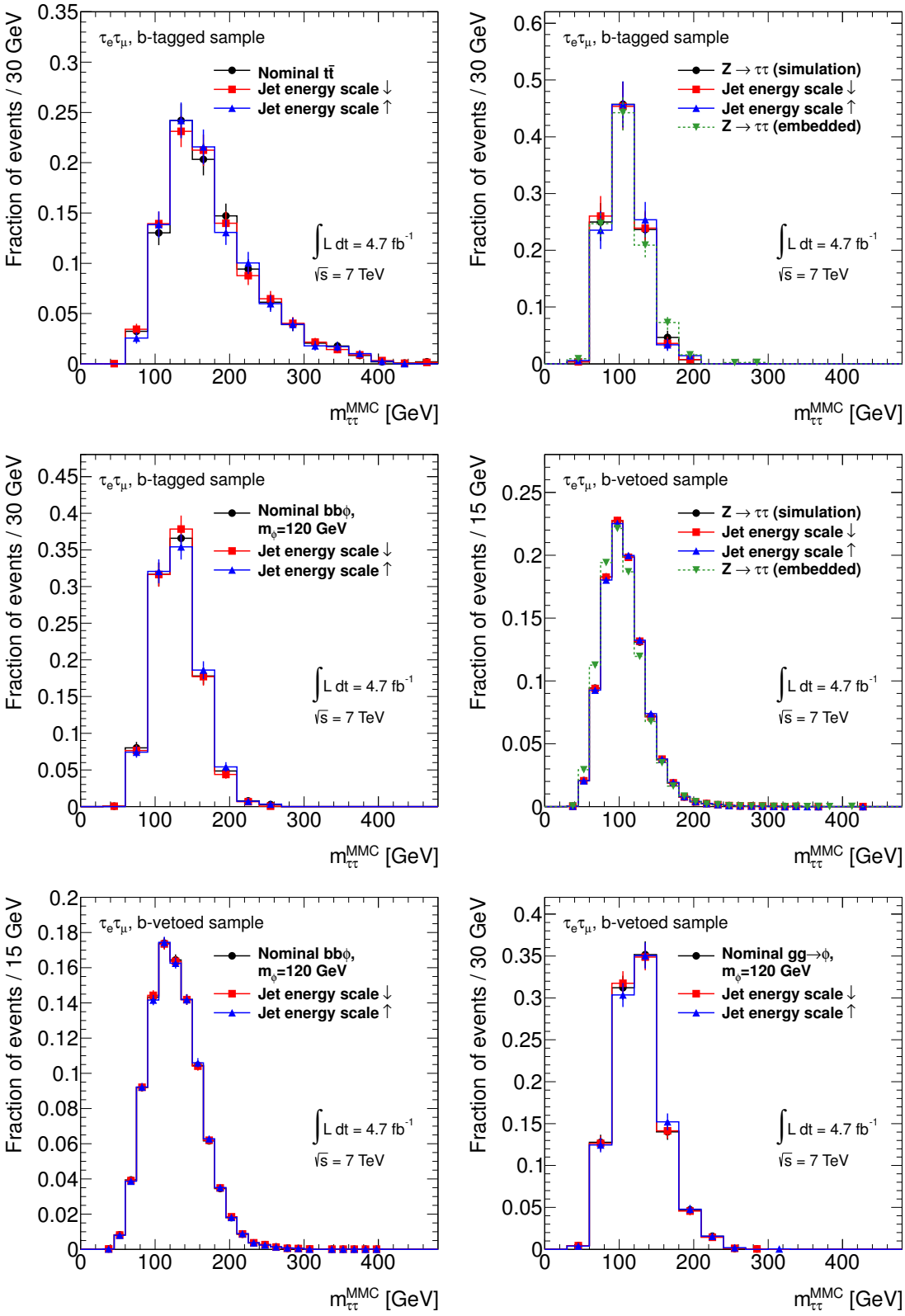

Figure 8.2.: Impact of the jet energy scale uncertainty on the shapes of the $m_{\tau\tau}^{\mathrm{MMC}}$ distributions of the b-tagged (first three Figures) and the b-vetoed (last three Figures) samples for $t\bar{t}$, simulated $Z/\gamma^* \to \tau\tau$ events, and the two Higgs boson production modes. Note that the statistical uncertainties for $t\bar{t}$ (gluon fusion) are too large to compare shapes in the b-vetoed (b-tagged) sample.

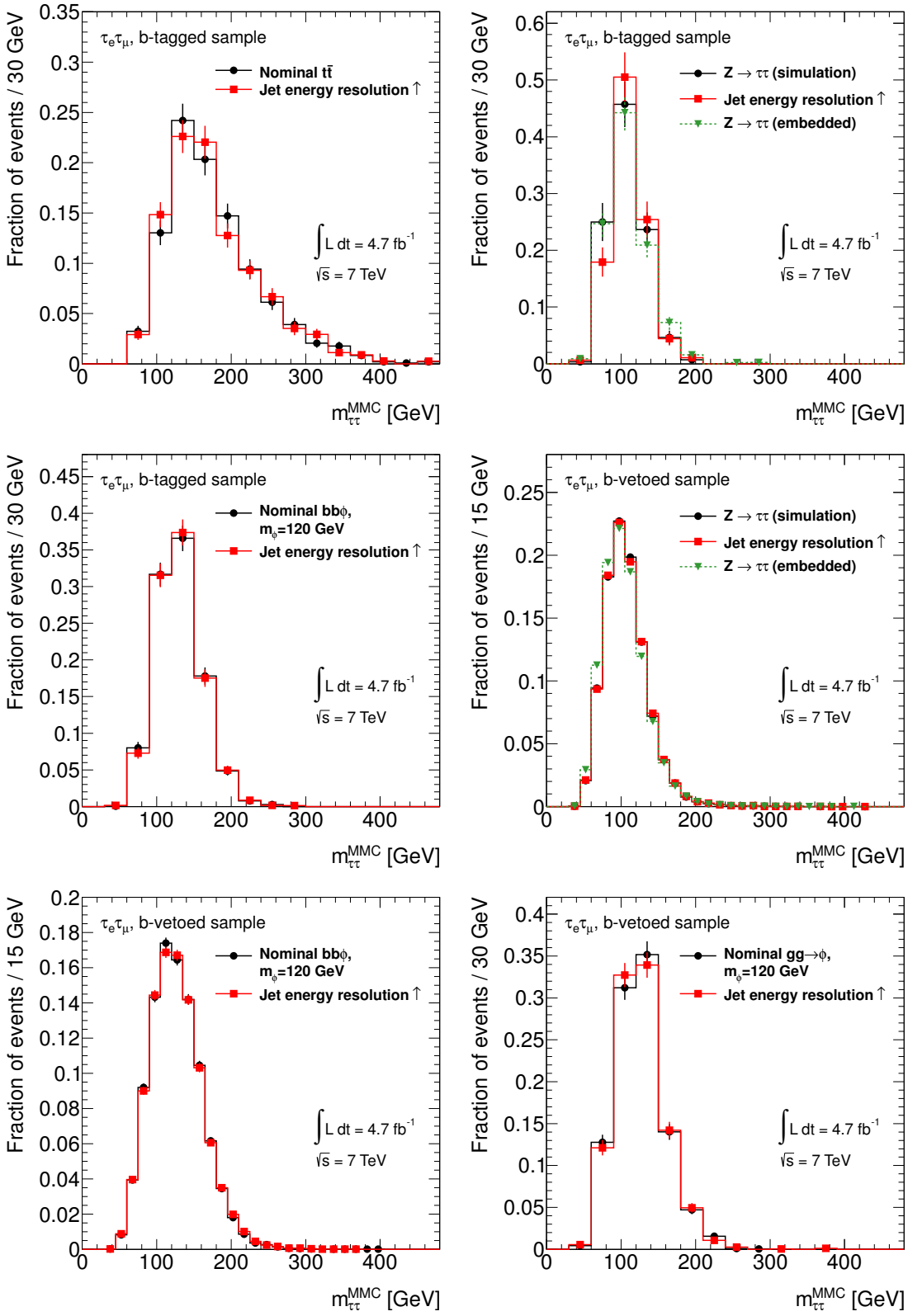

Figure 8.3.: Impact of the jet energy resolution on the shapes of the $m_{\tau\tau}^{\mathrm{MMC}}$ distributions of the b-tagged (first three Figures) and the b-vetoed (last three Figures) samples for $t\bar{t}$, simulated $Z/\gamma^* \to \tau\tau$ events, and the two Higgs boson production modes. Note that the statistical uncertainties for $t\bar{t}$ (gluon fusion) are too large to compare shapes in the b-vetoed (b-tagged) sample.

b-jets (see below). The given variations are used to quantify the shape uncertainties of the $m_{\tau\tau}^{\mathrm{MMC}}$ distributions for signal and background events.

In the description of $Z/\gamma^* \to \tau\tau$ events, different shapes have been observed in the H_{T} distribution (see Figure 7.5) at the preselection stage in simulation on one hand and in the embedded sample on the other hand. As discussed in Subsection 8.2.1, the data-driven estimate from the embedded sample is preferred over the estimate based purely on simulation because of the lower overall uncertainties.

Furthermore, the flavor tagging result in simulated events is calibrated to reproduce the efficiency measured in data by reweighting the event according to the flavor and kinematic properties of the jets (see Subsection 6.1.4). The systematic uncertainties of the efficiency measurements of light jets, b-jets and c-jets [200] are represented by the "Mistag light ↑"/"Mistag light ↓", "ε_b ↑"/"ε_b ↓", and "ε_c ↑"/"ε_c ↓" variations, respectively. The impact on the shapes of the $m_{\tau\tau}^{\mathrm{MMC}}$ distributions is negligible (see Figures B.10 through B.12).

Missing Transverse Energy

The reconstruction of missing transverse energy (see Subsection 6.1.6) depends on the measured momenta of all objects in the event. For the missing transverse energy calculation [206], the quality criteria detailed in Subsection 6.1.6 are applied to the various reconstructed objects. The impact of all object-related systematic variations on the missing transverse energy and $\sum E_{\mathrm{T}}$ values is considered [228].

The missing transverse energy value is also sensitive to changes of the pileup activity and the calibration of calorimeter clusters that do not belong to any reconstructed objects. The associated uncertainties are evaluated by considering the variations "Pileup ↑"/"Pileup ↓" and "Calo. clusters ↑"/"Calo. clusters ↓", respectively.

As shown in Figures 8.4 and 8.5, these variations have a significant impact on the shapes of the $m_{\tau\tau}^{\mathrm{MMC}}$ distributions: The "Pileup ↑" and "Calo. clusters ↑" variations shift the $m_{\tau\tau}^{\mathrm{MMC}}$ distributions to higher values, while the shift for the "Pileup ↓" and "Calo. clusters ↓" variations goes into the opposite direction. The impact on the b-tagged and b-vetoed samples by the $E_{\mathrm{T}}^{\mathrm{miss}}$ uncertainties is similarly pronounced. The given variations are used to quantify the shape uncertainties for the $m_{\tau\tau}^{\mathrm{MMC}}$ distributions of signal and background events.

In the description of $Z/\gamma^* \to \tau\tau$ events, different shapes have been observed in the missing transverse energy and $m_{\tau\tau}^{\mathrm{MMC}}$ distributions (see Figure 7.4) at the preselection stage in simulation on one hand and in the embedded sample on the other hand. As discussed in Subsection 8.2.1, the data-driven estimate from the embedded sample is preferred over the estimate based purely on simulation because of the lower overall uncertainties.

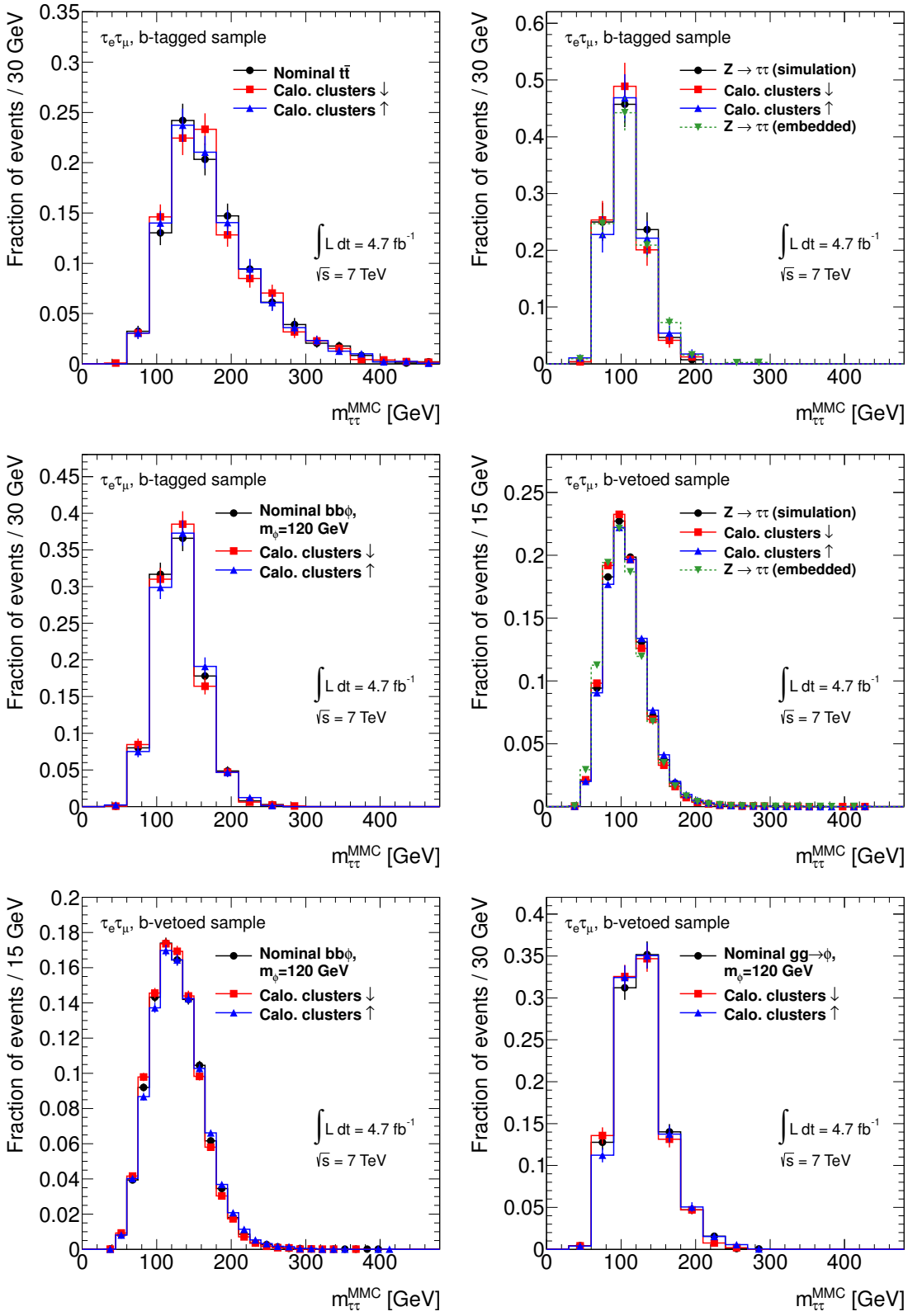

Figure 8.4.: Impact of the "Calo. clusters ↑"/"Calo. clusters ↓" variations on the shapes of the $m_{\tau\tau}^{\mathrm{MMC}}$ distributions of the b-tagged (first three Figures) and the b-vetoed (last three Figures) samples for $t\bar{t}$, simulated $Z/\gamma^* \to \tau\tau$ events, and the two Higgs boson production modes. Note that the statistical uncertainties for $t\bar{t}$ (gluon fusion) are too large to compare shapes in the b-vetoed (b-tagged) sample.

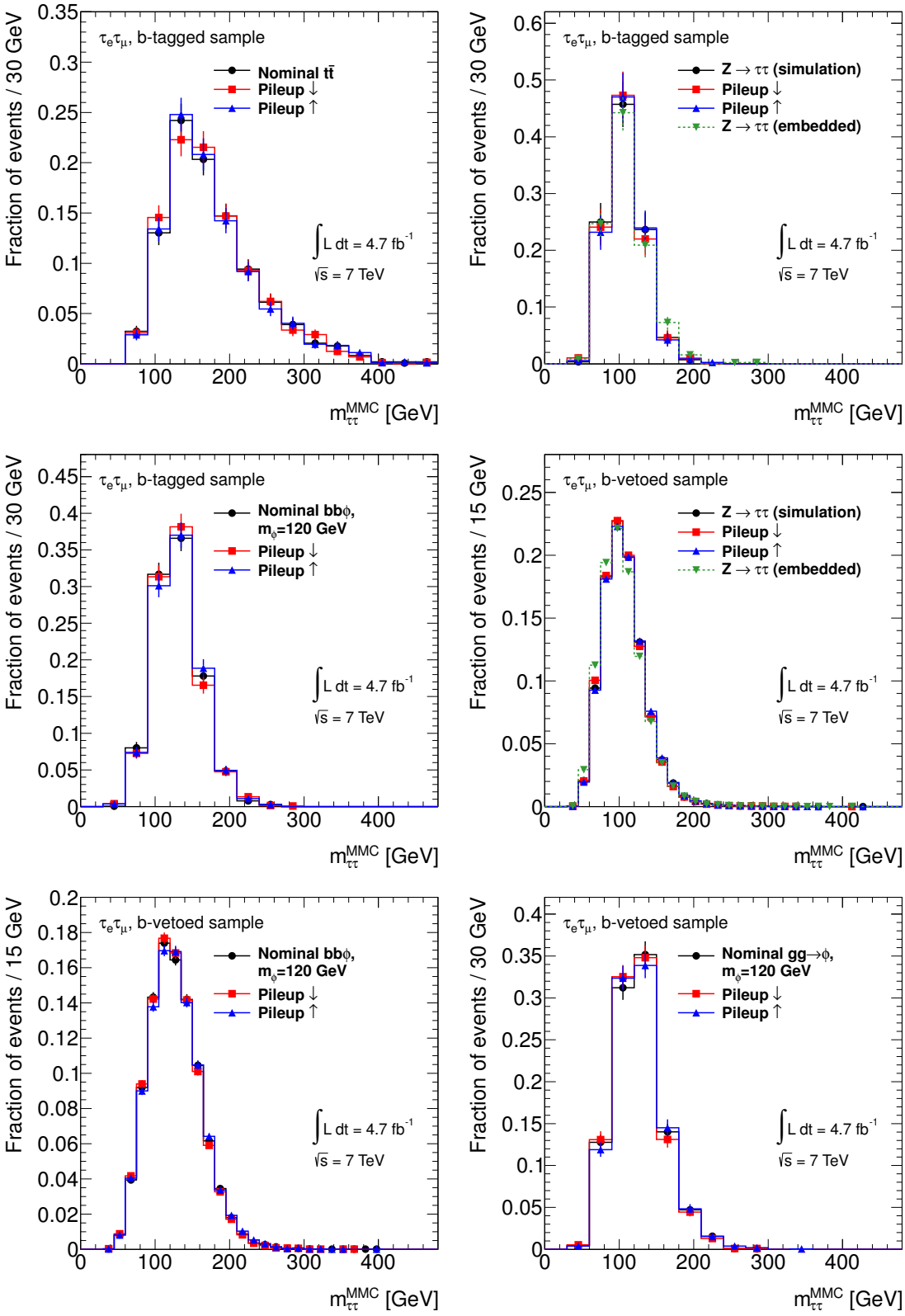

Figure 8.5.: Impact of the "Pileup ↑"/"Pileup ↓" variations on the shapes of the $m_{\tau\tau}^{\mathrm{MMC}}$ distributions of the b-tagged (first three Figures) and the b-vetoed (last three Figures) samples for $t\bar{t}$, simulated $Z/\gamma^* \to \tau\tau$ events, and the two Higgs boson production modes. Note that the statistical uncertainties for $t\bar{t}$ (gluon fusion) are too large to compare shapes in the b-vetoed (b-tagged) sample.

8.2. Uncertainties of Data-Driven Methods

Data-driven background estimation techniques can mitigate or even eliminate some of the uncertainties discussed in Section 8.1. This Section gives an overview of the uncertainties that these methods carry.

8.2.1. Method Uncertainties of the Embedding Technique

The embedding technique produces hybrid events by selecting collision data event and subsequently subtracting and adding detector hits and energy deposits from the original muons and the simulated τ_{lep} decay products (see Subsection 7.1.1). Uncertainties related to the modeling of the UE and pileup effects therefore only affect the normalization, which relies on simulating the event yield at the preselection stage. The simulated detector response to jets plays only a minor role because no cuts on jets are applied at the preselection stage, but energy deposits by jets impact the lepton isolation variables and other quantities used for their identification in the case of overlap. For the b-tagged sample, on the other hand, it constitutes the dominant contribution to the systematic uncertainty for a simulation-based estimation of the $Z/\gamma^* \to \tau\tau$ contribution (see Table 8.9): By using the embedding technique instead of simulation to estimate the $m_{\tau\tau}^{\text{MMC}}$ shape and the cut efficiencies for the $Z/\gamma^* \to \tau\tau$ contribution, the detector-related normalization uncertainty is reduced from $^{+13.5\,\%}_{-15.6\,\%}$ to $^{+6.9\,\%}_{-6.1\,\%}$, including the uncertainties introduced by the embedding procedure, which are explained in Subsection 7.1.1.

All applicable variations are evaluated at the preselection level for the Alpgen and embedded samples and after the kinematic selection for the embedded sample to quantify their impact:

- The removal of the original muons includes a subtraction of their energy deposits in the calorimeters. In order to account for mismodeling, the subtracted energy in each calorimeter cell is scaled up (down) by 30 % in the "Subtracted μ calo. deposits ↑" ("Subtracted μ calo. deposits ↓") variation.

- In order to estimate the potential bias of the isolation requirements applied to the original muons (see Subsection 7.1.1), the isolation requirements are dropped in the "No isolation" variation and tightened in the "Tighter isolation" variation (applying the same isolation cuts as in this analysis, see Subsection 6.1.1).

- The uncertainty of the emulation of a trigger decision in embedded events in the b-vetoed sample is evaluated by assigning a shape uncertainty to the central shape from trigger emulation, using the "Trigger reweighting" variation (see Subsection 7.1.1).

As shown in Figure 8.6, these variations have a significant impact on the shapes of the $m_{\tau\tau}^{\text{MMC}}$ distributions in the b-tagged and the b-vetoed samples. They are therefore used to define shape uncertainties for signal and background events. Because of the larger statistical uncertainties in the b-tagged sample (compared to the b-vetoed sample), the impact of the lack of trigger simulation in embedded events is insignificant, so no trigger correction and no additional shape uncertainty needs to be applied for the central prediction in the b-tagged sample (`noTrig`, which carries smaller statistical uncertainties than the trigger emulation or event reweighting variations).

As mentioned in Subsection 7.1.1, the selection of $Z/\gamma^* \to \mu\mu$ events for the embedded sample has a purity of about 99 % [210]. The largest other contribution comes from $t\bar{t}$ events. Because of the b-jet veto in the b-vetoed sample and further kinematic cuts particularly in the

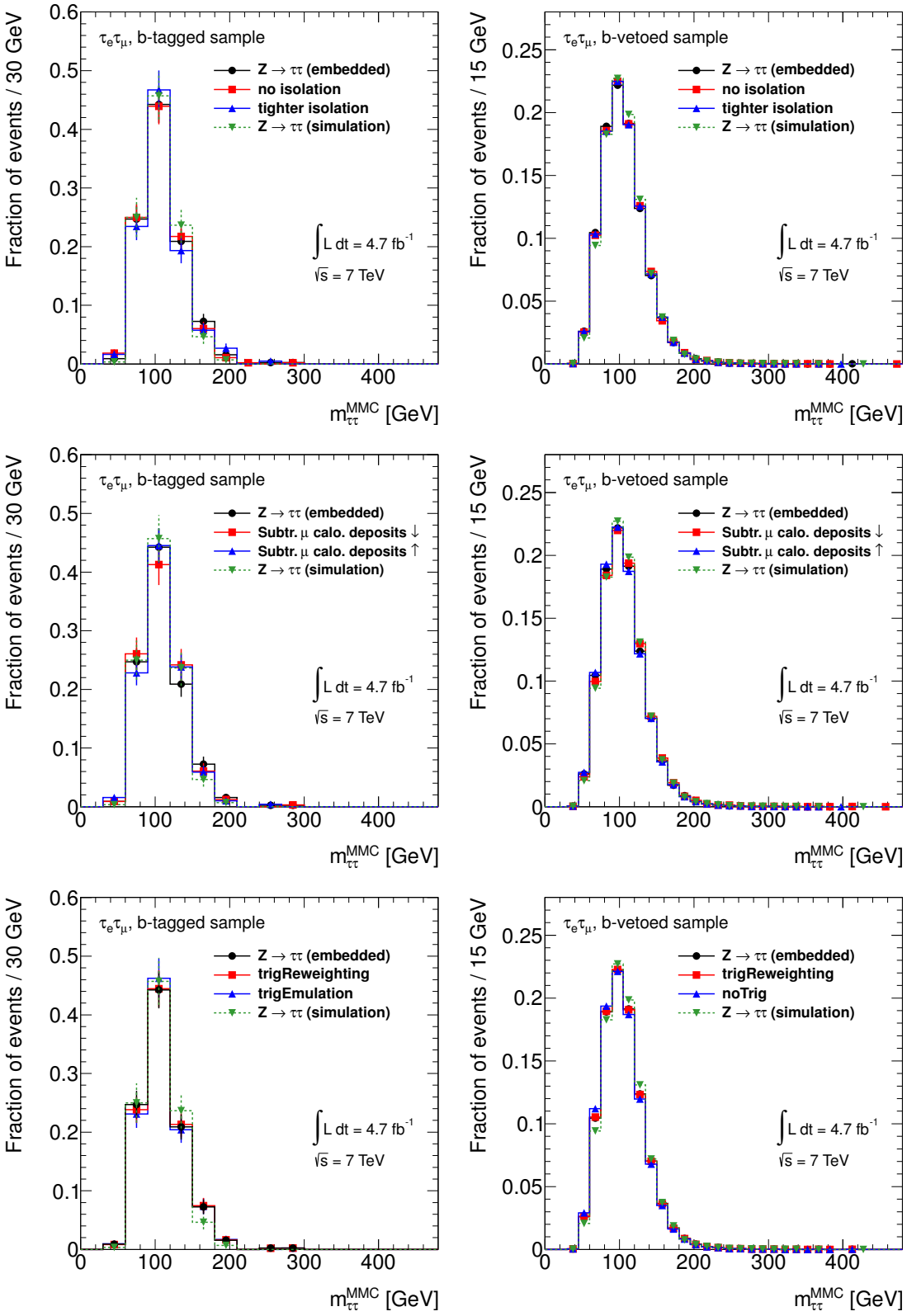

Figure 8.6.: Impact of the uncertainties introduced by the embedding technique on the shapes of the $m_{\tau\tau}^{\mathrm{MMC}}$ distributions of the b-tagged (left) and the b-vetoed (right) samples.

b-tagged sample, such events constitute an even smaller fraction of the b-tagged and b-vetoed samples at the end of the selection and therefore do not significantly bias the $Z/\gamma^* \to \tau\tau$ prediction.

In comparison to the uncertainties which affect simulated samples (related to the modeling of the UE, the detector response to jets, and pileup effects), the embedding method offers significantly lower normalization uncertainties in the b-tagged sample (see Table 8.7). For the b-vetoed sample, the contribution from jets to the normalization uncertainty plays only a small role (see Table 8.8), leading to a relative uncertainty of $\pm 4.0\,\%$ stemming from uncertainties related to the description of the detector performance in both the embedded sample and in simulation. As shown in Table 8.9, the total relative systematic uncertainty of the embedded sample ($^{+11}_{-10}\,\%$) is lower than that of a prediction purely based on simulation ($^{+16}_{-18}\,\%$) in the b-tagged sample, while the total relative systematic uncertainty of both methods is $\pm 9.0\,\%$ in the b-vetoed sample.

As mentioned before, simulation and embedded events have significantly different $m_{\tau\tau}^{\mathrm{MMC}}$ distributions, which are covered by neither the detector-related shape uncertainties (see Figures 8.2 through 8.5) nor by those related to the embedding method (see Figure 8.6). The observed differences in the $m_{\tau\tau}^{\mathrm{MMC}}$ distributions at the preselection stage persist even after correcting for trigger effects (see Subsection 7.1.1), and they can be attributed to the different $E_{\mathrm{T}}^{\mathrm{miss}}$ distributions (see Figure 7.4). The shape from the embedded sample is therefore preferred, estimating $E_{\mathrm{T}}^{\mathrm{miss}}$ from a data-driven method.

8.2.2. Uncertainties of the Multi-Jet Estimation

The estimation of the multi-jet background has been introduced in Subsection 7.1.2. It uses control regions of different lepton isolation and lepton charge criteria to predict the event yield and shape of the $m_{\tau\tau}^{\mathrm{MMC}}$ distributions in the signal region. The other backgrounds are subtracted in the control regions to obtain the multi-jet contribution, taking the associated uncertainties into account. Either anti-isolated regions C_R, D_R or half-isolated regions E_R, F_R can then be used in conjunction with the isolated region with same-sign requirement (B_R) to obtain a prediction:

$$N_{A_R}^{\text{multi-jet}} = \frac{N_{C_R}^{\text{multi-jet}}}{N_{D_R}^{\text{multi-jet}}} \cdot N_{B_R}^{\text{multi-jet}} \tag{7.4}$$

or

$$N_{A_R}^{\text{multi-jet}} = \frac{N_{E_R}^{\text{multi-jet}}}{N_{F_R}^{\text{multi-jet}}} \cdot N_{B_R}^{\text{multi-jet}}. \tag{7.5}$$

The value of $\frac{N_{E_R}^{\text{multi-jet}}}{N_{F_R}^{\text{multi-jet}}}$ is lower than that of $\frac{N_{C_R}^{\text{multi-jet}}}{N_{D_R}^{\text{multi-jet}}}$ by 24 % (23 %) for the b-tagged (b-vetoed) sample (see Table 7.1) because of correlations between the isolation criteria and the lepton p_{T} spectra. To take this discrepancy into account, the full difference is taken as systematic uncertainty of the multi-jet estimate.

Similarly, the shape differences between regions C_R and E_R are used to estimate the shape uncertainties of the $m_{\tau\tau}^{\mathrm{MMC}}$ distributions in the signal regions (see Figure 7.6).

8.2.3. Uncertainties of the t-Quark Pair Background Prediction

As introduced in Subsection 7.1.3, the contribution of $t\bar{t}$ events to the signal regions is estimated by extrapolation from control regions:

$$N_{t\bar{t}}^{\text{SR } b\text{-tag}/b\text{-veto}} = k_{\text{MC}}^{b\text{-tag}/b\text{-veto}} \cdot N_{t\bar{t}}^{\text{CR } b\text{-tag}/b\text{-veto}}. \tag{7.6}$$

Because the control regions have a high purity of $t\bar{t}$ events of 92 % (96 %) in the control regions of the b-tagged (b-vetoed) sample, the uncertainties introduced by the subtraction of other backgrounds are negligible compared to the uncertainties of $k_{\text{MC}}^{b\text{-tag}/b\text{-veto}}$, but taken into account for the final results nonetheless.

One source of systematic uncertainty on $k_{\text{MC}}^{b\text{-tag}/b\text{-veto}}$ arises from the underlying theoretical uncertainty: The different kinematic cuts of the signal and control regions require an accurate description of quantities such as the b-jet multiplicity and the jet p_{T} spectra in $t\bar{t}$ events. These uncertainties are taken into account by comparing the predictions from MC@NLO [151], which uses Herwig [154] for the parton shower (PS), and POWHEG+Jimmy [167, 168]. The values of $k_{\text{MC}}^{b\text{-tag}/b\text{-veto}}$ are determined for both generators, and the weighted mean is taken as central value because both generators lead to similar values. As mentioned in Subsection 7.1.3, half the difference of the predicted values is cited as theoretical uncertainty (see Table 7.4). The uncertainty on the event yields is 0.9 % for the b-tagged sample and 17 %[4] for the b-vetoed sample.

The uncertainties of the simulated detector response also contribute to the $k_{\text{MC}}^{b\text{-tag}/b\text{-veto}}$ uncertainty. The variations cited in Subsection 8.1.3 are therefore evaluated for MC@NLO in the signal and control regions. Because cuts on the b-jet multiplicity and on jet energies are applied, uncertainties on flavor tagging efficiency and the jet energy scale dominate the overall uncertainty on the $t\bar{t}$ contribution to the b-tagged and b-vetoed samples (see Tables 8.7 and 8.8).

As shown in Figure 7.9, the $m_{\tau\tau}^{\text{MMC}}$ shapes that the two generators predict agree in the signal regions. In the control regions, there is also good agreement with the shape obtained from data, and the *ABCD* method shown in Appendix A demonstrates the agreement with a data-driven shape estimate in the signal region of the b-tagged sample. MC@NLO is therefore used to predict the $m_{\tau\tau}^{\text{MMC}}$ shapes in the signal regions in order to reduce the statistical uncertainties of the shape prediction. The shape uncertainties associated to the prediction of the event kinematics are negligible, and shape uncertainties from the description of the detector performance (see Subsection 8.1.3) dominate.

Compared to a purely simulation-based $t\bar{t}$ estimation, the cross-section and preselection acceptance uncertainties are avoided. The lepton reconstruction, identification, and isolation efficiency uncertainties cancel, and the impact of the uncertainties of the jet energy scale and resolution as well as the flavor tagging efficiency uncertainty are more pronounced because they oppositely impact the event yields in the signal and control regions: The signal regions have upper cuts on the number of tagged b-jets and, in the b-tagged sample, on H_{T}, while the control regions require at least two tagged b-jets and impose no H_{T} requirement. In the b-tagged sample, to which the $t\bar{t}$ background contributes about 28 % of the total background, the total relative uncertainty is reduced from $^{+17}_{-19}$ % to $^{+17}_{-12}$ % by the use of the data-driven background estimation technique. In the b-vetoed sample, the total uncertainty of the data-driven method ($^{+38}_{-33}$ %) is larger than that of a simulation-based $t\bar{t}$ estimation (±23 %). Because of the much smaller relative contribution of $t\bar{t}$ production to the b-vetoed

[4] The uncertainty is expected to be larger because there is a larger difference in the b-jet requirements of the control region (at least two tagged b-jets) and the b-vetoed sample (no tagged b-jets) than for the b-tagged sample (exactly one tagged b-jet).

sample (about 1.2 %), the larger uncertainty has a negligible impact on the sensitivity of the search.

8.3. Summary of the Systematic Uncertainties

The detector-related normalization uncertainties and the normalization uncertainties introduced by the embedding technique are summarized in Tables 8.7 and 8.8 for three Higgs boson mass hypotheses, the dominant backgrounds, and the cumulated other electroweak backgrounds for the b-tagged and b-vetoed samples, respectively. Furthermore, the horizontal lines group uncertainties which have been assumed to be fully correlated in the limit derivation in Ref. [10].

In the b-tagged sample, jet-related uncertainties dominate the overall normalization uncertainties for most background processes. Consequently, the use of the embedding technique for the $Z/\gamma^* \to \tau\tau$ estimation reduces the detector-related normalization uncertainty from $^{+13.5\,\%}_{-15.6\,\%}$ to $^{+6.9\,\%}_{-6.1\,\%}$ despite the uncertainties introduced by the selection and subtraction of the original muons in the embedded sample.

Due to the low jet multiplicity in the b-vetoed sample, the impact of jet-related uncertainties is much smaller. An exception is the flavor tagging efficiency of the $t\bar{t}$ background because the event yields in the signal and control regions have a stronger anti-correlation than in the b-tagged sample. As mentioned before, the uncertainty of the $t\bar{t}$ estimation from a control region with at least two b-jets is larger than that of an estimation that relies purely on simulation in the b-vetoed sample. However, because $t\bar{t}$ contributes only about 1.2 % of the total background in the b-vetoed sample, the impact on the overall sensitivity is negligible, so the same technique as in the b-tagged sample can be employed. In the b-tagged sample, the total relative uncertainty can be reduced from $^{+17}_{-19}$ % to $^{+17}_{-12}$ %, and the normalization is corrected by a factor consistent with the findings of Ref. [215] (see Subsection 7.1.3).

Apart from detector-related uncertainties, the uncertainties of the integrated luminosity, the cross-section, and the acceptance are considered for the appropriate processes. The resulting overall uncertainties are shown in Figures 8.7 through 8.10 and Table 8.9. Figures 8.7 and 8.9 show a bin-by-bin assessment of the uncertainties of the background contributions, which—in contrast to the previous Figures—are evaluated separately for each process and also take shape uncertainties into account. In order to simplify the background model, the subdominant backgrounds have been merged, and the binning has been adjusted to limit statistical uncertainties. Figures 8.8 and 8.10 show the same for the signal processes of the $m_{h^0}^{\text{max}}$ scenario with $m_{A^0} = 150\,\text{GeV}$, $\tan\beta = 20$. Only the shape uncertainties with a significant impact on the $m_{\tau\tau}^{\text{MMC}}$ distributions are taken into account in Figures 8.7 through 8.10. The impact of the jet energy scale and resolution as well as the contributions from pileup and calorimeter clusters dominate. In the embedded $Z/\gamma^* \to \tau\tau$ sample, these uncertainties are eliminated by taking the respective quantities from data. Instead, the uncertainties from the subtraction of energy deposits from calorimeter cells and the shape uncertainty stemming from the trigger emulation are taken into account as most important shape uncertainties. The $m_{\tau\tau}^{\text{MMC}}$ shapes of $Z/\gamma^* \to \tau\tau$ events taken from simulation on one hand and from the embedded sample on the other hand differ beyond their respective evaluated shape uncertainties. The difference is attributed to differences in the missing transverse energy distributions, which is estimated from data in the embedded sample, justifying the preference of the embedded sample over simulation also for the estimation of the $m_{\tau\tau}^{\text{MMC}}$ shape.

Figures 8.7 through 8.10 represent the input from the signal regions that is used for the statistical assessment of the results in Chapter 9.

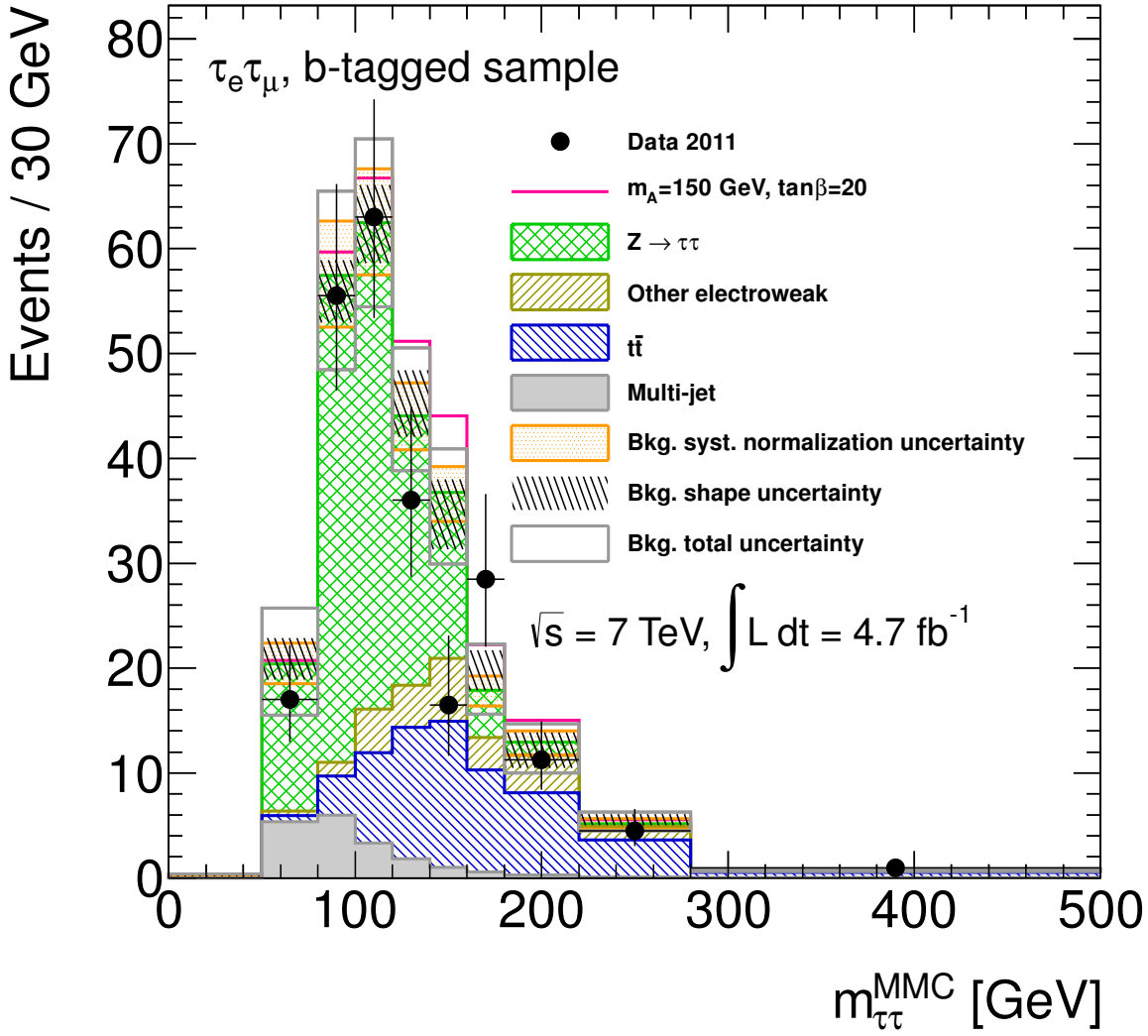

Figure 8.7.: $m_{\tau\tau}^{\mathrm{MMC}}$ distribution in the b-tagged sample. The background prediction shown uses the techniques detailed in Chapter 7 to predict the background composition in each bin and the respective uncertainties. The variations described in this Chapter have been used to assess the systematic uncertainties. The statistical uncertainties as well as the systematic normalization uncertainties (including the uncertainty on the integrated luminosity) and the shape uncertainties have been added in quadrature to estimate the total background uncertainty.

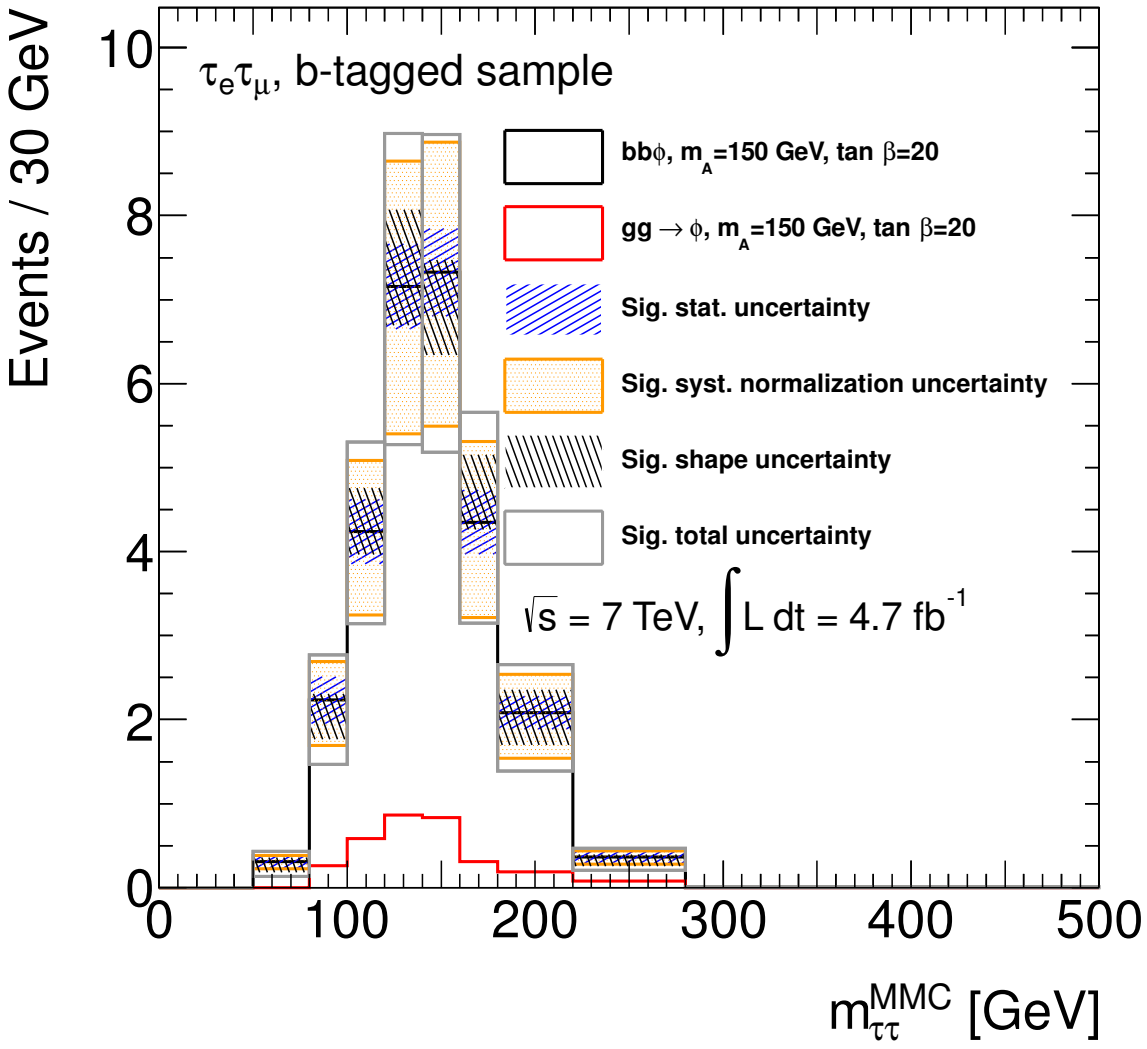

Figure 8.8.: Expected $m_{\tau\tau}^{\mathrm{MMC}}$ distribution of the signal processes in the b-tagged sample. The variations described in this Chapter have been used to assess the systematic uncertainties. The statistical uncertainties as well as the systematic normalization uncertainties (including the uncertainty on the integrated luminosity) and the shape uncertainties have been added in quadrature to estimate the total background uncertainty.

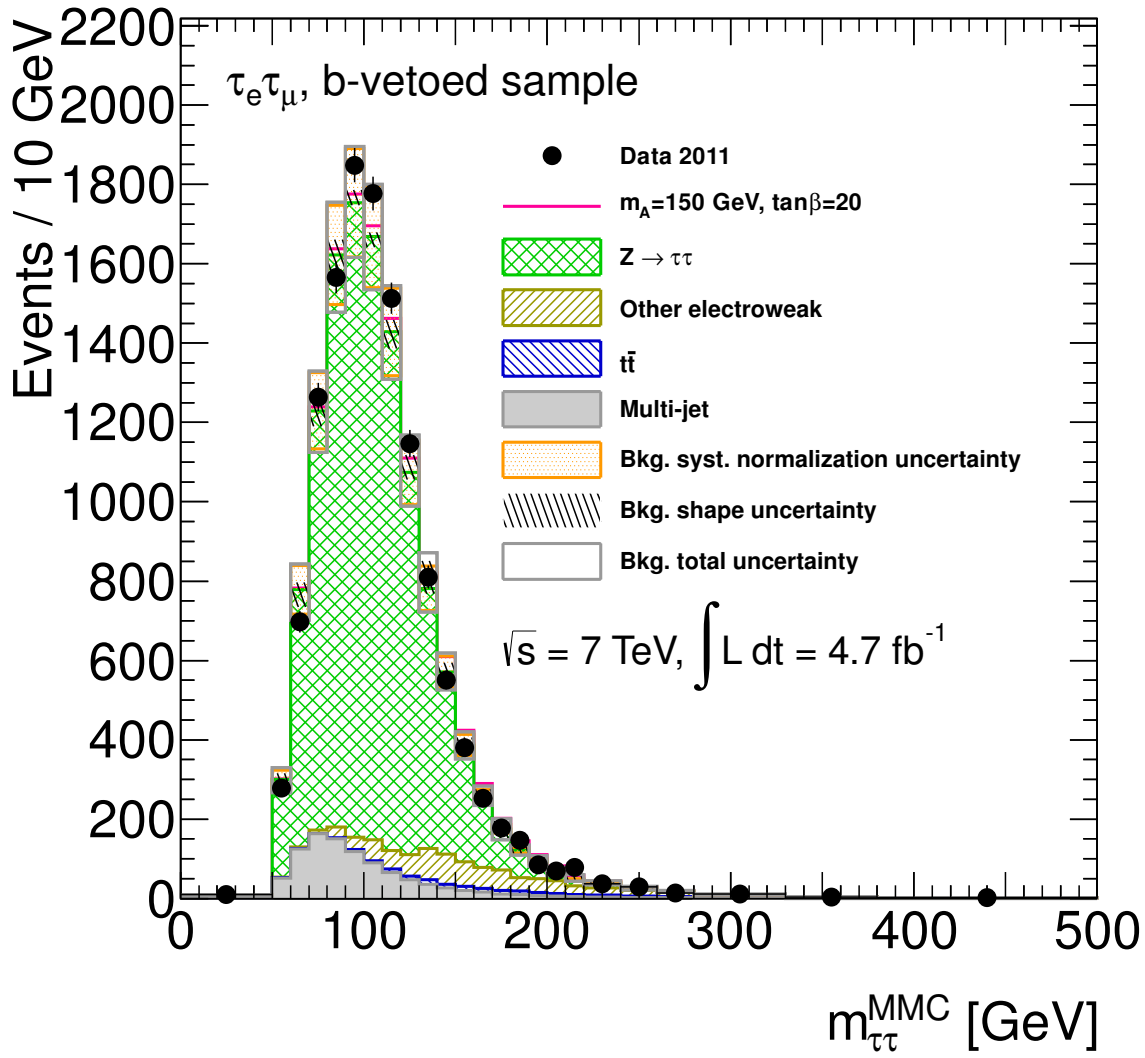

Figure 8.9.: $m_{\tau\tau}^{\mathrm{MMC}}$ distribution in the b-vetoed sample. The background prediction shown uses the techniques detailed in Chapter 7 to predict the background composition in each bin and the respective uncertainties. The variations described in this Chapter have been used to assess the systematic uncertainties. The statistical uncertainties as well as the systematic normalization uncertainties (including the uncertainty on the integrated luminosity) and the shape uncertainties have been added in quadrature to estimate the total background uncertainty.

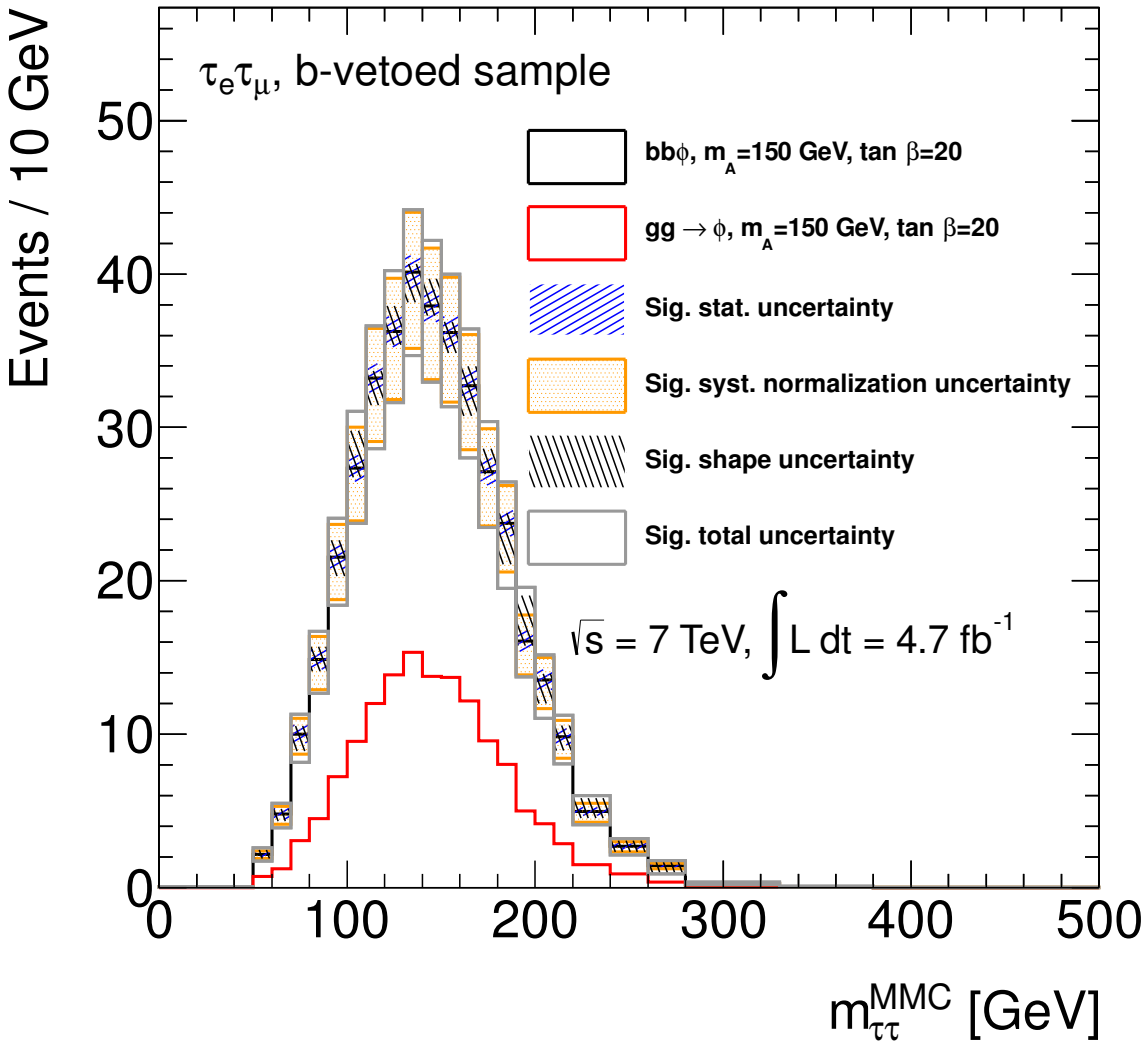

Figure 8.10.: Expected $m_{\tau\tau}^{\mathrm{MMC}}$ distribution of the signal processes in the b-vetoed sample. The variations described in this Chapter have been used to assess the systematic uncertainties. The statistical uncertainties as well as the systematic normalization uncertainties (including the uncertainty on the integrated luminosity) and the shape uncertainties have been added in quadrature to estimate the total background uncertainty.

Table 8.7.: Relative uncertainties in percent from the modeling of the simulated detector response for the b-tagged sample. The horizontal lines group variations that have been merged in the statistical combination with the other channels.

	Signal Process						Background Process				
	$bb\phi, m_\phi =$			$gg \to \phi, m_\phi =$			$t\bar{t}$		$Z/\gamma^* \to \tau\tau$		Other
	90 GeV	150 GeV	200 GeV	90 GeV	150 GeV	200 GeV	from CR	simulation	embedded	Alpgen	ew.
e ID ↑	1.6	1.3	1.3	1.6	1.4	1.3	< 0.1	1.2	1.7	1.6	1.3
e ID ↓	−1.6	−1.3	−1.3	−1.6	−1.4	−1.3	< 0.1	−1.2	−1.7	−1.6	−1.3
e recon./track qual. eff. ↑	0.9	0.9	0.8	0.7	0.8	0.8	< 0.1	0.2	0.8	0.8	0.9
e recon./track qual. eff. ↓	−0.9	−0.9	−0.8	−0.7	−0.8	−0.8	< 0.1	−0.9	−0.8	−0.8	−0.9
e iso. SF ↑	2.5	2.2	2.2	2.5	2.3	2.1	< 0.1	2.1	2.5	2.4	2.3
e iso. SF ↓	−2.5	−2.2	−2.2	−2.5	−2.3	−2.1	< 0.1	−2.1	−2.5	−2.4	−2.3
μ recon./ID eff. ↑	0.2	0.2	0.2	0.2	0.2	0.2	< 0.1	0.2	0.2	0.2	0.2
μ recon./ID eff. ↓	−0.2	−0.2	−0.2	−0.2	−0.2	−0.2	< 0.1	−0.2	−0.2	−0.2	−0.2
μ iso. SF ↑	2.4	1.9	1.8	1.6	1.8	2.2	−0.1	1.6	2.4	2.6	1.6
μ iso. SF ↓	−2.4	−1.9	−1.8	−1.6	−1.8	−2.2	0.1	−1.6	−2.4	−2.6	−1.6
e energy scale ↑	3.3	3.2	3.0	2.4	2.4	2.0	−4.0	1.3	0.4	2.0	3.8
e energy scale ↓	−0.2	< 0.1	0.2	< 0.1	−2.4	< 0.1	−0.2	0.1	−0.4	−0.7	0.6
e energy res. ↑	−0.3	0.3	−0.1	< 0.1	3.2	< 0.1	−0.1	−0.1	−0.7	0.3	0.8
e energy res. ↓	−0.3	0.8	0.7	< 0.1	< 0.1	1.7	0.2	0.2	−0.2	−0.2	−0.3
μ ID track p_T ↑	< 0.1	< 0.1	0.2	< 0.1	< 0.1	< 0.1	< 0.1	< 0.1	−0.2	< 0.1	< 0.1
μ ID track p_T ↓	< 0.1	< 0.1	−0.1	< 0.1	< 0.1	< 0.1	< 0.1	−0.1	< 0.1	< 0.1	< 0.1
μ MS track p_T ↑	0.3	−0.7	−0.7	< 0.1	< 0.1	< 0.1	−1.8	−4.4	−0.5	−0.1	−0.8
μ MS track p_T ↓	< 0.1	< 0.1	0.2	< 0.1	< 0.1	< 0.1	−0.4	−0.3	< 0.1	< 0.1	< 0.1
Jet energy scale ↑	−0.1	−2.9	−4.7	1.1	< 0.1	−9.6	−6.1	−11.6		−2.7	−6.8
Jet energy scale ↓	−4.9	−5.7	−2.3	−11.9	−0.9	−4.0	11.9	10.1		−7.3	3.1
Jet energy resolution ↑	1.4	−1.4	−4.3	23.6	−8.0	−2.5	2.6	−0.1		−2.6	−10.3
Pileup ↑	< 0.1	−0.5	−2.4	< 0.1	< 0.1	−3.3	0.2	−0.7		−1.4	−2.7
Pileup ↓	−0.6	1.7	1.0	< 0.1	4.2	−4.2	0.8	0.9		0.2	−0.6
Calo. clusters ↑	0.2	−1.8	−3.0	< 0.1	−3.6	−4.8	−0.2	−2.1		−1.6	−1.7
Calo. clusters ↓	−1.9	1.9	1.0	< 0.1	5.6	−4.2	1.1	1.5		0.1	−0.3
Mistag light ↑	1.2	0.9	1.1	11.3	11.3	10.4	−0.4	< 0.1		11.8	3.2
Mistag light ↓	−1.2	−0.9	−1.1	−11.3	−11.4	−10.4	0.4	< 0.1		−11.9	−3.2
ε_b ↑	4.7	4.6	4.7	0.8	1.0	0.9	−9.7	1.8		0.5	3.6
ε_b ↓	−4.7	−4.7	−4.7	−0.8	−1.0	−0.9	11.3	−2.0		−0.5	−3.7
ε_c ↑	0.1	0.4	0.1	5.9	3.0	4.0	−0.1	< 0.1		4.8	0.6
ε_c ↓	−0.1	−0.4	−0.1	−5.9	−3.0	−4.0	0.1	< 0.1		−4.8	−0.6
Subtracted μ calo. deposits ↑									−1.0		
Subtracted μ calo. deposits ↓									−3.9		
No isolation									5.7		
Tighter isolation									−2.4		
Total up	7.2	7.1	6.7	27.1	14.6	11.9	16.7	14.8	6.9	13.5	7.6
Total down	−8.2	−8.5	−9.5	−17.8	−15.4	−16.6	−12.3	−16.9	−6.1	−15.6	−14.1

Table 8.8.: Relative uncertainties in percent from the modeling of the simulated detector response for the b-vetoed sample. The horizontal lines group variations that have been merged in the statistical combination with the other channels.

	Signal Process						Background Process				
	$bb\phi, m_\phi =$			$gg \to \phi, m_\phi =$			$t\bar{t}$		$Z/\gamma^* \to \tau\tau$		Other
	90 GeV	150 GeV	200 GeV	90 GeV	150 GeV	200 GeV	from CR	simulation	embedded	Alpgen	ew.
e ID ↑	1.7	1.3	1.2	1.7	1.3	1.2	< 0.1	1.2	1.8	1.7	1.4
e ID ↓	−1.7	−1.3	−1.2	−1.7	−1.3	−1.2	< 0.1	−1.2	−1.8	−1.7	−1.4
e recon./track qual. eff. ↑	0.8	0.9	0.9	0.8	0.8	0.9	< 0.1	0.4	0.8	0.8	0.8
e recon./track qual. eff. ↓	−0.8	−0.9	−0.9	−0.8	−0.8	−0.9	< 0.1	−0.8	−0.8	−0.8	−0.8
e iso. SF ↑	2.5	2.2	2.2	2.5	2.2	2.2	< 0.1	2.1	2.5	2.5	2.1
e iso. SF ↓	−2.5	−2.2	−2.2	−2.5	−2.2	−2.2	< 0.1	−2.1	−2.5	−2.5	−2.1
μ recon./ID eff. ↑	0.2	0.2	0.2	0.2	0.2	0.2	< 0.1	0.2	0.2	0.2	0.3
μ recon./ID eff. ↓	−0.2	−0.2	−0.2	−0.2	−0.2	−0.2	< 0.1	−0.2	−0.2	−0.2	−0.3
μ iso. SF ↑	2.4	1.8	1.6	2.4	1.9	1.7	−0.1	1.5	2.3	2.4	1.4
μ iso. SF ↓	−2.4	−1.8	−1.6	−2.4	−1.9	−1.7	0.1	−1.5	−2.3	−2.4	−1.4
e energy scale ↑	0.6	0.1	−0.2	0.2	0.3	−0.1	−12.4	−7.6	0.7	0.7	−0.5
e energy scale ↓	−0.7	−0.3	−0.1	−0.7	−0.2	< 0.1	−0.2	0.2	−0.5	−0.7	0.1
e energy res. ↑	0.1	< 0.1	0.1	−0.1	−0.3	0.2	−0.2	−0.2	< 0.1	−0.1	0.1
e energy res. ↓	< 0.1	< 0.1	−0.1	0.1	−0.1	0.1	0.6	0.4	< 0.1	0.1	0.1
μ ID track p_{T} ↑	< 0.1	< 0.1	< 0.1	< 0.1	< 0.1	< 0.1	< 0.1	< 0.1	< 0.1	< 0.1	< 0.1
μ ID track p_{T} ↓	< 0.1	< 0.1	< 0.1	< 0.1	−0.1	< 0.1	0.4	0.1	< 0.1	< 0.1	−0.3
μ MS track p_{T} ↑	0.1	< 0.1	−0.2	< 0.1	−0.1	0.1	0.7	−1.8	< 0.1	< 0.1	< 0.1
μ MS track p_{T} ↓	< 0.1	< 0.1	< 0.1	< 0.1	−0.1	0.1	−0.1	< 0.1	< 0.1	< 0.1	0.1
Jet energy scale ↑	0.1	−0.1	−0.4	0.2	−0.7	−1.2	0.8	−4.1		< 0.1	0.1
Jet energy scale ↓	0.6	0.7	0.8	0.1	0.2	0.2	4.3	3.0		0.1	0.2
Jet energy resolution ↑	−0.3	−0.1	−0.4	−0.1	< 0.1	−0.4	1.5	−1.6		−0.3	−1.6
Pileup ↑	< 0.1	−0.2	−0.5	−0.3	−0.3	−0.8	−0.7	−1.3		−0.1	−0.3
Pileup ↓	−0.2	0.3	0.4	0.4	0.2	0.6	0.9	1.2		< 0.1	0.2
Calo. clusters ↑	< 0.1	−0.5	−1.3	−0.4	−0.7	−1.4	−0.6	−1.7		−0.4	−0.7
Calo. clusters ↓	−0.4	0.4	0.7	0.7	0.3	0.9	1.2	2.1		0.1	0.2
Mistag light ↑	−0.1	−0.1	−0.2	−0.2	−0.3	−0.2	−0.9	−0.4		−0.1	−0.2
Mistag light ↓	0.1	0.1	0.2	0.2	0.3	0.2	0.9	0.4		0.1	0.2
ε_b ↑	−0.4	−0.5	−0.5	< 0.1	< 0.1	< 0.1	−25.2	−15.8		< 0.1	−0.4
ε_b ↓	0.4	0.5	0.5	< 0.1	< 0.1	< 0.1	33.5	17.7		< 0.1	0.4
ε_c ↑	< 0.1	< 0.1	< 0.1	< 0.1	−0.1	−0.1	−0.2	−0.1		< 0.1	−0.1
ε_c ↓	< 0.1	< 0.1	< 0.1	< 0.1	0.1	0.1	0.2	0.1		< 0.1	0.1
Subtracted μ calo. deposits ↑									0.1		
Subtracted μ calo. deposits ↓									−0.4		
No isolation									−0.2		
Tighter isolation									−0.2		
Trigger reweighting									< 0.1		
Total up	4.0	3.5	3.4	4.1	3.4	3.4	33.9	10.9	4.0	4.0	3.1
Total down	−4.1	−3.4	−3.5	−4.1	−3.5	−3.8	−28.2	−13.1	−4.0	−4.0	−3.6

Table 8.9.: Relative systematic uncertainties in percent in the b-tagged and b-vetoed samples. Three Higgs boson mass hypotheses are shown. For the $t\bar{t}$ and $Z/\gamma^* \to \tau\tau$ backgrounds, both the data-driven estimation methods (along with the uncertainties introduced by the method) and an estimation from simulation are shown. For $t\bar{t}$, the cross-section uncertainty pertains to the MC@NLO prediction. The uncertainties of the other electroweak backgrounds and the multi-jet background are also given.

	Signal Process						Background Process					
	$bb\phi, m_\phi =$			$gg \to \phi, m_\phi =$			$t\bar{t}$		$Z/\gamma^* \to \tau\tau$		Other	Multi-
	90 GeV	150 GeV	200 GeV	90 GeV	150 GeV	200 GeV	from CR	simulation	embedded	Alpgen	ew.	jet bg.
b-TAGGED SAMPLE												
Det. response up	7.2	7.2	6.7	27.1	13.5	11.9	16.7	10.9	4.0	13.5	7.6	
Det. response down	−8.2	−8.2	−9.5	−17.8	−15.6	−16.6	−12.3	−13.1	−4.1	−15.6	−14.1	
Luminosity	3.9	3.9	3.9	3.9	3.9	3.9		3.9	3.9	3.9	3.9	
Prod. cross-section								} 13	5	5	} 13	
Acceptance up	20	20	21	20	20	20			5	5		
Acceptance down	−21	20	18	20	20	20			−5	−5		
Method uncert. up							0.9		5.7			24
Method uncert. down							−0.9		−4.6			−24
Total up	22	22	22	34	24	24	17	17	11	16	16	24
Total down	−23	−22	−21	−27	−26	−26	−12	−19	−10	−18	−20	−24
b-VETOED SAMPLE												
Det. response up	4.1	4.1	3.4	4.1	4	3.4	33.9	18.3	4.0	4	3.1	
Det. response down	−4.1	−4.1	−3.5	−4.1	−4	−3.8	−28.2	−18.6	−4.0	−4	−3.6	
Luminosity	3.9	3.9	3.9	3.9	3.9	3.9		3.9	3.9	3.9	3.9	
Prod. cross-section								} 13	5	5	} 7	
Acceptance up	5	5.5	6.2	5.1	5.1	5.1			5	5		
Acceptance down	−5.5	−4.5	−3.2	0	0	0			−5	−5		
Method uncert. up							17		0.1			23
Method uncert. down							−17		−0.5			−23
Total up	7.6	7.9	8.1	7.6	7.6	7.3	38	23	9.0	9.0	8.6	23
Total down	−7.9	−7.2	−6.1	−5.7	−5.6	−5.4	−33	−23	−9.0	−9.0	−8.8	−23

9 Statistical Assessment of Results

The $m_{\tau\tau}^{\text{MMC}}$ distributions in the b-tagged and b-vetoed samples are used to quantitatively evaluate the signal–plus–background and background–only hypotheses.

In absence of a clear signal, exclusion limits are derived, using the CL_s method [88]. The procedure, summarized in Section 9.1, uses the profile likelihood as a test statistic [229] to assess the compatibility of binned distributions under the two hypotheses. Section 9.2 describes the signal and background model used to construct the likelihood functions that enter the calculation of the test statistic.

The individual and combined results from the b-tagged and b-vetoed samples are shown in Section 9.3. The combination with the other decay channels is discussed in Section 9.4.

9.1. The Profile Likelihood and the CL_s Method

In the most basic terms, the evaluation of an upper limit on the cross-section of a signal process is performed by considering a test statistic derived from the expected $m_{\tau\tau}^{\text{MMC}}$ distributions under the assumption of the background–only and the signal–plus–background hypotheses and evaluating it for the measured $m_{\tau\tau}^{\text{MMC}}$ distributions. The profile likelihood ratio (PLR) is selected as test statistic [229], and the limit is calculated using the *modified frequentist method* [88], called CL_s *method* in the following.

The expected event yield in bin i of the $m_{\tau\tau}^{\text{MMC}}$ histogram from region R is given by the sum of the expected signal event yield (S_R^i) and the expected background event yield (B_R^i). A *signal strength* parameter (μ) is defined to scale the signal event yield, leading to an expected event yield of $\mu S_R^i + B_R^i$ in the signal–plus–background hypothesis. The signal strength is defined as parameter of interest of the test, with a value of zero pertaining to the background–only hypothesis and a value of one to the signal–plus–background hypothesis.

Taking into account the expected contributions from signal and background events, a single-bin likelihood function for the signal strength is given for N_R^i events in this bin by a Poisson distribution with expectation value $\langle N_R^i \rangle = \mu S_R^i + B_R^i$:

$$\mathcal{L}_R^i(\mu) = \mathcal{F}_{\text{Poisson}}(N_R^i | \mu S_R^i + B_R^i). \tag{9.1}$$

The overall likelihood value is obtained by multiplying all single-bin likelihood functions:

$$\mathcal{L}_{\text{stat.}}(\mu) = \prod_{R,i} \mathcal{L}_R^i(\mu). \tag{9.2}$$

The signal and background models are parametrized in such a way that they can accommodate systematic uncertainties. The additional parameters are called *nuisance parameters (NPs)* of the model ($\vec{\theta}$). Using the systematic normalization and shape variations pertaining to the $+1\sigma/-1\sigma$ variations[1] of the model, the NPs are inserted into the model in such a way that a value of $\alpha = +1$ ($\alpha = -1$) in the model then leads to the normalization or shape of

[1] which are obtained from auxiliary measurements

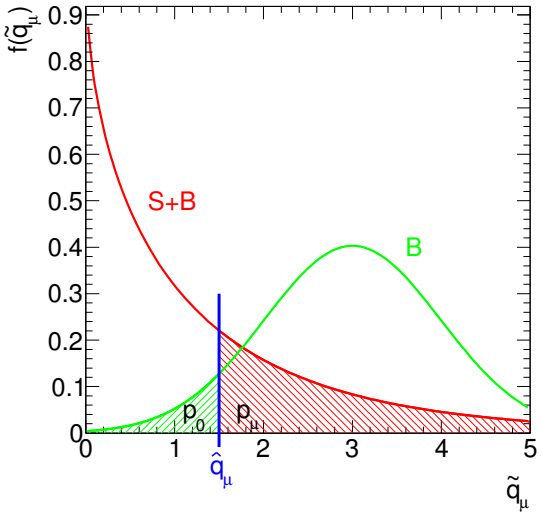

Figure 9.1.: Illustration of the distributions of the test statistic for the signal–plus–background and background–only hypotheses. The p-values p_0 and p_μ for an observed value $\hat{q}_\mu$ of the test statistic are also shown.

the $+1\sigma$ (-1σ) variation of the associated source of systematic uncertainty. Assuming each NP follows a normal distribution, the likelihood function becomes:

$$\mathcal{L}(\mu, \vec{\theta}\,) = \mathcal{L}_{\text{stat.}}(\mu) \prod_{\alpha \in \vec{\theta}} \mathcal{F}_{\text{normal}}(\alpha). \tag{9.3}$$

The test statistic is derived from the overall likelihood:

$$\tilde{q}_\mu = \begin{cases} -2 \ln \dfrac{\mathcal{L}(\mu, \hat{\vec{\theta}}_\mu)}{\mathcal{L}(0, \hat{\vec{\theta}}_0)} & \text{for } \hat{\mu} < 0, \\ -2 \ln \dfrac{\mathcal{L}(\mu, \hat{\vec{\theta}}_\mu)}{\mathcal{L}(\hat{\mu}, \hat{\vec{\theta}}\,)} & \text{for } 0 \leq \hat{\mu} \leq \mu \\ 0 & \text{for } \hat{\mu} > \mu. \end{cases} \tag{9.4}$$

The first and last cases limit the model to non-negative signal strength values and enforce the requirement that a one-sided limit is to be obtained, respectively. The hat symbol $(\hat{\mu}, \hat{\vec{\theta}})$ refers to the corresponding maximum-likelihood estimators (MLEs) from a global fit to data. $\hat{\vec{\theta}}_\mu$ and $\hat{\vec{\theta}}_0$ refer to MLEs from a fit to data which constrains μ to the given value (called *profiling*). The test statistic is therefore called PLR, and the MLEs of the NPs are functions of the parameter of interest (μ). This enables the straight-forward evaluation of a confidence interval for μ.

Figure 9.1 illustrates the probability distributions of the test statistic for the signal–plus–background and background–only cases. The distribution of the signal–plus–background case is shifted to the left with respect to the background–only case because the numerator in Eq. (9.4) is larger in the former case.

The probability density functions for the signal–plus–background ($f(q_\mu|\mu, \hat{\vec{\theta}}_\mu)$) and background–only ($f(q_\mu|0, \hat{\vec{\theta}}_0)$) hypotheses can be obtained by performing a large number of pseudo-experiments. The median of q_μ along with the surrounding ranges that contain 68 or 95 % of the results of the pseudo-experiments from background–only pseudo-experiments can

be used to obtain an expected limit with error bands corresponding to one or two standard deviations.

It has been verified by comparison to pseudo-experiments in the context of Ref. [10] that the median values and the associated error bands of the test statistic under the background–only and signal–plus–background hypotheses can be obtained by the so-called *asymptotic approximation*: As shown in Ref. [229] by use of Wilks' theorem [230] and the Wald approximation [231], an *Asimov dataset* can be used to estimate the median and error bands of the test statistic in under the background–only hypothesis.

The separation of the probability density functions for the signal–plus–background ($f(\tilde{q}_\mu|\mu, \hat{\vec{\theta}}_\mu)$) and background–only ($f(\tilde{q}_\mu|0, \hat{\vec{\theta}}_0)$) hypotheses is a measure for the sensitivity of the measurement. It can be calculated from the p-values of the two hypotheses for an observed value ($\hat{q}_\mu$) of the test statistic: p_0 is the probability to observe a more signal-like outcome of the experiment (compared to the actual outcome) under the background–only hypothesis. It constitutes the probability to reject the background–only hypothesis based on the experiment if the background–only hypothesis is true. p_μ is the probability to observe a more background-like outcome of the experiment (compared to the actual outcome) under the signal–plus–background hypothesis. It constitutes the probability to reject the signal–plus–background hypothesis based on the experiment if the signal–plus–background hypothesis is true:

$$p_0 = \int_{-\infty}^{\hat{q}_\mu} dq_\mu \, f(q_\mu|0, \hat{\vec{\theta}}_0) \tag{9.5}$$

$$p_\mu = \int_{\hat{q}_\mu}^{\infty} dq_\mu \, f(q_\mu|\mu, \hat{\vec{\theta}}_\mu). \tag{9.6}$$

The two p-values can be used to define [88]:

$$CL_s(\mu) = \frac{p_\mu}{1 - p_0}. \tag{9.7}$$

An upper limit on the signal strength at a confidence level (CL) of $95\,\% = 1 - \alpha$ can be computed by setting $\alpha = CL_s(\mu) = 5\,\%$. Eq. (9.6) is tested for different values of μ to iteratively find the smallest value of μ with $CL_s(\mu) < 5\,\%$. Larger signal strengths are thus excluded at the 95 % CL.

An important advantage of the CL_s method lies in the behavior for very similar distributions of the test statistic in the signal–plus–background and background–only cases, i.e., the case of vanishing sensitivity to the signal: In this case, an exclusion based solely on the requirement $p_\mu < \alpha$ occurs with approximately the same probability whether the background–only or the signal–plus–background hypothesis is true. With the CL_s method, the signal–plus–background hypothesis is not excluded in the case of a downward fluctuation of the background because the numerator and the denominator of Eq. (9.7) have almost identical values.

9.2. Summary of the Full Signal and Background Models

Events passing the kinematic cuts are collected with respect to their $m_{\tau\tau}^{\mathrm{MMC}}$ value in histograms with these bin borders:

b-tagged sample: $[0, 50, 80, 100, 120, 140, 160, 180, 220, 280, 500]$ GeV
b-vetoed sample: $[0, 50, 60, 70, 80, 90, 100, 110, 120, 130, 140, 150,$
$160, 170, 180, 190, 200, 210, 220, 240, 260, 280, 330, 380, 500]$ GeV.

This binning enables the distinction between various Higgs boson mass hypotheses, while avoiding large statistical uncertainties in the individual bins.

For the production of neutral Higgs bosons in association with b-quarks or from gluon fusion, simulated signal events are available for the mass hypotheses $m_\phi = 90$, 100, 110, 120, 130, 140, 150, 170, 200, 250, and 300 GeV.

Out of these templates, two types of signal models are formed:

- For upper limits on cross-sections of neutral Higgs boson production in association with b-quarks or in gluon fusion, a single signal template (containing only $\phi \to \tau\tau \to \ell\ell + 4\nu$ decays) is normalized corresponding to an arbitrary cross-section. The product of this cross-section value, the branching fraction for di-leptonic $\tau\tau$ decays, and the resulting upper limit on the signal strength is given as upper limit on the product of production cross-section and decay branching fraction into τ leptons.[2] Given the low sensitivity to the width of the decaying bosons (because of the low $m_{\tau\tau}$ resolution, see Section 5.3), this signal model can be used to obtain model-independent limits on the production of generic Higgs bosons (ϕ) that couple to τ leptons.

- In order to probe the m_{A^0}–$\tan\beta$ plane of the $m_{h^0}^{\mathrm{max}}$ scenario of the Minimal Supersymmetric Standard Model (MSSM), the contributions of the three neutral Higgs bosons h^0, A^0, and H^0 are matched to the templates with the smallest mass differences, which are then assigned the associated cross-section times branching ratio values. The same signal strength (μ) is used to scale the (up to six) signal templates of a given choice of $m_{A^0}, \tan\beta$. A value of 1 corresponds to cross-section values equal to the MSSM prediction. The respective point in the m_{A^0}–$\tan\beta$ plane is (expected to be) excluded if the observed (expected) upper limit on μ is smaller than one[3]. Because the signal event yield grows with $\tan\beta$ for a fixed value of m_{A^0}, an upper limit on the signal strength translates to an upper limit on $\tan\beta$.

These signal models define the signal contributions μS_R^i for each region R and bin i. The uncertainty introduced by the distinction of events according to the number of tagged b-jets is taken into account as described in Subsection 8.1.2.

As mentioned in Section 9.1, the likelihood function can accommodate statistical and systematic uncertainties, which are modeled by Poisson and Gaussian distributions. For both the b-tagged and the b-vetoed samples, the likelihood function is the product of the single-bin likelihood functions from one $t\bar{t}$ control region (CR), three multi-jet control regions

[2] The efficiency of the `2LepEF` generator event filter (GEF) (see Table 6.5), which applies to the $bb\phi$ samples with $90\,\mathrm{GeV} \leq m_\phi \leq 200\,\mathrm{GeV}$, is also applied as a factor.

[3] The excluded contour is evaluated by linear interpolation between the points in the m_{A^0}–$\tan\beta$ plane for which the CL_s values are explicitly calculated.

(B-D), and all bins of the respective signal region (SR):

$$\mathcal{L}_{b\text{-tag}/b\text{-veto}}(\mu,\vec{\theta}) = \mathcal{L}_{\text{CR}}^{b\text{-tag}/b\text{-veto}}(\mu,\vec{\theta}) \cdot \mathcal{L}_{B}^{b\text{-tag}/b\text{-veto}}(\mu,\vec{\theta}) \cdot \mathcal{L}_{C}^{b\text{-tag}/b\text{-veto}}(\mu,\vec{\theta}) \cdot \mathcal{L}_{D}^{b\text{-tag}/b\text{-veto}}(\mu,\vec{\theta}) \cdot \prod_{m_{\tau\tau}\text{ bin } i} \mathcal{L}_{\text{SR},i}^{b\text{-tag}/b\text{-veto}}(\mu,\vec{\theta}). \tag{9.8}$$

The impact of shape uncertainties of other backgrounds, which are subtracted in control regions C_R and E_R, on the shape of the $m_{\tau\tau}^{\text{MMC}}$ distributions of multi-jet events is neglected. This simplification is justified by the high purity of multi-jet events (particularly) in regions C_R, which leads to very small correlations between the shapes of the $m_{\tau\tau}^{\text{MMC}}$ distributions of multi-jet events observed in the control regions and variations of the other backgrounds.

As explained in Subsection 7.1.3, only the event yield is taken from data for $t\bar{t}$ events, while the shape of the $m_{\tau\tau}^{\text{MMC}}$ distributions in the signal regions is taken from simulation. The $t\bar{t}$ contribution to bin i in the signal regions ($k_{\text{MC}}^{b\text{-tag}/b\text{-veto}} t\bar{t}_R^i$) carries a common normalization factor for the b-tagged (b-vetoed) sample ($k_{\text{MC}}^{b\text{-tag}/b\text{-veto}}$), which is constrained in the fit predominantly from the $t\bar{t}$ control region due to its high purity. The MC@NLO prediction for $t\bar{t}_R^i$ is used in the signal and control regions, so this definition of $k_{\text{MC}}^{b\text{-tag}/b\text{-veto}}$ does not take the (small) difference of the MC@NLO prediction of $k_{\text{MC}}^{b\text{-tag}/b\text{-veto}}$ ($k_{\text{MC@NLO}}^{b\text{-tag}/b\text{-veto}}$ in Table 7.3) and the weighted mean of the two generators (see Table 7.4) into account. The contribution is therefore corrected by a factor $k_{\text{corr}}^{b\text{-tag}/b\text{-veto}}$, which is equal to one in the $t\bar{t}$ control regions and equal to the ratio of the combined value and the MC@NLO prediction in the signal and multi-jet control regions. Because the statistical uncertainty in the $t\bar{t}$ control regions is much smaller than the systematic uncertainties, the impact of the overlap between the $t\bar{t}$ control regions on the statistical uncertainties of the $t\bar{t}$ estimation is neglected in the background model. As mentioned in Subsection 7.1.3, half the difference of the extrapolation factors obtained from MC@NLO and POWHEG+Jimmy and the statistical error of their weighted mean are assigned as normalization uncertainties (with NPs $\vec{\alpha}$ following normal distributions) in the signal regions.

In the multi-jet estimate with the $ABCD$ method (see Subsection 7.1.2), the normalization in the signal regions $\left(N_{A_R}^{\text{multi-jet}}\right)$ is constrained from the event yields in the control regions B_R through D_R. They are implemented as:

$$N_{\text{multi-jet},R}^{i} = \begin{cases} N_{A_R}^{\text{multi-jet}} \cdot R_{\text{same charge/opposite charge}} & \text{for region } B_R \\ N_{A_R}^{\text{multi-jet}} \cdot R_{\text{anti-isol./isol.}} & \text{for region } C_R \\ N_{A_R}^{\text{multi-jet}} \cdot R_{\text{same charge/opposite charge}} \cdot R_{\text{anti-isol./isol.}} & \text{for region } D_R, \end{cases} \tag{9.9}$$

with

$$R_{\text{same charge/opposite charge}} = \frac{N_{D_R}^{\text{multi-jet}}}{N_{C_R}^{\text{multi-jet}}} \qquad R_{\text{anti-isol./isol.}} = \frac{N_{D_R}^{\text{multi-jet}}}{N_{B_R}^{\text{multi-jet}}}. \tag{9.10}$$

The uncertainty on $R_{\text{anti-isol./isol.}}$, which is determined by comparing $\frac{N_{C_R}^{\text{multi-jet}}}{N_{D_R}^{\text{multi-jet}}}$ and $\frac{N_{E_R}^{\text{multi-jet}}}{N_{F_R}^{\text{multi-jet}}}$, is taken into account as an explicit normalization uncertainty; the corresponding shape difference, as an independent shape uncertainty.

All other background contributions are merged into a category "other electroweak", which is dominated by single t-quark production in the b-tagged sample and by di-boson production in the b-vetoed sample and assigned the corresponding cross-section and acceptance uncertainties.

The bin-wise expectation value of Eq. (9.1) is thus extended to:

$$\langle N_R^i \rangle = \mu S_R^i + k_{\mathrm{MC}}^{b\text{-tag}/b\text{-veto}} k_{\mathrm{corr}}^{b\text{-tag}/b\text{-veto}} t\bar{t}_R^i + N_{\mathrm{others},R}^i + N_{\text{multi-jet},R}^i. \tag{9.11}$$

Contributions which are normalized from simulation additionally carry cross-section[4], acceptance, and luminosity uncertainties, which are modeled by NPs ($\vec{\alpha}$) with underlying normal distributions as described above. The shape uncertainties mentioned in Subsection 8.1.3 and Section 8.2 are taken into account. They are treated as fully correlated to the respective normalization uncertainties.

The parameters $k_{\mathrm{MC}}^{b\text{-tag}/b\text{-veto}}$, $N_{A_R}^{\text{multi-jet}}$, $R_{\text{same charge/opposite charge}}$, and $R_{\text{anti-isol./isol.}}$ are modeled as NPs with underlying flat probability density distributions ($\vec{\tau}$), so the likelihood function only depends on them implicitly (due to their correlations with the other NPs and B_R^i).

If the relative statistical uncertainty of the total background estimation ($\frac{\sigma_{\mathrm{stat},R}^i}{B_R^i}$) exceeds 5 % and thus becomes relevant for a bin i, it is taken into account by an additional NP (γ_R^i) with an underlying Gamma distribution. The Gamma distribution of a variable (x) depends on three parameters: the shape parameter (θ), the location parameter (μ), and the scale parameter (β):

$$\mathcal{F}_{\mathrm{Gamma}}(x|\delta,\chi,\beta) = \frac{\left(\frac{x-\chi}{\beta}\right)^{\delta-1} \exp\left(-\frac{x-\chi}{\beta}\right)}{\beta\Gamma(\delta)}. \tag{9.12}$$

$\Gamma(\delta) = \int_0^\infty dt\, t^{\delta-1} \exp(-t)$ is the Gamma function. For each bin in each region with a relative statistical uncertainty larger than 5 % of the background expectation (B_R^i), the shape parameter is set to $\delta = \left(\sigma_{\mathrm{stat},R}^i\right)^{-2} + 1$, the location parameter to $\chi = 0$, and the scale parameter to $\beta = \left(\sigma_{\mathrm{stat},R}^i\right)^2$.

The full likelihood function is therefore given by:

$$\begin{aligned}\mathcal{L}(\mu,\vec{\theta}) = &\prod_{\substack{R\in\text{regions}\\ i\in\text{bins}}} \mathcal{F}_{\mathrm{Poisson}}\left(N_R^i|\mu S_R^i(\vec{\theta}) + B_R^i(\vec{\theta})\right)\cdot \\ &\prod_{j\in\text{syst. uncert.}} \mathcal{F}_{\mathrm{normal}}(\alpha_j)\cdot \\ &\prod_{\substack{R\in\text{regions}\\ k\in{}^{\text{bins with large}}_{\text{rel. stat. uncert.}}}} \mathcal{F}_{\mathrm{Gamma}}\left(\gamma_R^k \middle| \left(\sigma_{\mathrm{stat},R}^k\right)^{-2}+1, 0, \left(\sigma_{\mathrm{stat},R}^k\right)^2\right).\end{aligned} \tag{9.13}$$

The expected signal (μS_R^i) and background (B_R^i) event yields depend on different subsets of the NPs: The signal event yields depend on the signal strength (μ) as parameter of interest and on the values of the NPs pertaining to simulated events ($\vec{\alpha}$, with underlying normal distributions). The background event yields depend on $\vec{\alpha}$ and also on the NP pertaining to the statistical uncertainty ($\vec{\gamma}$) and the free parameters ($\vec{\tau}$):

$$S_R^i(\vec{\theta}) = S_R^i(\vec{\alpha}) \tag{9.14}$$

$$B_R^i(\vec{\theta}) = B_R^i(\vec{\alpha},\vec{\gamma},\vec{\tau}). \tag{9.15}$$

The likelihood functions for the b-tagged and the b-vetoed samples each contain twelve NPs pertaining to statistical uncertainties ($\vec{\gamma}$) and four free parameters ($\vec{\tau}$). Fifteen NPs with

[4] except for signal processes in the determination of limits on cross-section times branching ratio $\phi \to \tau\tau$

underlying normal distributions ($\vec{\alpha}$) appear in both samples, which have four (five[5]) unique NPs to accommodate the uncertainties of the data-driven background estimation methods.

For the published results, the signal and background models have been simplified as described in Appendix C to improve the numerical stability of the combination with the other channels.

9.3. Results from the b-Tagged and b-Vetoed Samples

Using the CL_s method, limits at the 95 % CL have been derived for three different scenarios.

9.3.1. Model-Independent Limit

As discussed in Section 9.2, the presence of the individual signal processes can be probed individually by computing a cross-section limit for each individual signal template. The excluded signal strength represents the product of the production cross-section and the branching ratio. By probing both processes across the mass range, a model-independent limit can be set. A wide range of models can be probed, including the parameter sets of the pMSSM-7 (see Subsubsection 2.3.2.3) that agree best with the observation of a Higgs boson at about 126 GeV, as discussed in Subsection 9.3.3.

The model-independent limits are shown in Figure 9.2 for the b-tagged and b-vetoed samples and their statistical combination. Because of the low signal acceptance of the gluon fusion process in the b-tagged sample, no limit is given for this case. For both production modes, lower values of the product of production cross-section and branching fraction to τ lepton pairs can be excluded with increasing Higgs boson mass. This is connected to the similarity of the $m_{\tau\tau}^{\mathrm{MMC}}$ shapes of the signal and $Z/\gamma^* \to \tau\tau$ background: In the case of coinciding Higgs boson and Z boson masses, the signal is concentrated in $m_{\tau\tau}^{\mathrm{MMC}}$ bins which also contain a large portion of the background, while the estimated background event yield is generally smaller for the high-mass region. Because $Z/\gamma^* \to \tau\tau$ events account for a smaller fraction of the total background in the b-tagged sample than in the b-vetoed sample, this effect is much less pronounced in the b-tagged sample. The combined cross-section limit is driven mainly by the b-vetoed sample—with the exception of the limit on b-associated Higgs boson production with m_ϕ values below approximately 150 GeV, where the reduced $Z/\gamma^* \to \tau\tau$ background yield in the b-tagged sample most benefits the sensitivity.

The inclusion of the b-tagged sample also leads to an improvement of the combined gluon fusion limit with respect to considering only the b-vetoed sample because it provides additional constraints to common NPs. Figure 9.3 shows a comparison for both signal processes between the expected and observed limits, using both samples in the limit calculation, with respect to the limits derived by considering only the b-vetoed sample. The expected limit shows the largest improvement for Higgs boson mass values close to the Z boson mass: about 8 % for gluon fusion and 55 % for b-associated Higgs boson production.

Another noteworthy feature of the limits on the product of production cross-section and branching fraction to τ lepton pairs is the similarity of the expected limits in the b-vetoed sample for both production modes. This is the consequence of two opposing effects, which almost cancel: On one hand, the multiplicity of tagged b-jets in b-associated Higgs boson production is larger than in gluon fusion (see Table 6.5), leading to a lower fraction of events entering of the b-vetoed sample. On the other hand, the efficiencies of the kinematic cuts

[5] As mentioned in Subsection 7.1.1, the shape uncertainty associated with the trigger emulation is only considered in the b-vetoed sample.

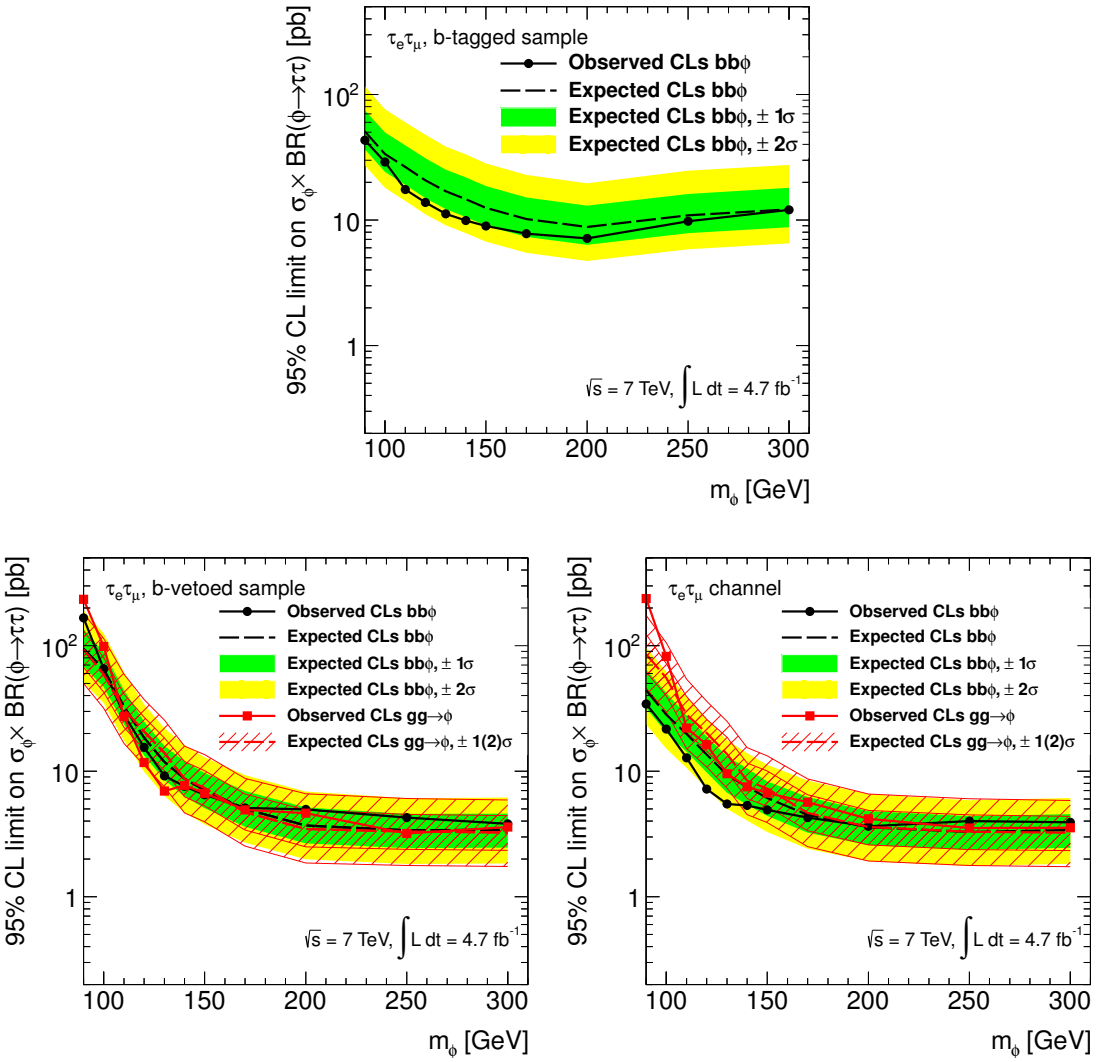

Figure 9.2.: Upper limits at 95 % CL on the product of production cross-section and branching fraction to τ lepton pairs for the signal processes. The results for Higgs boson production in association with b-quarks (black) are given for the b-tagged sample (top), the b-vetoed sample (bottom left), and their statistical combination (bottom right), while a limit on Higgs boson production in gluon fusion events (red) has been evaluated only for the b-vetoed sample and the statistical combination of both samples.

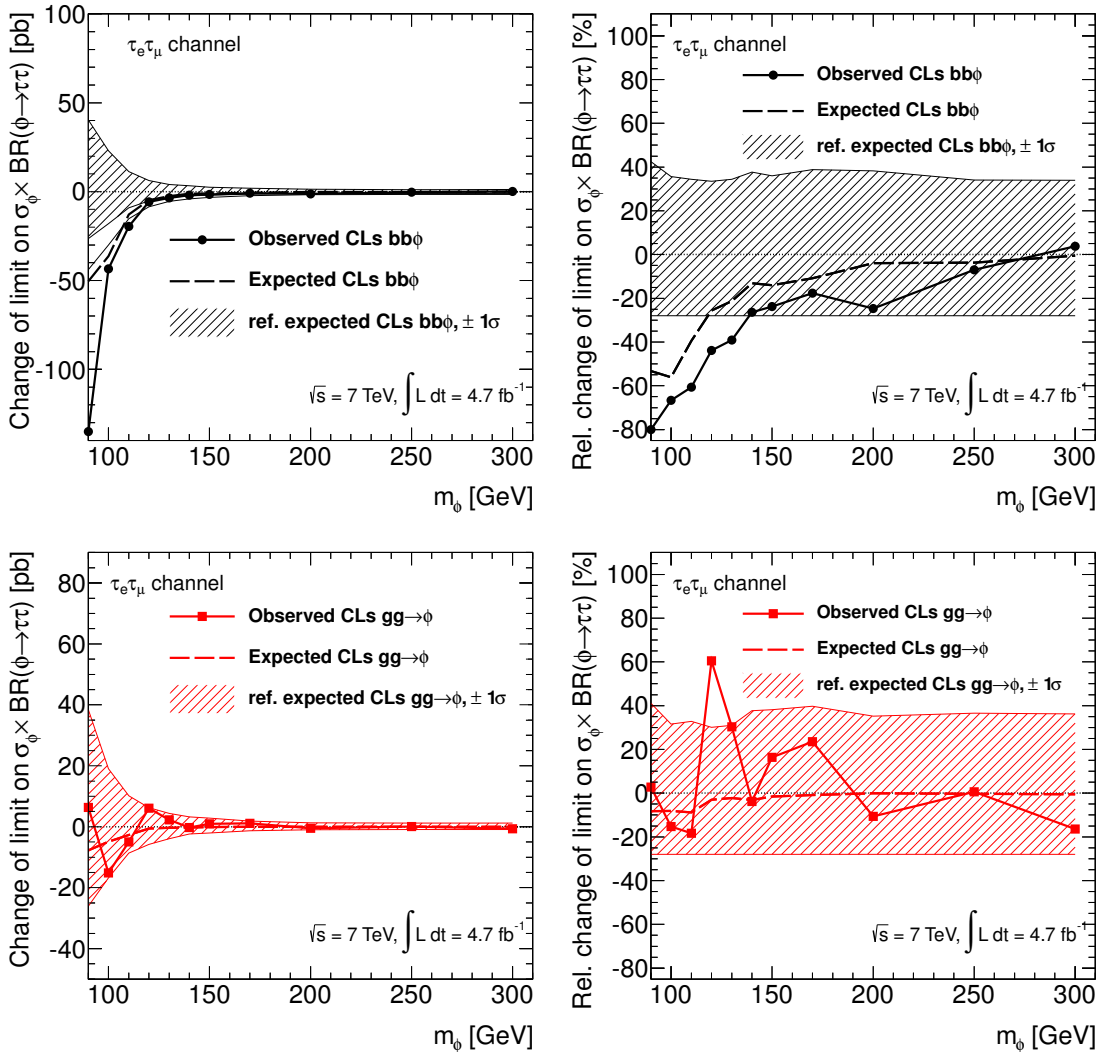

Figure 9.3.: Absolute (left) and relative (right) impact of the inclusion of the b-tagged sample on the expected and observed 95 % CL limit on the product of production cross-section and branching fraction to τ lepton pairs for b-associated Higgs boson production (top) and the gluon fusion production mode (bottom). The width of the $\pm 1\sigma$ bands of the results from only the b-vetoed sample are given for reference.

imposed are generally larger for signal events with Higgs bosons produced in association with b-quarks than in signal events with gluon fusion (see Table 6.9).

The shape differences between simulated and embedded $Z/\gamma^* \to \tau\tau$ samples that were observed for boson masses near the Z boson mass impact the observed limit in the b-vetoed sample because they are larger than the estimated uncertainty in the individual bins. Despite a good agreement of the event yield predicted by the background–only hypothesis (see Table 6.8), a small signal admixture is favored by the fit to the corresponding missing mass calculator (MMC) mass distribution of the b-vetoed sample for $m_\phi \lesssim 110\,\text{GeV}$. This effect is not observed in the combined observed limit on b-associated Higgs boson production from the combination of the two samples. Here, the b-tagged sample constrains common NPs (such as those connected to the electron and muon scale factors and those connected to the

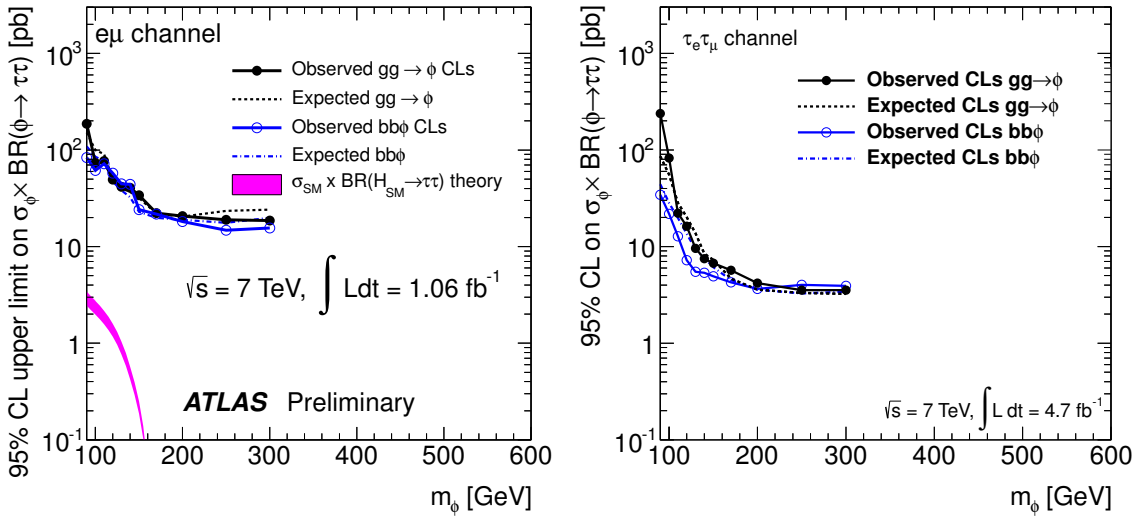

Figure 9.4.: Comparison of the upper limits on the product of the production cross-section of neutral Higgs bosons and the branching fraction to τ lepton pairs for gluon fusion (solid black dots) and b-associated production (hollow blue dots). The left Figure shows the previous ATLAS result from Ref. [13], while the right Figure shows the results of this thesis on the same scale.

cross-section and acceptance uncertainties of the $Z/\gamma^* \to \tau\tau$ and di-boson backgrounds) and the signal strength, leading to a combined observed limit that is smaller than the combined expected limit[6].

In consequence, the production of neutral Higgs bosons can be excluded up to values of $3-5\,\text{pb}$ for the product of the production cross-section and the branching fraction to τ lepton pairs for both production modes in the Higgs boson mass range between 170 and 300 GeV (see Figure 9.2). The exclusion limit gradually declines to about 230 pb (32 pb) at $m_\phi = 90\,\text{GeV}$ for gluon fusion (b-associated Higgs boson production) because of growing overlap between the expected signal shape and that of $Z/\gamma^* \to \tau\tau$ decays. The much weaker limit for gluon fusion at $m_\phi = 90\,\text{GeV}$ is a result of the very low signal acceptance of the b-tagged sample for this process.

Figure 9.4 shows a comparison of the results of the $\tau_e\tau_\mu$ channel to the previous ATLAS result of $\tau_e\tau_\mu$ final states [13], which does not rely on the distinction of a b-tagged and a b-vetoed sample and uses a dataset that corresponds to $1.06\,\text{fb}^{-1}$. While the observed fluctuation prevented an improvement of the observed limit for gluon fusion for $m_\phi = 90 - 100\,\text{GeV}$, the overall sensitivity was improved by a factor of about four.

9.3.2. Limit in the m_{A^0}–$\tan\beta$ plane of the MSSM

The results are also interpreted in the $m_{h^0}^{\text{max}}$ scenario of the MSSM (see Figure 9.5). The m_{A^0} dependence of the expected sensitivity is a convolution of the expected limit on the product of production cross-section and branching fraction to τ lepton pairs and the decline of the production cross-section with growing values of m_{A^0} (see Figures 2.7 through 2.9). Furthermore, in the intense coupling region ($m_{A^0} \approx 130\,\text{GeV}, \tan\beta \gg 1$), the mass differences

[6]The event yield for gluon fusion in the b-tagged sample is too small to impose a strong constraint on the signal strength.

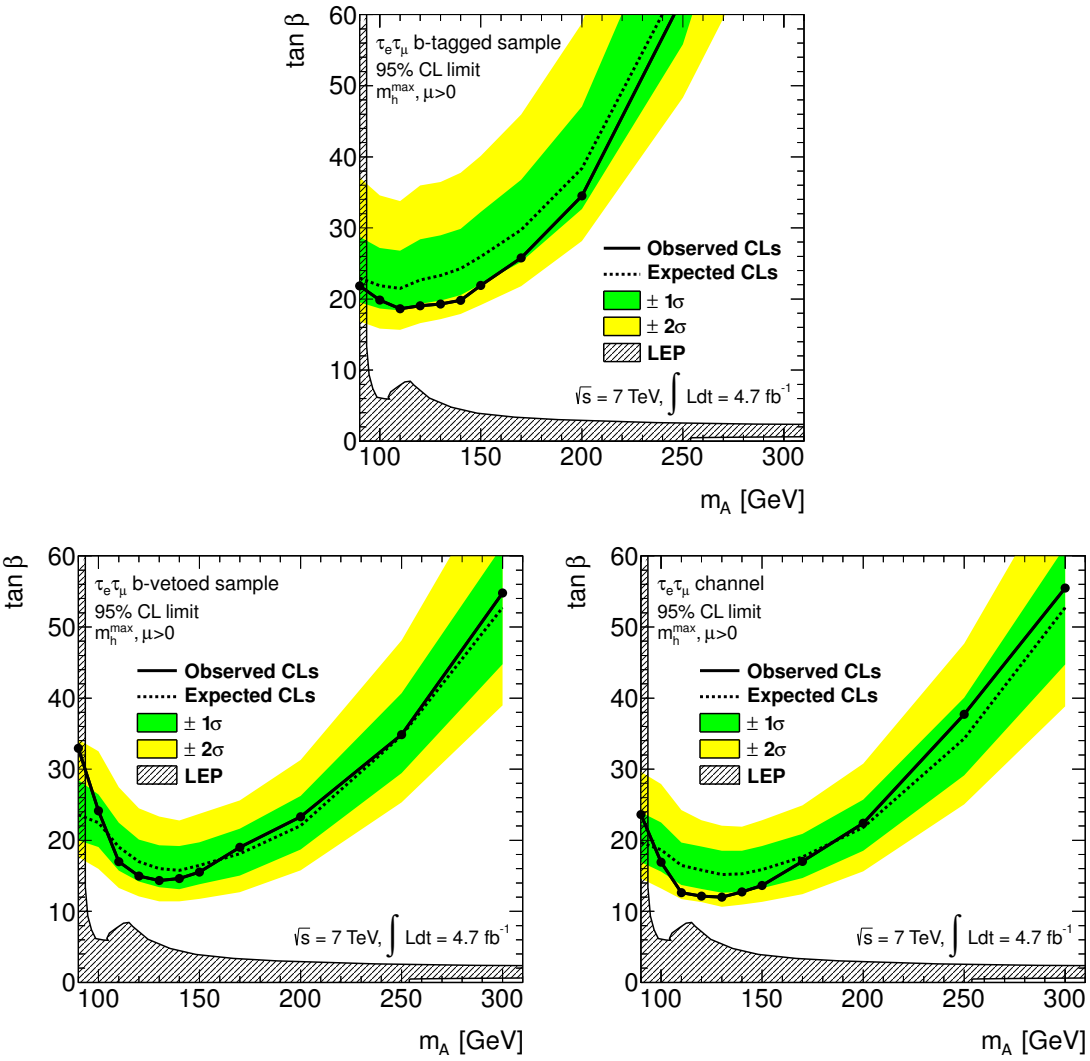

Figure 9.5.: Upper limits at 95 % CL on $\tan\beta$ in the $m_{h^0}^{\max}$ scenario of the MSSM as a function of m_{A^0} and the exclusion area from the LEP experiments, which is taken from Ref. [71]. The results are given for the b-tagged sample (top), the b-vetoed sample (bottom left), and their statistical combination (bottom right).

between all neutral Higgs bosons are small compared to the $m_{\tau\tau}^{\mathrm{MMC}}$ resolution, resulting in a single, narrow signal peak.

As in the model-independent limit, the fit to the b-vetoed sample favors a small—but non-zero—signal strength value at $m_\phi = 90 - 100\,\mathrm{GeV}$. As shown in the $m_{h^0}^{\max}$ interpretation, the observed limit of the statistical combination of both processes does not exceed the 2σ band in the b-vetoed sample. Furthermore, the combined limit from the $\tau_e\tau_\mu$ channel stays within one standard deviation of the expected exclusion for $m_{A^0} = 90\,\mathrm{GeV}$ because $\mu = 0$ is favored by the data from the b-tagged sample.

From the $\tau_e\tau_\mu$ channel, an upper limit on $\tan\beta$ of about 12–14 for m_{A^0} values between 110 and 150 GeV is derived (see Figure 9.5). For lower masses, the proximity of the Z boson resonance deteriorates the exclusion limit to about 24 at $m_{A^0} = 90\,\mathrm{GeV}$. Both the cuts against high-p_{T} objects and the declining production cross-section values predicted by the MSSM lead to weaker limits with growing m_{A^0} values above $m_{A^0} = 130\,\mathrm{GeV}$.

9.3.3. Limit on pMSSM-7 Scenarios

As mentioned in Subsubsection 2.3.2.3, Ref. [118] demonstrates the compatibility of the MSSM with various Standard Model (SM) precision measurements and an interpretation of the observed Higgs boson as either the lightest Higgs boson (h^0 interpretation) or as the heavier CP-even Higgs boson (H^0 interpretation). FeynHiggs 2.9.4 has been used for obtaining the corresponding values for the production cross-section, branching fraction to τ lepton pairs, and Higgs boson mass for each of the Higgs bosons h^0, H^0, and A^0. Their decay widths are below 5 GeV whenever a mass below 300 GeV is predicted—and each of the best-fitting pMSSM-7 points predicts at least one Higgs boson in the mass range probed. Consequently, the model-independent limits of Subsection 9.3.1 can be used to evaluate the compatibility of a given pMSSM-7 point with the results from the $\tau_e\tau_\mu$ channel.

The limit calculation for the combined signal contributions from gluon fusion and b-associated production for each parameter set requires considerable computational effort. Therefore, the contributions ($\sigma_\phi \times \mathrm{BR}(\phi \to \tau\tau)$) of the three neutral Higgs bosons of the pMSSM-7 are computed for the pMSSM-7 points with a low χ^2 value of the fit to data (see Subsubsection 2.3.2.3). The contributions are then compared to the model-independent limit, merging the signal expectation from Higgs bosons that are not individually resolved due to the limited $m_{\tau\tau}^{\mathrm{MMC}}$ resolution: The contributions of Higgs bosons within 15 GeV of a given sliding mass m_ϕ are added and drawn at the weighted[7] mean m_ϕ value, color-coded according to the goodness of the fit from Ref. [118], in Figure 9.6. As in Subsubsection 2.3.2.3, the color-coding refers to the difference of the χ^2 values ($\Delta\chi^2$) to the best-fitting parameter sets of the two scenarios. In the Gaussian limit, the thresholds of $\Delta\chi^2 = 2.3$ and $\Delta\chi^2 = 5.99$ correspond to the 68 and 95 % CL contours for two degrees of freedom, respectively.

Depending on how many Higgs boson masses lie within the same mass windows, a given pMSSM-7 point can thus correspond to between one and three dots in the $\sigma_\phi \times \mathrm{BR}(\phi \to \tau\tau)$–$m_\phi$ plane. Only the dot with the largest value of the ratio of $\sum_\phi \sigma_\phi \times \mathrm{BR}(\phi \to \tau\tau)$ to the expected limit is drawn to provide a measure for the sensitivity to this scenario. For both signal processes and interpretations, most parameter points feature their most prominent signal contribution near the mass of the discovered Higgs boson. Because the sensitivity of the search improves with growing values of m_ϕ and because the coupling of a SM-like h^0 boson to b-quarks is small, a fraction of the best-fitting pMSSM-7 points exist in another region of the m_{A^0}–$\tan\beta$ plane: For the green dots and the red dots points at higher m_ϕ values, the sensitivity to decays of A^0 and H^0 bosons exceeds the sensitivity to the observed Higgs boson.

The measured signal strengths in the individual SM search channels favor SM-like contributions near the measured Higgs boson mass for the best-fitting pMSSM-7 point in the h^0 interpretation. In comparison, the H^0 interpretation results in larger signal contributions near the mass of the discovered Higgs boson. The bulk of the best-fitting points in the H^0 interpretation corresponds to signal contributions below the excluded level by a factor of three to five, while only a few of the best-fitting points in the h^0 interpretation are within one to two orders of magnitude of the observed cross-section limit.

Because of smaller Yukawa couplings to down-type fermions in the SM and, as a consequence, a smaller contribution of the b-quark loop, its gluon fusion prediction is out of the reach of the presented analysis by at least one order of magnitude despite sensitivity to previously not excluded parts of the MSSM parameter space. The same holds true for the SM prediction for Higgs boson production in association with b-quarks, which is out of reach by four orders of magnitude.

[7] according to their $\sigma_\phi \times \mathrm{BR}(\phi \to \tau\tau)$ contribution

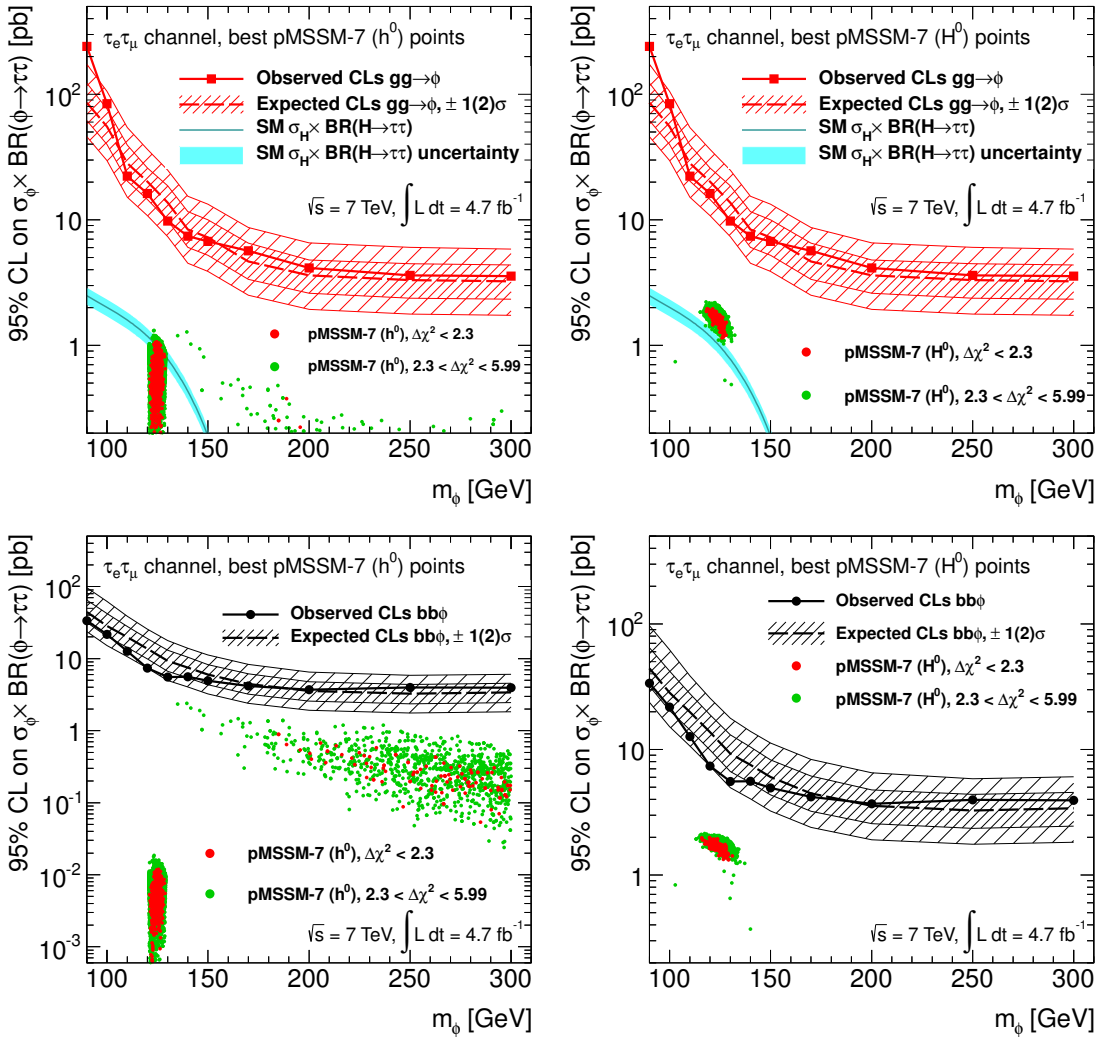

Figure 9.6.: Comparison of the upper limits at 95 % CL on the product of production cross-section and branching fraction to τ lepton pairs for the signal processes gluon fusion (top row) and b-associated Higgs boson production (bottom row) with the predictions of the SM [29] (only gluon fusion) and the best-fitting pMSSM-7 parameter sets for the h^0 (left) and H^0 interpretations (right) [118]. Red points pertain to a deviation of the goodness of the fit from the respective best-fitting sets ($\Delta\chi^2_{h^0/H^0}$) below 2.3, while the green points pertain to values of $2.3 < \Delta\chi^2_{h^0/H^0} < 5.99$.

9.4. Statistical Combination

In Ref. [10], the analysis of the $\tau_e\tau_\mu$ channel from this thesis is combined with the $\tau_{\text{lep}}\tau_{\text{had}}$, $\tau_{\text{had}}\tau_{\text{had}}$, and $\mu\mu$ decay channels to maximize the sensitivity to neutral MSSM Higgs bosons. A brief description of the corresponding analyses is given in this Section, followed by a discussion of the results of the combined results.

The signal and background uncertainty models in the b-tagged and b-vetoed samples have been simplified as described in Appendix C to overcome computational problems in the combination with the other decay channels. It has been verified that the expected exclusion limit is robust under these simplifications: The expected limit on the product of the production cross-section and the branching ratio to τ lepton pairs obtained from the simplified signal and background models agrees with the result of the full model within 5 % for the b-tagged sample and within 15 % for the b-vetoed sample and the $\tau_e\tau_\mu$ combination. The widths of the 1σ bands of the expected limit, for comparison, are about $^{+50}_{-30}$ % for the b-tagged sample and $^{+40}_{-30}$ % for the b-vetoed sample.

The $\mu\mu$ Channel

The good momentum resolution for muon candidates and the good rejection against fake muon signatures can be exploited for the search for Higgs boson decays to muon pairs. The same single-muon trigger and subsequent p_{T} cuts as in the $\tau_e\tau_\mu$ channel are used. The oppositely charged muon pair with the largest transverse momenta in the event are subjected to a cut on their invariant mass: $m_{\mu\mu} > 70\,\text{GeV}$. Also, the absolute value of the missing transverse energy vector is required to be smaller than 40 GeV. Depending on whether a b-tagged jet with a transverse momentum $p_{\text{T}} > 20\,\text{GeV}$ exists, events are collected in a b-tagged or a b-vetoed sample [10].

The shape of the total background contribution is modeled by a rational function which depends on the natural width of the Z boson and five other parameters, which are constrained from sidebands in data [10].

The shape of the signal contributions is also parametrized, taking the sum of a Landau function and the convolution of a Breit–Wigner function and a Gaussian function. The resulting parametrization is fitted to each available fully simulated signal sample and interpolated to obtain templates for other signal hypotheses [10].

Because of the good mass resolution, the b-tagged and b-vetoed samples can achieve an expected upper limit on the product of the production cross-section and the branching fraction to muon pairs which is better than that of the di-τ channel combination by a factor of about 100 in the mass range $120\,\text{GeV} < m_\phi < 300\,\text{GeV}$ [10]. In the $m_{h^0}^{\text{max}}$ scenario of the MSSM, however, the contribution to the combined sensitivity is small because of the smaller predicted decay branching fraction to muon pairs (about 0.04 %), compared to $8 - 10$ % for τ lepton pairs. The best expected limit ($\tan\beta \lesssim 20$) is achieved at $m_{A^0} = 120\,\text{GeV}$, and it rapidly deteriorates at larger Higgs boson masses.

The $\tau_{\text{had}}\tau_{\text{had}}$ Channel

The analysis of the $\tau_{\text{had}}\tau_{\text{had}}$ channel relies on the reconstruction and identification of τ_{had} candidates. The presence of at least one τ lepton with a transverse momentum above 29 GeV and another τ lepton with $p_{\text{T}} > 20\,\text{GeV}$ is required at the trigger level. This requirement is tightened to 45 GeV and 30 GeV, respectively, at the analysis level and opposite reconstructed charge signs of the τ_{had} candidates are required [10].

The absolute value of the missing transverse energy vector is required to be larger than 25 GeV. Events with jets with a transverse momentum value above 50 GeV are rejected. If the jet with the largest transverse momentum value is identified as a b-jet, the event enters the b-tagged sample; otherwise, it is sorted into the b-vetoed sample. The cut on the τ lepton with the largest p_{T} value is tightened to 60 GeV for the b-vetoed sample [10].

The electroweak backgrounds are estimated from simulation, while an $ABCD$ method is used for the contribution of multi-jet backgrounds, using the τ lepton charge product and τ_{had} identification criteria as discriminants [10].

Because of the tight p_{T} cuts applied to the τ_{had} candidates, the sensitivity deteriorates quickly below Higgs boson masses of 150 GeV, but a good suppression of Z boson decays and a good sensitivity to heavy Higgs bosons are achieved [10]. For Higgs boson masses above 190 GeV, the $\tau_{\mathrm{had}}\tau_{\mathrm{had}}$ channel constitutes the second-largest contribution to the combined sensitivity.

The $\tau_{\mathrm{lep}}\tau_{\mathrm{had}}$ Channel

Events containing neutral Higgs bosons that decay via the $\tau_{\mathrm{lep}}\tau_{\mathrm{had}}$ channel can be selected by using the same single-lepton triggers as in the $\tau_e\tau_\mu$ channel. A transverse momentum cut of 25 (20) GeV is applied to the electron (muon) in the event, the τ_{had} candidates must be of opposite charge and have a transverse momentum above 20 GeV [10].

A cut on the transverse mass (as defined in Eq. (7.1)) of the momentum vector of the light lepton and the missing transverse energy vector ($m_{\mathrm{T}} < 30$ GeV) reduces the contributions from the W + jets and $t\bar{t}$ backgrounds. Events are sorted into a b-tagged and a b-vetoed sample, following the same prescription as in the $\tau_{\mathrm{had}}\tau_{\mathrm{had}}$ channel. A cut on the missing transverse energy vector ($E_{\mathrm{T}}^{\mathrm{miss}} > 20$ GeV) is applied to the b-vetoed sample [10].

The $t\bar{t}$ contribution is normalized from a control region with at least two b-tagged jets and with a modified requirement for the jet with the largest transverse momentum value (50 GeV $< p_{\mathrm{T,jet}} <$ 150 GeV instead of 20 GeV $< p_{\mathrm{T,jet}} <$ 50 GeV in the signal regions). The $Z/\gamma^* \to \tau\tau$ background is estimated with the embedding technique. The multi-jet background is estimated with an $ABCD$ method, like in the other di-τ channels, using the relative charge sign of the τ lepton and the light lepton as well as the light lepton isolation variables as discriminants [10].

The $\tau_{\mathrm{lep}}\tau_{\mathrm{had}}$ channel dominates the sensitivity for Higgs boson masses above 100 GeV. This dominance stems from the large branching fraction of $\tau_{\mathrm{lep}}\tau_{\mathrm{had}}$ decays, low p_{T} thresholds, and a good background rejection. Because the contributions from t-quark and di-boson decays play a smaller role, the selection in both samples of the $\tau_{\mathrm{lep}}\tau_{\mathrm{had}}$ channel does not rely on kinematic cuts against large momenta of Higgs boson decay products (like the cut on $E_{\mathrm{T}}^{\mathrm{miss}} + p_{\mathrm{T},e} + p_{\mathrm{T},\mu}$ in the $\tau_e\tau_\mu$ channel). The $\tau_{\mathrm{lep}}\tau_{\mathrm{had}}$ channel thus offers the best sensitivity also for large Higgs boson masses [10].

Combined Results

Results for the products of production cross-section and branching fraction to τ lepton pairs and to muon pairs as well as their interpretation in the $m_{h^0}^{\mathrm{max}}$ scenario of the MSSM are published in Ref. [10] (see Figure 9.7).

As for the $\tau_e\tau_\mu$ channel, the combined model-independent limit is lowest for large Higgs boson masses, where the production of neutral Higgs bosons can be excluded down to values of about 0.27 pb for the product of the production cross-section and the branching fraction to τ lepton pairs for both production modes. The limit gradually declines to about 105 pb (38 pb) at $m_\phi = 90$ GeV for gluon fusion (b-associated Higgs boson production). A limit on

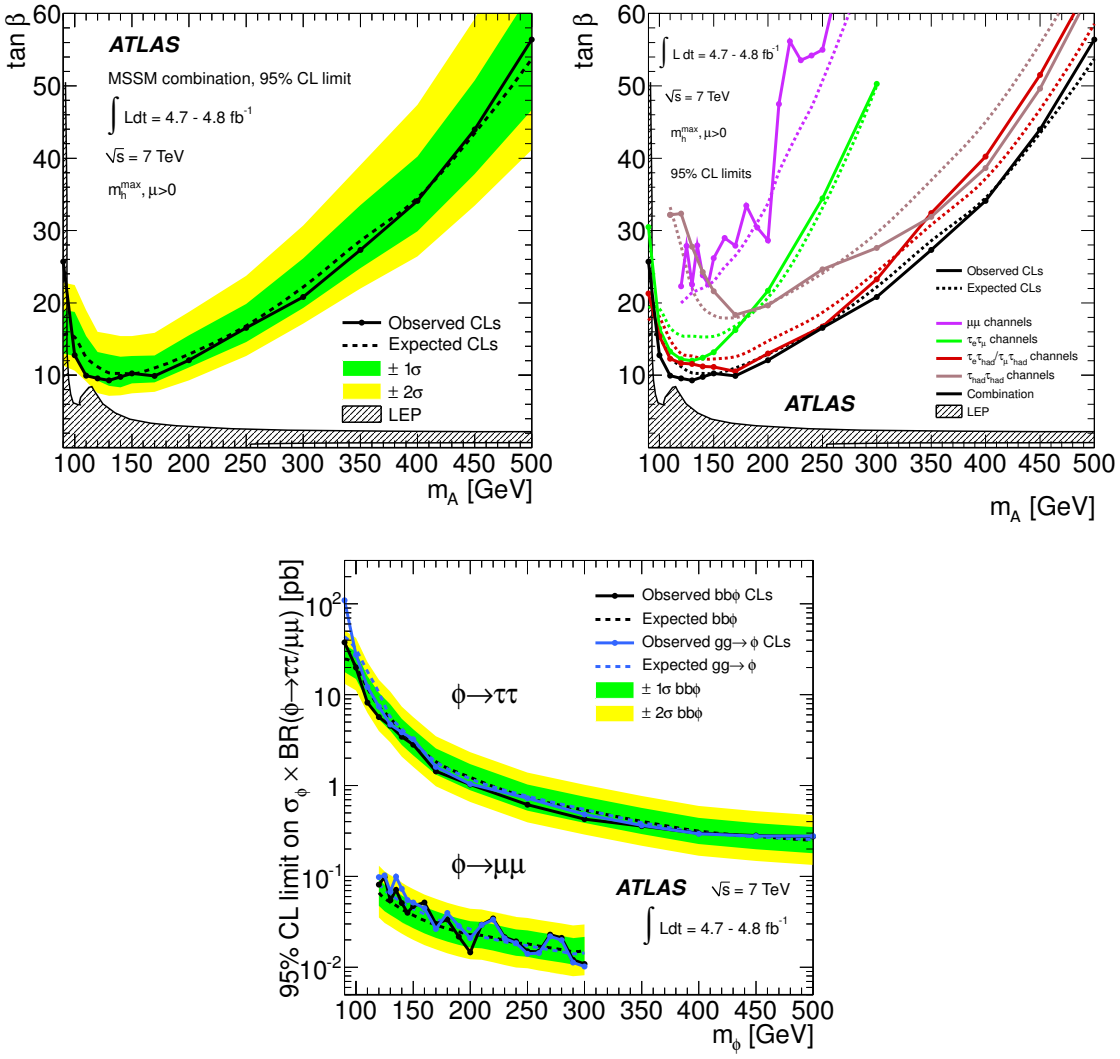

Figure 9.7.: Published combined upper limits on $\tan\beta$ in the $m_{h^0}^{\max}$ scenario of the MSSM as a function of m_{A^0} [10] and the exclusion area from the LEP experiments [71] (top row). The top right Figure shows the expected and observed limits from each of the contributing channels individually and their statistical combination. The bottom Figure shows the corresponding limits on the products of production cross-section and branching fraction to τ lepton pairs and to muon pairs [10].

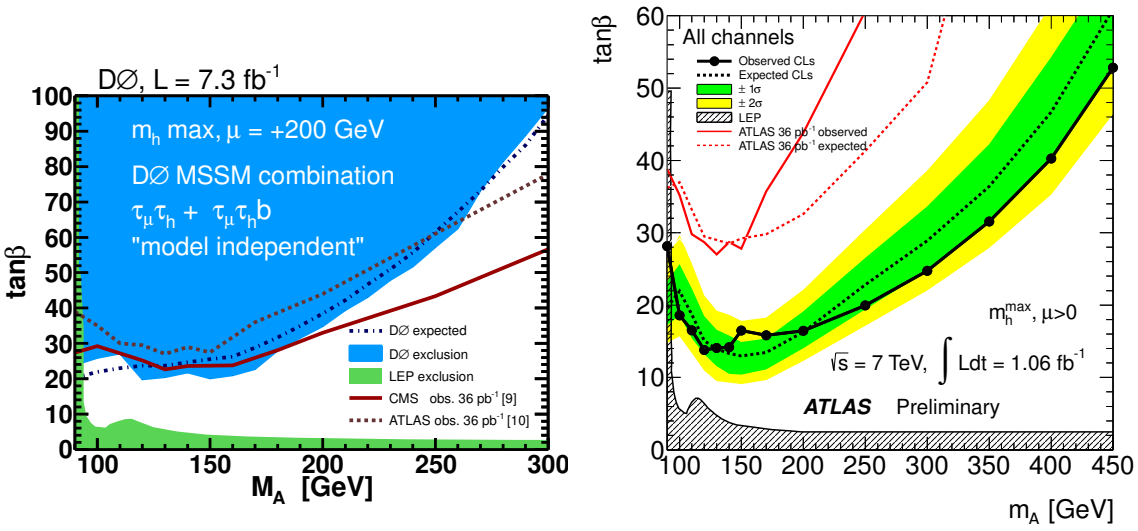

Figure 9.8.: Upper limits on $\tan\beta$ in the $m_{h^0}^{\max}$ scenario of the MSSM as a function of m_{A^0}. The left Figure shows the expected and observed upper limits from the searches by DØ, using $7.3\,\text{fb}^{-1}$ of $p\bar{p}$ collision data [110]. They are compared to the earliest results from ATLAS [232] and CMS [233]. The sensitivity from the Tevatron searches was already surpassed by the subsequent ATLAS searches, which used $1.06\,\text{fb}^{-1}$ of pp collision data [13] (right). The exclusion area from the LEP experiments [71] is also shown.

the product of the production cross-section and the branching fraction to muon pairs is set at values that are about a factor of 50 lower than the respective values for τ lepton pairs.

Even though the sensitivity in the m_{A^0}–$\tan\beta$ plane of the MSSM by a previous ATLAS search for the di-τ channels [13] already surpassed the reach of the latest published results from the Tevatron and a first ATLAS search for neutral MSSM Higgs bosons (see Figure 9.8), the new ATLAS combination presented in Ref. [10] again constitutes a significant improvement of the sensitivity across the entire investigated range of Higgs boson masses (see Figure 9.9). As shown in the top right of Figure 9.7, the $\tau_e\tau_\mu$ channel contributes significantly to the sensitivity in the range $90\,\text{GeV} < m_{A^0} < 170\,\text{GeV}$.

Figure 9.9 also shows a comparison to the results published by CMS for datasets corresponding to $4.6\,\text{fb}^{-1}$ at a center–of–mass energy of 7 TeV [234] and $25\,\text{fb}^{-1}$ at $7-8\,\text{TeV}$ [115]. A significantly better sensitivity is claimed already with $4.6\,\text{fb}^{-1}$, mostly because of lower levels of systematic uncertainties [234]. The analysis of $25\,\text{fb}^{-1}$ of data significantly improves the reach again to provide the most stringent limit available for the $m_{h^0}^{\max}$ scenario of the MSSM [115]. Figure 9.9 illustrates that the deviation of the observed limit from the expected limit in $25\,\text{fb}^{-1}$ of CMS data, which is below two standard deviations across the mass range, is consistent with the presence of a SM-like Higgs boson at $m_{H^{\text{SM}}} = 126\,\text{GeV}$.

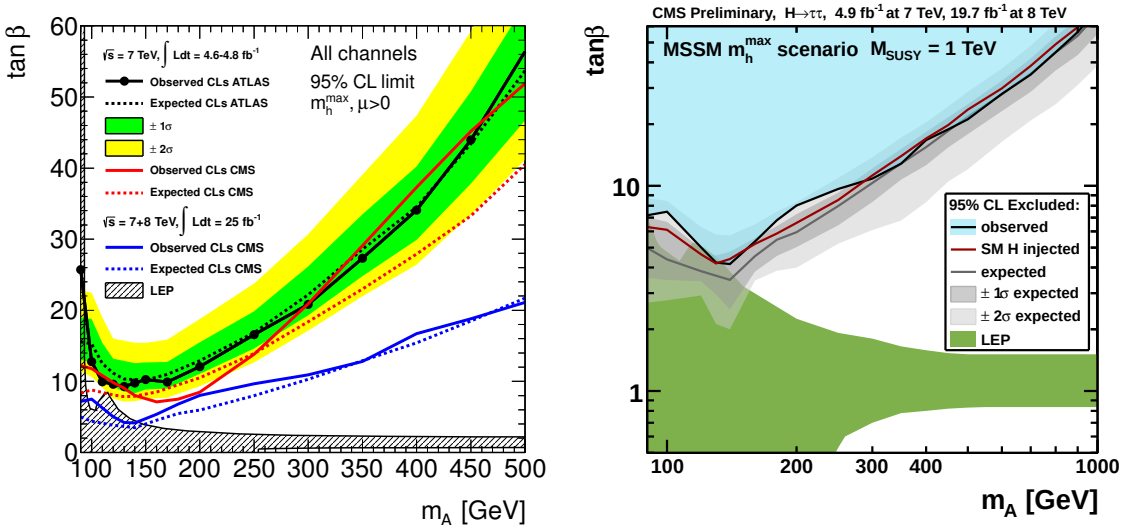

Figure 9.9.: Comparison of the upper limits on $\tan\beta$ in the $m_{h^0}^{\max}$ scenario of the MSSM as a function of m_{A^0}. The results of the combination with the other decay channels are compared to the respective results from CMS in the left Figure: The upper limits from CMS for the same LHC run [234] are given along with the results of the update to $25\,\mathrm{fb}^{-1}$ [115]. The region excluded by the LEP experiments is also shown [71]. The right Figure shows a comparison of the observed MSSM limit by CMS to the expected limit in the absence of Higgs bosons and under the assumption of a single SM-like Higgs boson at $m_{H^{\mathrm{SM}}} = 126\,\mathrm{GeV}$ [115].

10 Conclusion

A search for Higgs bosons decaying to τ lepton pairs has been performed in the $\tau_e\tau_\mu$ final state, using $4.6\,\text{fb}^{-1}$ of ATLAS pp collision data at a center–of–mass energy of 7 TeV.

In order to exploit the signatures of b-associated Higgs boson production and of Higgs boson production in gluon fusion events, the signal selection distinguishes events with exactly one b-tagged jet and events without b-tagged jets. The analysis presented within this thesis was combined with other searches for neutral Minimal Supersymmetric Standard Model (MSSM) Higgs bosons with ATLAS and jointly published in Ref. [10].

By selecting events with exactly one electron and one muon of opposite charge with low p_T thresholds on the final-state leptons and applying a set of kinematic cuts, a good signal acceptance is achieved for low Higgs boson mass values (close to the mass of the Z boson) and backgrounds with different kinematic properties are strongly suppressed.

Because Z boson decays constitute an irreducible background, the detection of one or more di-τ resonances in the vicinity of the Z boson peak is intrinsically challenging and relies on a good reconstruction of the di-τ invariant mass ($m_{\tau\tau}$). This is particularly true for the decay channels whose final-states contain neutrinos because of their adverse impact on the mass resolution. The use of the missing mass calculator (MMC) technique [186,187] offers the best di-τ mass resolution of all available methods.

After the application of the kinematic selection, 181 and 12947 events have been observed in the b-tagged and b-vetoed samples, respectively. This is compatible with the background–only expectation of $201 \pm 12(\text{stat.})^{+15}_{-14}(\text{syst.})$ events in the b-tagged sample and $12664 \pm 89(\text{stat.})^{+993}_{-996}(\text{syst.})$ events in the b-vetoed sample. The background estimation uses data-driven techniques for the main backgrounds. The $Z/\gamma^* \to \tau\tau$ contribution is estimated with the embedding technique [14], and the background contribution from multi-jet events is estimated with the $ABCD$ method [15]. The $t\bar{t}$ contribution to the background event yield is estimated from a control region, and the MMC mass shape is taken from simulation.

Given the agreement with the background–only hypothesis, exclusion limits for two different signal models are derived from a test statistic based on the profile likelihood of MMC mass distributions after the kinematic selection.

The production of neutral MSSM-like Higgs bosons can be excluded up to values of $3-5\,\text{pb}$ for the product of the production cross-section and the branching fraction to τ lepton pairs for both production modes in the Higgs boson mass range between 170 and 300 GeV. The exclusion limit gradually declines to about 230 pb (32 pb) at $m_\phi = 90\,\text{GeV}$ for gluon fusion (b-associated Higgs boson production) because of growing overlap between the expected signal shape and that of $Z/\gamma^* \to \tau\tau$ decays.

When interpreted in the $m_{h^0}^{\text{max}}$ scenario of the MSSM, this corresponds to an upper limit on $\tan\beta$ of about $12-14$ for m_{A^0} values between 110 and 150 GeV. For lower masses, the proximity of the Z boson resonance deteriorates the exclusion limit to about 24 at $m_{A^0} = 90\,\text{GeV}$. Both the cuts against high-p_T objects and the declining production cross-section values predicted by the MSSM lead to weaker limits with growing m_{A^0} values above $m_{A^0} = 130\,\text{GeV}$.

ATLAS is currently preparing an update that exploits the dataset of 2012, corresponding to an integrated luminosity of $20\,\text{fb}^{-1}$, collected at a center–of–mass energy of 8 TeV. Given the exclusion of the lowest m_{A^0} values that are compatible with the results from the Large

Electron–Positron Collider (LEP) experiments by Ref. [115], the improvement of the sensitivity to high Higgs boson masses ($m_{A^0} \gtrsim 200\,\text{GeV}$) is particularly interesting. The analysis of $\tau_e\tau_\mu$ final states presented within this thesis has been developed to optimally contribute to the sensitivity to light Higgs bosons, so several aspects could be modified for a search focusing on heavier Higgs bosons:

- The same-flavor decay modes $\tau_e\tau_e$ and $\tau_\mu\tau_\mu$ should be taken into account: Because of a better separation between the di-lepton invariant mass distributions of Z boson decays and decays of heavier Higgs bosons, the sensitivity of analyses of these decay modes can be expected to gain disproportionately.

- Because the MMC mass distributions of the $t\bar{t}$ and di-boson backgrounds differ significantly from those expected for the signal, it is promising to trade off background rejection for a better signal acceptance for higher Higgs bosons mass values by loosening kinematic cuts.

- Heavier Higgs bosons that are produced at similar momenta result in larger opening angles between the τ leptons. This has consequences both for the efficiency of the kinematic cuts described within this thesis (especially the cut on $\Delta\phi_{e\mu}$) and for the performance of the di-τ mass reconstruction.

The last two points suggest that it might be beneficial to optimize a future analysis separately for various points in the parameter space to achieve the optimal sensitivity everywhere.

Because of the expected reach to $\tan\beta \approx 5$ for $m_{A^0} \lesssim 200\,\text{GeV}$ of an analysis of $20\,\text{fb}^{-1}$ of data taken at a center–of–mass energy of 8 TeV, squark contributions and electroweak corrections should be taken into account in the calculation of the gluon fusion cross-section. Furthermore, the result of Ref. [115] indicates that the sensitivity of a search with $20\,\text{fb}^{-1}$ of ATLAS data to the Higgs sector of the Standard Model (SM) might also be considerable: The background–only hypothesis would, in this case, have to be amended to include the SM prediction, and the signal prediction taken into account by the statistical evaluation would refer to the difference of the MSSM and SM predictions.

All in all, neither the discovery of a SM-like Higgs boson nor the results of this thesis can falsify the existence of supersymmetry. The work presented in this thesis has contributed to the sensitivity of the combined search [10] and thus to the exclusion of a significant portion of the MSSM ($m_{h^0}^{\text{max}}$) parameter space that could not be probed before. The background estimation methods that were developed or refined in the context of this thesis can, by and large, be applied to upcoming Large Hadron Collider (LHC) searches at higher center–of–mass energies and with larger datasets.

Appendix

A Alternative Estimation of the $t\bar{t}$ Contribution in the b-Tagged Sample

Among the variables of the kinematic selection of the b-tagged sample, $E_{\mathrm{T}}^{\mathrm{miss}}+p_{\mathrm{T},e}+p_{\mathrm{T},\mu}$ and H_{T} are most suitable for an estimation of the $t\bar{t}$ background with the $ABCD$ method because they suppress the $t\bar{t}$ background more effectively than other processes (see Table 6.6).

An estimation method based on four regions with different cuts on $E_{\mathrm{T}}^{\mathrm{miss}}+p_{\mathrm{T},e}+p_{\mathrm{T},\mu}$ and H_{T} has been evaluated for the b-tagged sample:

A_R Events that satisfy the signal selection cuts $E_{\mathrm{T}}^{\mathrm{miss}}+p_{\mathrm{T},e}+p_{\mathrm{T},\mu}<125\,\mathrm{GeV}$, $H_{\mathrm{T}}<100\,\mathrm{GeV}$ enter the signal region ($A_{b\text{-tag}}$).

$\tilde{B}_R$ Events with $E_{\mathrm{T}}^{\mathrm{miss}}+p_{\mathrm{T},e}+p_{\mathrm{T},\mu}>125\,\mathrm{GeV}$, $H_{\mathrm{T}}<100\,\mathrm{GeV}$ enter region $\tilde{B}_R$.

$\tilde{C}_R$ Events with $E_{\mathrm{T}}^{\mathrm{miss}}+p_{\mathrm{T},e}+p_{\mathrm{T},\mu}<125\,\mathrm{GeV}$, $H_{\mathrm{T}}>100\,\mathrm{GeV}$ enter region $\tilde{C}_R$. The veto on additional b-jets is dropped. The shape of the $m_{\tau\tau}^{\mathrm{MMC}}$ distribution in the signal region is extracted from this region.

$\tilde{D}_R$ Events with $E_{\mathrm{T}}^{\mathrm{miss}}+p_{\mathrm{T},e}+p_{\mathrm{T},\mu}>125\,\mathrm{GeV}$, $H_{\mathrm{T}}>100\,\mathrm{GeV}$ enter region $\tilde{D}_R$. The veto on additional b-jets is dropped.

Each of those regions contains multi-jet events, which are estimated by an $ABCD$ method as described in Subsection 7.1.2. The signal and background contributions for regions $\tilde{B}_{b\text{-tag}}$ through $\tilde{D}_{b\text{-tag}}$ are summarized in Table A.1. The expected fraction of $t\bar{t}$ events is 93 % in region $\tilde{C}_{b\text{-tag}}$, which is comparable to the control region introduced in Subsection 7.1.3 (92 %). In contrast, regions $\tilde{B}_{b\text{-tag}}$ and $\tilde{D}_{b\text{-tag}}$ exhibit only purities of $75-78$ %.

Table A.1.: Estimated contributions of non-$t\bar{t}$ backgrounds to the $t\bar{t}$ control regions ($\tilde{B}_{b\text{-tag}}$ through $\tilde{D}_{b\text{-tag}}$) and the signal region ($A_{b\text{-tag}}$). All cuts of the kinematic selection have been applied, with the exception of the veto on additional b-jets in regions $\tilde{C}_{b\text{-tag}}$ and $\tilde{D}_{b\text{-tag}}$. The numbers of $t\bar{t}$ events as predicted by MC@NLO and POWHEG+Jimmy are given along with the purity in parentheses. The expected signal contribution for the $m_{h^0}^{\mathrm{max}}$ scenario and $m_{A^0}=150\,\mathrm{GeV}$, $\tan\beta=20$ is also shown. The given uncertainties only reflect the statistical component.

	Signal	$Z/\gamma^*\to\tau\tau$	Single t	Multi-jet	Others	$t\bar{t}$		Data
						MC@NLO	POWHEG	
$A_{b\text{-tag}}$	20.7±0.7	109 ± 5	15.7±1.2	15 ± 9	6.1 ±1.2	44.8±1.5	49±6	181
$\tilde{B}_{b\text{-tag}}$	5.0±0.4	3.7± 1.0	43 ±2	0.3± 2.0	4.9 ±0.8	170±3 (77 %)	160±12 (75 %)	225
$\tilde{C}_{b\text{-tag}}$	3.2±0.3	40 ± 3	6.9±0.7	2.1± 2.8	0.74±0.15	181±3 (78 %)	168±12 (77 %)	249
$\tilde{D}_{b\text{-tag}}$	2.4±0.3	11.9± 1.8	54 ±2	3.4± 3.1	2.4 ±0.5	965±7 (93 %)	940±29 (93 %)	1124

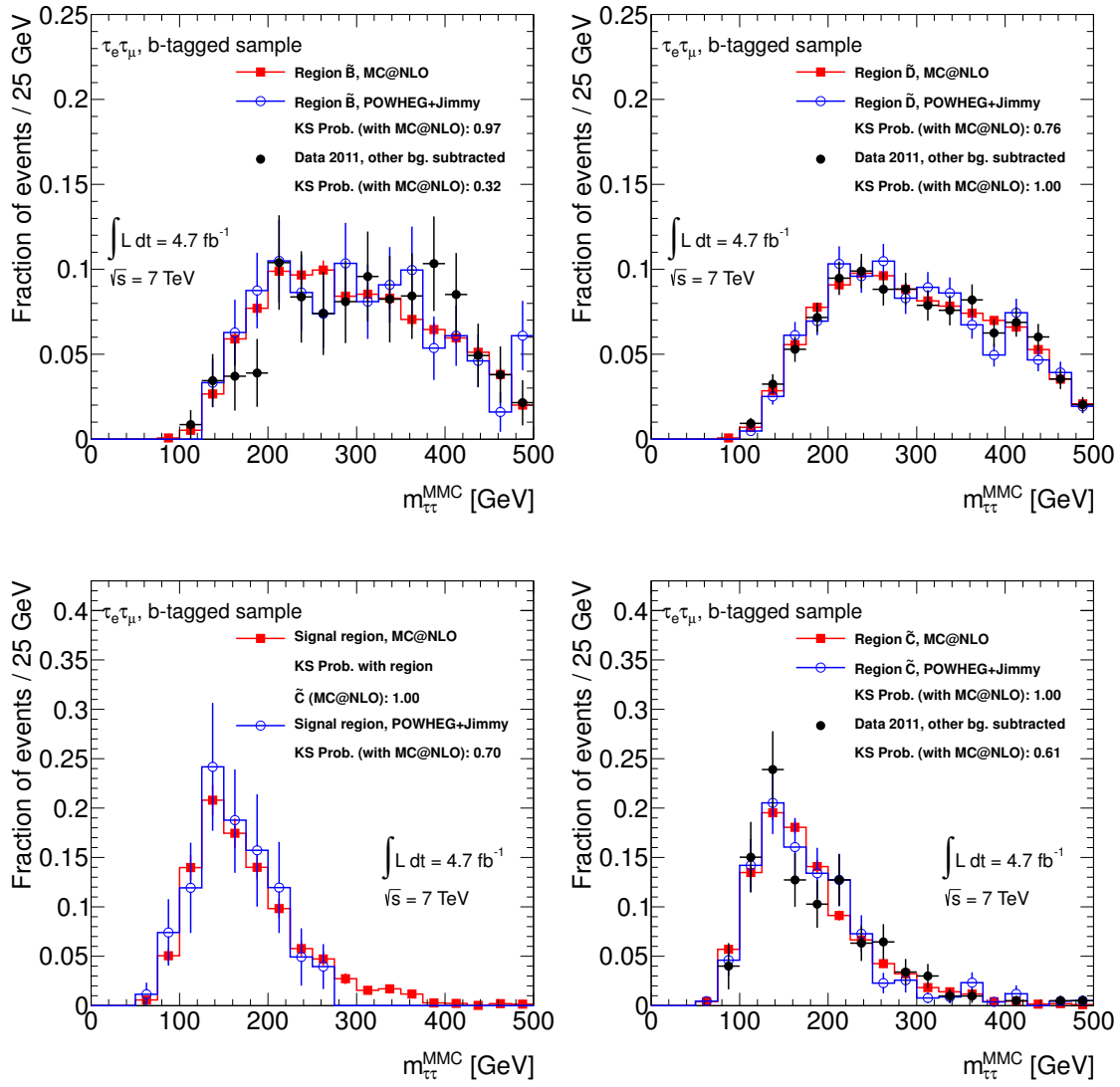

Figure A.1.: Shape of the reconstructed MMC mass in the signal region of the b-tagged sample and the associated $t\bar{t}$ control regions of the alternative estimation method after the full selection. Other background contributions have been subtracted from data in the control regions. The KS test results between the distributions from the same region and between the MC@NLO predictions in the signal region and region $\tilde{C}_{b\text{-tag}}$ are also given.

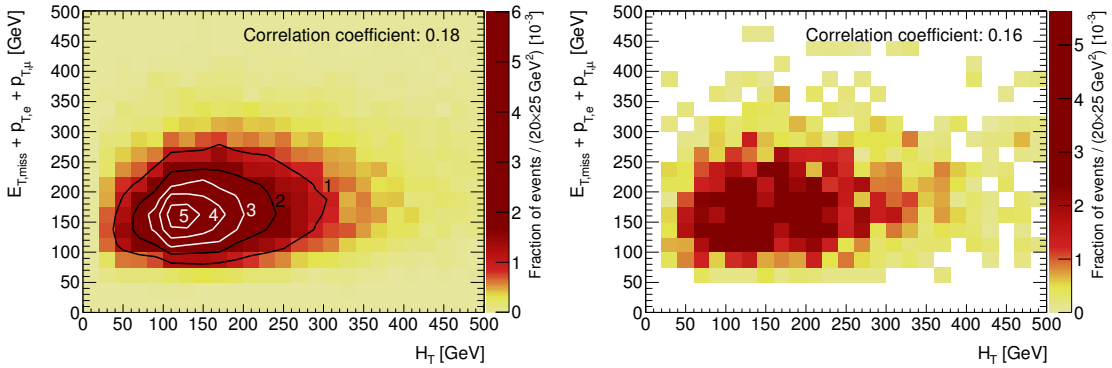

Figure A.2.: Correlation of $E_{\mathrm{T}}^{\mathrm{miss}} + p_{\mathrm{T},e} + p_{\mathrm{T},\mu}$ and H_{T} in the signal region of the b-tagged sample and the associated $t\bar{t}$ control regions of the alternative estimation method after the full selection.

By subtracting all other background contributions from the collision data in the control regions, the $m_{\tau\tau}^{\mathrm{MMC}}$ shape of the $t\bar{t}$ contribution is obtained (see Figure A.1). The shape obtained from the MC@NLO sample matches that from POWHEG+Jimmy well in all control regions and the signal region: Kolmogorov–Smirnov (KS) tests yield p-values of at least 70 %. The shape obtained by MC@NLO in the signal region agrees with the MC@NLO prediction for region $\tilde{C}_{b\text{-tag}}$, and the ratio of the predicted event yield for region $\tilde{C}_{b\text{-tag}}$ to that of the signal region is about four. Therefore, it can be used to obtain the $m_{\tau\tau}^{\mathrm{MMC}}$ shape of the $t\bar{t}$ contribution in the signal region.

In order to estimate the event yield of the $t\bar{t}$ contribution in the signal region ($N_{t\bar{t}}^{A_{b\text{-tag}}}$), correlations must be taken into account. Figure A.2 shows the correlation between $E_{\mathrm{T}}^{\mathrm{miss}} + p_{\mathrm{T},e} + p_{\mathrm{T},\mu}$ and H_{T} in the four regions ($A_{b\text{-tag}}$, $\tilde{B}_{b\text{-tag}}$ through $\tilde{D}_{b\text{-tag}}$). A visible correlation exists both in the MC@NLO dataset and in the POWHEG+Jimmy dataset, resulting in correlation coefficients of 0.18 and 0.16, respectively.

In the absence of correlations, the event yield can be calculated from the event yields in the control regions (after subtraction of other backgrounds, denoted as $N_{t\bar{t}}^{\tilde{B}_{b\text{-tag}}}$ through $N_{t\bar{t}}^{\tilde{B}_{b\text{-tag}}}$) as in Eq. (7.4). Otherwise, the formula can be amended by including the correlations seen in the simulated samples:

$$N_{t\bar{t}}^{A_{b\text{-tag}}} = \underbrace{\frac{N_{t\bar{t}}^{\tilde{C}_{b\text{-tag}}}}{N_{t\bar{t}}^{\tilde{D}_{b\text{-tag}}}} N_{t\bar{t}}^{\tilde{B}_{b\text{-tag}}}}_{\text{taken from data}} \times \underbrace{\frac{N_{t\bar{t}}^{A_{b\text{-tag}}} N_{t\bar{t}}^{\tilde{D}_{b\text{-tag}}}}{N_{t\bar{t}}^{\tilde{B}_{b\text{-tag}}} N_{t\bar{t}}^{\tilde{C}_{b\text{-tag}}}}}_{\text{taken from simulation}} . \tag{A.1}$$

The value of the first brace (33±4 events) in Eq. (A.1) is thus corrected by values of 1.41±0.06 (MC@NLO) or 1.71 ± 0.28 (POWHEG+Jimmy).

As for the extrapolation factors in the estimation method described in Subsection 7.1.3, the two values can be combined to a weighted mean, using half the difference of the two input values as systematic error, resulting in a correction factor of $1.42 \pm 0.06(\mathrm{stat.}) \pm 0.14(\mathrm{syst.})$.

The estimated event yield from $t\bar{t}$ events in the b-tagged sample is thus evaluated to be $(46 \pm 5(\mathrm{stat.}) \pm 5(\mathrm{syst.}))$ events. The extrapolation method and the *ABCD* method agree within the uncertainties (see Table 7.5, in both cases excluding other sources of systematic uncertainty).

The illustrated method confirms the goodness of the shape estimate obtained from the

MC@NLO sample for the signal region. The estimate of the systematic uncertainty from the comparison of the two simulated datasets is larger than that of the method described in Subsection 7.1.3. Because the optimal selection for the b-vetoed sample does not include H_{T} or an adequate substitute, the $ABCD$ method as presented here can only be applied to the b-tagged sample.

B Systematic Variations Without Significant Impact on the MMC Mass Shape

This Appendix shows the systematic variations with the smallest observed impact on the shapes of the missing mass calculator (MMC) mass distributions. The description of the variations is given in Subsection 8.1.3.

Note that the statistical uncertainties for $t\bar{t}$ (gluon fusion) are too large to compare shapes in the b-vetoed (b-tagged) sample.

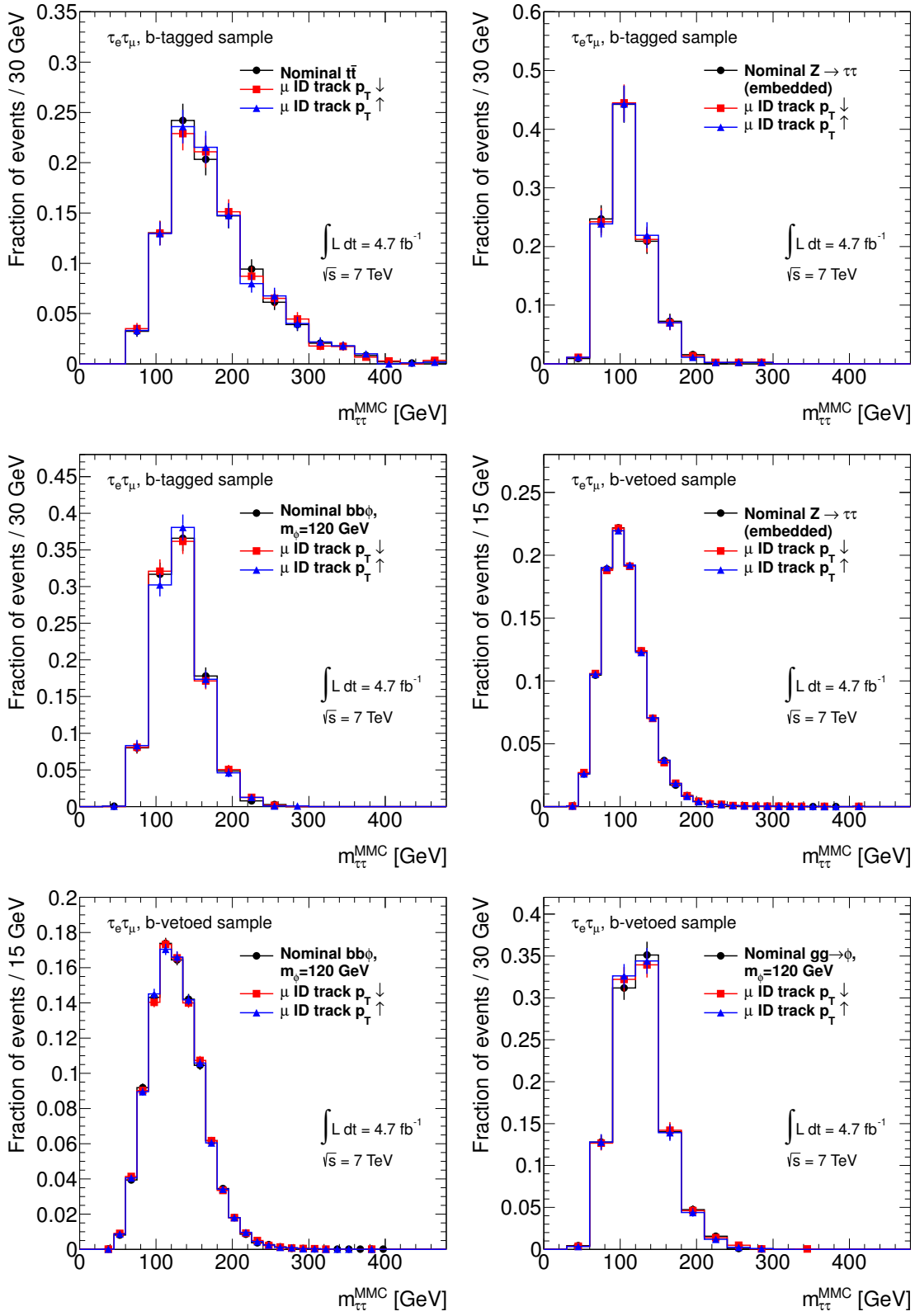

Figure B.1.: Impact of the muon momentum uncertainty from the Inner Detector measurement ("μ ID track p_{T} $\uparrow$"/"μ ID track p_{T} $\downarrow$" variations) on the shapes of the $m_{\tau\tau}^{\mathrm{MMC}}$ distributions of the b-tagged (first three Figures) and the b-vetoed (last three Figures) samples for $t\bar{t}$, embedded $Z/\gamma^* \to \tau\tau$ events, and the two Higgs boson production modes.

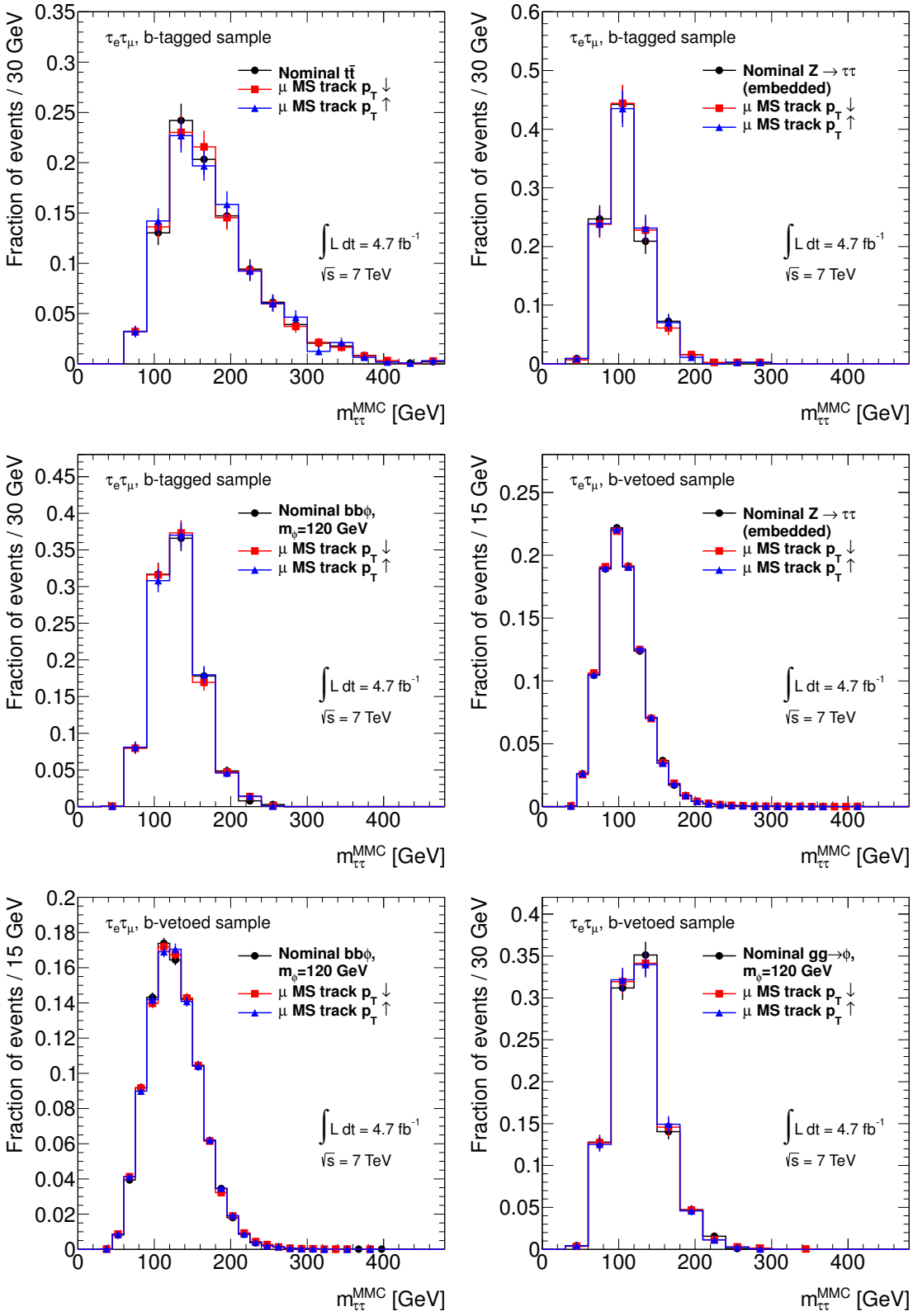

Figure B.2.: Impact of the muon momentum uncertainty from the Muon Spectrometer measurement ("μ MS track $p_{\mathrm{T}}\uparrow$"/"μ MS track $p_{\mathrm{T}}\downarrow$" variations) on the shapes of the $m_{\tau\tau}^{\mathrm{MMC}}$ distributions of the b-tagged (first three Figures) and the b-vetoed (last three Figures) samples for $t\bar{t}$, embedded $Z/\gamma^{*} \to \tau\tau$ events, and the two Higgs boson production modes.

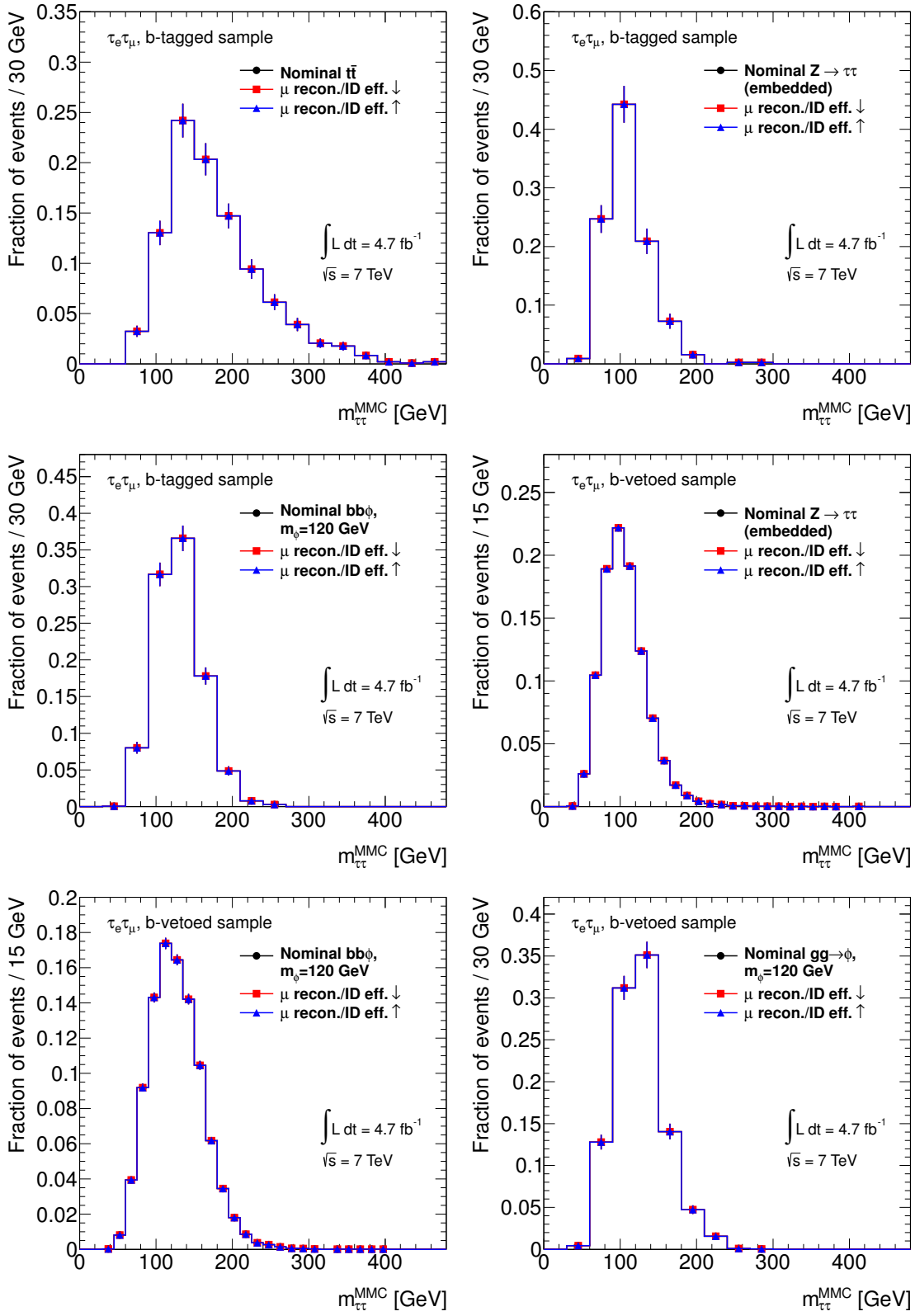

Figure B.3.: Impact of the muon combined efficiency of the reconstruction and identification ("μ recon./ID eff. ↑"/"μ recon./ID eff. ↓" variations) on the shapes of the $m_{\tau\tau}^{\mathrm{MMC}}$ distributions of the b-tagged (first three Figures) and the b-vetoed (last three Figures) samples for $t\bar{t}$, embedded $Z/\gamma^* \to \tau\tau$ events, and the two Higgs boson production modes.

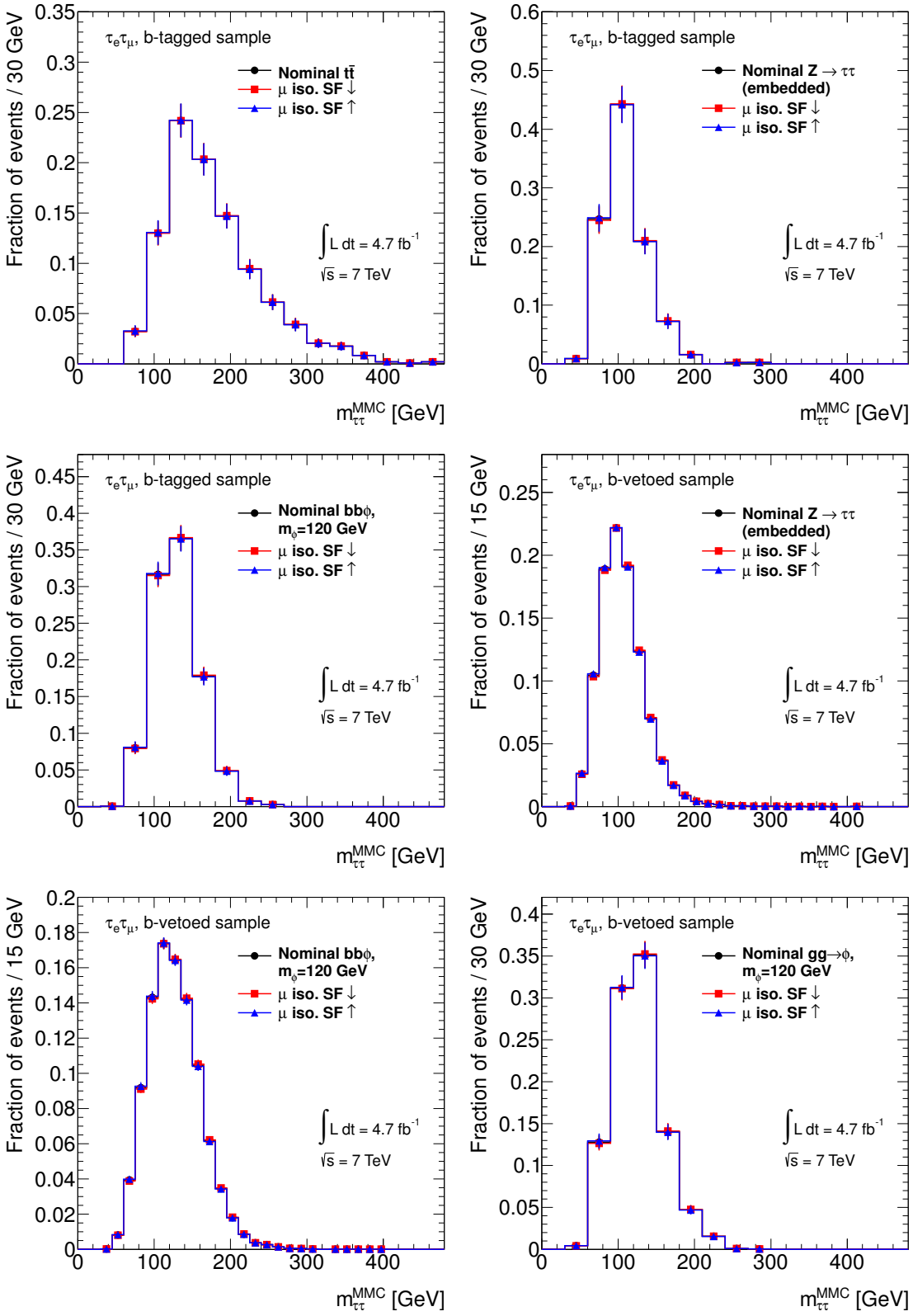

Figure B.4.: Impact of the muon isolation efficiency uncertainty ("μ iso. SF ↑"/"μ iso. SF ↓" variations) on the shapes of the $m_{\tau\tau}^{\mathrm{MMC}}$ distributions of the b-tagged (first three Figures) and the b-vetoed (last three Figures) samples for $t\bar{t}$, embedded $Z/\gamma^* \to \tau\tau$ events, and the two Higgs boson production modes.

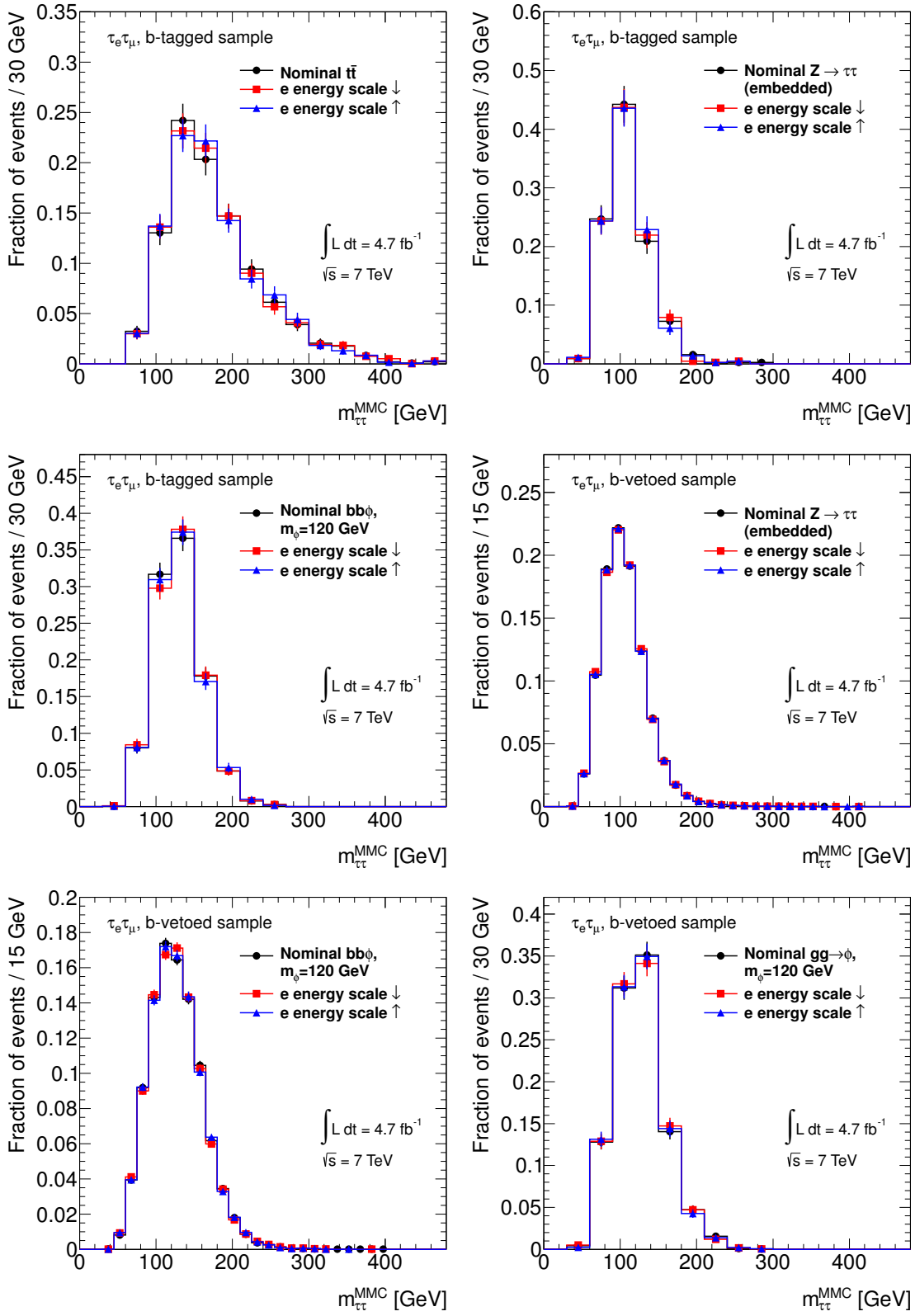

Figure B.5.: Impact of the electron energy scale uncertainty ("e energy scale ↑"/"e energy scale ↓") on the shapes of the $m_{\tau\tau}^{\mathrm{MMC}}$ distributions of the b-tagged (first three Figures) and the b-vetoed (last three Figures) samples for $t\bar{t}$, embedded $Z/\gamma^* \to \tau\tau$ events, and the two Higgs boson production modes.

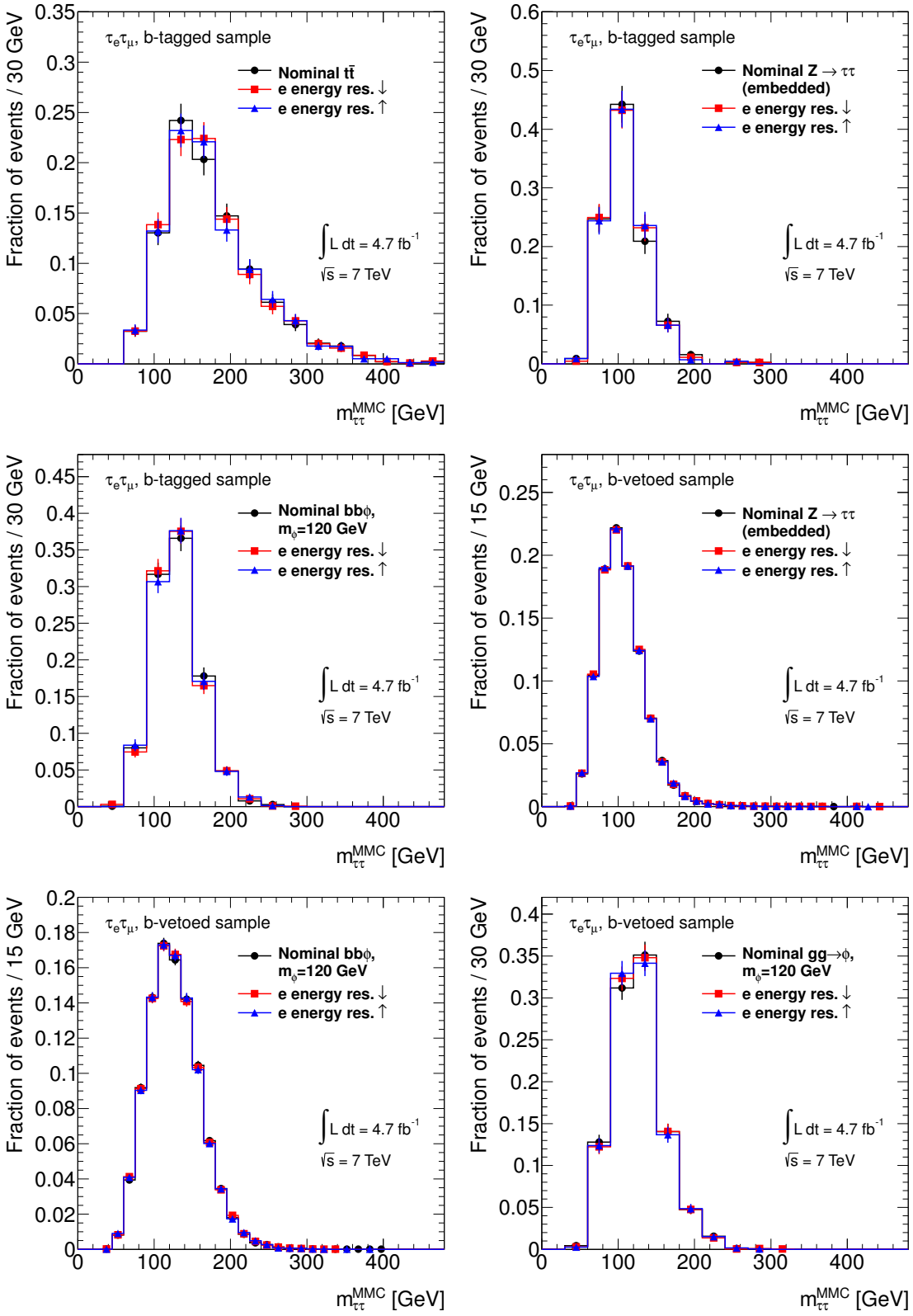

Figure B.6.: Impact of the electron energy resolution uncertainty ("e energy res. ↑"/"e energy res. ↓" variations) on the shapes of the $m_{\tau\tau}^{\mathrm{MMC}}$ distributions of the b-tagged (first three Figures) and the b-vetoed (last three Figures) samples for $t\bar{t}$, embedded $Z/\gamma^* \to \tau\tau$ events, and the two Higgs boson production modes.

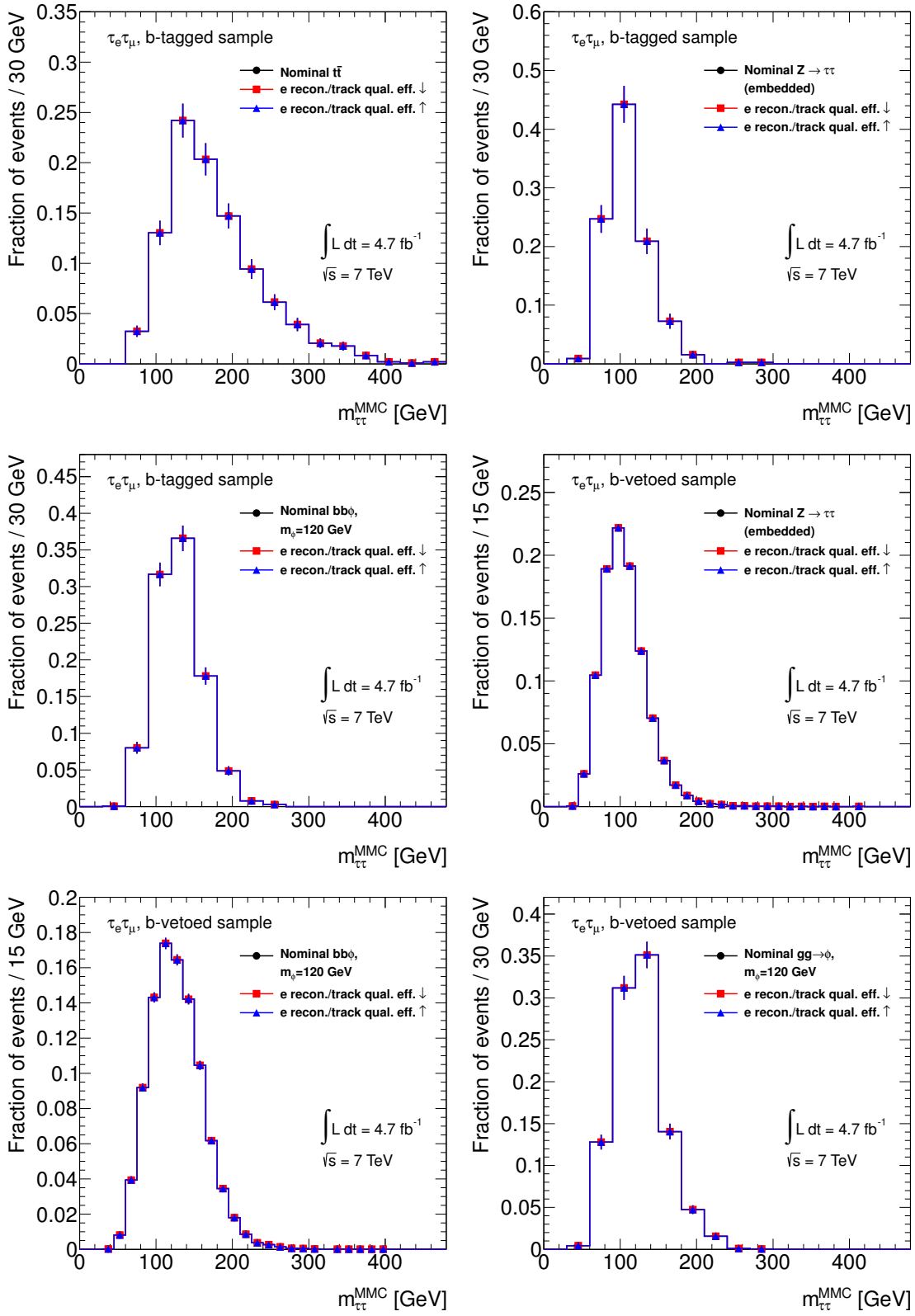

Figure B.7.: Impact of the electron reconstruction efficiency uncertainty ("e recon./track qual. eff. ↑"/"e recon./track qual. eff. ↓" variations) on the shapes of the $m_{\tau\tau}^{\mathrm{MMC}}$ distributions of the b-tagged (first three Figures) and the b-vetoed (last three Figures) samples for $t\bar{t}$, embedded $Z/\gamma^* \to \tau\tau$ events, and the two Higgs boson production modes.

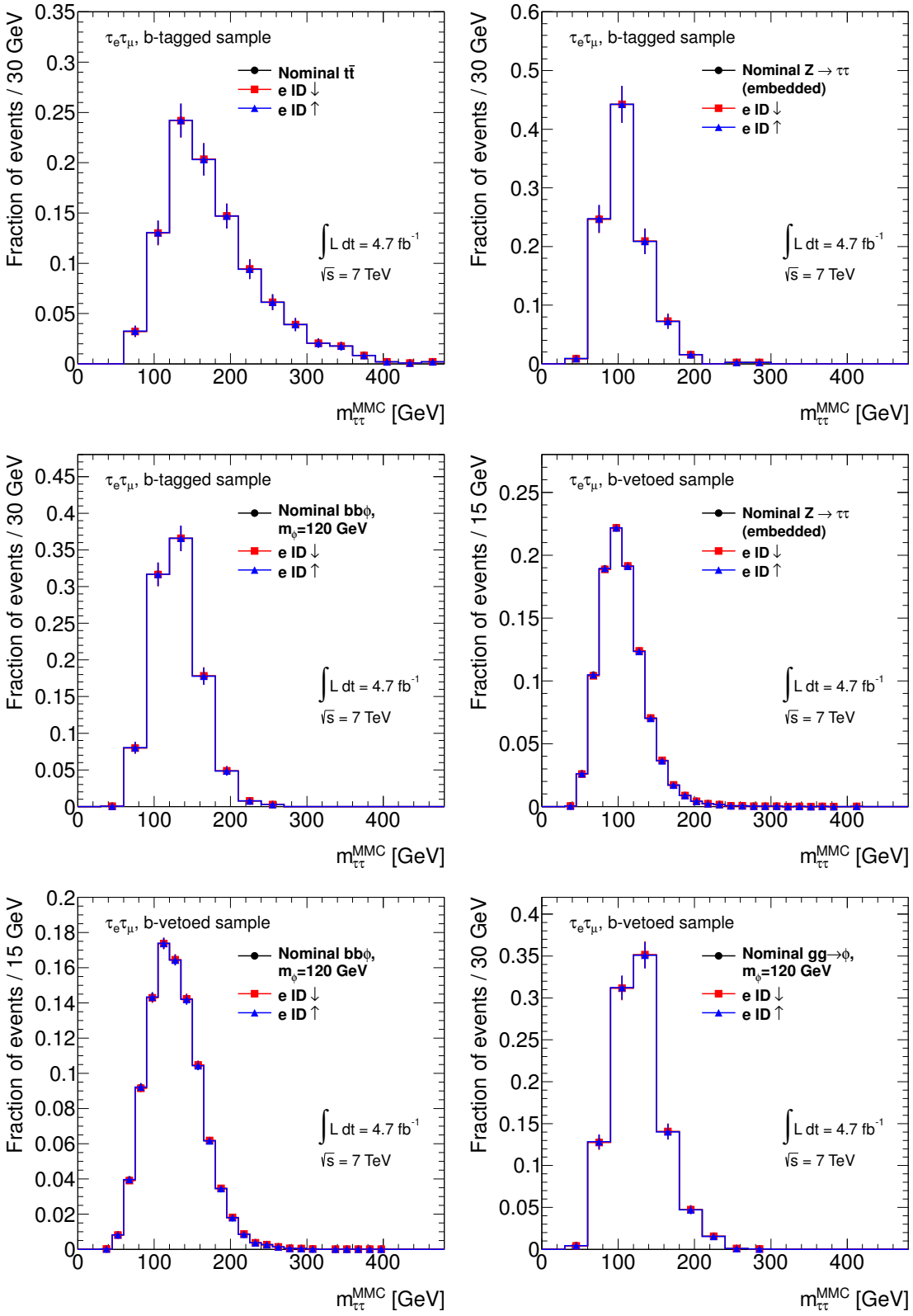

Figure B.8.: Impact of the electron identification efficiency uncertainty ("e ID ↑"/"e ID ↓" variations) on the shapes of the $m_{\tau\tau}^{\mathrm{MMC}}$ distributions of the b-tagged (first three Figures) and the b-vetoed (last three Figures) samples for $t\bar{t}$, embedded $Z/\gamma^* \to \tau\tau$ events, and the two Higgs boson production modes.

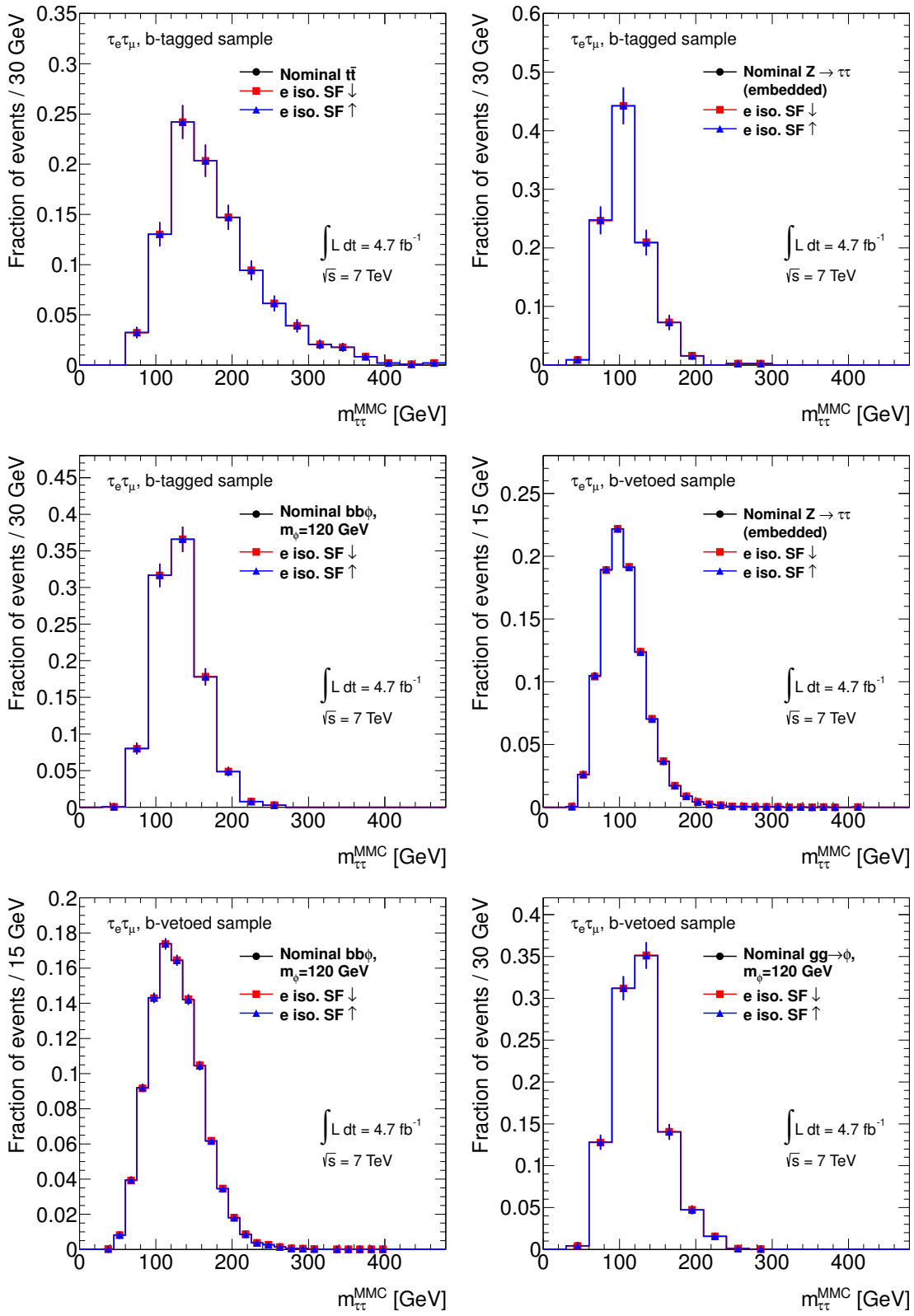

Figure B.9.: Impact of the electron isolation efficiency uncertainty ("e iso. SF ↑"/"e iso. SF ↓" variations) on the shapes of the $m_{\tau\tau}^{\mathrm{MMC}}$ distributions of the b-tagged (first three Figures) and the b-vetoed (last three Figures) samples for $t\bar{t}$, embedded $Z/\gamma^* \to \tau\tau$ events, and the two Higgs boson production modes.

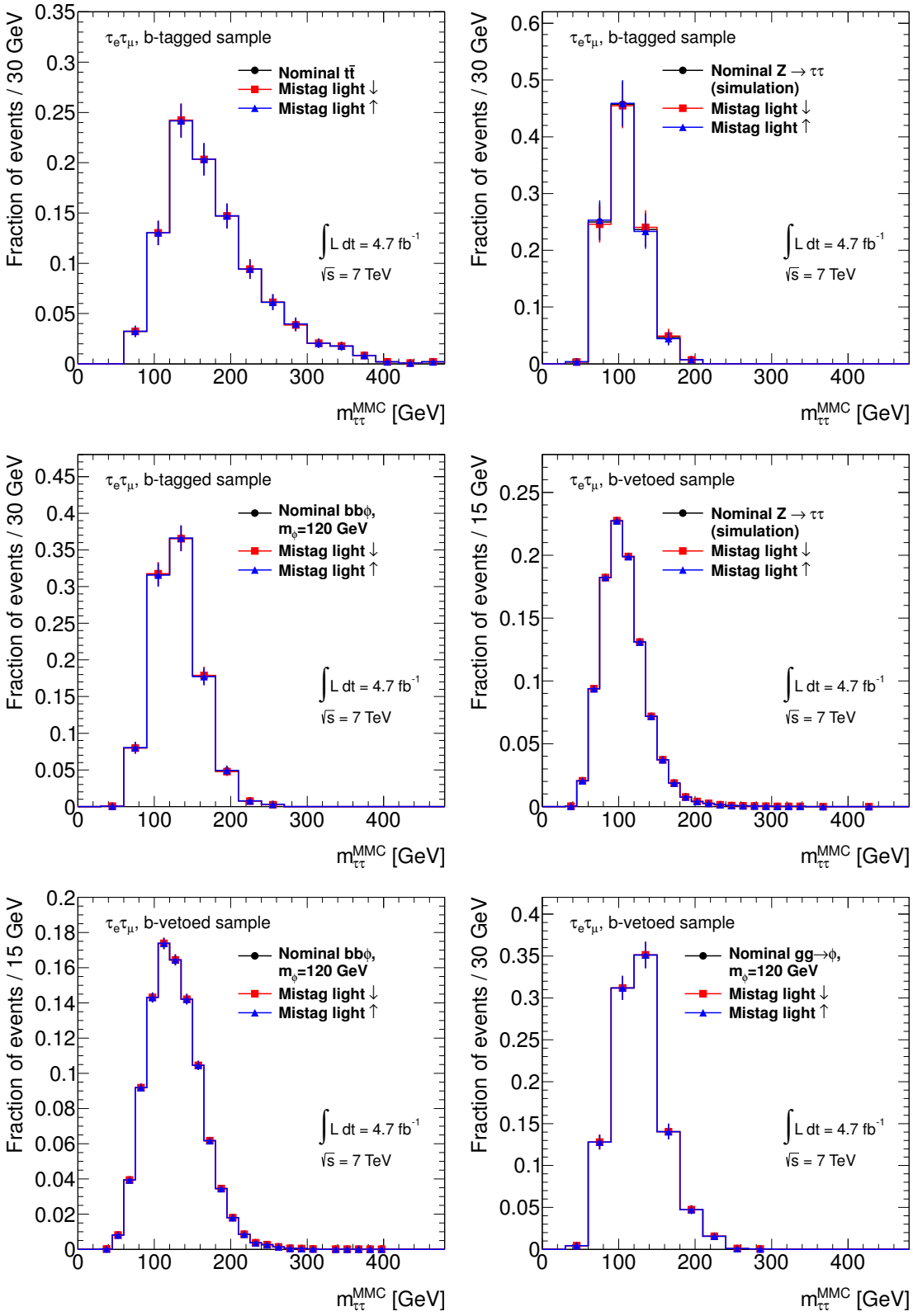

Figure B.10.: Impact of the flavor tagging efficiency uncertainty for light jets ("Mistag light ↑"/"Mistag light ↓" variations) on the shapes of the $m_{\tau\tau}^{\mathrm{MMC}}$ distributions of the b-tagged (first three Figures) and the b-vetoed (last three Figures) samples for $t\bar{t}$, simulated $Z/\gamma^* \to \tau\tau$ events, and the two Higgs boson production modes.

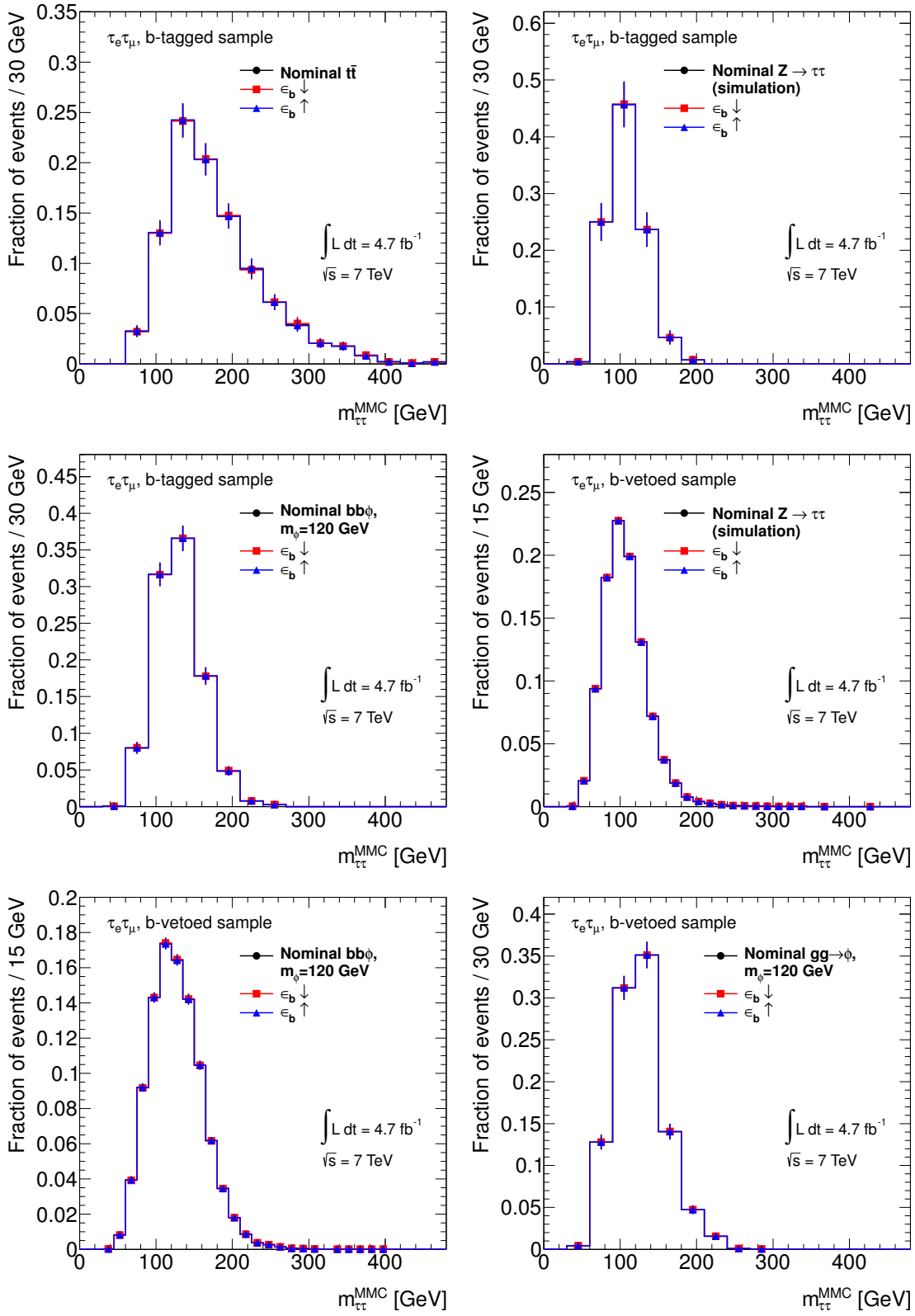

Figure B.11.: Impact of the flavor tagging efficiency uncertainty for b-jets ("ε_b $\uparrow$"/"ε_b $\downarrow$" variations) on the shapes of the $m_{\tau\tau}^{\mathrm{MMC}}$ distributions of the b-tagged (first three Figures) and the b-vetoed (last three Figures) samples for $t\bar{t}$, simulated $Z/\gamma^* \to \tau\tau$ events, and the two Higgs boson production modes.

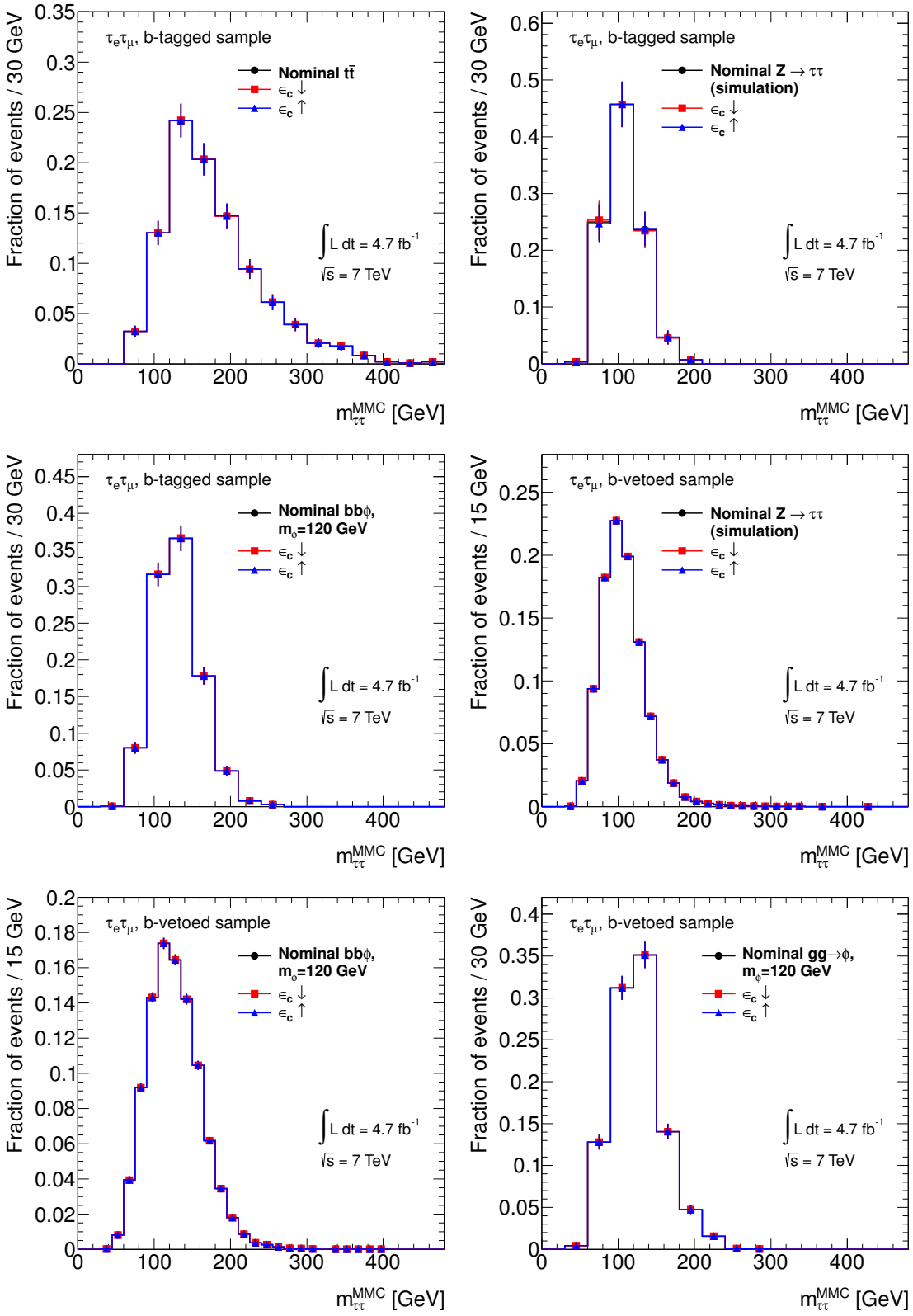

Figure B.12.: Impact of the flavor tagging efficiency uncertainty for c-jets ("ε_c ↑"/"ε_c ↓" variations) on the shapes of the $m_{\tau\tau}^{\mathrm{MMC}}$ distributions of the b-tagged (first three Figures) and the b-vetoed (last three Figures) samples for $t\bar{t}$, simulated $Z/\gamma^* \to \tau\tau$ events, and the two Higgs boson production modes.

C Simplified Signal and Background Models for the Published Results

In the combination with the $\tau_{\text{lep}}\tau_{\text{had}}$, $\tau_{\text{had}}\tau_{\text{had}}$, and $\mu\mu$ decay channels [10], the complexity of the signal and background models complicates the fit to the likelihood function. The least significant shape uncertainties have therefore been removed, and nuisance parameters (NPs) have been coupled. The impact of each change has been verified to result only in small changes of the combined limit from the b-tagged and b-vetoed samples of this thesis:

- The "Jet energy scale ↑"/"Jet energy scale ↓", "Jet energy resolution ↑", "Calo. clusters ↑"/"Calo. clusters ↓", and "Pileup ↑"/"Pileup ↓" variations have been merged[1], and the shape variations "Jet energy scale ↑"/"Jet energy scale ↓"—as most significant variations—are used to represent the correlated shape uncertainty (see Subsection 8.1.3).

- The normalization uncertainty from the isolation criteria on muons in the selection of $Z/\gamma^* \to \mu\mu$ events for the embedded sample (see Subsection 8.2.1) is determined only from the "Tighter isolation" variation. The difference (Δ) to the central value is symmetrized as estimate of the uncertainty: $\pm\Delta$.

- Small shape uncertainties have been neglected for the following processes and variations:
  - The merged "Jet energy scale ↑"/"Jet energy scale ↓" variations (see Subsection 8.1.3) have been demoted to pure normalization uncertainties for the "other electroweak" contribution and Higgs boson production in association with b-quarks in both samples and for the $t\bar{t}$ contribution to the b-tagged sample.
  - The shape uncertainties of the "Tighter isolation" and "No isolation" variations of the embedded $Z/\gamma^* \to \tau\tau$ events (see Subsection 8.2.1) have been neglected in both samples.
  - The shape uncertainties of the "Subtracted μ calo. deposits ↑"/"Subtracted μ calo. deposits ↓" variations of the embedded $Z/\gamma^* \to \tau\tau$ events (see Subsection 8.2.1) have been neglected in the b-tagged sample.

- The resolution and scale uncertainties for simulated electrons (see Subsection 8.1.3) have been merged.

- The NPs associated to the uncertainty of $R_{\text{anti-isol./isol.}}$ and the corresponding shape uncertainty (see Subsection 8.2.2 and Section 9.2) have been coupled both in the b-tagged and the b-vetoed sample.

- Normalization uncertainties whose associated 1σ variations impact the event yield of a contribution by less than 0.5 % have been neglected.

[1] adding separately in quadrature the upper and the lower uncertainties

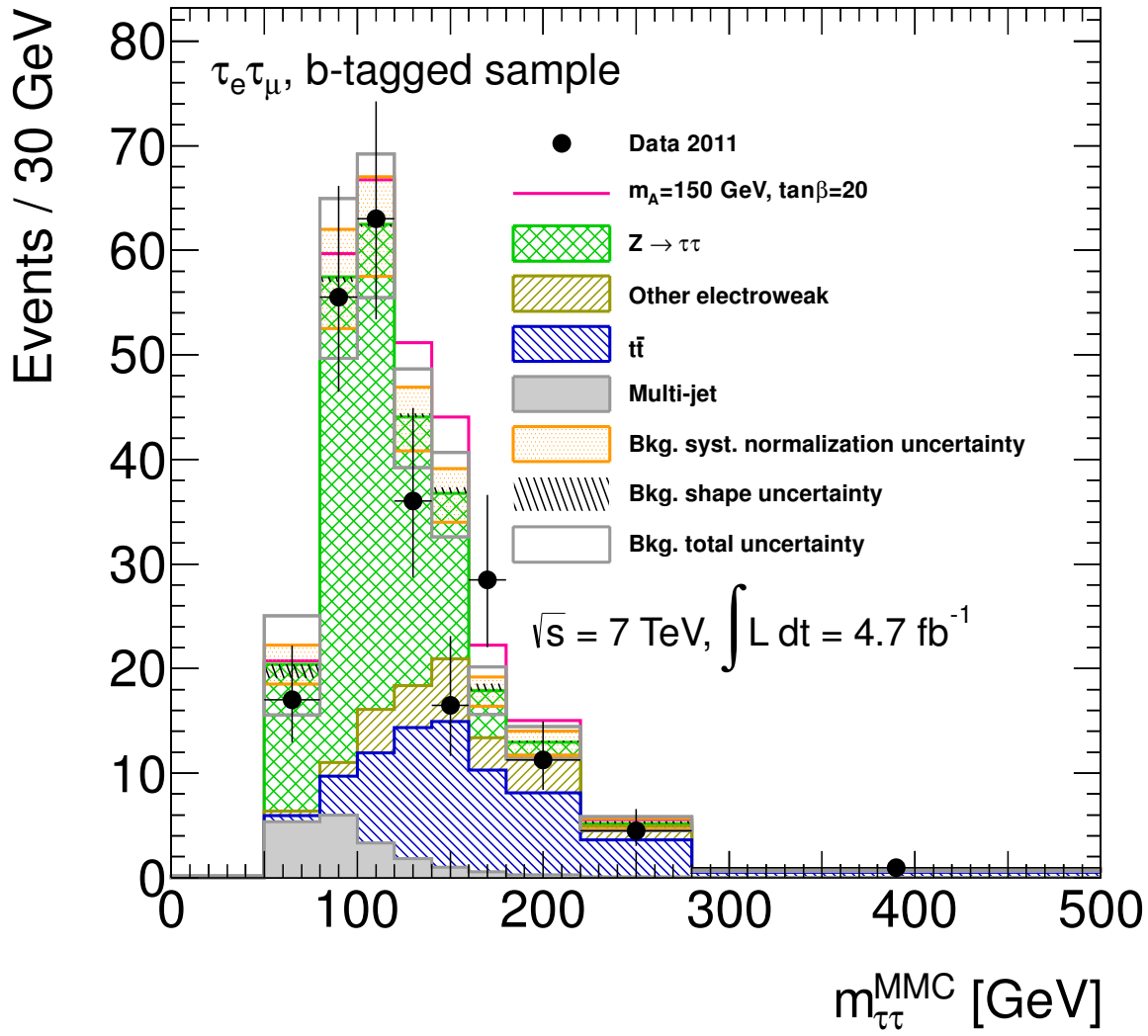

Figure C.1.: $m_{\tau\tau}^{\mathrm{MMC}}$ distribution in the b-tagged sample. The background prediction shown uses the techniques detailed in Chapter 7 to predict the background composition in each bin and the respective uncertainties. The variations described in Chapter 8 have been used to assess the systematic uncertainties, and the signal and background uncertainty models have been simplified for the combination with the $\tau_{\mathrm{lep}}\tau_{\mathrm{had}}$, $\tau_{\mathrm{had}}\tau_{\mathrm{had}}$, and $\mu\mu$ decay channels. The statistical uncertainties as well as the systematic normalization uncertainties (including the uncertainty on the integrated luminosity) and the shape uncertainties have been added in quadrature to estimate the total background uncertainty.

- The acceptance uncertainty contribution from the distinction of samples with no, one, or more b-jets (see Subsection 8.1.2) has been neglected. Its impact on expected limits on the product of the production cross-section and the branching ratio to τ leptons has been evaluated to be below 0.5 %.

As shown in Figures 8.7 through 8.10 for the full signal and background models, Figures C.1 through C.4 show the simplified signal region input to the limit calculation. The published exclusion limits are shown in Figure C.5.

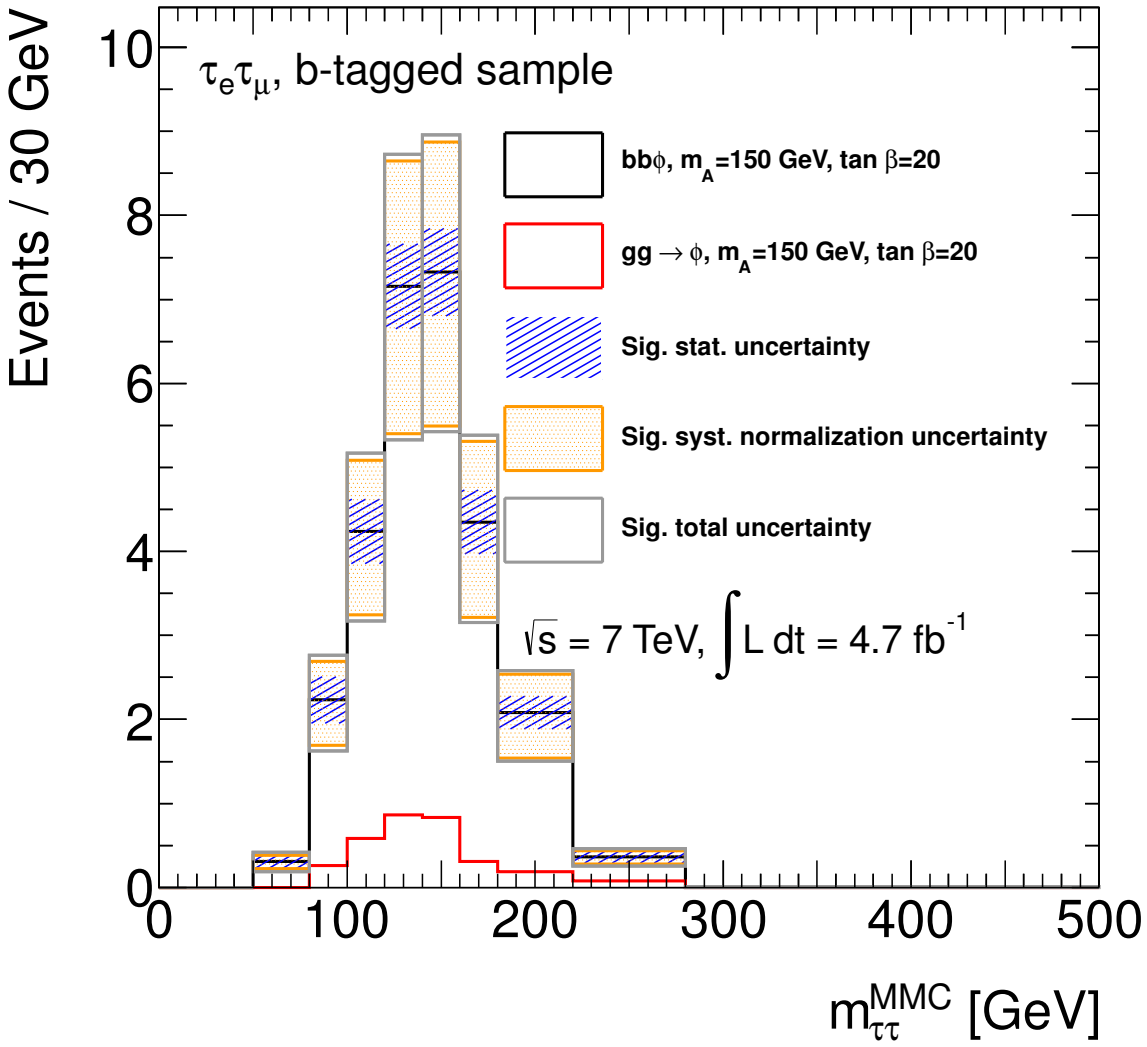

Figure C.2.: Expected $m_{\tau\tau}^{\mathrm{MMC}}$ distribution of the signal processes in the b-tagged sample. The variations described in Chapter 8 have been used to assess the systematic uncertainties, and the signal and background uncertainty models have been simplified for the combination with the $\tau_{\mathrm{lep}}\tau_{\mathrm{had}}$, $\tau_{\mathrm{had}}\tau_{\mathrm{had}}$, and $\mu\mu$ decay channels. The statistical uncertainties and the systematic normalization uncertainties (including the uncertainty on the integrated luminosity) have been added in quadrature to estimate the total background uncertainty. All shape uncertainties have been neglected.

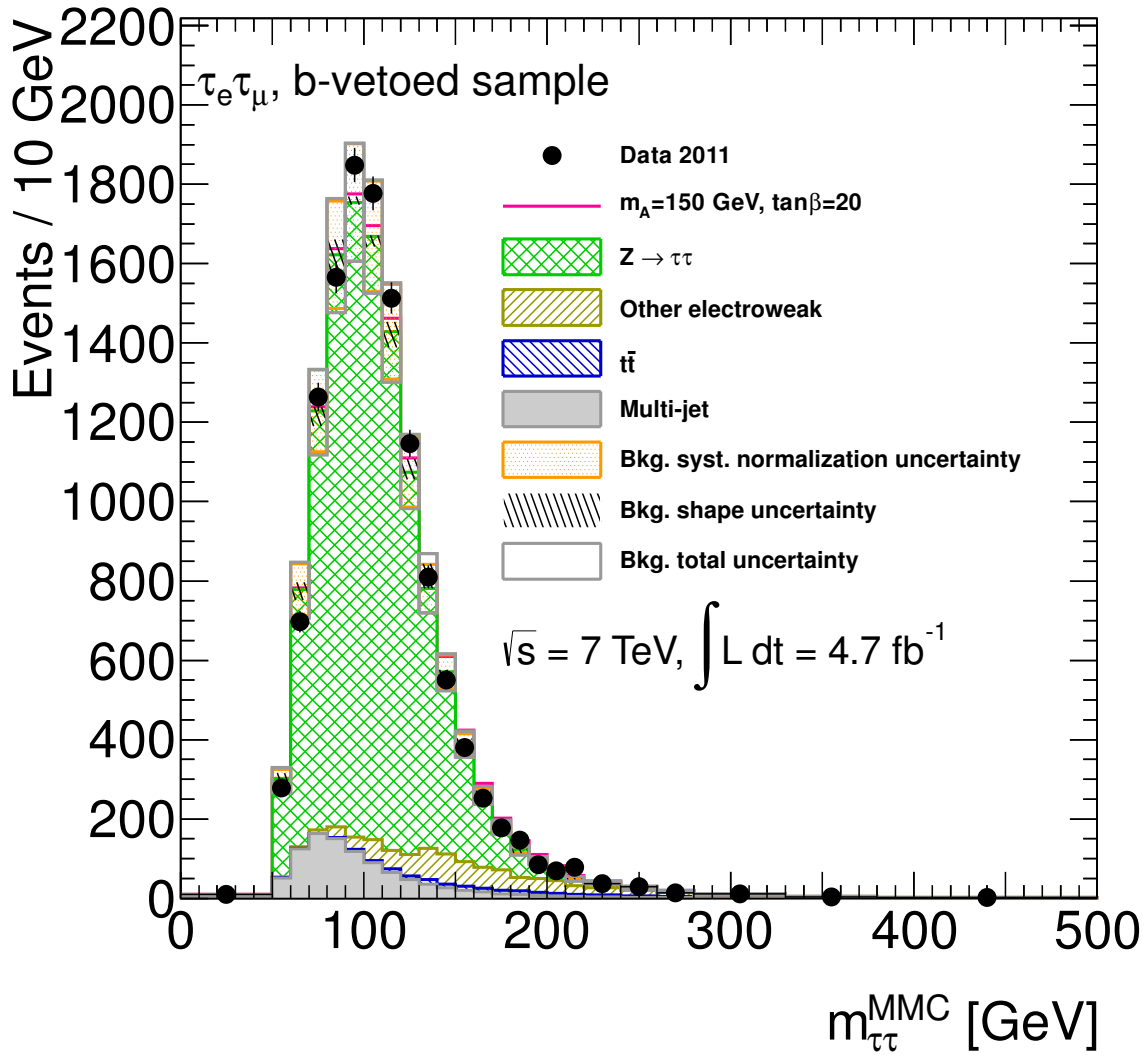

Figure C.3.: $m_{\tau\tau}^{\mathrm{MMC}}$ distribution in the b-vetoed sample. The background prediction shown uses the techniques detailed in Chapter 7 to predict the background composition in each bin and the respective uncertainties. The variations described in Chapter 8 have been used to assess the systematic uncertainties, and the signal and background uncertainty models have been simplified for the combination with the $\tau_{\mathrm{lep}}\tau_{\mathrm{had}}$, $\tau_{\mathrm{had}}\tau_{\mathrm{had}}$, and $\mu\mu$ decay channels. The statistical uncertainties as well as the systematic normalization uncertainties (including the uncertainty on the integrated luminosity) and the shape uncertainties have been added in quadrature to estimate the total background uncertainty.

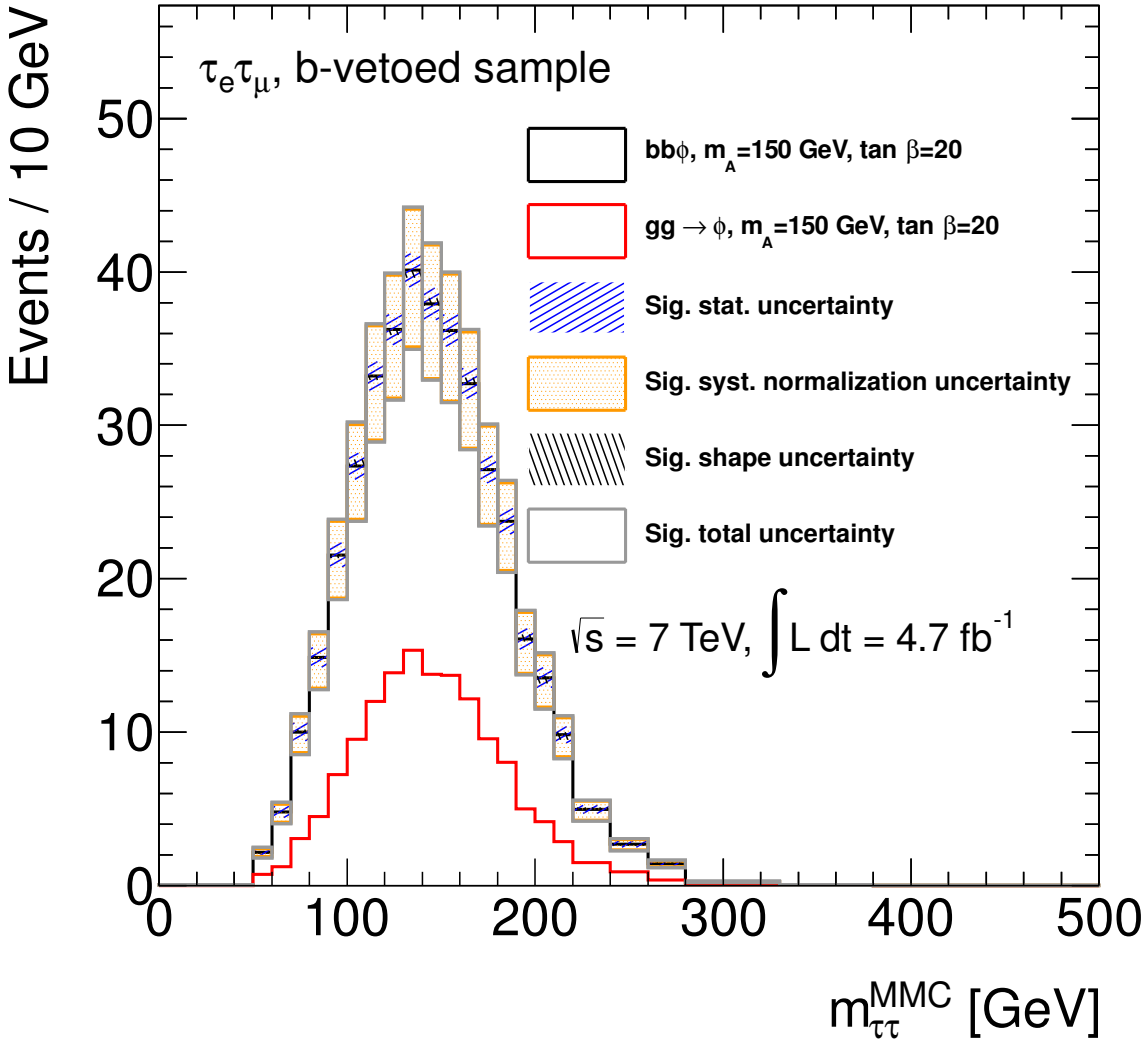

Figure C.4.: Expected $m_{\tau\tau}^{\mathrm{MMC}}$ distribution of the signal processes in the b-vetoed sample. The variations described in Chapter 8 have been used to assess the systematic uncertainties, and the signal and background uncertainty models have been simplified for the combination with the $\tau_{\mathrm{lep}}\tau_{\mathrm{had}}$, $\tau_{\mathrm{had}}\tau_{\mathrm{had}}$, and $\mu\mu$ decay channels. The statistical uncertainties as well as the systematic normalization uncertainties (including the uncertainty on the integrated luminosity) and the shape uncertainties have been added in quadrature to estimate the total background uncertainty.

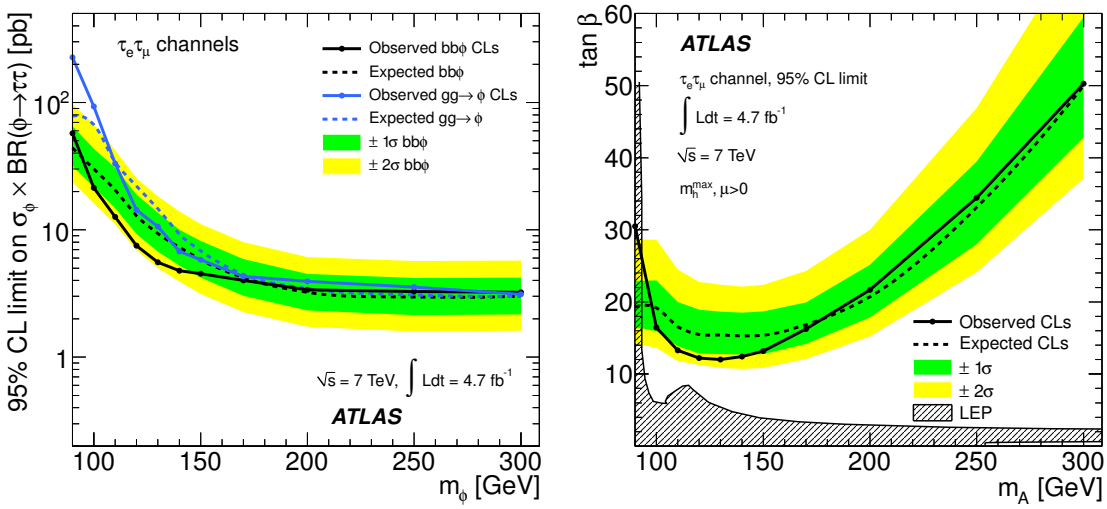

Figure C.5.: Published upper limits at 95 % CL on the product of production cross-section and branching fraction to τ lepton pairs for the signal processes, using the simplified signal and background models (left). The right Figure shows the interpretation of these results in the $m_{h^0}^{\max}$ scenario of the MSSM [10].

Bibliography

[1] S. Glashow, *Partial Symmetries of Weak Interactions*, Nucl.Phys. **22** (1961) 579–588.

[2] S.L. Glashow, J. Iliopoulos, and L. Maiani, *Weak Interactions with Lepton-Hadron Symmetry*, Phys. Rev. D **2** (1970) 1285–1292.
A. Salam, *Weak and Electromagnetic Interactions*, originally printed in Svartholm: Elementary Particle Theory, Proceedings Of The Nobel Symposium Held 1968 At Lerum, Sweden. Stockholm 1968, 367-377.
S. Weinberg, *A Model of Leptons*, Phys. Rev. Lett. **19** (1967) 1264–1266.

[3] F. Englert and R. Brout, *Broken Symmetry and the Mass of Gauge Vector Mesons*, Phys.Rev.Lett. **13** (1964) 321–323.
P. W. Higgs, *Broken symmetries, massless particles and gauge fields*, Phys.Lett. **12** (1964) 132–133.
P. W. Higgs, *Broken Symmetries and the Masses of Gauge Bosons*, Phys.Rev.Lett. **13** (1964) 508–509.
P. W. Higgs, *Spontaneous Symmetry Breakdown without Massless Bosons*, Phys.Rev. **145** (1966) 1156–1163.
G. Guralnik, C. Hagen, and T. Kibble, *Global Conservation Laws and Massless Particles*, Phys.Rev.Lett. **13** (1964) 585–587.
T. Kibble, *Symmetry Breaking in Non-Abelian Gauge Theories*, Phys.Rev. **155** (1967) 1554–1561.

[4] P. Fayet, *Supersymmetry and Weak, Electromagnetic and Strong Interactions*, Phys.Lett. **B64** (1976) 159.
P. Fayet, *Spontaneously Broken Supersymmetric Theories of Weak, Electromagnetic and Strong Interactions*, Phys.Lett. **B69** (1977) 489.
P. Fayet, *Relations Between the Masses of the Superpartners of Leptons and Quarks, the Goldstino Couplings and the Neutral Currents*, Phys.Lett. **B84** (1979) 416.
P. Fayet and S. Ferrara, *Supersymmetry*, Phys.Rept. **32** (1977) 249–334.

[5] G. R. Farrar and P. Fayet, *Phenomenology of the Production, Decay, and Detection of New Hadronic States Associated with Supersymmetry*, Phys.Lett. **B76** (1978) 575–579.

[6] ATLAS Collaboration, *Observation of a new particle in the search for the Standard Model Higgs boson with the ATLAS detector at the LHC*, Phys.Lett. **B716** (2012) 1–29, `arXiv:1207.7214 [hep-ex]`.

[7] CMS Collaboration, *Observation of a new boson at a mass of 125 GeV with the CMS experiment at the LHC*, Phys.Lett. **B716** (2012) 30–61, `arXiv:1207.7235 [hep-ex]`.

[8] ATLAS Collaboration, *The ATLAS Experiment at the CERN Large Hadron Collider*, JINST **3** (2008) S08003.

[9] CMS Collaboration, *The CMS experiment at the CERN LHC*, JINST **3** (2008) S08004.

[10] ATLAS Collaboration, *Search for the neutral Higgs bosons of the Minimal Supersymmetric Standard Model in pp collisions at $\sqrt{s} = 7$ TeV with the ATLAS detector*, JHEP **1302** (2013) 095, arXiv:1211.6956 [hep-ex].

[11] ATLAS Collaboration, *Search for the neutral Higgs bosons of the Minimal Supersymmetric Standard Model in pp collisions at $\sqrt{s} = 7$ TeV with the ATLAS detector*, https://atlas.web.cern.ch/Atlas/GROUPS/PHYSICS/PAPERS/HIGG-2012-11/, supplementary material for entry [10], 2013.

[12] E. Barberio, M. Beckingham, X. Chen, A. Ferrer, L. Fiorini, M. Flechl, E. Gross, C. Gumpert, B. Mellado, Y. Pan, M. Pitt, H. von Radziewski, M. Schumacher, C. Schillo, T. Shao, O. Silbert, C. Solans, J. Tanaka, G. Torralba, N. Utecht, J. Valls, and M. Warsinsky, *Search for neutral Higgs bosons in the decay mode $H \to \tau\tau \to \ell\ell + 4\nu$ in proton-proton collisions at $\sqrt{s} = 7\,TeV$ with the ATLAS Experiment*, ATLAS-Internal Communication, ATL-COM-PHYS-2011-758, June, 2011.

[13] ATLAS Collaboration, *Search for neutral MSSM Higgs bosons decaying to $\tau^+\tau^-$ pairs in proton-proton collisions at $\sqrt{s} = 7$ TeV with the ATLAS detector*, Conference Contribution, ATLAS-CONF-2011-132, 2011.

[14] M. Schmitz, *Higgs production in Vector Boson Fusion in the $H \to \tau\tau \to ll + 4\nu$ final state with ATLAS: a sensitivity study*, PhD thesis, BONN-IR-2011-06, Universität Bonn, 2011.
N. Möser, *A Sensitivity Study for Higgs Boson Production in Vector Boson Fusion in the $H \to \tau\tau \to lh + 3\nu$ Final State with ATLAS*, PhD thesis, BONN-IR-2011-14, Universität Bonn, 2011.

[15] ATLAS Collaboration, *Search for Neutral Higgs Bosons $H \to \tau^+\tau^- \to \ell\tau_h$ with the ATLAS Detector in 7 TeV Collisions*, ATLAS-Internal Communication, ATL-COM-PHYS-2011-939, July, 2011.

[16] A. Djouadi, *The Anatomy of electro-weak symmetry breaking. I: The Higgs boson in the standard model*, Phys.Rept. **457** (2008) 1–216, arXiv:hep-ph/0503172 [hep-ph].

[17] A. Djouadi, *The Anatomy of electro-weak symmetry breaking. II. The Higgs bosons in the minimal supersymmetric model*, Phys.Rept. **459** (2008) 1–241, arXiv:hep-ph/0503173 [hep-ph].

[18] D. Gross and F. Wilczek, *Ultraviolet Behavior of Nonabelian Gauge Theories*, Phys.Rev.Lett. **30** (1973) 1343–1346.
D. Gross and F. Wilczek, *Asymptotically Free Gauge Theories. 1*, Phys.Rev. **D8** (1973) 3633–3652.
H. D. Politzer, *Reliable Perturbative Results for Strong Interactions?*, Phys.Rev.Lett. **30** (1973) 1346–1349.
H. D. Politzer, *Asymptotic Freedom: An Approach to Strong Interactions*, Phys.Rept. **14** (1974) 129–180.

[19] UA1 Collaboration, *Experimental Observation of Isolated Large Transverse Energy Electrons with Associated Missing Energy at $\sqrt{s} = 540$ GeV*, Phys.Lett. **B122** (1983) 103–116.
UA2 Collaboration, *Observation of Single Isolated Electrons of High Transverse Momentum in Events with Missing Transverse Energy at the CERN anti-p p Collider*,

Phys.Lett. **B122** (1983) 476–485.
UA1 Collaboration, *Experimental Observation of Lepton Pairs of Invariant Mass Around 95 GeV/c^2 at the CERN SPS Collider*, Phys.Lett. **B126** (1983) 398–410.
UA2 Collaboration, *Evidence for $Z^0 \to e^+e^-$ at the CERN anti-p p Collider*, Phys.Lett. **B129** (1983) 130–140.

[20] DONUT Collaboration, *Observation of tau neutrino interactions*, Phys.Lett. **B504** (2001) 218–224, arXiv:hep-ex/0012035 [hep-ex].

[21] Particle Data Group, *Review of Particle Physics (RPP)*, Phys.Rev. **D86** (2012) 010001.

[22] I. I. Bigi, M. A. Shifman, N. Uraltsev, and A. Vainshtein, *The Pole mass of the heavy quark. Perturbation theory and beyond*, Phys.Rev. **D50** (1994) 2234–2246, arXiv:hep-ph/9402360 [hep-ph].

[23] G. Ecker, *Quantum chromodynamics*, arXiv:hep-ph/0604165 [hep-ph].

[24] N. Cabibbo, *Unitary Symmetry and Leptonic Decays*, Phys. Rev. Lett. **10** (1963) 531–533.
M. Kobayashi and T. Maskawa, *CP Violation in the Renormalizable Theory of Weak Interaction*, Prog. Theor. Phys. **49** (1973) 652–657.

[25] Z. Maki, M. Nakagawa, and S. Sakata, *Remarks on the unified model of elementary particles*, Prog. Theor. Phys. **28** (1962) 870–880.
B. Pontecorvo, *Neutrino Experiments and the Problem of Conservation of Leptonic Charge*, Sov.Phys.JETP **26** (1968) 984–988.

[26] R. N. Mohapatra and G. Senjanovic, *Neutrino Mass and Spontaneous Parity Violation*, Phys.Rev.Lett. **44** (1980) 912.
T. Yanagida, *Horizontal Symmetry and Masses of Neutrinos*, Prog. Theor. Phys. **64** (1980) 1103.

[27] G. 't Hooft, *Renormalizable Lagrangians for Massive Yang-Mills Fields*, Nucl.Phys. **B35** (1971) 167–188.
G. 't Hooft, *Renormalization of Massless Yang-Mills Fields*, Nucl.Phys. **B33** (1971) 173–199.

[28] M. Spira and P. M. Zerwas, *Electroweak symmetry breaking and Higgs physics*, Lect.Notes Phys. **512** (1998) 161–225, arXiv:hep-ph/9803257 [hep-ph].

[29] LHC Higgs Cross Section Working Group, S. Dittmaier, C. Mariotti, G. Passarino, and R. Tanaka (Eds.), *Handbook of LHC Higgs Cross Sections: 1. Inclusive Observables*, CERN-2011-002, 2011, arXiv:1101.0593 [hep-ph].

[30] C. Anastasiou, R. Boughezal, and F. Petriello, *Mixed QCD-electroweak corrections to Higgs boson production in gluon fusion*, JHEP **0904** (2009) 003, arXiv:0811.3458 [hep-ph].
D. de Florian and M. Grazzini, *Higgs production through gluon fusion: Updated cross sections at the Tevatron and the LHC*, Phys.Lett. **B674** (2009) 291–294, arXiv:0901.2427 [hep-ph].

[31] J. Baglio and A. Djouadi, *Predictions for Higgs production at the Tevatron and the associated uncertainties*, JHEP **1010** (2010) 064, arXiv:1003.4266 [hep-ph].

J. Baglio and A. Djouadi, *Higgs production at the lHC*, JHEP **1103** (2011) 055, arXiv:1012.0530 [hep-ph].

[32] M. Ciccolini, A. Denner, and S. Dittmaier, *Strong and electroweak corrections to the production of Higgs + 2jets via weak interactions at the LHC*, Phys.Rev.Lett. **99** (2007) 161803, arXiv:0707.0381 [hep-ph].
M. Ciccolini, A. Denner, and S. Dittmaier, *Electroweak and QCD corrections to Higgs production via vector-boson fusion at the LHC*, Phys.Rev. **D77** (2008) 013002, arXiv:0710.4749 [hep-ph].
A. Denner, S. Dittmaier, and A. Mück, *HAWK: A Monte Carlo generator for the production of Higgs bosons Attached to WeaK bosons at hadron colliders*, http://omnibus.uni-freiburg.de/~sd565/programs/hawk/hawk.html, 2010.

[33] K. Arnold, M. Bahr, G. Bozzi, F. Campanario, C. Englert, *et al.*, *VBFNLO: A Parton level Monte Carlo for processes with electroweak bosons*, Comput.Phys.Commun. **180** (2009) 1661–1670, arXiv:0811.4559 [hep-ph].

[34] P. Bolzoni, F. Maltoni, S.-O. Moch, and M. Zaro, *Higgs production via vector-boson fusion at NNLO in QCD*, Phys.Rev.Lett. **105** (2010) 011801, arXiv:1003.4451 [hep-ph].

[35] O. Brein, A. Djouadi, and R. Harlander, *NNLO QCD corrections to the Higgs-strahlung processes at hadron colliders*, Phys.Lett. **B579** (2004) 149–156, arXiv:hep-ph/0307206 [hep-ph].

[36] M. Ciccolini, S. Dittmaier, and M. Kramer, *Electroweak radiative corrections to associated WH and ZH production at hadron colliders*, Phys.Rev. **D68** (2003) 073003, arXiv:hep-ph/0306234 [hep-ph].
O. Brein, M. Ciccolini, S. Dittmaier, A. Djouadi, R. Harlander, *et al.*, *Precision calculations for associated WH and ZH production at hadron colliders*, arXiv:hep-ph/0402003 [hep-ph].

[37] W. Beenakker, S. Dittmaier, M. Kramer, B. Plumper, M. Spira, *et al.*, *Higgs radiation off top quarks at the Tevatron and the LHC*, Phys.Rev.Lett. **87** (2001) 201805, arXiv:hep-ph/0107081 [hep-ph].
W. Beenakker, S. Dittmaier, M. Kramer, B. Plumper, M. Spira, *et al.*, *NLO QCD corrections to t anti-t H production in hadron collisions*, Nucl.Phys. **B653** (2003) 151–203, arXiv:hep-ph/0211352 [hep-ph].
L. Reina and S. Dawson, *Next-to-leading order results for t anti-t h production at the Tevatron*, Phys.Rev.Lett. **87** (2001) 201804, arXiv:hep-ph/0107101 [hep-ph].
S. Dawson, L. Orr, L. Reina, and D. Wackeroth, *Associated top quark Higgs boson production at the LHC*, Phys.Rev. **D67** (2003) 071503, arXiv:hep-ph/0211438 [hep-ph].

[38] M. Spira, *QCD effects in Higgs physics*, Fortsch.Phys. **46** (1998) 203–284, arXiv:hep-ph/9705337 [hep-ph].
A. Djouadi, J. Kalinowski, and M. Spira, *HDECAY: A Program for Higgs boson decays in the standard model and its supersymmetric extension*, Comput.Phys.Commun. **108** (1998) 56–74, arXiv:hep-ph/9704448 [hep-ph].
J. Butterworth, F. Maltoni, F. Moortgat, P. Richardson, S. Schumann, *et al.*, *The Tools and Monte Carlo working group Summary Report*, arXiv:1003.1643 [hep-ph].

[39] A. Bredenstein, A. Denner, S. Dittmaier, and M. Weber, *Precise predictions for the Higgs-boson decay $H \to WW/ZZ \to 4$ leptons*, Phys.Rev. **D74** (2006) 013004, arXiv:hep-ph/0604011 [hep-ph].
A. Bredenstein, A. Denner, S. Dittmaier, and M. Weber, *Radiative corrections to the semileptonic and hadronic Higgs-boson decays $H \to W\,W\,/\,Z\,Z \to 4$ fermions*, JHEP **0702** (2007) 080, arXiv:hep-ph/0611234 [hep-ph].
A. Bredenstein, A. Denner, S. Dittmaier, A. Mück, and M. Weber, *Prophecy4f: A Monte Carlo generator for a proper description of the Higgs decay into 4 fermions*, http://omnibus.uni-freiburg.de/~sd565/programs/prophecy4f/prophecy4f.html, 2010.

[40] M. S. Turner, *Dark matter: Theoretical perspectives*, arXiv:astro-ph/9302003 [astro-ph].

[41] G. 't Hooft, C. Itzykson, A. Jaffe, H. Lehmann, P. Mitter (Eds.), *et al.*, *Recent Developments in Gauge Theories. Proceedings, Nato Advanced Study Institute, Cargese, France, August 26 - September 8, 1979*, NATO Adv.Study Inst.Ser.B Phys. **59** (1980) 1–438.

[42] L. Susskind, *Dynamics of Spontaneous Symmetry Breaking in the Weinberg-Salam Theory*, Phys.Rev. **D20** (1979) 2619–2625.

[43] E. Gildener, *Gauge Symmetry Hierarchies*, Phys.Rev. **D14** (1976) 1667.

[44] S. Weinberg, *Implications of Dynamical Symmetry Breaking: An Addendum*, Phys.Rev. **D19** (1979) 1277–1280.

[45] S. Weinberg, *Implications of Dynamical Symmetry Breaking*, Phys.Rev. **D13** (1976) 974–996.

[46] K. D. Lane, *An Introduction to technicolor*, arXiv:hep-ph/9401324 [hep-ph].

[47] J. R. Ellis, *Beyond the standard model for hill walkers*, arXiv:hep-ph/9812235 [hep-ph].

[48] K. D. Lane, *Technicolor and precision tests of the electroweak interactions*, arXiv:hep-ph/9409304 [hep-ph].

[49] S. P. Martin, *A Supersymmetry primer*, arXiv:hep-ph/9709356 [hep-ph].

[50] S. R. Coleman and J. Mandula, *All Possible Symmetries of the S Matrix*, Phys.Rev. **159** (1967) 1251–1256.

[51] R. Haag, J. T. Lopuszanski, and M. Sohnius, *All Possible Generators of Supersymmetries of the S Matrix*, Nucl.Phys. **B88** (1975) 257.

[52] S. Dimopoulos and S. Raby, *Supercolor*, Nucl.Phys. **B192** (1981) 353.
E. Witten, *Dynamical Breaking of Supersymmetry*, Nucl.Phys. **B188** (1981) 513.
M. Dine, W. Fischler, and M. Srednicki, *Supersymmetric Technicolor*, Nucl.Phys. **B189** (1981) 575–593.
S. Dimopoulos and H. Georgi, *Softly Broken Supersymmetry and SU(5)*, Nucl.Phys. **B193** (1981) 150.
N. Sakai, *Naturalness in Supersymmetric Guts*, Z.Phys. **C11** (1981) 153.
R. K. Kaul and P. Majumdar, *Cancellation of Quadratically Divergent Mass Corrections in Globally Supersymmetric Spontaneously Broken Gauge Theories*, Nucl.Phys. **B199** (1982) 36.

[53] J. R. Ellis, J. Hagelin, D. V. Nanopoulos, K. A. Olive, and M. Srednicki, *Supersymmetric Relics from the Big Bang*, Nucl.Phys. **B238** (1984) 453–476.

[54] H. Goldberg, *Constraint on the Photino Mass from Cosmology*, Phys.Rev.Lett. **50** (1983) 1419.

[55] G. Jungman, M. Kamionkowski, and K. Griest, *Supersymmetric dark matter*, Phys.Rept. **267** (1996) 195–373, arXiv:hep-ph/9506380 [hep-ph].
K. A. Olive, *TASI lectures on dark matter*, arXiv:astro-ph/0301505 [astro-ph].
J. L. Feng, *Supersymmetry and cosmology*, eConf **C0307282** (2003) L11, arXiv:hep-ph/0405215 [hep-ph].
M. Drees, *Neutralino Dark Matter in 2005*, AIP Conf.Proc. **805** (2006) 48–54, arXiv:hep-ph/0509105 [hep-ph].
J. L. Feng, *Dark Matter Candidates from Particle Physics and Methods of Detection*, Ann.Rev.Astron.Astrophys. **48** (2010) 495–545, arXiv:1003.0904 [astro-ph.CO].

[56] J. R. Ellis, S. Kelley, and D. V. Nanopoulos, *Probing the desert using gauge coupling unification*, Phys.Lett. **B260** (1991) 131–137.
U. Amaldi, W. de Boer, and H. Furstenau, *Comparison of grand unified theories with electroweak and strong coupling constants measured at LEP*, Phys.Lett. **B260** (1991) 447–455.
P. Langacker and M.-x. Luo, *Implications of precision electroweak experiments for M_t, ρ_0, $\sin^2\theta_W$ and grand unification*, Phys.Rev. **D44** (1991) 817–822.
C. Giunti, C. Kim, and U. Lee, *Running coupling constants and grand unification models*, Mod.Phys.Lett. **A6** (1991) 1745–1755.

[57] D. Kazakov, *Beyond the standard model: In search of supersymmetry*, arXiv:hep-ph/0012288 [hep-ph].

[58] K. Choi, J. E. Kim, and H. P. Nilles, *Cosmological constant and soft terms in supergravity*, Phys.Rev.Lett. **73** (1994) 1758–1761, arXiv:hep-ph/9404311 [hep-ph].
K. Choi, J. E. Kim, and G. T. Park, *Phenomenology of soft terms in the presence of nonvanishing hidden sector potential energy*, Nucl.Phys. **B442** (1995) 3–20, arXiv:hep-ph/9412397 [hep-ph].
N. Tsamis and R. Woodard, *Relaxing the cosmological constant*, Phys.Lett. **B301** (1993) 351–357.
N. Tsamis and R. Woodard, *Quantum gravity slows inflation*, Nucl.Phys. **B474** (1996) 235–248, arXiv:hep-ph/9602315 [hep-ph].
N. Tsamis and R. Woodard, *The Quantum gravitational back reaction on inflation*, Annals Phys. **253** (1997) 1–54, arXiv:hep-ph/9602316 [hep-ph].
N. Tsamis and R. Woodard, *Nonperturbative models for the quantum gravitational back reaction on inflation*, Annals Phys. **267** (1998) 145–192, arXiv:hep-ph/9712331 [hep-ph].
M. Dine and W. Fischler, *A Phenomenological Model of Particle Physics Based on Supersymmetry*, Phys.Lett. **B110** (1982) 227.
C. R. Nappi and B. A. Ovrut, *Supersymmetric Extension of the SU(3) x SU(2) x U(1) Model*, Phys.Lett. **B113** (1982) 175.
L. Alvarez-Gaume, M. Claudson, and M. B. Wise, *Low-Energy Supersymmetry*, Nucl.Phys. **B207** (1982) 96.

[59] E. A. Mirabelli and M. E. Peskin, *Transmission of supersymmetry breaking from a four-dimensional boundary*, Phys.Rev. **D58** (1998) 065002, arXiv:hep-th/9712214

[hep-th].
D. E. Kaplan, G. D. Kribs, and M. Schmaltz, *Supersymmetry breaking through transparent extra dimensions*, Phys.Rev. **D62** (2000) 035010, arXiv:hep-ph/9911293 [hep-ph].
Z. Chacko, M. A. Luty, A. E. Nelson, and E. Ponton, *Gaugino mediated supersymmetry breaking*, JHEP **0001** (2000) 003, arXiv:hep-ph/9911323 [hep-ph].
M. Schmaltz and W. Skiba, *Minimal gaugino mediation*, Phys.Rev. **D62** (2000) 095005, arXiv:hep-ph/0001172 [hep-ph].
M. Schmaltz and W. Skiba, *The Superpartner spectrum of gaugino mediation*, Phys.Rev. **D62** (2000) 095004, arXiv:hep-ph/0004210 [hep-ph].
C. Csaki, J. Erlich, C. Grojean, and G. D. Kribs, *4-D constructions of supersymmetric extra dimensions and gaugino mediation*, Phys.Rev. **D65** (2002) 015003, arXiv:hep-ph/0106044 [hep-ph].
H. Cheng, D. Kaplan, M. Schmaltz, and W. Skiba, *Deconstructing gaugino mediation*, Phys.Lett. **B515** (2001) 395–399, arXiv:hep-ph/0106098 [hep-ph].

[60] V. Rubakov and M. Shaposhnikov, *Do We Live Inside a Domain Wall?*, Phys.Lett. **B125** (1983) 136–138.
V. Rubakov and M. Shaposhnikov, *Extra Space-Time Dimensions: Towards a Solution to the Cosmological Constant Problem*, Phys.Lett. **B125** (1983) 139.
L. Randall and R. Sundrum, *A Large mass hierarchy from a small extra dimension*, Phys.Rev.Lett. **83** (1999) 3370–3373, arXiv:hep-ph/9905221 [hep-ph].
L. Randall and R. Sundrum, *An Alternative to compactification*, Phys.Rev.Lett. **83** (1999) 4690–4693, arXiv:hep-th/9906064 [hep-th].
C. Csaki, *TASI lectures on extra dimensions and branes*, arXiv:hep-ph/0404096 [hep-ph].
A. Perez-Lorenzana, *An Introduction to extra dimensions*, J.Phys.Conf.Ser. **18** (2005) 224–269, arXiv:hep-ph/0503177 [hep-ph].
R. Sundrum, *TASI 2004 lectures: To the fifth dimension and back*, arXiv:hep-th/0508134 [hep-th].
G. D. Kribs, *TASI 2004 lectures on the phenomenology of extra dimensions*, arXiv:hep-ph/0605325 [hep-ph].

[61] L. Randall and R. Sundrum, *Out of this world supersymmetry breaking*, Nucl.Phys. **B557** (1999) 79–118, arXiv:hep-th/9810155 [hep-th].
G. F. Giudice, M. A. Luty, H. Murayama, and R. Rattazzi, *Gaugino mass without singlets*, JHEP **9812** (1998) 027, arXiv:hep-ph/9810442 [hep-ph].

[62] P. Nath and R. L. Arnowitt, *Generalized Supergauge Symmetry as a New Framework for Unified Gauge Theories*, Phys.Lett. **B56** (1975) 177.
R. L. Arnowitt, P. Nath, and B. Zumino, *Superfield Densities and Action Principle in Curved Superspace*, Phys.Lett. **B56** (1975) 81.
D. Z. Freedman, P. van Nieuwenhuizen, and S. Ferrara, *Progress Toward a Theory of Supergravity*, Phys.Rev. **D13** (1976) 3214–3218.
S. Deser and B. Zumino, *Consistent Supergravity*, Phys.Lett. **B62** (1976) 335.
D. Z. Freedman and P. van Nieuwenhuizen, *Properties of Supergravity Theory*, Phys.Rev. **D14** (1976) 912.
E. Cremmer, B. Julia, J. Scherk, S. Ferrara, L. Girardello, *et al.*, *Spontaneous Symmetry Breaking and Higgs Effect in Supergravity Without Cosmological Constant*, Nucl.Phys. **B147** (1979) 105.

J. A. Bagger, *Coupling the Gauge Invariant Supersymmetric Nonlinear Sigma Model to Supergravity*, Nucl.Phys. **B211** (1983) 302.
E. Cremmer, S. Ferrara, L. Girardello, and A. Van Proeyen, *Yang-Mills Theories with Local Supersymmetry: Lagrangian, Transformation Laws and SuperHiggs Effect*, Nucl.Phys. **B212** (1983) 413.

[63] H. E. Haber, *The Status of the minimal supersymmetric standard model and beyond*, Nucl.Phys.Proc.Suppl. **62** (1998) 469–484, `arXiv:hep-ph/9709450 [hep-ph]`.

[64] J. R. Ellis and D. V. Nanopoulos, *Flavor Changing Neutral Interactions in Broken Supersymmetric Theories*, Phys.Lett. **B110** (1982) 44.
R. Barbieri and R. Gatto, *Conservation Laws for Neutral Currents in Spontaneously Broken Supersymmetric Theories*, Phys.Lett. **B110** (1982) 211.
B. Campbell, *Supersymmetry and Neutral Flavor Nonconservation*, Phys.Rev. **D28** (1983) 209–216.
M. J. Duncan, *Generalized Cabibbo Angles in Supersymmetric Gauge Theories*, Nucl.Phys. **B221** (1983) 285.
J. Donoghue, H. P. Nilles, and D. Wyler, *Flavor Changes in Locally Supersymmetric Theories*, Phys.Lett. **B128** (1983) 55.
A. Bouquet, J. Kaplan, and C. A. Savoy, *On Flavor Mixing in Broken Supergravity*, Phys.Lett. **B148** (1984) 69.
M. Dugan, B. Grinstein, and L. J. Hall, *CP Violation in the Minimal N=1 Supergravity Theory*, Nucl.Phys. **B255** (1985) 413.
L. J. Hall, V. A. Kostelecky, and S. Raby, *New Flavor Violations in Supergravity Models*, Nucl.Phys. **B267** (1986) 415.
F. Gabbiani and A. Masiero, *Superheavy Contributions to FCNC in the Flipped $SU(5) \times U(1)$*, Phys.Lett. **B209** (1988) 289–294.
R. Barbieri and L. Hall, *Signals for supersymmetric unification*, Phys.Lett. **B338** (1994) 212–218, `arXiv:hep-ph/9408406 [hep-ph]`.
R. Barbieri, L. J. Hall, and A. Strumia, *Violations of lepton flavor and CP in supersymmetric unified theories*, Nucl.Phys. **B445** (1995) 219–251, `arXiv:hep-ph/9501334 [hep-ph]`.
J. R. Ellis, S. Ferrara, and D. V. Nanopoulos, *CP Violation and Supersymmetry*, Phys.Lett. **B114** (1982) 231.
W. Buchmuller and D. Wyler, *CP Violation and R Invariance in Supersymmetric Models of Strong and Electroweak Interactions*, Phys.Lett. **B121** (1983) 321.
J. Polchinski and M. B. Wise, *The Electric Dipole Moment of the Neutron in Low-Energy Supergravity*, Phys.Lett. **B125** (1983) 393.
F. del Aguila, M. Gavela, J. Grifols, and A. Mendez, *Specifically Supersymmetric Contribution to Electric Dipole Moments*, Phys.Lett. **B126** (1983) 71.
R. Barbieri and G. Giudice, *$b \to s\gamma$ decay and supersymmetry*, Phys.Lett. **B309** (1993) 86–90, `arXiv:hep-ph/9303270 [hep-ph]`.
J. Hisano, T. Moroi, K. Tobe, M. Yamaguchi, and T. Yanagida, *Lepton flavor violation in the supersymmetric standard model with seesaw induced neutrino masses*, Phys.Lett. **B357** (1995) 579–587, `arXiv:hep-ph/9501407 [hep-ph]`.
F. Gabbiani, E. Gabrielli, A. Masiero, and L. Silvestrini, *A Complete analysis of FCNC and CP constraints in general SUSY extensions of the standard model*, Nucl.Phys. **B477** (1996) 321–352, `arXiv:hep-ph/9604387 [hep-ph]`.
J. L. Hewett and J. D. Wells, *Searching for supersymmetry in rare B decays*, Phys.Rev. **D55** (1997) 5549–5560, `arXiv:hep-ph/9610323 [hep-ph]`.

Y. Grossman, Y. Nir, and R. Rattazzi, *CP violation beyond the standard model*, Adv.Ser.Direct.High Energy Phys. **15** (1998) 755–794, arXiv:hep-ph/9701231 [hep-ph].
S. Pokorski, J. Rosiek, and C. A. Savoy, *Constraints on phases of supersymmetric flavor conserving couplings*, Nucl.Phys. **B570** (2000) 81–116, arXiv:hep-ph/9906206 [hep-ph].
S. Abel, S. Khalil, and O. Lebedev, *EDM constraints in supersymmetric theories*, Nucl.Phys. **B606** (2001) 151–182, arXiv:hep-ph/0103320 [hep-ph].
M. Misiak, S. Pokorski, and J. Rosiek, *Supersymmetry and FCNC effects*, Adv.Ser.Direct.High Energy Phys. **15** (1998) 795–828, arXiv:hep-ph/9703442 [hep-ph].
M. Ciuchini, E. Franco, V. Lubicz, G. Martinelli, I. Scimemi, *et al.*, *Next-to-leading order QCD corrections to $\Delta F = 2$ effective Hamiltonians*, Nucl.Phys. **B523** (1998) 501–525, arXiv:hep-ph/9711402 [hep-ph].
M. Ciuchini, V. Lubicz, L. Conti, A. Vladikas, A. Donini, *et al.*, *ΔM_K and ε_K in SUSY at the next-to-leading order*, JHEP **9810** (1998) 008, arXiv:hep-ph/9808328 [hep-ph].
A. Masiero and H. Murayama, *Can ε'/ε be supersymmetric?*, Phys.Rev.Lett. **83** (1999) 907–910, arXiv:hep-ph/9903363 [hep-ph].
S. Khalil, T. Kobayashi, and A. Masiero, *CP violation in supersymmetric model with nondegenerate A terms*, Phys.Rev. **D60** (1999) 075003, arXiv:hep-ph/9903544 [hep-ph].
A. Buras, G. Colangelo, G. Isidori, A. Romanino, and L. Silvestrini, *Connections between ε'/ε and rare kaon decays in supersymmetry*, Nucl.Phys. **B566** (2000) 3–32, arXiv:hep-ph/9908371 [hep-ph].
F. Borzumati, C. Greub, T. Hurth, and D. Wyler, *Gluino contribution to radiative B decays: Organization of QCD corrections and leading order results*, Phys.Rev. **D62** (2000) 075005, arXiv:hep-ph/9911245 [hep-ph].
A. Buras, P. Gambino, M. Gorbahn, S. Jager, and L. Silvestrini, *ε'/ε and rare K and B decays in the MSSM*, Nucl.Phys. **B592** (2001) 55–91, arXiv:hep-ph/0007313 [hep-ph].
P. H. Chankowski and L. Slawianowska, *$B^0_{d,s} \to \mu^-\mu^+$ decay in the MSSM*, Phys.Rev. **D63** (2001) 054012, arXiv:hep-ph/0008046 [hep-ph].
A. J. Buras, P. H. Chankowski, J. Rosiek, and L. Slawianowska, *$\Delta M_{d,s}, B^0_{d,s} \to \mu^+\mu^-$ and $B \to X_s\gamma$ in supersymmetry at large* $\tan\beta$, Nucl.Phys. **B659** (2003) 3, arXiv:hep-ph/0210145 [hep-ph].
M. Ciuchini, E. Franco, A. Masiero, and L. Silvestrini, *$b \to s$ transitions: A New frontier for indirect SUSY searches*, Phys.Rev. **D67** (2003) 075016, arXiv:hep-ph/0212397 [hep-ph].

[65] LHCb collaboration, *First evidence for the decay $B_s \to \mu^+\mu^-$*, Phys.Rev.Lett. **110** (2013) 021801, arXiv:1211.2674 [hep-ex].

[66] I. Simonsen, *A Review of minimal supersymmetric electroweak theory*, arXiv:hep-ph/9506369 [hep-ph].

[67] K. Inoue, A. Kakuto, H. Komatsu, and S. Takeshita, *Low-Energy Parameters and Particle Masses in a Supersymmetric Grand Unified Model*, Prog. Theor. Phys. **67** (1982) 1889.

R. A. Flores and M. Sher, *Higgs Masses in the Standard, Multi-Higgs and Supersymmetric Models*, Annals Phys. **148** (1983) 95.

[68] H. E. Haber and R. Hempfling, *Can the mass of the lightest Higgs boson of the minimal supersymmetric model be larger than m(Z)?*, Phys.Rev.Lett. **66** (1991) 1815–1818.
Y. Okada, M. Yamaguchi, and T. Yanagida, *Upper bound of the lightest Higgs boson mass in the minimal supersymmetric standard model*, Prog. Theor. Phys. **85** (1991) 1–6.
Y. Okada, M. Yamaguchi, and T. Yanagida, *Renormalization group analysis on the Higgs mass in the softly broken supersymmetric standard model*, Phys.Lett. **B262** (1991) 54–58.
J. R. Ellis, G. Ridolfi, and F. Zwirner, *Radiative corrections to the masses of supersymmetric Higgs bosons*, Phys.Lett. **B257** (1991) 83–91.
J. R. Ellis, G. Ridolfi, and F. Zwirner, *On radiative corrections to supersymmetric Higgs boson masses and their implications for LEP searches*, Phys.Lett. **B262** (1991) 477–484.
G. Gamberini, G. Ridolfi, and F. Zwirner, *On Radiative Gauge Symmetry Breaking in the Minimal Supersymmetric Model*, Nucl.Phys. **B331** (1990) 331–349.
R. Barbieri, M. Frigeni, and F. Caravaglios, *The Supersymmetric Higgs for heavy superpartners*, Phys.Lett. **B258** (1991) 167–170.
J. Espinosa and M. Quiros, *Two loop radiative corrections to the mass of the lightest Higgs boson in supersymmetric standard models*, Phys.Lett. **B266** (1991) 389–396.
A. Brignole, *Radiative corrections to the supersymmetric neutral Higgs boson masses*, Phys.Lett. **B281** (1992) 284–294.
M. Drees and M. M. Nojiri, *Radiative symmetry breaking in minimal $N = 1$ supergravity with large Yukawa couplings*, Nucl.Phys. **B369** (1992) 54–98.
M. Drees and M. M. Nojiri, *One loop corrections to the Higgs sector in minimal supergravity models*, Phys.Rev. **D45** (1992) 2482–2492.
H. E. Haber and R. Hempfling, *The Renormalization group improved Higgs sector of the minimal supersymmetric model*, Phys.Rev. **D48** (1993) 4280–4309, `arXiv:hep-ph/9307201 [hep-ph]`.
P. H. Chankowski, S. Pokorski, and J. Rosiek, *Charged and neutral supersymmetric Higgs boson masses: Complete one loop analysis*, Phys.Lett. **B274** (1992) 191–198.
P. H. Chankowski, S. Pokorski, and J. Rosiek, *Is the lightest supersymmetric Higgs Boson distinguishable from the minimal standard model one?*, Phys.Lett. **B281** (1992) 100–105.
R. Hempfling and A. H. Hoang, *Two loop radiative corrections to the upper limit of the lightest Higgs boson mass in the minimal supersymmetric model*, Phys.Lett. **B331** (1994) 99–106, `arXiv:hep-ph/9401219 [hep-ph]`.
M. S. Carena, M. Quiros, and C. Wagner, *Effective potential methods and the Higgs mass spectrum in the MSSM*, Nucl.Phys. **B461** (1996) 407–436, `arXiv:hep-ph/9508343 [hep-ph]`.
H. E. Haber, R. Hempfling, and A. H. Hoang, *Approximating the radiatively corrected Higgs mass in the minimal supersymmetric model*, Z.Phys. **C75** (1997) 539–554, `arXiv:hep-ph/9609331 [hep-ph]`.
S. Heinemeyer, W. Hollik, and G. Weiglein, *QCD corrections to the masses of the neutral CP - even Higgs bosons in the MSSM*, Phys.Rev. **D58** (1998) 091701, `arXiv:hep-ph/9803277 [hep-ph]`.
S. Heinemeyer, W. Hollik, and G. Weiglein, *Precise prediction for the mass*

of the lightest Higgs boson in the MSSM, Phys.Lett. **B440** (1998) 296–304, arXiv:hep-ph/9807423 [hep-ph].

[69] S. Heinemeyer, W. Hollik, and G. Weiglein, *The Masses of the neutral CP - even Higgs bosons in the MSSM: Accurate analysis at the two loop level*, Eur.Phys.J. **C9** (1999) 343–366, arXiv:hep-ph/9812472 [hep-ph].

[70] R.-J. Zhang, *Two loop effective potential calculation of the lightest CP even Higgs boson mass in the MSSM*, Phys.Lett. **B447** (1999) 89–97, arXiv:hep-ph/9808299 [hep-ph].
J. R. Espinosa and R.-J. Zhang, *MSSM lightest CP even Higgs boson mass to $O(\alpha_s\alpha_t)$: The Effective potential approach*, JHEP **0003** (2000) 026, arXiv:hep-ph/9912236 [hep-ph].
J. R. Espinosa and R.-J. Zhang, *Complete two loop dominant corrections to the mass of the lightest CP even Higgs boson in the minimal supersymmetric standard model*, Nucl.Phys. **B586** (2000) 3–38, arXiv:hep-ph/0003246 [hep-ph].
M. S. Carena, J. R. Ellis, A. Pilaftsis, and C. Wagner, *Higgs boson pole masses in the MSSM with explicit CP violation*, Nucl.Phys. **B625** (2002) 345–371, arXiv:hep-ph/0111245 [hep-ph].
M. S. Carena, H. Haber, S. Heinemeyer, W. Hollik, C. Wagner, *et al.*, *Reconciling the two loop diagrammatic and effective field theory computations of the mass of the lightest CP - even Higgs boson in the MSSM*, Nucl.Phys. **B580** (2000) 29–57, arXiv:hep-ph/0001002 [hep-ph].
J. Espinosa and I. Navarro, *Radiative corrections to the Higgs boson mass for a hierarchical stop spectrum*, Nucl.Phys. **B615** (2001) 82–116, arXiv:hep-ph/0104047 [hep-ph].
G. Degrassi, P. Slavich, and F. Zwirner, *On the neutral Higgs boson masses in the MSSM for arbitrary stop mixing*, Nucl.Phys. **B611** (2001) 403–422, arXiv:hep-ph/0105096 [hep-ph].
A. Brignole, G. Degrassi, P. Slavich, and F. Zwirner, *On the $O(\alpha_t^2)$ two loop corrections to the neutral Higgs boson masses in the MSSM*, Nucl.Phys. **B631** (2002) 195–218, arXiv:hep-ph/0112177 [hep-ph].
A. Brignole, G. Degrassi, P. Slavich, and F. Zwirner, *On the two loop sbottom corrections to the neutral Higgs boson masses in the MSSM*, Nucl.Phys. **B643** (2002) 79–92, arXiv:hep-ph/0206101 [hep-ph].
S. P. Martin, *Complete two loop effective potential approximation to the lightest Higgs scalar boson mass in supersymmetry*, Phys.Rev. **D67** (2003) 095012, arXiv:hep-ph/0211366 [hep-ph].
S. P. Martin, *Two loop scalar self energies in a general renormalizable theory at leading order in gauge couplings*, Phys.Rev. **D70** (2004) 016005, arXiv:hep-ph/0312092 [hep-ph].
T. Hahn, W. Hollik, S. Heinemeyer, and G. Weiglein, *Precision Higgs masses with FeynHiggs 2.2*, eConf **C050318** (2005) 0106, arXiv:hep-ph/0507009 [hep-ph].

[71] ALEPH Collaboration, DELPHI Collaboration, L3 Collaboration, OPAL Collaborations, LEP Working Group for Higgs Boson Searches, *Search for neutral MSSM Higgs bosons at LEP*, Eur.Phys.J. **C47** (2006) 547–587, arXiv:hep-ex/0602042 [hep-ex].

[72] M. S. Carena, S. Heinemeyer, C. Wagner, and G. Weiglein, *Suggestions for benchmark scenarios for MSSM Higgs boson searches at hadron colliders*, Eur.Phys.J. **C26** (2003) 601–607, arXiv:hep-ph/0202167 [hep-ph].
M. S. Carena, S. Heinemeyer, C. Wagner, and G. Weiglein, *Suggestions for improved*

benchmark scenarios for Higgs boson searches at LEP-2, CERN-TH-99-374, DESY-99-186, 1999, arXiv:hep-ph/9912223 [hep-ph].
G. Altarelli, T. Sjostrand, and F. Zwirner, *Physics at LEP2: Vol. 1*, CERN-96-01-V-1, 1996.

[73] S. Heinemeyer, W. Hollik, and G. Weiglein, *FeynHiggs: A Program for the calculation of the masses of the neutral CP even Higgs bosons in the MSSM*, Comput.Phys.Commun. **124** (2000) 76–89, arXiv:hep-ph/9812320 [hep-ph].

[74] G. Degrassi, S. Heinemeyer, W. Hollik, P. Slavich, and G. Weiglein, *Towards high precision predictions for the MSSM Higgs sector*, Eur.Phys.J. **C28** (2003) 133–143, arXiv:hep-ph/0212020 [hep-ph].
M. Frank, T. Hahn, S. Heinemeyer, W. Hollik, H. Rzehak, *et al.*, *The Higgs Boson Masses and Mixings of the Complex MSSM in the Feynman-Diagrammatic Approach*, JHEP **0702** (2007) 047, arXiv:hep-ph/0611326 [hep-ph].

[75] E. Boos, A. Djouadi, M. Mühlleitner, and A. Vologdin, *The MSSM Higgs bosons in the intense coupling regime*, Phys.Rev. **D66** (2002) 055004, arXiv:hep-ph/0205160 [hep-ph].

[76] M. Warsinsky, *Studies of b-associated production and muonic decays of neutral Higgs bosons at the ATLAS experiment within the minimal supersymmetric standard model*, PhD thesis, Technische Universität Dresden, 2008.

[77] M. Spira, *HIGLU: A program for the calculation of the total Higgs production cross-section at hadron colliders via gluon fusion including QCD corrections*, DESY-T-95-05, 1995, arXiv:hep-ph/9510347 [hep-ph].

[78] R. V. Harlander and W. B. Kilgore, *Production of a pseudoscalar Higgs boson at hadron colliders at next-to-next-to leading order*, JHEP **0210** (2002) 017, arXiv:hep-ph/0208096 [hep-ph].

[79] R. V. Harlander and W. B. Kilgore, *Higgs boson production in bottom quark fusion at next-to-next-to leading order*, Phys.Rev. **D68** (2003) 013001, arXiv:hep-ph/0304035 [hep-ph].

[80] S. Dittmaier, M. Kramer, and M. Spira, *Higgs radiation off bottom quarks at the Tevatron and the CERN LHC*, Phys.Rev. **D70** (2004) 074010, arXiv:hep-ph/0309204 [hep-ph].

[81] T. Hambye and K. Riesselmann, *Matching conditions and Higgs mass upper bounds revisited*, Phys.Rev. **D55** (1997) 7255–7262, arXiv:hep-ph/9610272 [hep-ph].

[82] LEP Electroweak Working Group, *Update March 2012*, http://lepewwg.web.cern.ch/LEPEWWG/.

[83] ALEPH Collaboration, DELPHI Collaboration, L3 Collaboration, OPAL Collaboration, SLD Collaboration, LEP Electroweak Working Group, SLD Electroweak Group, SLD Heavy Flavour Group, *Precision electroweak measurements on the Z resonance*, Phys.Rept. **427** (2006) 257–454, arXiv:hep-ex/0509008 [hep-ex].

[84] LEP Working Group for Higgs boson searches, ALEPH Collaboration, DELPHI Collaboration, L3 Collaboration, OPAL Collaboration, *Search for the standard model Higgs boson at LEP*, Phys.Lett. **B565** (2003) 61–75, arXiv:hep-ex/0306033 [hep-ex].

[85] CMS Collaboration, *Combination of SM Higgs Searches*, Conference Contribution, CMS-PAS-HIG-11-032, December, 2011.

[86] ATLAS Collaboration, *Combination of Higgs Boson Searches with up to 4.9 fb^{-1} of pp Collisions Data Taken at a center-of-mass energy of 7 TeV with the ATLAS Experiment at the LHC*, Conference Contribution, ATLAS-CONF-2011-163, December, 2011.

[87] Tevatron New Physics Higgs Working Group, CDF Collaboration, DØ Collaboration, *Updated Combination of CDF and DØ Searches for Standard Model Higgs Boson Production with up to 10.0 fb^{-1} of Data*, arXiv:1207.0449 [hep-ex].

[88] A. L. Read, *Presentation of search results: The CL(s) technique*, J.Phys. **G28** (2002) 2693–2704.

[89] S. Dittmaier and M. Schumacher, *The Higgs Boson in the Standard Model - From LEP to LHC: Expectations, Searches, and Discovery of a Candidate*, arXiv:1211.4828 [hep-ph].

[90] ALEPH Collaboration, *Mass limit for the standard model Higgs boson with the full LEP-1 ALEPH data sample*, Phys.Lett. **B384** (1996) 427–438.

[91] DELPHI Collaboration, *Search for the standard model Higgs boson in Z^0 decays*, Nucl.Phys. **B421** (1994) 3–37.

[92] L3 Collaboration, *Search for neutral Higgs boson production through the process $e^+e^- \to Z^*H^0$*, Phys.Lett. **B385** (1996) 454–470.

[93] OPAL Collaboration, *Search for neutral Higgs bosons in Z^0 decays using the OPAL detector at LEP*, Z.Phys. **C73** (1997) 189–199.

[94] CDF Collaboration, DØ Collaboration, *Higgs Boson Studies at the Tevatron*, Phys.Rev. **D88** (2013) 052014, arXiv:1303.6346 [hep-ex].

[95] CMS Collaboration, *Combination of standard model Higgs boson searches and measurements of the properties of the new boson with a mass near 125 GeV*, Conference Contribution, CMS-PAS-HIG-12-045, November, 2012.

[96] ATLAS Collaboration, *Combined coupling measurements of the Higgs-like boson with the ATLAS detector using up to 25 fb^{-1} of proton-proton collision data*, Conference Contribution, ATLAS-CONF-2013-034, March, 2013.

[97] ATLAS Collaboration, *Evidence for Higgs Boson Decays to the $\tau^+\tau^-$ Final State with the ATLAS Detector*, Conference Contribution, ATLAS-CONF-2013-108, November, 2013.

[98] CMS Collaboration, *Combination of standard model Higgs boson searches and measurements of the properties of the new boson with a mass near 125 GeV*, Conference Contribution, CMS-PAS-HIG-13-005, 2013.

[99] ATLAS Collaboration, *Evidence for the spin-0 nature of the Higgs boson using ATLAS data*, Phys.Lett. **B726** (2013) 120–144, arXiv:1307.1432 [hep-ex].

[100] CMS Collaboration, *Study of the Mass and Spin-Parity of the Higgs Boson Candidate Via Its Decays to Z Boson Pairs*, Phys.Rev.Lett. **110** (2013) 081803, arXiv:1212.6639 [hep-ex].

[101] F. Zwirner, *The quest for low-energy supersymmetry and the role of high-energy e^+e^- colliders*, arXiv:hep-ph/9203204 [hep-ph].

[102] O. Buchmueller, R. Cavanaugh, A. De Roeck, S. Heinemeyer, G. Isidori, *et al.*, *Prediction for the Lightest Higgs Boson Mass in the CMSSM using Indirect Experimental Constraints*, Phys.Lett. **B657** (2007) 87–94, arXiv:0707.3447 [hep-ph].

[103] BaBar Collaboration, *Evidence for an excess of $\bar{B} \to D^{(*)}\tau^-\bar{\nu}_\tau$ decays*, Phys.Rev.Lett. **109** (2012) 101802, arXiv:1205.5442 [hep-ex].

[104] WMAP Collaboration, *Wilkinson Microwave Anisotropy Probe (WMAP) three year results: implications for cosmology*, Astrophys.J.Suppl. **170** (2007) 377, arXiv:astro-ph/0603449 [astro-ph].
WMAP Collaboration, *First year Wilkinson Microwave Anisotropy Probe (WMAP) observations: Preliminary maps and basic results*, Astrophys.J.Suppl. **148** (2003) 1, arXiv:astro-ph/0302207 [astro-ph].
WMAP Collaboration, *First year Wilkinson Microwave Anisotropy Probe (WMAP) observations: Determination of cosmological parameters*, Astrophys.J.Suppl. **148** (2003) 175–194, arXiv:astro-ph/0302209 [astro-ph].

[105] J. R. Ellis, S. Heinemeyer, K. Olive, A. Weber, and G. Weiglein, *The Supersymmetric Parameter Space in Light of B^- physics Observables and Electroweak Precision Data*, JHEP **0708** (2007) 083, arXiv:0706.0652 [hep-ph].
J. R. Ellis, S. Heinemeyer, K. A. Olive, and G. Weiglein, *Phenomenological indications of the scale of supersymmetry*, JHEP **0605** (2006) 005, arXiv:hep-ph/0602220 [hep-ph].

[106] S. Heinemeyer, W. Hollik, A. Weber, and G. Weiglein, *Z Pole Observables in the MSSM*, JHEP **0804** (2008) 039, arXiv:0710.2972 [hep-ph].
S. Heinemeyer, W. Hollik, D. Stockinger, A. Weber, and G. Weiglein, *Precise prediction for M(W) in the MSSM*, JHEP **0608** (2006) 052, arXiv:hep-ph/0604147 [hep-ph].

[107] M. Tanaka and R. Watanabe, *Tau longitudinal polarization in $B \to D\tau\nu$ and its role in the search for charged Higgs boson*, Phys.Rev. **D82** (2010) 034027, arXiv:1005.4306 [hep-ph].

[108] M. Tanaka, *Charged Higgs effects on exclusive semitauonic B decays*, Z.Phys. **C67** (1995) 321–326, arXiv:hep-ph/9411405 [hep-ph].
H. Itoh, S. Komine, and Y. Okada, *Tauonic B decays in the minimal supersymmetric standard model*, Prog. Theor. Phys. **114** (2005) 179–204, arXiv:hep-ph/0409228 [hep-ph].
U. Nierste, S. Trine, and S. Westhoff, *Charged-Higgs effects in a new $B \to D\tau\nu$ differential decay distribution*, Phys.Rev. **D78** (2008) 015006, arXiv:0801.4938 [hep-ph].
S. Fajfer, J. F. Kamenik, and I. Nisandzic, *On the $B \to D^*\tau\bar{\nu}_\tau$ Sensitivity to New Physics*, Phys.Rev. **D85** (2012) 094025, arXiv:1203.2654 [hep-ph].

[109] V. D. Barger, J. Hewett, and R. Phillips, *New Constraints on the Charged Higgs Sector in Two Higgs Doublet Models*, Phys.Rev. **D41** (1990) 3421–3441.

[110] DØ Collaboration, *Search for Higgs bosons of the minimal supersymmetric standard model in $p\bar{p}$ collisions at $\sqrt(s) = 1.96$ TeV*, Phys.Lett. **B710** (2012) 569–577, arXiv:1112.5431 [hep-ex].

[111] ALEPH Collaboration, DELPHI Collaboration, L3 Collaboration, OPAL Collaboration, LEP working group for Higgs boson searches, *Search for Charged Higgs bosons: Combined Results Using LEP Data*, Eur.Phys.J. **C73** (2013) 2463, arXiv:1301.6065 [hep-ex].

[112] CDF Collaboration, DØ Collaboration, *Search for Neutral Higgs Bosons in Events with Multiple Bottom Quarks at the Tevatron*, Phys.Rev. **D86** (2012) 091101, arXiv:1207.2757 [hep-ex].

[113] Tevatron New Phenomena Working Group, Higgs Working Group, *Combined CDF and DØ Upper Limits on MSSM Higgs Boson Production in tau-tau Final States with up to 2.2 fb^{-1}*, arXiv:1003.3363 [hep-ex].

[114] DØ Collaboration, *Measurements of the t anti-t cross section at DØ and interpretations*, Conference Contribution, FERMILAB-CONF-10-082-PPD, 2010.
CDF Collaboration, *Search for charged Higgs in top quark decays at CDF*, AIP Conf.Proc. **1078** (2009) 198–200.

[115] CMS Collaboration, *Higgs to tau tau (MSSM)*, Conference Contribution, CMS-PAS-HIG-13-021, 2013.

[116] *Search for charged Higgs bosons decaying via $H^+ \to \tau\nu$ in ttbar events using 4.6 fb^{-1} of pp collision data at $\sqrt{s}$ = 7 TeV with the ATLAS detector*, Conference Contribution, ATLAS-CONF-2012-011, March, 2012.

[117] CMS Collaboration, *Search for a light charged Higgs boson in top quark decays in pp collisions at $\sqrt{s}$ = 7 TeV*, JHEP **1207** (2012) 143, arXiv:1205.5736 [hep-ex].

[118] P. Bechtle, S. Heinemeyer, O. Stal, T. Stefaniak, G. Weiglein, *et al.*, *MSSM Interpretations of the LHC Discovery: Light or Heavy Higgs?*, Eur.Phys.J. **C73** (2013) 2354, arXiv:1211.1955 [hep-ph].

[119] ATLAS Collaboration, *Updated ATLAS results on the signal strength of the Higgs-like boson for decays into WW and heavy fermion final states*, Conference Contribution, ATLAS-CONF-2012-162, November, 2012.

[120] O. S. Bruning, P. Collier, P. Lebrun, S. Myers, R. Ostojic, *et al.*, *LHC Design Report. 1. The LHC Main Ring*, CERN-2004-003, 2004.

[121] J.-L. Caron, *The LHC injection complex*, May, 1993.

[122] V. Frigo, *LHC map in 3D*, March, 1997.

[123] ATLAS Collaboration, https://twiki.cern.ch/twiki/bin/view/AtlasPublic/LuminosityPublicResults#Publications_and_Conference_Resu, revision of February 11, 2014.

[124] ATLAS Collaboration, *Performance of the ATLAS Inner Detector Track and Vertex Reconstruction in the High Pile-Up LHC Environment*, Conference Contribution, ATLAS-CONF-2012-042, 2012.

[125] ATLAS Collaboration, *Luminosity Determination in pp Collisions at $\sqrt{s} = 7$ TeV Using the ATLAS Detector at the LHC*, Eur.Phys.J. **C71** (2011) 1630, arXiv:1101.2185 [hep-ex].

[126] ATLAS Collaboration, *Luminosity Determination in pp Collisions at $\sqrt{s}$ = 7 TeV using the ATLAS Detector in 2011*, Conference Contribution, ATLAS-CONF-2011-116, 2011.

[127] ATLAS Collaboration, `https://twiki.cern.ch/twiki/bin/view/AtlasPublic/LuminosityPublicResults#2011_pp_Collisions`, revision of June 10, 2013.

[128] ATLAS Collaboration, `https://twiki.cern.ch/twiki/bin/view/AtlasPublic/InDetTrackingPerformanceApprovedPlots#Vertex_performance`, revision of June 28, 2013.

[129] J.-L. Caron, *ATLAS detector in A4 format with English captions*, March, 1998.

[130] ATLAS Collaboration, *ATLAS: Technical proposal for a general-purpose p p experiment at the Large Hadron Collider at CERN*, CERN-LHCC-94-43, 1994.

[131] A. Wildauer, K. Prokofiev, and S. Pagan Griso, *Update of primary vertex plots on 7 TeV data from 2011*, ATLAS-Internal Communication, ATL-COM-PHYS-2011-571, May, 2011.

[132] *ATLAS: Detector and physics performance technical design report*, CERN-LHCC-99-14, 1999.

[133] T. Sjostrand, S. Mrenna, and P. Z. Skands, *PYTHIA 6.4 Physics and Manual*, JHEP **0605** (2006) 026, `arXiv:hep-ph/0603175 [hep-ph]`.

[134] R. Frühwirth, W. Waltenberger, and P. Vanlaer, *Adaptive vertex fitting*, J.Phys. **G34** (2007) N343.

[135] R. Frühwirth, *Application of Kalman filtering to track and vertex fitting*, Nucl.Instrum.Meth. **A262** (1987) 444–450.

[136] ATLAS Collaboration, *Electron performance measurements with the ATLAS detector using the 2010 LHC proton-proton collision data*, Eur.Phys.J. **C72** (2012) 1909, `arXiv:1110.3174 [hep-ex]`.

[137] ATLAS Collaboration, *Jet energy scale and its systematic uncertainty in proton-proton collisions at $\sqrt{s}$=7 TeV with ATLAS 2011 data*, Conference Contribution, ATLAS-CONF-2013-004, January, 2013.

[138] ATLAS Collaboration, *ATLAS muon spectrometer: Technical design report*, CERN-LHCC-97-22, 1997.

[139] O. Kortner and E. Moyse, *Pile-up Depedence of the ATLAS Muon Performance*, ATLAS-Internal Communication, ATL-COM-PHYS-2011-1640, December, 2011.

[140] ATLAS Collaboration, *Performance of Missing Transverse Momentum Reconstruction in ATLAS with 2011 Proton-Proton Collisions at $\sqrt{s}$ = 7 TeV*, Conference Contribution, ATLAS-CONF-2012-101, 2012.

[141] S. van der Meer, *Calibration of the Effective Beam Height in the ISR*, CERN-ISR-PO-68-31, 1968.

[142] ATLAS Collaboration, *Performance of the ATLAS Electron and Photon Trigger in p-p Collisions at $\sqrt{s}$ = 7 TeV in 2011*, Conference Contribution, ATLAS-CONF-2012-048, 2012.

[143] ATLAS Collaboration, *Performance of the ATLAS muon trigger in 2011*, Conference Contribution, ATLAS-CONF-2012-099, 2012.

[144] I. Bird, K. Bos, N. Brook, D. Duellmann, C. Eck, *et al.*, *LHC computing Grid. Technical design report*, CERN-LHCC-2005-024, 2005.

[145] T. Gleisberg, S. Hoeche, F. Krauss, M. Schonherr, S. Schumann, *et al.*, *Event generation with SHERPA 1.1*, JHEP **0902** (2009) 007, arXiv:0811.4622 [hep-ph].

[146] Y. L. Dokshitzer, *Calculation of the Structure Functions for Deep Inelastic Scattering and e^+e^- Annihilation by Perturbation Theory in Quantum Chromodynamics.*, Sov.Phys.JETP **46** (1977) 641–653.
V. Gribov and L. Lipatov, *Deep inelastic e p scattering in perturbation theory*, Sov.J.Nucl.Phys. **15** (1972) 438–450.
G. Altarelli and G. Parisi, *Asymptotic Freedom in Parton Language*, Nucl.Phys. **B126** (1977) 298.
F. Halzen and A. D. Martin, *Quarks and Leptons: An Introductory Course in Modern Particle Physics*, ISBN 0-471-88741-2, Wiley, 1984.

[147] A. Martin, W. Stirling, R. Thorne, and G. Watt, *Parton distributions for the LHC*, Eur.Phys.J. **C63** (2009) 189–285, arXiv:0901.0002 [hep-ph].

[148] B. P. Kersevan and E. Richter-Was, *The Monte Carlo event generator AcerMC version 2.0 with interfaces to PYTHIA 6.2 and HERWIG 6.5*, arXiv:hep-ph/0405247 [hep-ph].

[149] A. Sherstnev and R. Thorne, *Different PDF approximations useful for LO Monte Carlo generators*, arXiv:0807.2132 [hep-ph].

[150] H.-L. Lai, M. Guzzi, J. Huston, Z. Li, P. M. Nadolsky, *et al.*, *New parton distributions for collider physics*, Phys.Rev. **D82** (2010) 074024, arXiv:1007.2241 [hep-ph].

[151] S. Frixione and B. R. Webber, *Matching NLO QCD computations and parton shower simulations*, JHEP **0206** (2002) 029, arXiv:hep-ph/0204244 [hep-ph].

[152] J. Pumplin, D. Stump, J. Huston, H. Lai, P. M. Nadolsky, *et al.*, *New generation of parton distributions with uncertainties from global QCD analysis*, JHEP **0207** (2002) 012, arXiv:hep-ph/0201195 [hep-ph].

[153] M. L. Mangano, M. Moretti, F. Piccinini, R. Pittau, and A. D. Polosa, *ALPGEN, a generator for hard multiparton processes in hadronic collisions*, JHEP **0307** (2003) 001, arXiv:hep-ph/0206293 [hep-ph].

[154] G. Corcella, I. Knowles, G. Marchesini, S. Moretti, K. Odagiri, *et al.*, *HERWIG 6: An Event generator for hadron emission reactions with interfering gluons (including supersymmetric processes)*, JHEP **0101** (2001) 010, arXiv:hep-ph/0011363 [hep-ph].

[155] E. Barberio and Z. Was, *PHOTOS: A Universal Monte Carlo for QED radiative corrections. Version 2.0*, Comput.Phys.Commun. **79** (1994) 291–308.

[156] W. Lampl, S. Laplace, D. Lelas, P. Loch, H. Ma, *et al.*, *Calorimeter clustering algorithms: Description and performance*, ATL-LARG-PUB-2008-002, 2008.

[157] J. E. Huth, N. Wainer, K. Meier, N. Hadley, F. Aversa, *et al.*, *Toward a standardization of jet definitions*, FERMILAB-CONF-90-249-E, 1990.

[158] S. Catani, Y. L. Dokshitzer, M. Olsson, G. Turnock, and B. Webber, *New clustering algorithm for multi-jet cross-sections in e^+e^- annihilation*, Phys.Lett. **B269** (1991) 432–438.

[159] S. D. Ellis and D. E. Soper, *Successive combination jet algorithm for hadron collisions*, Phys.Rev. **D48** (1993) 3160–3166, arXiv:hep-ph/9305266 [hep-ph].

[160] M. Cacciari, G. P. Salam, and G. Soyez, *The Anti-k_t jet clustering algorithm*, JHEP **0804** (2008) 063, arXiv:0802.1189 [hep-ph].

[161] Y. L. Dokshitzer, G. Marchesini, and B. Webber, *Dispersive approach to power behaved contributions in QCD hard processes*, Nucl.Phys. **B469** (1996) 93–142, arXiv:hep-ph/9512336 [hep-ph].
M. Dasgupta, L. Magnea, and G. P. Salam, *Non-perturbative QCD effects in jets at hadron colliders*, JHEP **0802** (2008) 055, arXiv:0712.3014 [hep-ph].

[162] S. Catani, F. Krauss, R. Kuhn, and B. Webber, *QCD matrix elements + parton showers*, JHEP **0111** (2001) 063, arXiv:hep-ph/0109231 [hep-ph].
F. Krauss, *Matrix elements and parton showers in hadronic interactions*, JHEP **0208** (2002) 015, arXiv:hep-ph/0205283 [hep-ph].

[163] V. Sudakov, *Vertex parts at very high-energies in quantum electrodynamics*, Sov.Phys.JETP **3** (1956) 65–71.

[164] J. Alwall, S. Hoche, F. Krauss, N. Lavesson, L. Lonnblad, *et al.*, *Comparative study of various algorithms for the merging of parton showers and matrix elements in hadronic collisions*, Eur.Phys.J. **C53** (2008) 473–500, arXiv:0706.2569 [hep-ph].

[165] S. Jadach, Z. Was, R. Decker, and J. H. Kuhn, *The tau decay library TAUOLA: Version 2.4*, Comput.Phys.Commun. **76** (1993) 361–380.

[166] R. Harlander, M. Kramer, and M. Schumacher, *Bottom-quark associated Higgs-boson production: reconciling the four- and five-flavour scheme approach*, arXiv:1112.3478 [hep-ph].

[167] P. Nason, *A New method for combining NLO QCD with shower Monte Carlo algorithms*, JHEP **0411** (2004) 040, arXiv:hep-ph/0409146 [hep-ph].

[168] S. Frixione, P. Nason, and C. Oleari, *Matching NLO QCD computations with Parton Shower simulations: the POWHEG method*, JHEP **0711** (2007) 070, arXiv:0709.2092 [hep-ph].

[169] D. de Florian, G. Ferrera, M. Grazzini, and D. Tommasini, *Transverse-momentum resummation: Higgs boson production at the Tevatron and the LHC*, JHEP **1111** (2011) 064, arXiv:1109.2109 [hep-ph].

[170] E. Bagnaschi, G. Degrassi, P. Slavich, and A. Vicini, *Higgs production via gluon fusion in the POWHEG approach in the SM and in the MSSM*, JHEP **1202** (2012) 088, arXiv:1111.2854 [hep-ph].

[171] S. Alioli, P. Nason, C. Oleari, and E. Re, *A general framework for implementing NLO calculations in shower Monte Carlo programs: the POWHEG BOX*, JHEP **1006** (2010) 043, arXiv:1002.2581 [hep-ph].

[172] R. V. Harlander, S. Liebler, and H. Mantler, *SusHi: A program for the calculation of Higgs production in gluon fusion and bottom-quark annihilation in the Standard Model and the MSSM*, Computer Physics Communications **184** (2013) pp. 1605–1617, arXiv:1212.3249 [hep-ph].

[173] J. Butterworth, J. R. Forshaw, and M. Seymour, *Multiparton interactions in photoproduction at HERA*, Z.Phys. **C72** (1996) 637–646, arXiv:hep-ph/9601371 [hep-ph].

[174] B. P. Kersevan and I. Hinchliffe, *A Consistent prescription for the production involving massive quarks in hadron collisions*, JHEP **0609** (2006) 033, arXiv:hep-ph/0603068 [hep-ph].

[175] J. Butterworth, E. Dobson, U. Klein, B. Mellado Garcia, T. Nunnemann, J. Qian, D. Rebuzzi, and R. Tanaka, *Single Boson and Diboson Production Cross Sections in pp Collisions at $\sqrt{s}$=7 TeV*, ATLAS-Internal Communication, ATL-COM-PHYS-2010-695, August, 2010.

[176] T. Binoth, M. Ciccolini, N. Kauer, and M. Kramer, *Gluon-induced W-boson pair production at the LHC*, JHEP **0612** (2006) 046, arXiv:hep-ph/0611170 [hep-ph].

[177] ATLAS Collaboration, *ATLAS computing: Technical design report*, CERN-LHCC-2005-022, 2005.

[178] G. Barrand, I. Belyaev, P. Binko, M. Cattaneo, R. Chytracek, *et al.*, *GAUDI - The software architecture and framework for building LHCb data processing applications* in *CHEP 2000 proceedings*, pp. 92–95, 2000.
G. Barrand, I. Belyaev, P. Binko, M. Cattaneo, R. Chytracek, *et al.*, *GAUDI - A software architecture and framework for building HEP data processing applications*, Comput.Phys.Commun. **140** (2001) 45–55.

[179] ATLAS Collaboration, *The ATLAS Simulation Infrastructure*, Eur.Phys.J. **C70** (2010) 823–874, arXiv:1005.4568 [physics.ins-det].

[180] GEANT4, *GEANT4: A Simulation toolkit*, Nucl.Instrum.Meth. **A506** (2003) 250–303.
J. Allison, K. Amako, J. Apostolakis, H. Araujo, P. Dubois, *et al.*, *Geant4 developments and applications*, IEEE Trans.Nucl.Sci. **53** (2006) 270.

[181] ATLAS Collaboration, *ATLAS tunes of Pythia 6 and Pythia 8 for MC11*, ATL-PHYS-PUB-2011-009, 2011.

[182] P. Z. Skands, *Tuning Monte Carlo Generators: The Perugia Tunes*, Phys.Rev. **D82** (2010) 074018, arXiv:1005.3457 [hep-ph].

[183] ATLAS Collaboration, *Search for the Standard Model Higgs boson in the H to $\tau^+\tau^-$ decay mode in $\sqrt{s}$ = 7 TeV pp collisions with ATLAS*, JHEP **1209** (2012) 070, arXiv:1206.5971 [hep-ex].

[184] ATLAS Collaboration, *Measuring the b-tag efficiency in a top-pair sample with 4.7 fb^{-1} of data from the ATLAS detector*, Conference Contribution, ATLAS-CONF-2012-097, 2012.

[185] R. K. Ellis, I. Hinchliffe, M. Soldate, and J. van der Bij, *Higgs Decay to $\tau^+\tau^-$: A Possible Signature of Intermediate Mass Higgs Bosons at the SSC*, Nucl.Phys. **B297** (1988) 221.

[186] A. Elagin, P. Murat, A. Pranko and A. Safonov, *A new mass reconstruction technique for resonances decaying to di-τ*, Nucl.Instrum.Meth. **A654** (2011) 481–489, arXiv:1012.4686 [hep-ex].

[187] J. Maluck, *Studien zur Optimierung und Massenrekonstruktion in der Suche nach dem Higgs-Boson des Standardmodells im Zerfall $H \to \tau\tau \to ll + 4\nu$ mit dem ATLAS-Experiment*, Diploma thesis, University of Freiburg, 2013.

[188] ATLAS Collaboration, *Expected Performance of the ATLAS Experiment - Detector, Trigger and Physics*, CERN-OPEN-2008-020, 2009, arXiv:0901.0512 [hep-ex].

[189] ATLAS Collaboration, https://twiki.cern.ch/twiki/bin/view/AtlasProtected/MCPAnalysisGuidelinesRel17MC11a, ATLAS-Internal Documentation, revision of November 8, 2011.

[190] ATLAS Collaboration, *Muon Combined Performance - summary report*, https://indico.cern.ch/getFile.py/access?contribId=15&sessionId=12&resId=0&materialId=slides&confId=155262, ATLAS-Internal Presentation, January, 2012.

[191] ATLAS Collaboration, https://twiki.cern.ch/twiki/bin/viewauth/AtlasProtected/IsEMIdentification#1_2_2011_data_analyses_with_rele, ATLAS-Internal Documentation, revision of January 15, 2013.
ATLAS Collaboration, https://twiki.cern.ch/twiki/bin/viewauth/AtlasProtected/TechnicalitiesForMedium1#Tight_2011_and_2012, ATLAS-Internal Documentation, revision of January 15, 2013.

[192] P. Sommer, *A Measurement of the Electron Identification Efficiency using $W \to e\nu$ Decays in the ATLAS Experiment*, Diploma thesis, Universität Freiburg, 2012.

[193] ATLAS Collaboration, https://twiki.cern.ch/twiki/bin/viewauth/AtlasProtected/EnergyScaleResolutionRecommendations, ATLAS-Internal Documentation, revision of January 15, 2013.

[194] ATLAS Collaboration, https://twiki.cern.ch/twiki/bin/viewauth/AtlasProtected/LArCleaningAndObjectQuality, ATLAS-Internal Documentation, revision of January 15, 2013.

[195] ATLAS Collaboration, https://twiki.cern.ch/twiki/bin/viewauth/AtlasProtected/CaloIsolationCorrections, ATLAS-Internal Documentation, revision of January 15, 2013.

[196] ATLAS Collaboration, https://twiki.cern.ch/twiki/bin/viewauth/Atlas/TrigMuonEfficiency, revision of January 17, 2013.

[197] M. Cacciari and G. P. Salam, *Dispelling the N^3 myth for the k_t jet-finder*, Phys.Lett. **B641** (2006) 57–61, arXiv:hep-ph/0512210 [hep-ph].
M. Cacciari, G. P. Salam, and G. Soyez, *FastJet User Manual*, Eur.Phys.J. **C72** (2012) 1896, arXiv:1111.6097 [hep-ph].

[198] D. Miller, *Measurement of Hadronic Event Shapes and Jet Substructure in Proton-Proton Collisions at 7.0 TeV Center-of-Mass Energy with the ATLAS Detector at the Large Hadron Collider*, PhD thesis, Stanford University, 2011.

[199] G. Piacquadio, *Identification of b-jets and investigation of the discovery potential of a Higgs boson in the $WH \to l\nu b\bar{b}$ channel with the ATLAS experiment*, PhD thesis, Universität Freiburg, 2010.

[200] ATLAS Collaboration, `https://twiki.cern.ch/twiki/bin/viewauth/AtlasProtected/BTaggingBenchmarks#b_tagging_Benchmarks_for_rel_AN1`, ATLAS-Internal Documentation, revision of January 21, 2013.

[201] ATLAS Collaboration, *Measurement of the b-tag Efficiency in a Sample of Jets Containing Muons with 5 fb^{-1} of Data from the ATLAS Detector*, Conference Contribution, ATLAS-CONF-2012-043, 2012.

[202] ATLAS Collaboration, *Commissioning of the ATLAS high-performance b-tagging algorithms in the 7 TeV collision data*, Conference Contribution, ATLAS-CONF-2011-102, 2011.

[203] ATLAS Collaboration, *Measurement of the Mistag Rate with 5 fb^{-1} of Data Collected by the ATLAS Detector*, Conference Contribution, ATLAS-CONF-2012-040, 2012.

[204] ATLAS Collaboration, *b-jet tagging calibration on c-jets containing D^{*+} mesons*, Conference Contribution, ATLAS-CONF-2012-039, 2012.

[205] M. Bosman, L. Fiorini, C. Helsens, A. Juste, L. Mir, J. Nadal, and V. Vorwerk, *Weighting method to propagate heavy-flavor tagging calibrations and related uncertainties*, ATLAS-Internal Communication, ATL-COM-PHYS-2010-331, June, 2010.

[206] ATLAS Collaboration, *Performance of Missing Transverse Momentum Reconstruction in ATLAS with 2011 Proton-Proton Collisions at $\sqrt{s}$ = 7 TeV*, Conference Contribution, ATLAS-CONF-2012-101, 2012.

[207] ATLAS Collaboration, *Local hadronic calibration*, ATL-LARG-PUB-2009-001-2, 2009. ATLAS Collaboration, *Jet energy measurement with the ATLAS detector in proton-proton collisions at $\sqrt{s}$ = 7 TeV*, Eur.Phys.J. **C73** (2013) 2304, `arXiv:1112.6426 [hep-ex]`.

[208] ATLAS Collaboration, `https://twiki.cern.ch/twiki/bin/viewauth/AtlasProtected/HowToCleanJets2011`, ATLAS-Internal Documentation, revision of December 19, 2011.

[209] ATLAS Collaboration, *Search for the Standard Model Higgs Boson in the Decay Mode $H \to \tau^+\tau^- \to ll+$ 4 Neutrinos in Proton-Proton Collisions at $\sqrt{s}$=7 TeV with the ATLAS Detector*, ATLAS-Internal Communication, ATL-COM-PHYS-2011-1611, November, 2011.

[210] ATLAS Collaboration, *Measurement of the inclusive $W^{\pm}$ and Z/γ cross sections in the electron and muon decay channels in pp collisions at $\sqrt{s}$ = 7 TeV with the ATLAS detector*, Phys.Rev. **D85** (2012) 072004, `arXiv:1109.5141 [hep-ex]`.

[211] C. Anastasiou, L. J. Dixon, K. Melnikov, and F. Petriello, *High precision QCD at hadron colliders: Electroweak gauge boson rapidity distributions at NNLO*, Phys.Rev. **D69** (2004) 094008, `arXiv:hep-ph/0312266 [hep-ph]`.

[212] K. Melnikov and F. Petriello, *Electroweak gauge boson production at hadron colliders through $O(\alpha_s^2)$*, Phys.Rev. **D74** (2006) 114017, arXiv:hep-ph/0609070 [hep-ph].
K. Melnikov and F. Petriello, *The W boson production cross section at the LHC through $O(\alpha_s^2)$*, Phys.Rev.Lett. **96** (2006) 231803, arXiv:hep-ph/0603182 [hep-ph].
R. Gavin, Y. Li, F. Petriello, and S. Quackenbush, *FEWZ 2.0: A code for hadronic Z production at next-to-next-to-leading order*, arXiv:1011.3540 [hep-ph].

[213] R. Hamberg, W. van Neerven, and T. Matsuura, *A Complete calculation of the order α_s^2 correction to the Drell-Yan K factor*, Nucl.Phys. **B359** (1991) 343–405, [Erratum *ibid* **B644** (2002) 403].

[214] ATLAS Collaboration, *Search for Neutral MSSM Higgs bosons in sqrts = 7 TeV pp collisions at ATLAS*, Conference Contribution, ATLAS-CONF-2012-094, 2012.

[215] ATLAS Collaboration, *Background estimates in the $H \to WW \to l\nu l\nu$ analysis with 4.7 fb^{-1} of data collected with the ATLAS detector at $\sqrt{s}$=7 TeV*, ATLAS-Internal Communication, ATL-COM-PHYS-2012-288, March, 2012.
ATLAS Collaboration, *Search for the Standard Model Higgs boson in the $H \to WW(*) \to \ell\nu\ell\nu$ decay mode with 4.7 /fb of ATLAS data at $\sqrt{s} = 7$ TeV*, Phys.Lett. **B716** (2012) 62–81, arXiv:1206.0756 [hep-ex].

[216] J. Pumplin, D. Stump, R. Brock, D. Casey, J. Huston, *et al.*, *Uncertainties of predictions from parton distribution functions. 2. The Hessian method*, Phys.Rev. **D65** (2001) 014013, arXiv:hep-ph/0101032 [hep-ph].

[217] M. Cacciari, M. Czakon, M. Mangano, A. Mitov, and P. Nason, *Top-pair production at hadron colliders with next-to-next-to-leading logarithmic soft-gluon resummation*, Phys.Lett. **B710** (2012) 612–622, arXiv:1111.5869 [hep-ph].

[218] S. Thoma, *Search for the neutral Higgs Bosons of the Minimal Supersymmetric Standard Model in the $\tau_{lep}\tau_{had}$ decay mode with the ATLAS experiment*, PhD thesis, Universität Freiburg, 2013.

[219] F. Siegert, private communication, December 2013.

[220] J. M. Campbell, J. Huston, and W. Stirling, *Hard Interactions of Quarks and Gluons: A Primer for LHC Physics*, Rept.Prog.Phys. **70** (2007) 89, arXiv:hep-ph/0611148 [hep-ph].

[221] R. Harlander and M. Wiesemann, *Jet-veto in bottom-quark induced Higgs production at next-to-next-to-leading order*, arXiv:1111.2182 [hep-ph].

[222] M. Wiesemann, private communication, October 2012.

[223] R. Harlander, M. Mühlleitner, J. Rathsman, M. Spira, and O. Stål, *Recommendations for the evaluation of Higgs production cross sections and branching ratios at the LHC in the Two-Higgs-Doublet Model*, arXiv:1312.5571 [hep-ph].

[224] ATLAS Collaboration, *Improved luminosity determination in pp collisions at $\sqrt{s}$ = 7 TeV using the ATLAS detector at the LHC*, arXiv:1302.4393 [hep-ex].

[225] ATLAS Collaboration, https://twiki.cern.ch/twiki/bin/view/AtlasPublic/MuonPerformancePublicPlots#AnchorPlots2011, revision of March 27, 2013.

[226] *Jet energy measurement and systematic uncertainties using tracks for jets and for b-quark jets produced in proton-proton collisions at* $\sqrt{s} = 7$ *TeV in the ATLAS detector*, Conference Contribution, ATLAS-CONF-2013-002, January, 2013.

[227] ATLAS Collaboration, *Probing the measurement of jet energies with the ATLAS detector using photon+jet events in proton-proton collisions at* $\sqrt{s} = 7$ *TeV*, Conference Contribution, ATLAS-CONF-2012-063, 2012.
ATLAS Collaboration, *Probing the measurement of jet energies with the ATLAS detector using Z+jet events from proton-proton collisions at* $\sqrt{s} = 7$ *TeV*, Conference Contribution, ATLAS-CONF-2012-053, 2012.

[228] ATLAS Collaboration, `https://twiki.cern.ch/twiki/bin/viewauth/AtlasProtected/MissingETUtility`, ATLAS-Internal Documentation, revision of February 13, 2012.

[229] G. Cowan, K. Cranmer, E. Gross, and O. Vitells, *Asymptotic formulae for likelihood-based tests of new physics*, Eur.Phys.J. **C71** (2011) 1554, `arXiv:1007.1727 [physics.data-an]`.

[230] S. Wilks, *The Large-Sample Distribution of the Likelihood Ratio for Testing Composite Hypotheses*, Annals Math.Statist. **9** (1938) 60–62.

[231] A. Wald, *Tests of Statistical Hypotheses Concerning Several Parameters When the Number of Observations is Large*, Trans. Amer. Math. Soc. **54** (1943) 426–482.

[232] ATLAS Collaboration, *Search for neutral MSSM Higgs bosons decaying to* tau^+tau^- *pairs in proton-proton collisions at* $\sqrt{s} = 7$ *TeV with the ATLAS detector*, Phys.Lett. **B705** (2011) 174–192, `arXiv:1107.5003 [hep-ex]`.

[233] CMS Collaboration, *Search for Neutral MSSM Higgs Bosons Decaying to Tau Pairs in pp Collisions at* $\sqrt{s} = 7$ *TeV*, Phys.Rev.Lett. **106** (2011) 231801, `arXiv:1104.1619 [hep-ex]`.

[234] CMS Collaboration, *Search for Neutral Higgs Bosons Decaying to Tau Pairs in pp Collisions at* $\sqrt{s}$*=7 TeV*, Conference Contribution, CMS-PAS-HIG-11-029, 2011.

[235] A. Zeileis, K. Hornik, and P. Murrell, *Escaping RGBland: Selecting colors for statistical graphics*, Comput. Stat. Data Anal. **53** (2009) 3259–3270.

[236] R. Brun and F. Rademakers, *ROOT: An object oriented data analysis framework*, Nucl.Instrum.Meth. **A389** (1997) 81–86.

Acknowledgments

All along the path that lead to the completion of this thesis, I enjoyed the company, counsel, and encouragement of many great people. I want to express my gratitude for the outstanding support by:

- my supervisor, Prof. Dr. Markus Schumacher, who set the scene for the conception and realization of this work and who was always there to give feedback and counsel—with my best interests at heart, and who never lost his sense for fairness nor his concept of the greater picture,
- Dr. Matthew Beckingham for helping me transition to Higgs physics, to CERN, and to Freiburg—serving as first post-doc and serving all kinds of grilled specialties,
- Dr. Henrik Nilsen for his support in understanding weak-boson backgrounds, his friendly collaboration, and his good sense of humor,
- Dr. Markus Warsinsky, to whom I owe a great debt of gratitude for prying open the black boxes of the MSSM, Monte Carlo event generators, and the modified frequentist method and for providing aid in an uncountable number of ways and at any hour of the night or day (last, but not least, by providing heartening references to literature and cinematography), and
- Dr. Stanley Lai, who always made time for discussing and thinking through whatever challenge had to be overcome and who never grew tired of proof-reading.

I thank Dr. Michael Böhler for proof-reading and for untiringly restoring service whenever the computing center went on strike. The same is true for the other members of the highly committed admin teams of the local and university clusters—one Appreciation Day a year is clearly insufficient. I further thank Markus Köhli for many cans of espresso, for bringing my first self-assembled PC to life, and for helping me "escape RGBland" [235] in ROOT [236]. I also thank my colleagues Dr. Julian Glatzer and Dr. Sascha Thoma as well as the other analysis teams from the TU Dresden and the University of Washington for their great work, fruitful discussions, and good "crisis management" in the context of preparing our paper [10] for publication. I thank Dr. Sven Heinemeyer and Dr. Oscar Stål for their help in obtaining the signal predictions of the pMSSM-7 points from their publication [118].

Very warm thanks go to all colleagues who shared an office with me and brightened my day when error messages and nonsensical output lingered and seemed to defeat any hope of progress.

I am very grateful for the friendly welcome into Prof. Dr. Karl Jakobs' and Markus' groups as well as the Reculet Hikers' Society—you will always have a place in my heart. Thanks to you, the respectful feeling that we are standing on the shoulders of giants (cf. the name ATLAS) gains a breathtaking impression of what we can achieve by friendly collaboration.

Finally, I want to thank my family and friends for their love, understanding, friendship, and help. What you do for me every day is beyond description!

Ich erkläre hiermit, dass ich die vorliegende Arbeit ohne unzulässige Hilfe Dritter und ohne Benutzung anderer als der angegebenen Hilfsmittel angefertigt habe. Die aus anderen Quellen direkt oder indirekt übernommenen Daten und Konzepte sind unter Angabe der Quelle gekennzeichnet. Insbesondere habe ich hierfür nicht die entgeltliche Hilfe von Vermittlungs- bzw. Beratungsdiensten (Promotionsberater/-beraterinnen oder anderer Personen) in Anspruch genommen. Die Arbeit wurde bisher weder im In- noch im Ausland in gleicher oder ähnlicher Form einer Prüfungsbehörde vorgelegt.

Die Bestimmungen der Promotionsordnung der Universität Freiburg für die Fakultät für Mathematik und Physik sind mir bekannt; insbesondere weiß ich, dass ich vor der Aushändigung der Doktorurkunde zur Führung des Doktorgrades nicht berechtigt bin.

Freiburg, 24. März 2014 (Holger von Radziewski)